Sensorless Control of Surface Mounted Permanent Magnet Machine Using Fundamental PWM Excitation

Yahan Hua (Bsc, MSc)

Thesis submitted to the University of Nottingham

for the degree of Doctor of Philosophy

July 2009

Sensorless Control of Surface Mounted Permanent Magnet Machine Using Fundamental PWM Excitation

August 8, 2009

Abstract

This thesis describes the development of a sensorless control method for a surface mounted permanent magnet synchronous machine drive system. The saturation saliency in the machine is tracked from the stator current transient response to the fundamental space vector PWM (pulse width modulation) excitation. The rotor position and speed signals are obtained from measurements of the stator current derivative during the voltage vectors contained in the normal fundamental PWM sequence.

In principle, this scheme can work over a wide speed range. However, the accuracy of the current derivative measurements made during narrow voltage vectors reduces. This is because high frequency current oscillations exist after each vector switching instant, and these take a finite time to die down. Therefore, in this thesis, vector extension and compensation schemes are proposed which ensure correct current derivative measurements are made, even during narrow voltage vectors, so that any induced additional current distortion is kept to a minimum.

The causes of the high frequency switching oscillations in the AC drive system are investigated and several approaches are developed to reduce the impact of these oscillations. These include the development of a novel modification to the IGBT gate drive circuit to reduce the requirement for PWM vector extension. Further improvements are made by modifications to the current derivative sensor design together with their associated signal processing circuits. In order to eliminate other harmonic disturbances and the high frequency noise appearing in the estimated position signals, an

adaptive disturbance identifier and a tracking observer are incorporated to improve the position and speed signals. Experimental results show that the final sensorless control system can achieve excellent speed and position control performance.

Acknowledgement

This thesis is a natural result of a PhD research as any of the others, in expectation but out of easy reach. Throughout the course of the research, support and help from many sides are motivating and impressive.

Prof. Greg Asher and Dr. Mark Sumner provide persistent support and guidance in these years. Their professional attitude and mode of thinking always make the problems clear and helps me out of being lost. Also genuine thank is given to Gao Qiang. I am very lucky to be his close colleague and friend. His kindness and patience is influential among the crowd.

I should thank many people from the PEMC(power electronics and motor control) group of University of Nottingham. In 2005 I started my PhD study with very poor practical experience. Pavol Makys and Matteo Tomasini showed me what is an engineer should behave like. Edward Christopher and Alan Waston patiently helped me with the instrumentation and safety measures. Lee Empringham and Liliana made me feel working in such a group can be such an interesting thing. Si Dung Huy taught me with the building work and paid enough patience and care to my project. Discussions with Kamel Saleh is also very helpful.

Also, I would express my appreciation to my examiners, Prof. Paul Acarnely, Dr. Chris Gerada, and Prof. Jon Clare, for their advice on the final corrections to this thesis.

Finally, this thesis should be attributed to my dear families and close friends. I always

know I will be safe with my parents and my elder brother, even in the high uncertainties and the troubles. Some of my close friends are always there ready for listening to me. They are my best treasure.

Contents

List of Figures

List of Tables

Chapter 1

Introduction

1.1 Background

Electric Motors are fundamental to the fast efficient operation of many industrial processes from fans, conveyers through to steel and paper mills. They are known as the main workhorse in industry and different reports [1] indicate that they consume approximately $60\% - 70\%$ of all electricity generated. With the introduction of high performance control techniques (such as "Vector Control" proposed in 1969[2]), three-phase AC motors, primarily induction motors(IM), have now taken over from DC motors for nearly all speed and torque controlled applications, due mainly to their simplicity and robustness.

The permanent magnet synchronous motor (PMSM) is another type of AC motor. Its advantages includes high efficiency, high power density and low inertia, due to the absence of rotor windings. Recently with the development and increased availability of permanent magnet (PM) materials, the cost of PMSM has reduced significantly. This has led to many opportunities for applying PMSM in more widespread industrial applications [3, 4].

An AC variable speed drive controls the speed and/or position of either an induction

motor or a synchronous motor by applying controlled voltages and currents to the motor using a power electronic converter. The most common three-phase AC to AC power converter consists of a three-phase rectifier, a DC link capacitor and a voltage source inverter (VSI). The VSI employs pulse width modulation (PWM) to synthesize the AC voltages from the DC link voltage. Advances in power electronic devices along with the development of high performance digital processors at low cost have enabled the realization of complicated control algorithms such as vector control for commercial AC drives. The vector control method, which is now available from most AC drive manufactures, uses mathematical transforms based on an estimate of the instantaneous flux position in the motor to decouple the stator current into independent field and torque producing components and thus enables fast control of the torque in the machine. This current decoupling requires the three-phase stator currents to be regarded as a current vector, which is then measured and controlled in a rotating coordinate frame. Speed or rotor position feedback is also necessary for the decoupling process and the correct operation of the speed control system. Usually the position signal is measured by a position sensor, such as a resolver or optical encoder, mounted directly on the shaft of the motor. The speed signal is derived from the changing rate of position. However, these position sensors add to the cost of the drive and can be comparable to the cost of the drive at low powers. The sensor and the wires carrying the sensor signals reduce system reliability. There is a need therefore to achieve high performance control of AC motors without using a shaft mounted speed or position sensor. This is commonly termed "sensorless" control.

The first types of sensorless control scheme researched derive the flux vector or rotor speed using some estimator or an observer based on the fundamental mathematical electromechanical model of the motor [5, 6, 7, 8, 9]. These types of methods always perform badly in the low speed range, because the stator or rotor flux signal is essentially derived from the machine's back-EMF, which tends to zero as the rotor speed reduces. Thus the motor position becomes unobservable when the stator frequency

approaches zero. The other drawback of the fundamental model based methods is that the performance of the observers relies on the precise knowledge of machine parameters. These parameter values may vary according to the operating conditions of the drive, which leads to the incorrect estimates of the flux position and speed, with a significant deterioration in drive performance. Alternative methods, independent of the estimation of the back-EMF and free from the parameter errors, have been investigated by researchers [10, 11, 12, 13, 14]. The main approach employed here is to track the rotating saliency properties of a motor. This appears to be the most promising technology to overcome the limitations at low speed. The saliency can be caused by the magnetic saturation or by the geometric and physical construction of the rotor. These saliencies can be exploited to extract a rotor position signal by measuring the motor's electrical response to an added high frequency sinusoidal voltage or current signal. Alternatively, specific test pulses can be employed.

Both approaches exploit the fact that the stator inductances are modulated by the saliency position. Therefore the measured transient current response is consequently a function of the saliency position. By measuring either the high frequency current response or the derivative of the motor current, it is possible to derive a rotor position estimate using suitable signal processing. The saliency tracking methods can guarantee correct, stable operation at very low and even zero fundamental frequency.

For the saliency tracking methods which employ high frequency signal injection, a high frequency pulsating or rotating voltage/current signal is superimposed on the fundamental input voltage/current to the motor. The current/voltage responses due to this injection is measured and the saliency position is identified using a suitable demodulation scheme. The disadvantages are that the measured modulated signal is also influenced by the non-linearities of the inverter and the current sensors, and can have a poor signal to noise ratio (SNR). More importantly, the signal injection may bring about additional torque ripple, increased motor losses, and higher acoustic noise.

It is however, relatively easy to implement, although it can only be used at low and zero speed.

The other group of methods utilize the switching pulses (and additional test vectors) applied to the motor by the VSI. This approach provides excitations with much higher amplitude than any other type of voltage signal injection, but with a smaller duration. The transient current changes caused by the switching of a specific switching state voltage vectors can be measured and used to detect the saliency position because of the saliency spatial modulation of the stator inductances. The INFORM method [13] is the simplest method to understand and was proposed in 1996. It applies three pairs of special test pulses during the inactive period (null vector) of the normal (fundamental) PWM sequence. The INFORM method is only applicable in the low speed range, because it may be difficult to apply these test vectors when the speed increases as the inactive state vector becomes shorter. The additional test pulses used by the INFORM method create additional current distortion in the motor (again with increased torque pulsations and acoustic noise), and may also introduce higher voltage stresses when switching between two test pulses. In addition, the complexity of embedding the scheme into the conventional PWM of a drive can make it difficult to program into a real time controller.

Previous research at the University of Nottingham has succeeded in integrating a rotor position estimation scheme for an induction motor into the normal fundamental PWM sequence, by using the active vectors of the fundamental PWM sequence for the required transient excitations [14, 15]. Rotor position information is extracted from the measurement of the rate of change of motor current (current derivative) to these normal PWM sequence vectors and no additional test vectors are required. A further advantage is that it can be used over a wider speed range, although some restrictions apply as the voltage limit is approached. The main difficulty of integrating the required transient excitations within the fundamental PWM sequence arises from

the high frequency current oscillations which occur after each power device switches. These oscillations are a consequence of the parasitic circuit within the motor, cable and inverter, and are excited by the high dv/dt when an IGBT switches. Measurement of the rate of stator current change has to be made after the switching oscillations die down to obtain a correct measurement, and a minimum time is required for these oscillations to die down sufficiently. The minimum waiting time is denoted as t_{dmin}. If the active vectors in the fundamental PWM sequence last for a time less than t_{dmin} ("narrow vectors"), modification of the PWM sequence is necessary. An extension and compensation scheme is required allowing correct current derivative sampling during the narrow vectors of the fundamental PWM sequence. This scheme extends the widths of the narrow active vectors to t_{dmin} and then compensates its resultant effect in order to keep the mean output voltage unchanged. However, it was shown in [14] that this method could be successfully applied to sensorless control of an induction motor with only a minor modification to the normal PWM strategy, and with operation over a wide speed range.

The aim of this project was therefore to develop a sensorless control system for a permanent magnet synchronous motor based on the fundamental PWM excitation technique. The fundamental PWM voltage waveforms are used as excitation signals to extract the saliency position information. This sensorless control method ideally should incur no additional losses, torque ripples or acoustic noise compared to a sensored system, and should be easier to embed into a drive than the sinusoidal injection or test pulse approaches. That is, clean position and speed estimation signals should be obtained only using the fundamental PWM sequence with the minimum stator current distortion, and it should work over a wide speed range.

Project Objectives

In this thesis, the development of a new sensorless control surface mounted PMSM drive system is described. The position and speed signals are estimated from the stator current transient measurements which are in response to the inverter's switching vectors in the fundamental PWM waveforms. The theory for this method is analyzed in this thesis. For narrow vectors in the fundamental PWM sequence, vector extensions are needed to ensure the current derivatives can be measured without the disturbance of high frequency switching noise. Several methods are provided in this thesis. A new extension and compensation scheme is proposed in this research, which can effectively minimize the induced line current distortion. For the current ripples or distortions caused by the test vectors or vector modifications, a new method is introduced for studying the current waveforms of different position estimation methods based on PWM vector excitation. The current ripples caused by these position estimation schemes are campared using the proposed ripple vectors and experimental results.

For the position estimation method only using fundamental PWM sequence, the extra current ripple or distortion mainly comes from the extensions of narrow vectors which are required for the current derivative sampling. If the required minimum vector duration t_{dmin} can be decreased, the additional current ripple will be reduced. In this research the high frequency switching oscillations, which decide the value of t_{dmin}, are investigated. Common mode oscillations and differential oscillations are categorized through their origins and flowing paths. Several measures to reduce the switching oscillations are discussed and tested. One effective way is to enlarge the gate resistance value during the current derivative measurements. A novel modification to the IGBT gate drive circuit is presented in the thesis, making the gate resistance changeabe and reducing the switching oscillations and thus the requirement for pulse extensions. Current derivative signals are obtained from specially designed di/dt sensors and signal

processing circuits, which improve the signal to noise ratio of these measurements. A $20kW$ power converter is designed and built up in this research. The power circuits, the control platform and the design considerations are all explained in this thesis.

An adaptive disturbance identifier (ADI) scheme is implemented for eliminating the harmonics appearing in the estimated position signals, which is effective in both low and high frequency range. The angle difference between the flux position estimated through saturation saliency tracking and the real rotor position, is investigated and compensated by looking up table. A mechanical tracking observer is also designed to further improve the quality of the position and speed estimations. Finally the experimental results are presented to demonstrate the excellent sensorless speed and position control performance for a surface mounted PM synchronous motor.

1.2 Overview of this Thesis

This thesis is presented as follows:

Chapter 2 reviews the development history of the sensorless control systems. The most significant methods and solutions proposed in literature are introduced. Sensorless control methods based on the machine fundamental models are introduced. Then the crucial problem of the sensorless control in the low and zero speed range is highlighted. The sensorless rotor position/speed estimators based on sailency tracking, which are the main solution for sensorless control at low speed, are categorized and explained. The main problems of achieving higher performance for these sensorless control schemes are summarized.

A promising method of sensorless control uses PWM transient excitations to exploit the saliency position of the rotor. There are a number of different implementations. In Chapter 3, the principles of these implementations are described. The position estimation method developed and implemented in this research is only using the fundamen-

tal PWM sequence. This kind of method is firstly applied on the surface mounted PM synchronous motor. One critical issue with these saliency tracking methods is the current distortions induced by these position estimation implementations. A new scheme for investigating the current distortions is proposed in Chapter 3, and then it is applied to evaluate the current ripples caused by the introduced position estimation schemes. In order to suppress further the current distortion caused by the method only using the fundamental PWM sequence, a new improved extension and compensation scheme is proposed and used. The current distortions with these different implementations are then compared.

Chapter 4 describes the measurement process of the stator current rate of change, which are essential for the sensorless control methods based on the PWM transient excitations. It is known that the voltage vectors providing the excitations for position estimation should last no less than the required minimum duration t_{dmin}. This is due to the current oscillations at the switching instants. In Chapter 4, these high frequency current switching oscillations are investigated. They are due to the common mode and the differential mode current flows. Because the requirement of the vector minimum duration t_{dmin} is the main reason of additional current distortion, several new schemes to reduce the switching oscillation effect have been discussed in Chapter 4. The schemes include increasing the IGBT gate resistance, increasing the snubber capacitance, and applying common mode compensation. The investigations of their effects are detailed in Chapter 4. The specially designed di/dt sensors and the signal filtering and amplifying circuits used in this research are also described.

In Chapter 5, the complete AC drive power converter built in this research is introduced from its overall system and the main functional parts. The design considerations of main power circuit, measurement and protection circuit, signal processing circuit and control platform, are all clarified. Particularly, the gate drive circuit has a special design to achieve a program controllable IGBT gate resistance, which en-

ables the investigations of di/dt measurements with different IGBT switching speed as explained in Chapter 4. The new circuit and its operation are explained in Chapter 5. The increased gate resistance suppresses the high frequency switching oscillations and thus helps to reduce the required minimum vector duration.

In Chapter 6 the schemes for enhancing the estimated position signal are proposed. If the estimated position signals from the di/dt measurements are directly used for the field orientation and closed-loop sensorless control, the positioning accuracy, the feedback quality and dynamic characteristics will be poor. This has a number of causes: the multiple saliencies and the non-sinusoidal distribution of the rotor flux; the error between the flux angle obtained from the saturation saliency and the actual rotor position angle; and the random noise present in the di/dt measurement. In this research, an adaptive disturbance identifier (ADI) is adopted to reduce the disturbing effects from other spacial harmonics. The error between flux angle and rotor angle is compensated by an online scheme. The position and speed signals for the closed-loop vector control are obtained by a mechanical tracking observer. All these schemes are explained in Chapter 6.

Chapter 7 details the implementation of the sensorless speed control schemes on a surface mounted PM synchronous motor. Both the sensorless speed control and the sensorless position control are designed and applied. Experimental results are presented to verify their excellent performance.

Chapter 8 presents conclusions to the whole thesis and recommendations for future research.

Chapter 2

Sensorless Control of AC Machines

VF (scalar) control was mainly used for AC drive control before Felix Blaschke proposed the concept of vector control in 1969[2]. Vector control, or field oriented control, allows for the quick torque response of AC machines similar to that of the DC motor. This is realized by controlling the rotor flux and torque efficiently through rotor flux orientation. In addition to induction motors, vector control has also been widely used on other AC motors, such as permanent magnet AC machines and double fed induction motors. However, the flux position or speed needs to be obtained for the field orientation and closed-loop control. Speed or position is normally measured by some kind of shaft mounted sensor, such as an encoder or resolver. Sensorless control aims at speed or position control without using any shaft mounted speed or position sensor. The main advantages of sensorless control are that the total cost is significantly reduced, the sensor, its connectors and its cable are removed, the installation becomes easier, and importantly the reliability can be greatly improved. In harsh environments, sensorless control is very important. Eliminating the sensor without sacrificing the good dynamic response and the operating accuracy is the main aim of research on the sensorless control.

Joetten and Maeder were among the researchers to firstly explore the sensorless vector

control of induction motors [5]. In their research a back EMF vector is generated from a sensorless slip frequency calculation scheme, from which the rotor frequency signal is then generated. The rotor frequency estimator forms an inner control loop, as part of the drive control system.

With the development of modern control approaches [16, 17], the state-space representation was proposed, which provides a precise and powerful tool for the analysis and synthesis of the control and observer algorithms. This development introduced advanced observer and estimators into the motor drives field. The models of the motor drive systems are gradually maturing and optimizing for estimator designs. Instantanous estimators of the flux position or speed based on the fundamental mathematical models of the machine, show good performance in the higher speed range. Using these estimators, the flux information is obtained essentially from the motor back EMF. They will fail at very low or zero speed, because the magnitude of the back-EMF voltage becomes quite small at low speed and will vanish at standstill[18]. Moreover, in the low speed range the signal-to-noise ratio degrades and the fundamental models are more sensitive to the parameter errors[6]. The fundamental model based methods do not yield good results if the machine exhibits unmodelled nonlinearities and disturbances[18].

In order to overcome these drawbacks, new types of position estimation schemes, which are based on the saliency phenomena in the motors, have been developed. Using a high frequency test signal, the resultant motor response to the test signal is measured and then used to find the anisotropy position and hence the rotor position. These kinds of methods are currently the main trend of research on the sensorless control in the very low or zero speed range.

This chapter will review the research in literature for sensorless control of AC drives. Both methods, the fundamental model based methods and the saliency tracking methods, will be presented. The principal schemes of each type will be introduced.

2.1 Fundamental Model Based Sensorless Control Methods

With the advanced control theories being developed and applied to AC motor drives, various machine models and observers have been designed for the estimation of the rotor flux and speed. Generally most of these methods can be classified into groups as described in the following sections.

2.1.1 Flux Position Estimators Based on Model Reference Adaptive System

The model reference adaptive system (MRAS) is a broad subject with wide applications and many realizations. The general idea is to create an adaptive closed loop scheme to drive the plant output to match with the output of a model with the desired performance. As shown in Fig 2.1, a typical MRAS consists of one reference model with the output y, one adaptive model including some unknown parameter(s) with the output $\hat{y}$, and an adaptive controller. The input signal u is fed to both the real system and the mathematical models. The error between y and $\hat{y}$ is driven to be zero by the adaptive controller by adjusting the unknown parameter(s) in the adaptive model. The proper adaptation law ensures the stability of the whole system, and the unknown parameter(s) will be guaranteed to approach the real value. In this diagram, when applied as the estimator of motor flux and speed, different candidates can be chosen as the output signal. The common ones are stator currents, rotor or stator flux linkage and reactive power.

Reference [6] uses MRAS in the speed estimation of an induction motor. It proposes a well-known MRAS estimator, using the voltage model expressed by (2.1) as the reference model and the current model of (2.2) as an adjustable model.

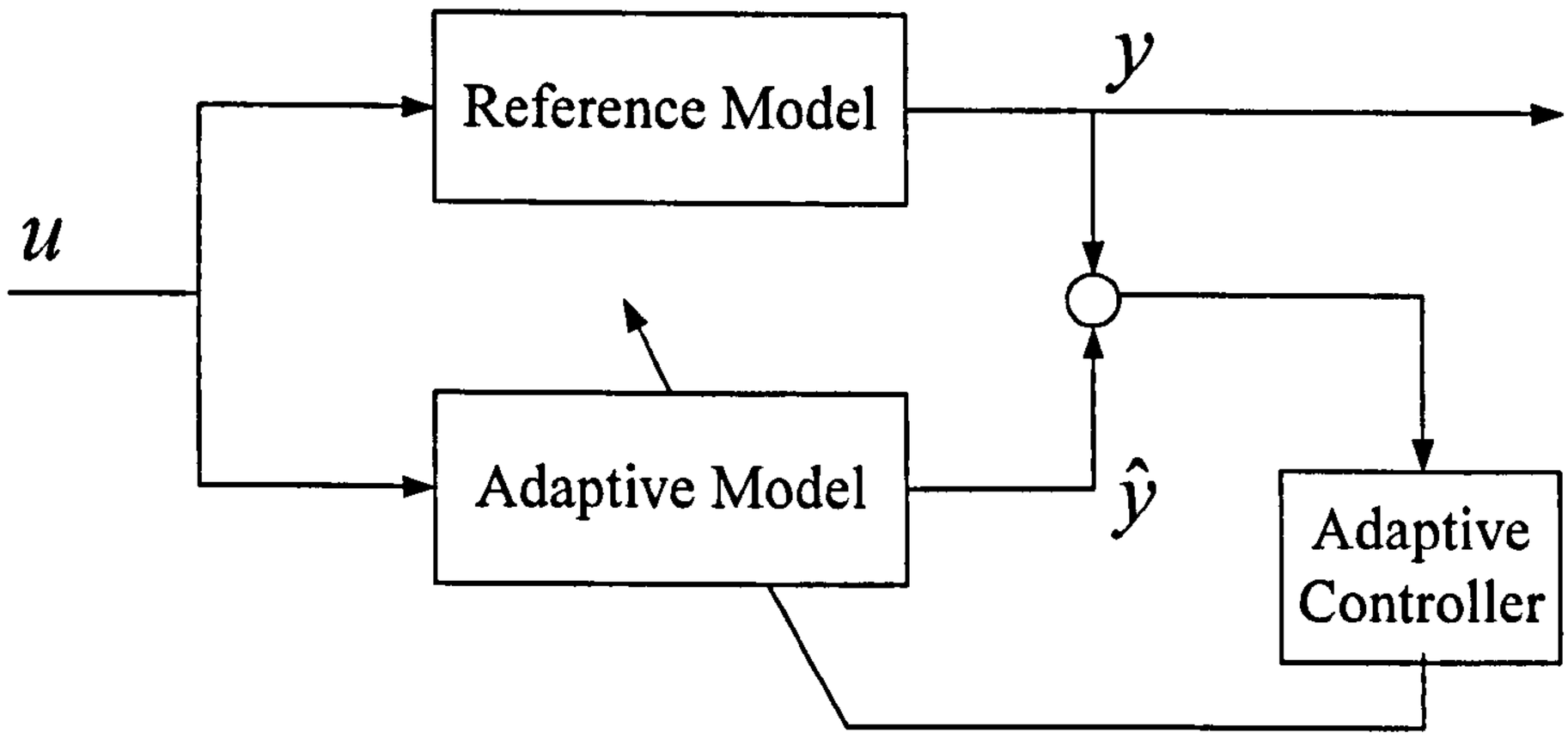

Figure 2.1: Basic configuration of MRAS

$$p\begin{bmatrix} \psi_{r\alpha} \\ \psi_{r\beta} \end{bmatrix} = \frac{L_r}{L_m}\left(\begin{bmatrix} u_{s\alpha} \\ u_{s\beta} \end{bmatrix} - \begin{bmatrix} R_s + \sigma L_s p & 0 \\ 0 & R_s + \sigma L_s p \end{bmatrix}\begin{bmatrix} i_{s\alpha} \\ i_{s\beta} \end{bmatrix}\right) \tag{2.1}$$

$$p\begin{bmatrix} \psi'_{r\alpha} \\ \psi'_{r\beta} \end{bmatrix} = \begin{bmatrix} -1/T_r & \omega_r \\ \omega_r & -1/T_r \end{bmatrix}\begin{bmatrix} \psi'_{r\alpha} \\ \psi'_{r\beta} \end{bmatrix} + \frac{L_M}{T_r}\begin{bmatrix} i_{s\alpha} \\ i_{s\beta} \end{bmatrix} \tag{2.2}$$

where $u_{s\alpha,s\beta}$, $i_{s\alpha,s\beta}$ and $\psi_{r\alpha,r\beta}$ are the stator voltages, stator currents and rotor flux in the stationary reference frame, which is represented by the commonly used two phase $(\alpha - \beta)$ representation [19]. L_r, L_s and L_M are the rotor inductance, stator self-inductance and the mutual inductance. R_s is the stator resistance. T_r is the rotor time constant. ω_r is the rotor electrical angular speed. $\sigma = 1 - \frac{L_m^2}{L_r L_s}$ is the total leakage factor. $p = \frac{d}{dt}$. The diagram of this speed and flux estimator is shown in Fig 2.2.

The rotor flux linkage vector calculated from the reference model $\psi_{r\alpha,r\beta}$ and calculated from the adaptive model $\psi'_{r\alpha,r\beta}$ are compared. The error signal ε obtained from their vector cross product is sent to the adaptive controller, which adjusts the estimated speed $\hat{\omega}_r$ that appears in the current model. Both the rotor flux and the rotating speed are identified in this structure. Pure integration in the reference voltage model (2.1) cannot be used in practice, and therefore both models are augmented with the first order low pass filters in [6]. It is also recognized that the instability can be brought

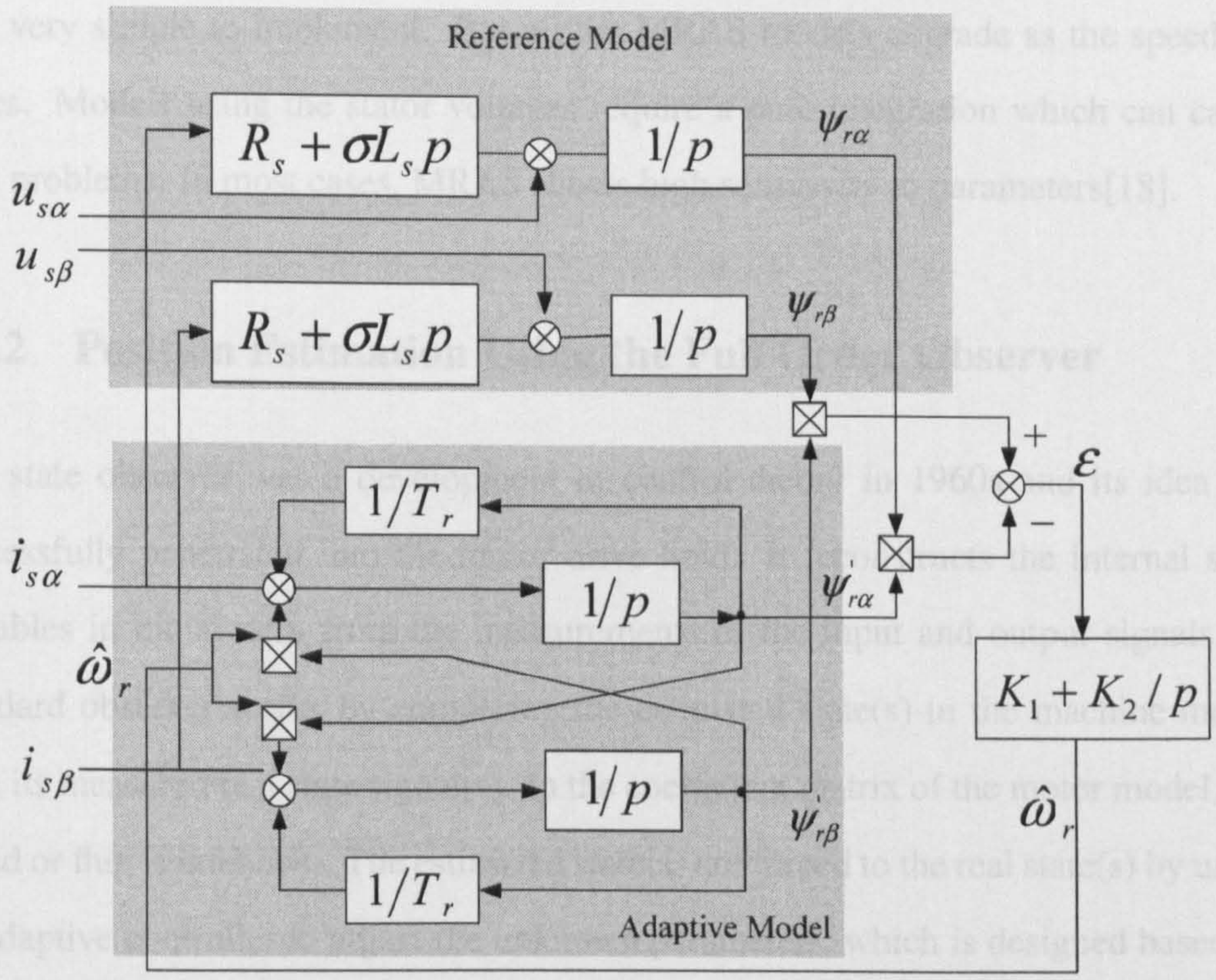

Figure 2.2: Diagram of the MRAS rotor speed identification system

about at low speed, depending on the pole/zero locus of the proposed system.

Another MRAS structure proposed in [7] derives the back-EMF from the reference and adaptive models and makes their difference as the error vector, avoiding the open-loop integration. It uses the cross product of the stator current vector and the back-EMF, representing the instantaneous reactive power. The advantage of this scheme is that it does not include the stator resistance which can change during operation.

An improvement in rotor flux and speed estimate at very low speed was obtained through a closed-loop flux observer MRAS (MRAS-CLFO)[20]. At higher frequencies the system is equivalent to the basic MRAS. When the speed approaches zero and the speed estimate forcing is lost, a mechanical model compensates for this effect. However the operation at low speed still depends on the precise knowledge of the mechanical parameters.

The MRAS scheme is sufficiently robust and accurate at higher stator frequencies.

It is very simple to implement. But all the MRAS models degrade as the speed reduces. Models using the stator voltages require a pure integration which can cause drift problems. In most cases, MRAS shows high sensitivity to parameters[18].

2.1.2 Position Estimation Using the Full Order Observer

The state observer was a development in control theory in 1960s and its idea has successfully penetrated into the motor drive field. It reconstructs the internal state variables in the system from the measurements of the input and output signals. A standard observer works by comparing the estimated state(s) in the machine model with its measured real state signal(s). In the coefficient matrix of the motor model, the speed or flux is unknown. The estimated state(s) are forced to the real state(s) by using an adaptive controller to adjust the unknown parameters, which is designed based on a stability analysis. If only part of the internal states are missing and are required, a reduced-order observer also works well by outputting a reduced-order state vector.

Reference [8] explored the use of observers for the flux estimation in induction motors. It views an observer as "a real time simulation corrected by feedback of a prediction error term, and thereby permits the observer approach to be directly related to the flux estimation schemes". The induction motor is modelled in [9] with the stator currents and the rotor flux as the inner states and the stator voltages as the input signals.

$$\frac{d}{dt}\begin{bmatrix} i_s \\ \psi_r \end{bmatrix} = \begin{bmatrix} A_{11} & A_{12} \\ A_{21} & A_{22} \end{bmatrix}\begin{bmatrix} i_s \\ \psi_r \end{bmatrix} + \begin{bmatrix} B_1 \\ 0 \end{bmatrix} u_s \tag{2.3}$$

$$i_s = C\begin{bmatrix} i_s \\ \psi_r \end{bmatrix} \tag{2.4}$$

where i_s is the stator current vector, ψ_r is the rotor flux vector, u_s is the stator voltage vector, and

$$A_{11} = -[r_s/(\sigma L_s) + (1-\sigma)/(\sigma\tau_r)]I$$

$$A_{12} = L_m/(\sigma L_s L_r)\,[(1/\tau_r)I - \omega_r J_1]$$

$$A_{21} = (L_m/\tau_r)I$$

$$A_{22} = -(1/\tau_r)I + \omega_r J_1$$

$$B_1 = 1/(\sigma L_s)I$$

$$C = \begin{bmatrix} I & 0 \end{bmatrix}$$

$$I = \begin{bmatrix} 1 & 0 \\ 0 & 1 \end{bmatrix}, J_1 = \begin{bmatrix} 0 & -1 \\ 1 & 0 \end{bmatrix}$$

where r_s is the stator phase resistance, σ is the total leakage coefficient, L_m,L_s and L_r are the mutual inductance, stator self inductance, and rotor self inductance, and $\tau_r = L_r/r_r$ is the rotor time constant.

The full-order observer is constructed by comparing the estimated states with the measured ones, stator current here, as shown in Fig 2.3 [9]. The unknown speed in the coefficient matrix A is obtained through an adaptive scheme, by forcing the observer to meet the Lyapunov criterion according to the stability analysis. The observer gain matrix G is carefully selected in order to ensure the stable operation and dynamic performance of the observer.

Sensorless motor drives with the observer based estimators may lose their stability at low speeds or in regenerating mode. Based on the linearized model of the observer system, the observer gain is redesigned in[21], so that the performance with regeneration mode at low speed is improved. Different diagrams of the flux or speed observer and different considerations for choosing the observer gain are proposed in [22, 23, 24]. However they all face stability problems in the low speed range.

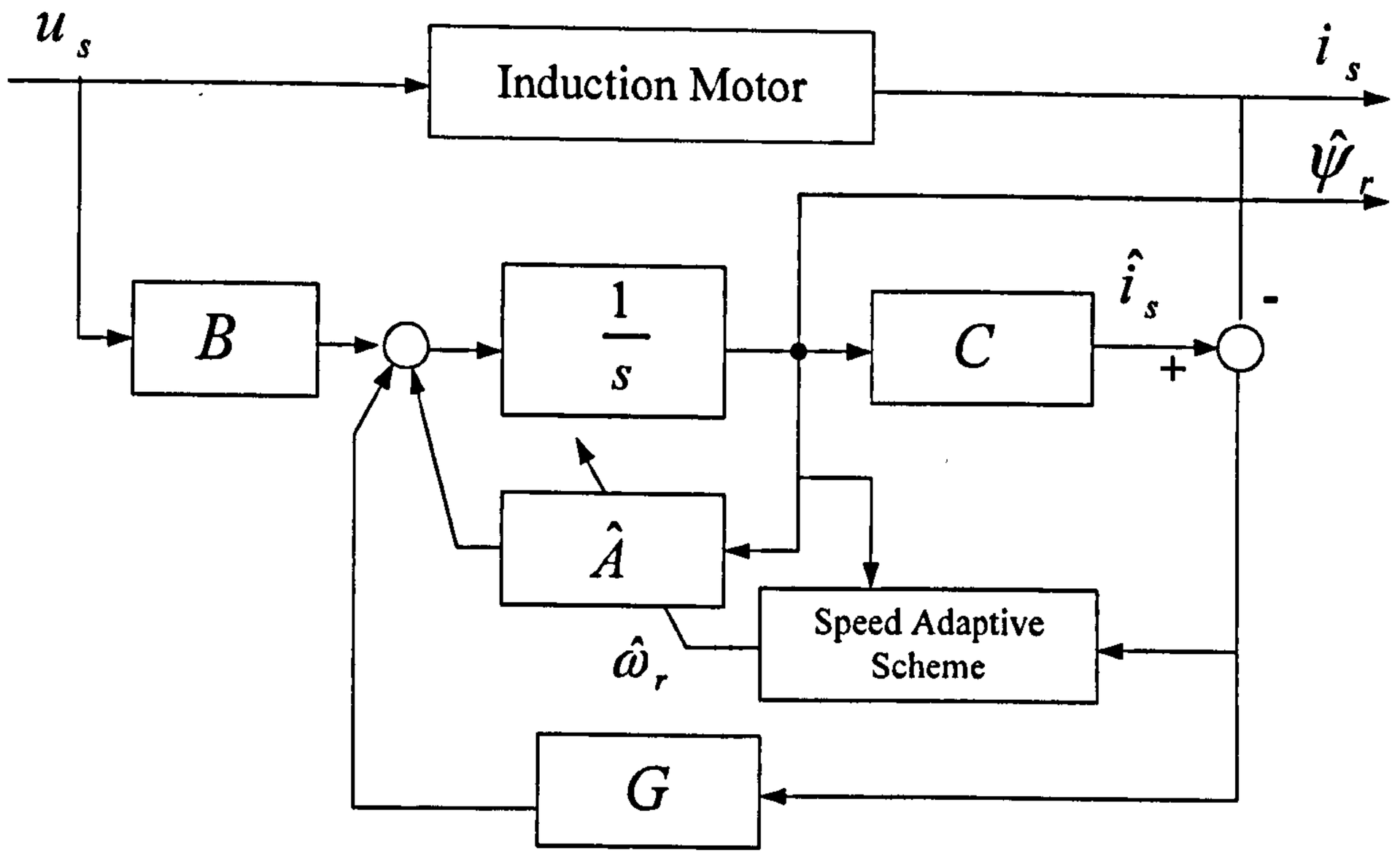

Figure 2.3: Block diagram of rotor speed and flux adaptive observer

2.1.3 Estimation Using the Extended Kalman Filter

When the rotor speed is regarded as one state variable of a machine system, the machine model becomes a non-linear one. The Kalman Filter is an efficient recursive filter that estimates the state of a dynamic system from a series of noisy measurements[17]. In the extended Kalman filter (EKF), the state transition and observation models are not limited to a linear assumption, and is thus applicable to estimation for non-linear motor models. The EKF is introduced to estimate the speed and rotor flux of an induction motor in [25], aiming to give an optimum estimation from the noisy measurements.

The application of the extended Kalman filter to speed and position estimation is demonstrated in [26] and [27]. The typical implementation involves the linearization of the model around some operation point, and a prediction of the state variables are finally made from the previous time step. The Kalman gain is then calculated and the updated error covariance is given with the measurement information at the present time step. The new prediction is then made with the Kalman filter correction equation,

and so forth.

The Kalman filter can be considered as one case of an observer with the observer gain yielding the minimum least square estimation error with white Gaussian noise [8]. The full-order observer has been compared in [28] with an extended Kalman filter for the speed and flux estimation of an induction motor. The conclusion is that the EKF is more sensitive to the parameter errors and its accuracy tends to be poor in the low speed range. But the EKF is more applicable to a noisy system.

The reduced-order observers for rotor flux oriented vector control have been considered in [29], which indicates that the voltage model and the current model can be obtained as special cases when selecting the observer gain. The resulting closed-loop flux dynamics are analyzed with an arbitrary observer gain. A framework for the gain selection, which is critical for the behaviour of an observer based system, is developed.

2.1.4 Discussions on the Fundamental Model Based Estimators

A large number of schemes and combinations from different principles have been developed for the sensorless control of motor drives. At the same time, various observer methods have appeared in an attempt to achieve better estimation performance, such as neural networks[30], sliding-mode control[31], fuzzy control[32], etc. Some researchers try to find the relationship between the different control schemes[33, 24, 34, 35]. For example, the MRAS, observer and EKF approaches are reviewed in [33], and the conclusion is that the Luenberger observer shows the best behaviour with respect to the dynamic response and parameter sensitivity, but EKF is the best if the noise parameters are known. In [24] the basic MRAC estimator is shown to be a special case of the full-order observer. In [34] the rotor-flux MRAS, torque-current MRAS and the adaptive observer are compared. A comparison between full-order observer, reduced-order observer and MRAS is made in [35]. No matter which type of observer is used, the same problems are always seen with the fundamental model based

sensorless control schemes, which are explained below.

At very low and zero frequency, as the rotor flux signal is essentially derived from the back-EMF, this tends to be lost when the rotor frequency reduces. As the stator voltage diminishes, the rotor flux and speed become unobservable from the models with stator currents and voltages[36]. Also, there always exists an unstable region at low speed, especially in the regenerating mode when the fundamental model based estimators are used. The instability comes from the inherent property of the estimation process and also the parameter error. It is difficult to design a sensorless system with complete stability.

Precise knowledge of machine parameters has a crucial effect on the performance of the model based estimators. However actual parameters of the motors may vary depending on the operating conditions. The stator resistance, the rotor time constant and also the permanent magnet flux may change with temperature. The stator inductances may be altered by the magnetic saturation. Also, the models do not exhibit enough immunity to measurement noise, especially for the conventional models including pure integrations[37, 38]. For good performance, online parameter estimation or adaptive controllers are always required[38].

2.2 Sensorless Control Methods Based on Saliency Tracking

All the fundamental model-based methods fail at low speed due to the inherent unobservability of the machine resulting from the lack of back-EMF information. Alternative methods, independent of the back-EMF, have been investigated by researchers. The tracking of the anisotropic properties of the rotor, represented by the variations of the stator impedances, especially leakage inductance, becomes an influential mechanism for the rotor position detection.

The saliency tracking methods may be categorized into two groups depending on the type of excitation used to exploit the reactance modulation:

1. Injecting a high frequency voltage or current signal

2. Applying voltage vector transient excitation

2.2.1 Types of Saliency

The saliency noted in the sensorless control means the asymmetric properties of the machine. It can be structural asymmetries arising from the machine geometric construction; or a flux imbalance distribution resulting from magnetic saturation; or some intentionally introduced anisotropies. Because the sensorless control methods investigated in this research are applicable to both permanent magnet machines and induction motors, the saliencies appearing in both machine types are described.

2.2.1.1 Permanent Magnet Synchronous Motors and their Saliencies

Permanent magnet (PM) machines have outstanding characteristics compared with other motor types. They show higher power density, lower maintenance cost, and higher efficiency. Two major classes of PM motors are the brushless DC motor and the PM synchronous motor (PMSM). The two classes are structurally similar, as permanent magnet-based, three phase AC motors. The main difference between the brushless DC motor and the PMSM is the shape of their back-emf induced in the stator windings and the resultant different excitation waveforms required for their control. A brushless DC motor needs a trapezoidal excitator, while PMSM needs a sinusoidal excitator similar to the control from standard AC drives. Hence brushless DC motors will not be considered in this research and it will focus on the sensorless control for AC machines.

The rotor of the PMSM can be constructed with different configurations. The cross

sections of three different rotor types of PMSM are shown in Fig 2.4. Figure 2.4(a) shows surface mounted PM with the magnets fixed to its surface. Because rare earth magnet have a relative permeability close to unity, this type of PM machine presents a constant effective air gap length resulting in a geometrically symmetric structure. The other type shown in Fig 2.4(b) is constructed by placing the magnets in shallow slots; this is called as inset-magnet rotor. This facilitates construction. The iron interpoles cause a structural saliency. The interior-magnet machine(IPM) shown in Fig 2.4(c) has rectangular magnets placed in slots inside the rotor, which provide more protection against centrifugal forces and demagnetization. This type is highly salient and shows a significant amount of reluctance torque.

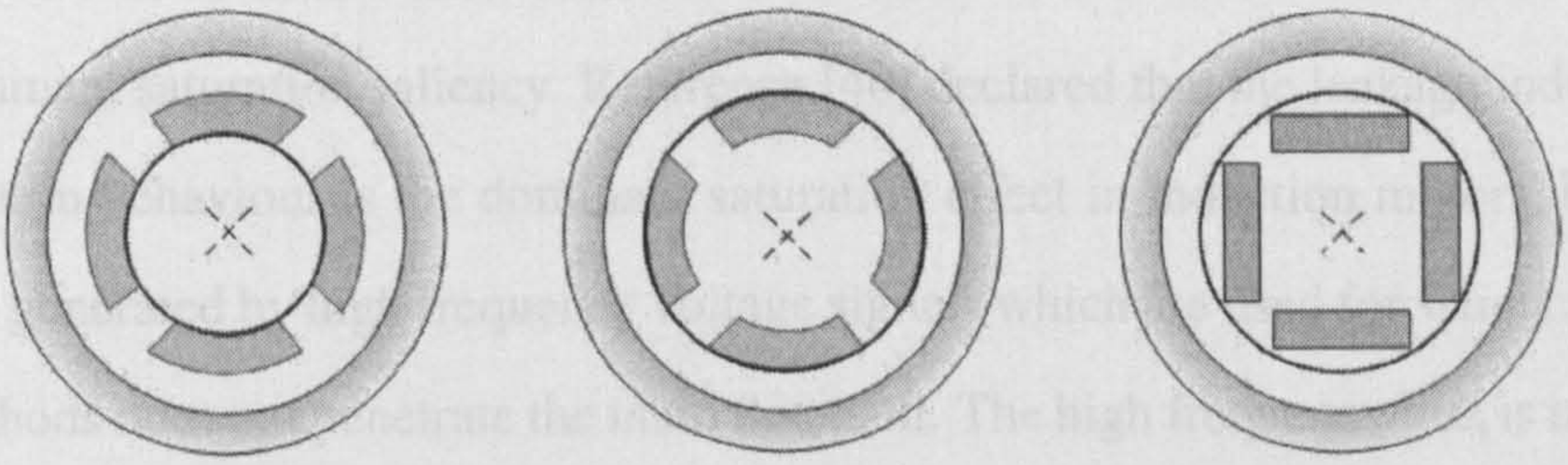

(a) (b) (c)

Figure 2.4: Different rotor configurations (a)Surface mounted (b) Inset (c) Interior

For the interior type PMSM the structural saliency is dominant. This rotor geometry effect can be represented as[39]:

$$\begin{aligned} L_{md} &= k_d L_m \\ L_{mq} &= k_q L_m \\ (k_d &< k_q) \end{aligned} \tag{2.5}$$

where L_{md}, L_{mq} are magnetizing inductances in the reference frame synchronous with the saliency, L_m is the average magnetizing inductance, k_d, k_q are the form factors, which can be analytically calculated from the rotor geometrical parameters. This saliency is directly oriented with the rotor and $L_{md} < L_{mq}$. This effect in interior

magnet motors is higher than that in inset magnet motors.

In a surface mounted PMSM, without significant structural saliency, the magnetic saturation due to the main flux causes the dominant spatial anisotropy in the synchronous stator inductances. The saturated iron presents a reduction in the permeability and thus a decrease of the inductance value of the coils whose flux linkage paths go through the saturated section. The saturation of the machine's iron may affect both the main and the leakage flux paths, modulating both the magnetic inductances (L_{md}, L_{mq}) and the leakage inductances (L_{ld}, L_{lq}) (which will be further explained in Chapter 6).

The saturation in the magnetizing inductance and in the leakage inductance are opposite and tend to cancel each other. The variation of total stator inductances reflect the dominant saturation saliency. Reference [40] declared that the leakage inductance modulation behaviour is the dominant saturation effect in induction motors, because the flux generated by high frequency voltage signals which are used for saliency tracking methods does not penetrate the main flux path. The high frequency flux is impeded from penetrating the main flux path by the induced high frequency currents in the rotor cage. In the PM machines with laminated rotors, the high frequency currents induced in the rotor are not significant, and thus the magnetizing inductance saleincies are tracked in the sensorless control methods.

The stator transient inductances modulated by the saturation induced saliency in the rotor speed synchronous reference frame can be modelled as[10]:

$$\mathbf{L}^{r}_{\sigma dq} = \begin{bmatrix} L_{\sigma d} & 0 \\ 0 & L_{\sigma q} \end{bmatrix} = \begin{bmatrix} \bar{L}_{\sigma} + \Delta L & 0 \\ 0 & \bar{L}_{\sigma} - \Delta L \end{bmatrix} \tag{2.6}$$

where $L_{\sigma d}$ and $L_{\sigma q}$ are the transient leakage inductances on $d-$ and $q-$ axes, $\bar{L}_{\sigma} = \frac{L_{\sigma d} + L_{\sigma q}}{2}$ and $\Delta L = \frac{L_{\sigma d} - L_{\sigma q}}{2}$.

In the stationary reference frame, this can be further represented by

$$\mathbf{L}^{s}_{\sigma\alpha\beta} = \begin{bmatrix} L_{\sigma\alpha} \\ L_{\sigma\beta} \end{bmatrix} = \begin{bmatrix} \bar{L}_{\sigma} + \Delta L cos(2\theta_r) & \Delta L sin(2\theta_r) \\ \Delta L sin(2\theta_r) & \bar{L}_{\sigma} - \Delta L cos(2\theta_r) \end{bmatrix} \tag{2.7}$$

where θ_r is the rotor position angle. The inductance modulation appears at twice the electrical frequency, because the saturation exists around the two rotor poles in one electrical period. For an inset type PMSM, the saturation effect causes its dominant saliency, but a geometrical saliency exists at the same time.

The saturation saliency moves along the air gap with the main flux and has a period of two cycles per pole pair. It should be noted that this saliency position angle will deviate from the rotor position when the PM is loaded. In this case the flux induced by the torque current creates a shift of the total air-gap flux distribution towards the q-axis. The maximum flux density in the iron changes its angular position and thus the saturation saliency deviates from the rotor axis. The error angle between the rotor position and the position estimated from saturation saliency tracking is proportional to the torque current i_{sq}. The shifted angle from the estimated frame to the real rotor frame, needs to be compensated.

2.2.1.2 Saliencies in Induction Motors (IM)

The investigations of the sensorless control in this research also apply to IM and so the saliencies in IM are also introduced in this section. Similar to the surface mounted PMSM, there is no prominent structural asymmetry in the configuration of IM. The possible saliencies of IM are caused by:

1. Saturation caused by the fundamental wave excitation. Similar to the surface mounted PM, the saturation effect of the fundamental wave flux changes the permeance of the leakage flux paths in the stator and rotor, and thus modulates the total

leakage inductances[41]. The saturation saliency is influenced by the point of operation of the machine and by the design of the laminations.

2. Rotor bar slotting harmonics. This saliency is explained by the variable magnetic coupling between the stator windings and the discrete rotor bars of an induction motor, which is influenced by the distribution of the stator and rotor winding in the slots. This phenomenon has been analyzed in [42, 43], which show that the air-gap lengths change with the slotting. The magnetic permeance of the flux paths and the stator transient reactances will therefore be modulated by the slotting harmonics. A quasi-continuous signal oriented with the rotor position can be obtained by measuring the total stator leakage inductance, which varies over one period for each rotor slot displacement. Therefore for an induction motor with N_r rotor slots, the stator inductance modulated by the rotor slotting saliency will appear as N_r cycles per revolution. The geometry of the rotor laminations have a large influence. Only rotors with open or semi-closed slots shows significant slotting modulated inductance variation[43]. Also skewing of the rotor slots will reduce the saliency effect. If the skew angle happens to be one rotor pitch, the rotor slot saliency will reduce. This saliency is tied directly to the angular position of the rotor[15].

3. Designed asymmetry. Besides these inherent asymmetric properties, it is also possible to introduce some engineered saliency in order to enhance the position dependent variation. The leakage inductance variation is increased in [11] by changing the widths of the rotor slot openings. A "double-cage" motor with designed rotor resistance variation has been proposed in [44] , which is independent of the main flux and load conditions.

2.2.2 Saliency Tracking by High-frequency Signal Injection

The basic idea is to superimpose a high-frequency signal on the fundamental electrical output of the inverter, and then to extract the position information from the measured

resultant signals on the motor side. For a high frequency signal, the stator leakage inductances are modulated by the saliencies existing in the machine. To detect the position signal through the saliency phenomenon, one can inject a high frequency voltage[40] or current [12] signal, and observe the corresponding current or voltage response. Due to the inherent limitations on the bandwidth of the current controller, voltage injection is mostly preferred and will be the only type of injection introduced in this thesis.

2.2.2.1 Position Estimation by $\alpha\beta$ Rotating Injection

In the $\alpha\beta$ injection method, a rotating voltage vector is applied in the stationary reference frame. The three-phase voltage vector rotating at the high frequency ω_c, as shown in (2.8), is generated, and added to the fundamental voltage output.

$$\mathbf{u}_c = u_c e^{j\omega_c t} \tag{2.8}$$

Its resultant current vector $\mathbf{i}_c$ with the injection frequency ω_c will appear in the measured stator current vector, which is modulated by the machine saliency The current response in the $\alpha\beta$ stationary reference frame is[44]:

$$\begin{bmatrix} i_{c\alpha} \\ i_{c\beta} \end{bmatrix} = \frac{\hat{V}_i}{\omega_c L_{\sigma d} L_{\sigma q}} \begin{bmatrix} \bar{L}_\sigma cos(\omega_c t) + \Delta L cos(2\theta_r - \omega_c t) \\ \bar{L}_\sigma sin(\omega_c t) + \Delta L sin(2\theta_r - \omega_c t) \end{bmatrix} \tag{2.9}$$

where $L_{\sigma d}$, $L_{\sigma q}$, $\bar{L}_\sigma$ and ΔL are the same as defined in (2.7).

This can be written as

$$\mathbf{i}_c = \frac{u_c}{\omega_c L_{\sigma d} L_{\sigma q}} \left(\bar{L}_\sigma e^{j\omega_c t} + \triangle L e^{j(-\omega_c t + 2\theta_r)} \right) = \mathbf{i}_{cp} + \mathbf{i}_{cn} \tag{2.10}$$

This shows that the current response to the high frequency rotating injection comprises

two components with opposite rotating directions. The current component rotating in the negative direction $\mathbf{i}_{cn}$ carries the rotor position information. $\mathbf{i}_{cn}$ has a magnitude much smaller than that of the component rotating in the positive direction $\mathbf{i}_{cp}$. Furthermore all the current signals at the injection frequency are hidden in the much stronger fundamental stator current and the switching harmonics. Many methods have been proposed for the demodulation of the rotor position signals from the measured stator currents[11, 44, 45].

A heterodyning demodulation strategy is used in [44]. The responding currents are separated from the measured stator currents by band-pass filters. Then this strategy filters the current response on the estimated reference frame synchronous with the negative rotating current vector, which is:

$$\mathbf{i}_c \cdot e^{-j(2\hat{\theta}_r - \omega_c t)} = \frac{u_c}{\omega_c L_d L_q} \left(\bar{L}_\sigma e^{j(2\omega_c t - 2\hat{\theta}_r)} + \triangle L e^{j(2\theta_r - 2\hat{\theta}_r)} \right) \tag{2.11}$$

This transformation allows the negative current component with rotor position information to be extracted by a low pass filter, obtaining:

$$\mathbf{i}_{cn} \cdot e^{-j(2\hat{\theta}_r - \omega_c t)} = \frac{u_c \Delta L}{\omega_c L_d L_q} e^{j(2\theta_r - 2\hat{\theta}_r)} \tag{2.12}$$

The rotor position estimation error can be obtained from the imaginary part in (2.12), which is then used to drive a position and speed observer. This strategy is shown in Fig 2.5.

Another mechanical observer with this heterodyne demodulation scheme is proposed in [11] for improving the dynamic performance. Synchronous reference frame filters are also proposed to filter off the undesired components in the stator currents[46].

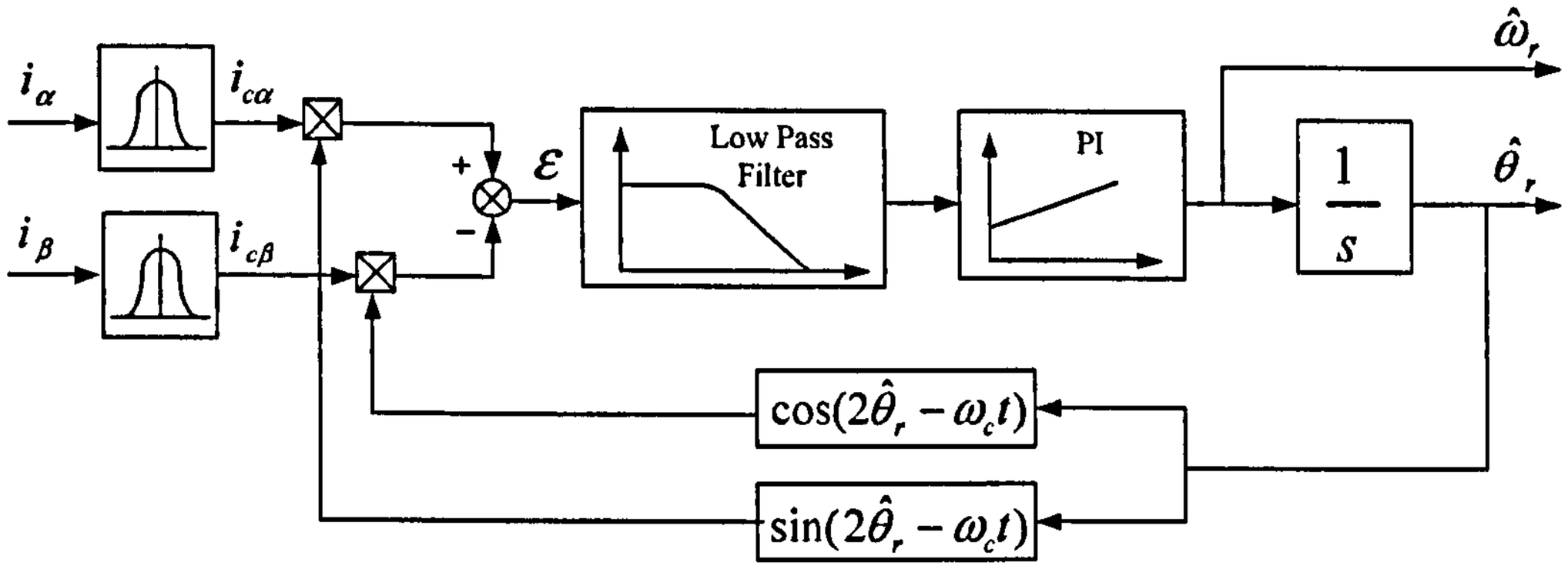

Figure 2.5: Position and speed observer including heterodyne demodulation technique

2.2.2.2 Position Estimation by d-axis Injection

Another high frequency signal injection method relies on a pulsating carrier signal that oscillates along a specific synchronous direction, normally along with the estimated $d-axis$. This idea was initially proposed in [12] with a current signal injection, but the alternating voltage signal is more applicable. The pulsating high frequency voltage signal as follows is superimposed in the estimated $\hat{d}-axis$:

$$\begin{bmatrix} u_{\hat{d}} \\ u_{\hat{q}} \end{bmatrix} = u_c \begin{bmatrix} sin(\omega_c t) \\ 0 \end{bmatrix} \tag{2.13}$$

Due to the main flux saturation saliency of the machine, the trajectory of the resulting current vector deviates from that of the injected voltage vector. The pulsating current response on the estimated $\hat{q}-axis$ is proportional to $sin(2\triangle\theta_d)$, which can be used to obtain the orientation angular error between the estimated $\hat{d}-\hat{q}$ axes and the actual $d-q$ frame directed by the saliency position[47, 48, 49]. The angular error is then used to drive the tracking observer to obtain the saliency position angle.

A measurement frame, displaced spatially 45^o from the estimated flux reference frame $\hat{d}-\hat{q}$, was proposed in [50]. Due to the saturation saliency in the motor, the stator impedance has its maximum value in the rotor flux direction and its minimum value

in its orthogonal direction. Assuming a symmetrical and sinusoidal distribution of the high frequency stator impedance, the orthogonal pulsating current components in this new reference frame should have the same amplitude if the estimated frame $\hat{d}-\hat{q}$ is correctly oriented with the flux position. Thus the difference between the amplitudes of these two current components in the measurement frame can be used as the error signal for position orientation.

Based on d-axis pulsating signal injection, various signal demodulation techniques have been developed. In [49], the pulsating current response is extracted by the fast Fourier transform (FFT) algorithm. A closed-loop tracking observer that corrects the estimated field angle at each sampling cycle of the current controller is given in [48]. This has the advantage of being independent from any machine parameters. In [51] a big improvement is obtained by using the measured pulsating current itself as the reference signal for the demodulator, instead of using the injected voltage. In this way both the estimated signal and the reference signal undergo the deadtime and nonlinear distortions of the inverter, and thus the resulting position signal should be free from these effects.

2.2.3 Saliency Tracking by Voltage Vector Excitations

Driven by a PWM inverter, the machine is under repetitious step-like high voltage pulses, which naturally provide high frequency excitations for exploiting the inherent saliency in the machine to obtain the position information. The switching pulses have much higher amplitudes than that of any injected high frequency signal. The transient flux generated by the PWM excitations can exhibit high rate of change. The transient fluxes link with the stator windings and contribute to the total leakage flux which is used for tracking the saliency modulated leakage inductances.

2.2.3.1 Transient Excitations Using Additional Test Vectors

The method denoted as INFORM (Indirect Flux Detection by Online Reactance Measurement) is described in [13]. Its principle and technique is widely accepted by researchers due to its easy implementation and good results.

The transient current response resulting from the voltage space vectors depends on the inverter switching state, the DC link voltage, the stator resistance, the back emf, and the phase leakage inductances. The relationship can be represented by the stator voltage equation:

$$\mathbf{u}_s = r_s \mathbf{i}_s + \mathbf{l}\frac{d\mathbf{i}_s}{dt} + \mathbf{e} \tag{2.14}$$

where $\mathbf{u}_s$ and $\mathbf{i}_s$ are the stator voltage and stator current vectors, $\mathbf{e}$ is the back EMF vector, and r_s and $\mathbf{l}$ are the stator resistance and stator total inductance. For each voltage vector applied on the machine, $\mathbf{u}_s$ is always taken as the DC link voltage.

The DC link voltage can be assumed constant during normal operation. If the effects caused by the back emf and the voltage drop on the stator resistances can be eliminated, the effect of the saliency modulation on the leakage inductances will be reflected by the measured current changes. INFORM solves this problem by inserting a pair of test vectors in opposite directions on the voltage phase plane, within a null vector of one PWM period. Their total effect on the output voltage is zero. Assuming the stator current and back emf values are unchanged during these two adjacent test vectors, the influence from back emf and resistive voltage drop can be easily cancelled.

Three pairs of test voltage vectors are applied to achieve one sample of the position estimation, assuming the rotor position is not changed in their operating periods, which is reasonable at low speed range. The current rate of changes during these test vectors are sampled. After some manipulations of the voltage equations, the saliency position signal, defined by a rotating position vector $\vec{p}$, can be obtained from the measured current derivative values.

In [52] a method was proposed using the same test vectors as INFORM , but the position estimation is achieved from the measured zero sequence voltage of a star-connected machine, avoiding the numerical calculations of the current derivatives. The back emf and resistive voltage drop are also cancelled by applying the opposite test vectors. This method requires the star point be available allowing the measurements of the phase voltages. A similar scheme exists for a delta-connected machine as explained in [53]. The zero sequence currents are measured for the position estimation, and in this case the six wire leads must be brought out from the motor.

Further development of the INFORM method have been carried out by the same group of researchers. Reference [54] concerns the estimation accuracy under different load and speed conditions, and the direct axis current is utilized for improvement, which also makes the INFORM-based method applicable to symmetrically constructed machines. The current deviation is analyzed during INFORM measurements in [55] and the INFORM vector sequence is modified in order to get the reduced current deviation. The new sequence for position estimation inhibits four vector states and leads to a symmetrical current deviation.

Theoretically, INFORM is only applicable for position estimation in the low speed range, because the inactive vector carrying the test vectors will become shorter when the speed increases. The combination of the saliency tracking and fundamental model has also been proposed. In [56] the voltage model is stabilized by the transient signal obtained from the INFORM scheme at low and zero frequency range, and the model based estimator will work independently at higher speed.

2.2.3.2 Transient Excitation Integrated with the Fundamental PWM Sequence

As the sensorless control methods are based on the transient excitations of the switching vectors, it is possible to integrate the transient excitations into the fundamental PWM scheme, which can enable a comprehensive controlling system. Integration

also has the advantages in terms of the current ripple and acoustic noise. However, the main difficulty of using the standard PWM for the sensorless transient excitations is that the excitation state should always have enough duration for the di/dt samplings. This is due to the presence of the stator current ringing, which is required to settle down before a measurement is taken.

Reference[57] indicates the area on the voltage phase plane where the standard PWM sequence needs to be modified for enough excitation. The low frequency and the sector crossing regions are highlighted on the phase plane. In this paper, when the PWM modulation index is low, separated test vectors are applied in the same ways as INFORM. If the modulation index increases and the inactive state becomes insufficient to carry the test vectors, the active vectors in the standard PWM sequence are used for the excitations. Extension of one active vector and the compensation by its opposite phasor are also introduced. But the construction of the position signals are not clear. The reduction in the current THD of the proposed integrated methods compared with that of INFORM using separated test vectors is also noted in [57].

In [58] the relationship between the position vector and the measured current derivatives in the low speed range is described. Two tables are set up for both star- and delta-connected machines. An extended modulation scheme is proposed, replacing the 60^osectors with the newly defined 120^o sectors. However, the extended modulation cannot solve the problem of di/dt sampling in the low speed range, and hence the compensating vector states are still needed.

A sensorless control scheme applicable across the whole speed range and using only the standard PWM switchings without addition test vectors was proposed by the author's research team in [14]. The two active vectors in one standard PWM cycle are used for the excitations. The back emf and resistive voltage drop in the voltage equations are cancelled by utilizing the measurements during null vectors, instead of adding opposite test vectors. The current derivatives during the inactive vectors in

the same PWM cycle are sampled. In cases where the standard PWM needs to be modified, the active vectors in the first half PWM period are extended and the compensation is made in the second half period. This method simplifies the extension and compensation by just shifting the switching edges. In this method, no additional test vectors are inserted and the sensorless control can be realized over the whole speed range.

A closed trace of the current response with the saturation saliency modulation is described in [59]. This combines the geometrical and mathematical estimation results in the six excitation sectors. The excitation necessary for the sensorless control schemes are integrated into the fundamental PWM, by introducing hysteresis control near the sector borders. But the sampling process is not clear, especially if the machine is running at low speed with light load when both active vectors are not wide enough for the di/dt sampling.

A novel technique that exploits the nature of the switching signals inherent in the PWM inverter output voltages is presented in [60]. The author investigates the 2^{nd} PWM switching harmonic, the strongest high frequency carrier signal, and uses its excitation for the position estimation. The 2^{nd} PWM carrier harmonic is described as a pulsating vector rotating almost synchronous with the fundamental voltage vector. Its resultant current is identified and then used for detecting the position signal underlying the stator impedance. In [60] this technique is used on an induction motor with a rotor slotting saliency. Further research confirming its feasibility is still required.

2.3 Problems with the Saliency Tracking Methods

Both the high frequency injection and the inverter voltage excitation techniques achieve good results for closed-loop control. However, there exist some aspects of concern and problems under further investigation. These are described as follows.

Problems arising from inverter non-linearity

For the methods based on high frequency signal injection, one main limiting factor in their accuracy is non-linearity of the power inverter. The high frequency currents can be distorted by the dead-time and the device voltage drop. Some inverter nonlinearities can produce a fictitious saliency, whose origin is not in the machine. An increase in the injection voltage amplitude would reduce the inverter's distorting effects, but it is only restricted in a small range or may not be applicable. Compensation schemes are always required[61, 62, 63]. Using converters with better switching characteristics, such as a zero deadtime matrix converter, is another way to improve the accuracy of rotor position estimation[64].

For the transient excitation based method, the influence of the nonlinear behaviour of the power converter is not obvious. The inverter deadtime adds an asymmetrical deviation to the machine current during the PWM pulse sequence, but its effect can be easily avoided by tuning the di/dt sampling instants[65]. Additional effort is not necessary when using machine without distinct nonlinear properties.

Problems Arising from Multiple Saliencies

One challenge of the position estimation through saliency tracking is that not more than one single saliency exists in the machine. When the dominant anisotropy is tracked, the influences from other saliencies and their non-sinusoidal distributions behave as the disturbances on the estimated results. A model for the AC machine including multiple saliencies is built up in [10]. This model represents these saliencies by a Fourier series summation. Incorporating the multiple saliencies, some modifications of the tracking observer are provided to improve the estimation accuracy . Three main spacial saliencies present in an induction motor are identified in [66]. They are from the saturation, the rotor slotting and the lamination material. The influence from the operating point of the machine, such as the flux level and the loading condition, on

the leakage inductance variation are evaluated in [67]. Also, the saliencies can come from other causes, such as the discrete nature of the machine windings, nonlinear magnetics, manufacturing asymmetries, and so on.

The phenomenon of multiple saliencies interferes with estimation accuracy, dynamic performance and robustness of all the saliency tracking methods. Different schemes have been published for reducing the effects from the harmonic saliencies[68][41][69], and significant improvement of the estimation result has been achieved. However, it is hard to properly incorporate and model all the saliencies present in the machine. Most schemes need offline commissioning process. Further investigations are being carried out to suppress the harmonics precisely and quickly.

Problems Arising from Signal to Noise Ratio (SNR)

SNR is the power ratio between a signal and the background noise. For the method based on high frequency voltage injection, the resultant current signal useful for position estimation is buried in the large stator current and other high frequency components. SNR is proportional to the amplitude of injected voltage signal. Larger SNR results in easier demodulation and better estimation results. Especially for the surface mounted PM machine, larger excitations are required because of its small saliency signal. But the increased injection signal amplifies the torque ripple, the power losses, and the acoustic noise. Compromise has to be made. For the method based on transient excitations, the high voltage pulses ensure sufficient excitation. Noise interfering with the position estimation mainly comes from the di/dt measurement. The sampling of the current transient signal needs to avoid the high frequency oscillations caused by the switching, which can cause the estimated position signal to deteriorate. The di/dt sensor property and the signal processing schemes influence the SNR. For both methods, the random noise picked up in the sensorless control process can be reduced by filtering [70] or by using an observer [10], but the cost is reduced bandwidth.

Problems Arising from Current Derivative Sensor.

The methods based on high frequency signal injection, detect the corresponding high frequency currents through the data processing of measured stator currents. For the methods based on the PWM transient excitation, the resultant current transients need to be measured. Specific current derivative sensors are usually employed instead of sampling currents and making differentiation. This is due to the measurement precision and the sampling frequency. When building a sensorless control system, suitable di/dt sensors should be selected or designed considering the high signal-to-noise ratio, the linearity in the desired frequency range, the cost, and the compact installation.

Problems Arising from Current Ripple.

When injecting a high frequency signal or modifying the PWM waveforms for di/dt sampling, the sensorless control schemes may introduce some level of deviations or ripples on the stator currents and also cause audible noise. These ripples reflect on the output torque or flux, which reduce the stability. Reducing or avoiding these current ripples is a big concern.

Problems Arising from Detection of Initial Position

For the PM machine drives, a particular problem is to determine the initial absolute position and the polarity of the rotor from the standstill condition. Several estimation techniques have been used for estimation at standstill. Some of them detect the saliency using revolving[71] or alternating[72] carrier injection to detect the magnetization axis, and the polarity is exploited from the second harmonic in the carrier current. In [73], voltage pulses are applied that cause a slight rotation of the rotor, and the position and polarity are obtained from the current responses. But sometimes the consideration is that no electromagnetic torque is generated during this process.

The scheme will behave in a more precise and robust manner if the calculation is independent of the machine parameters.

2.4 Conclusion

This Chapter has reviewed the research in literature for sensorless control of AC drives. Two principal methods are identified: the fundamental model based methods and the saliency tracking methods. Based on the mathematical model of an AC machine, the fundamental model based methods are briefly described. These are the MRAS method, the full-order observer method, and the Kalman filter method. These methods can achieve excellent performance at higher speed, but all fail in the low frequency range.

The saliency tracking methods obtain the rotor position and speed at very low and zero speed. One technique to exploit the saliency effect in AC machine injects a high frequency signal into the motor, which can be either a rotating or pulsating voltage/current signal, and measures the resultant current/voltage response. The other technique takes advantage of the transient excitations from the PWM switchings on the machine. By applying additional test vectors or utilizing the fundamental PWM sequence, the transient currents are measured for the position estimation. The problems of saliency tracking has been discussed.

This thesis will concentrate on the sensorless control based on the fundamental PWM excitation. A sensorless control AC drive is developed and applied to a surface mounted PM synchronous motor. The position and speed estimations are obtained from the measurements of the stator current transients, which are excited by the switching vectors of the inverter which provide the fundamental motor excitation. When di/dt measurements are difficult during some short vectors due to the high frequency switching oscillations, extensions of these vectors become necessary. In this research a new

extension and compensation scheme is proposed for the position estimation, which intends to further reduce the current distortions caused by the PWM modifications. The required minimum time duration of the vectors for di/dt measurement, t_{dmin}, depends on the high frequency switching oscillations appearing on the stator current waveforms. In this research, the high frequency switching oscillations are studied. Some approaches are put forward to reduce the switching oscillation effect and thus decrease the requirement for the vector extensions. A novel modification is made on the IGBT gate drive circuit to provide changeable gate resistance and thus controllable IGBT switching dynamics, which can reduce the switching oscillations during the current transient sampling cycles. Specially designed di/dt sensors and the filtering and amplifying circuits are made to obtain the accurate current transient measurements. Saliency position information are then extracted from these di/dt signals. To ensure the estimated position and speed signals have good quality for the sensorless control, an adaptive disturbance identifier (ADI) and a mechanical tracking observer are designed to compensate for the harmonics and filter the noise appearing in the estimated position signals. After the proposed improvements, excellent sensorless speed and position control is achieved for a surface mounted PMSM with a low structural saliency. Their performance is validated by experimental results.

Chapter 3

Position Estimation Using PWM Transient Excitation

Saliency tracking is the most promising method of estimating the rotor/flux position in the very low speed range and at standstill.By using the transient excitations of PWM voltage vectors output from the power inverter, various methods have obtained satisfactory estimation results and realized high performance sensorless control. In this section, the main position estimation approaches relying on the PWM excitation will be described.

3.1 Principle of the Position Estimation Using PWM Transient Excitation

The stator impedance (mainly the leakage inductance) is modulated by the saliency existing in the motor. The three phase stator inductances with saliency modulation can be expressed by[13]:

$$l_a = l_0 + \Delta l cos(n_{an}\theta_{an})$$

$$l_b = l_0 + \Delta l cos(n_{an}(\theta_{an} - 2\pi/3)) \tag{3.1}$$

$$l_c = l_0 + \Delta l cos(n_{an}(\theta_{an} - 4\pi/3))$$

where l_0 is the average inductance, Δl is the amplitude of inductance variation caused by the saliency and n_{an} indicates the number of the anisotropy cycles for each revolution, e.g. $n = 2$ for magnet saturation induced anisotropy and $n = Nr/pp$ for rotor slotting saliency, etc. In this research, the anisotropy existing in surface mounted PM synchronous motor mainly comes from the magnet saturation effect.

When an AC motor is connected to a PWM voltage source inverter, it is excited by a series of short voltage pulses to achieve the control of the machine's stator currents. These voltage pulses cause the transient changes of the armature currents. The dynamic current response is determined by the DC-link voltage, three-phase transient inductances, back EMF and the stator resistances. By measuring the stator current transient response to these voltage pulses, the saliency position can be tracked, because the transient phase inductances are modulated by the inherent anisotropies of the machine.

In this research, the star-connected surface mounted PMSM is driven by a voltage source inverter which employs the Space Vector PWM(SVPWM). SVPWM is one standard modulation scheme appropriate for DSP implementation [74, 75]. It is characterized by low current distortion, high output voltage range and flexible control. This technique essentially makes decomposition of the reference voltage vector into basic voltage vectors realizable by a three-phase inverter. Each basic vector is in accordance with one inverter switching state. As shown in Fig 3.1(a), the basic vectors, V_1, V_2, ..., V_6, representing the six active switching states of the inverter, and the null vectors, V_0 and V_7, representing the two inactive states, separate the phase plane into six sectors numbered by I, II,...,VI. In each PWM cycle, the two active vectors adjacent to the voltage reference vector and the two null vectors are applied in sequence

ensuring only one phase changing in each transition. The PWM sequence for a reference voltage vector in Sector I is shown in Fig 3.1(b).

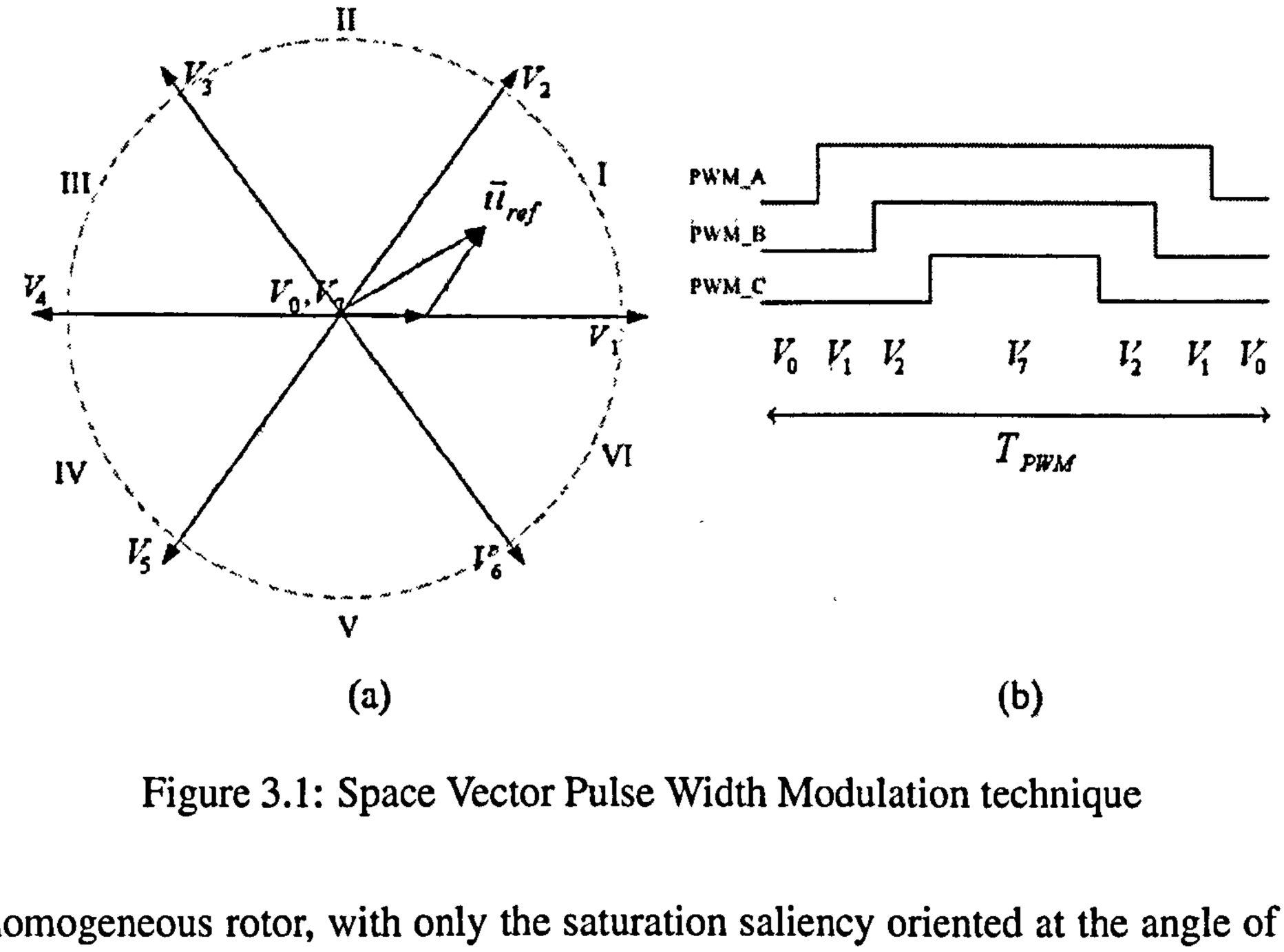

Figure 3.1: Space Vector Pulse Width Modulation technique

A homogeneous rotor, with only the saturation saliency oriented at the angle of θ_{an}, is taken as an example in this investigation. According to the equivalent stator phase circuit, the three-phase stator voltages are expressed as:

$$\begin{aligned} u_a &= i_a r_s + l_a \frac{di_a}{dt} + e_a \\ u_b &= i_b r_s + l_b \frac{di_b}{dt} + e_b \\ u_c &= i_c r_s + l_c \frac{di_c}{dt} + e_c \end{aligned} \tag{3.2}$$

where $u_{a,b,c}$ are the stator phase voltages, $i_{a,b,c}$ are the stator phase currents, $l_{a,b,c}$ are the stator inductances, r_s is the stator resistance and $e_{a,b,c}$ are the back EMF voltages. The phase voltages, u_a, u_b and u_c, are output from the inverter. At low speed, the back EMF and resistance voltage drop are very small in these equations and can be eliminated by schemes described later, and so they will not be included in this analysis. Thus the resultant current transient response is a function of the leakage inductance

values, which is modulated by the saturation saliency as (3.1).

When V_1 is applied to the surface mounted PMSM, the three-phase voltages $u_{a,b,c}$ will be $+\frac{2}{3}U_{DC}$,$-\frac{1}{3}U_{DC}$ and $-\frac{1}{3}U_{DC}$ respectively. If the resistance voltage drop and the back-EMF items are neglected, the resultant phase current derivative components will take the direction along the phase voltage vector, as shown in Fig 3.2(b). However, for any given rotor position θ_r, the saturation saliency modulates the stator leakage inductances and thus displaces the current derivative vector. The resultant current derivative components move along the circles indicated in Fig 3.2(b) with the circle centred situating on the basic vector axes. The circle radius depends on the values of $\triangle l$ and l_0. The waveforms of the di/dt signals will reflect both the applied voltage vectors and the inductance changes modulated by the saliency effect.

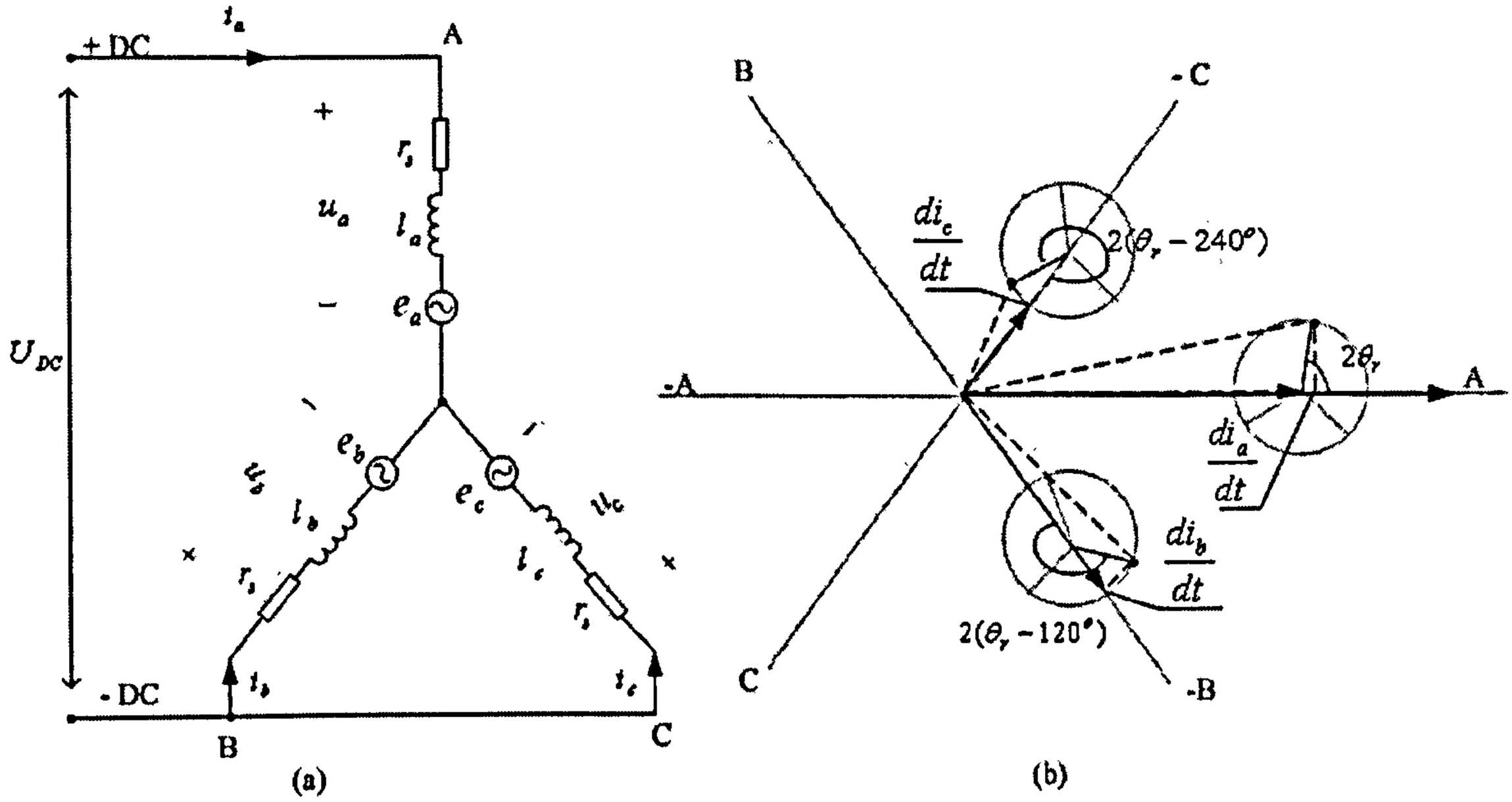

Figure 3.2: Stator circuit and the current transients under the excitation of V_1 with the saturation saliency effect

When other switching state vectors are applied, similar results exist. Under the same operating conditions, i.e. the same machine parameters and the same load level, the three circles will only shift between different switching axes with their radius unchanged. This can be clarified by Fig 3.3, which shows the cases when V_2 and V_3

are applied respectively. In order to extract the saliency position angle θ_{an} from the current transient signals, two voltage vector excitations in the known but unaligned directions are enough, because the exact values of the circle centre coordinates and the circle radius are not necessary.

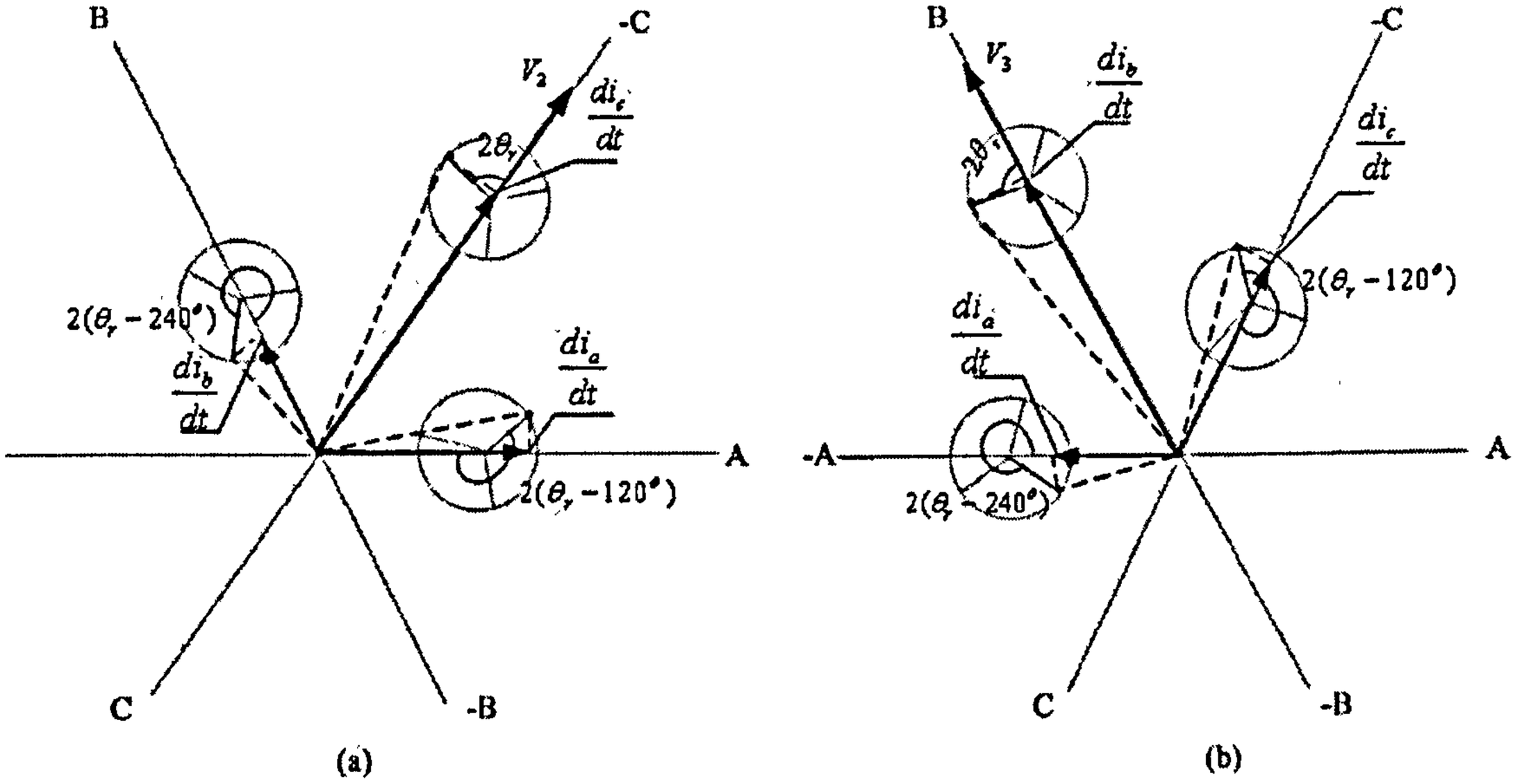

Figure 3.3: Current transients under the excitation of (a)V_2 and (b)V_3, with the saturation saliency effect

3.2 Sensorless Control Methods Using PWM Transient Excitations

3.2.1 The INFORM Method

The INFORM (Indirect Flux Detection by On-line Reactance Measurement) was the first proposed method to use PWM voltage vectors excitations and then to measure the current transient responses for tracking saliencies in the electric motors[13].

When the active switching vector V_1 is applied on the star-connected machine, the connections of the stator windings with the DC link is shown in Fig 3.2(a). According

to this circuit, the stator line voltage equations are written as:

$$U_{DC} = (i_a^{(1)} r_s + l_a \frac{di_a^{(1)}}{dt} + e_a) - (i_b^{(1)} r_s + l_b \frac{di_b^{(1)}}{dt} + e_b)$$

$$-U_{DC} = (i_c^{(1)} r_s + l_c \frac{di_c^{(1)}}{dt} + e_c) - (i_a^{(1)} r_s + l_a \frac{di_a^{(1)}}{dt} + e_a) \tag{3.3}$$

$$0 = (i_b^{(1)} r_s + l_b \frac{di_b^{(1)}}{dt} + e_b) - (i_c^{(1)} r_s + l_c \frac{di_c^{(1)}}{dt} + e_c)$$

where the subscript $^{(1)}$ denotes quantities during the switching vector V_1.

Similar equations can be derived when its opposite switching vector V_4 is applied:

$$-U_{DC} = (i_a^{(4)} r_s + l_a \frac{di_a^{(4)}}{dt} + e_a) - (i_b^{(4)} r_s + l_b \frac{di_b^{(4)}}{dt} + e_b)$$

$$U_{DC} = (i_c^{(4)} r_s + l_c \frac{di_c^{(4)}}{dt} + e_c) - (i_a^{(4)} r_s + l_a \frac{di_a^{(4)}}{dt} + e_a) \tag{3.4}$$

$$0 = (i_b^{(4)} r_s + l_b \frac{di_b^{(4)}}{dt} + e_b) - (i_c^{(4)} r_s + l_c \frac{di_c^{(4)}}{dt} + e_c)$$

where the subscript $^{(4)}$ denotes quantities during the switching vector V_4. Comparing the equations for V_1 and V_4, (3.3) and (3.4), the relationship between the transient currents and the stator inductances can be achieved after eliminating the resistive voltage drop and back-EMF voltage:

$$2U_{DC} = l_a(\frac{di_a^{(1)}}{dt} - \frac{di_a^{(4)}}{dt}) - l_b(\frac{di_b^{(1)}}{dt} - \frac{di_b^{(4)}}{dt})$$

$$2U_{DC} = l_c(\frac{di_c^{(1)}}{dt} - \frac{di_c^{(4)}}{dt}) - l_a(\frac{di_a^{(1)}}{dt} - \frac{di_a^{(4)}}{dt}) \tag{3.5}$$

$$0 = l_b(\frac{di_b^{(1)}}{dt} - \frac{di_b^{(4)}}{dt}) - l_c(\frac{di_c^{(1)}}{dt} - \frac{di_c^{(4)}}{dt})$$

Considering

$$\frac{di_a^{(k)}}{dt} + \frac{di_b^{(k)}}{dt} + \frac{di_c^{(k)}}{dt} = 0 \tag{3.6}$$

$$k = 1,2...,6$$

(3.5) and (3.6) yield

$$2U_{DC} = \frac{l_a l_b + l_b l_c + l_c l_a}{l_b + l_c} \cdot (\frac{di_a^{(1)}}{dt} - \frac{di_a^{(4)}}{dt}) \tag{3.7}$$

The current derivatives are expressed by

$$\frac{di_a^{(1)}}{dt} - \frac{di_a^{(4)}}{dt} = \frac{l_b + l_c}{l_a l_b + l_b l_c + l_c l_a} \cdot 2U_{DC} \tag{3.8}$$

Substituting the inductance phasor in (3.8) with the inductance phasor with saliency modulation as (3.1) yields

$$\frac{di_a^{(1)}}{dt} - \frac{di_a^{(4)}}{dt} = \frac{2}{g}(2 - \frac{\Delta l}{l_0} cos(n_{an}\theta_{an})) \tag{3.9}$$

where $g = \dfrac{3l_0(1 - (\frac{\Delta l}{2l_0})^2)}{U_{DC}}$.

Similar equations can be obtained when the other two pairs of opposite switching state vectors, V_2 and V_5, V_3 and V_6, are applied:

$$\frac{di_c^{(2)}}{dt} - \frac{di_c^{(5)}}{dt} = \frac{2}{g}(2 - \frac{\Delta l}{l_0} cos(n_{an}(\theta_{an} - 4\pi/3))) \tag{3.10}$$

and

$$\frac{di_b^{(3)}}{dt} - \frac{di_b^{(6)}}{dt} = \frac{2}{g}(2 - \frac{\Delta l}{l_0} cos(n_{an}(\theta_{an} - 2\pi/3))) \tag{3.11}$$

A position vector $\vec{p}$ is defined as

$$\vec{p} = p_a + \alpha p_b + \alpha^2 p_c \tag{3.12}$$

where

$$p_a = \frac{\Delta l}{l_0} cosn_{an}\theta_{an} = 2 - \frac{g}{2}(\frac{di_a^{(1)}}{dt} - \frac{di_a^{(4)}}{dt})$$

$$p_b = \frac{\Delta l}{l_0} cosn_{an}(\theta_{an} - 2\pi/3) = 2 - \frac{g}{2}(\frac{di_b^{(3)}}{dt} - \frac{di_b^{(6)}}{dt}) \tag{3.13}$$

$$p_c = \frac{\Delta l}{l_0} cosn_{an}(\theta_{an} - 4\pi/3) = 2 - \frac{g}{2}(\frac{di_c^{(2)}}{dt} - \frac{di_c^{(5)}}{dt})$$

For this position vector ($\vec{p} = p_a + \alpha p_b + \alpha^2 p_c = p_\alpha + j p_\beta$), its orthogonal components p_α and p_β can be derived free from the offset value, +2, which appears in the expressions of p_a, p_b and p_c:

$$p_\alpha = p_a - \frac{1}{2}(p_b + p_c) = -\frac{g}{2}((\frac{di_a^{(1)}}{dt} - \frac{di_a^{(4)}}{dt}) - \frac{1}{2}(\frac{di_b^{(3)}}{dt} - \frac{di_b^{(6)}}{dt}) - \frac{1}{2}(\frac{di_c^{(2)}}{dt} - \frac{di_c^{(5)}}{dt}))$$

$$p_\beta = \frac{\sqrt{3}}{2}(p_b - p_c) = \frac{\sqrt{3}}{2} \cdot (-\frac{g}{2}) \cdot ((\frac{di_b^{(3)}}{dt} - \frac{di_b^{(6)}}{dt}) - (\frac{di_c^{(2)}}{dt} - \frac{di_c^{(5)}}{dt})) \tag{3.14}$$

Furthermore, the saliency position angle can be obtained by the following equation, cancelling all of the unknown coefficients and only relying on the current derivatives:

$$\theta_{an} = \frac{1}{n_{an}} tan^{-1}(\frac{p_\beta}{p_\alpha}) \tag{3.15}$$

The position vector and the position angle are computed online from the measured current derivatives. For every sample of the position estimation, three pairs of the opposite switching state voltage vectors must be applied to the machine. In INFORM method, these opposite test vectors are added during the dwelling time of the null vectors (V_0 or V_7) of the PWM cycles.

However, there always exist the high frequency current oscillations after each switching instant. The current derivatives can be measured accurately only after these high frequency switching oscillations die out. Thus the added voltage vectors must meet the minimum vector duration t_{dmin}. The null vector in one PWM cycle may not provide the width enough for all the test vector pairs. Assuming the rotor or flux holds the same position over several successive PWM periods, these three vector pairs can be applied in three consecutive PWM cycles as shown in Fig 3.4. These opposite state vectors can not only cancel the influence of the resistance voltage drop and back EMF influence, but also keep the mean output voltage unchanged.

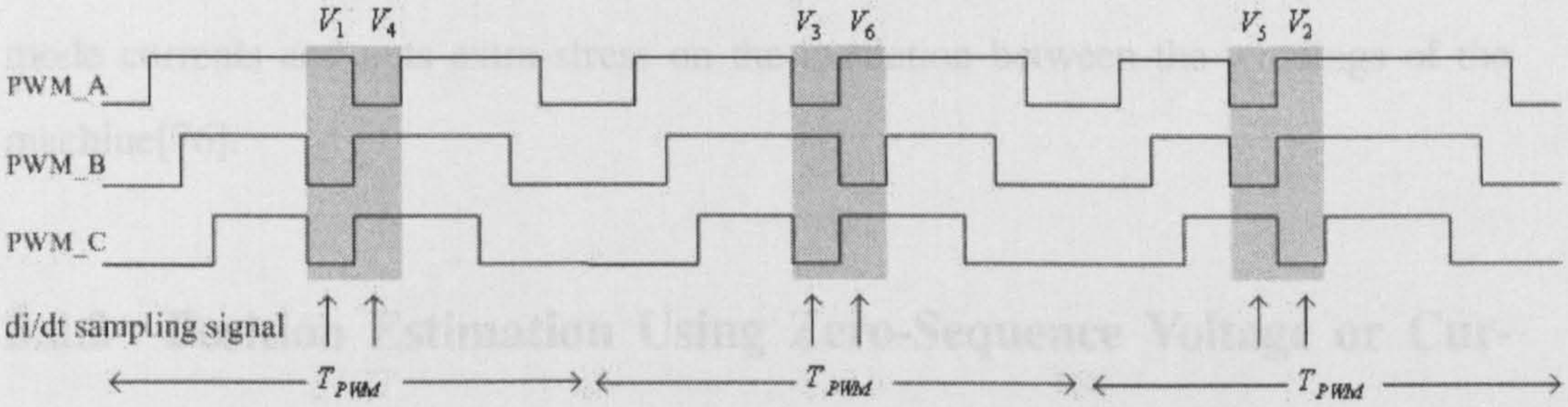

Figure 3.4: PWM sequence of INFORM method

An improvement of the INFORM measurement sequence is proposed in [55]. The PWM sequence in one PWM cycle is shown in Fig 3.5. The transient current responses are measured during the switching states II and III, and used for the position estimation as discussed above. Two more inverter switching states, I and IV, are added, in order to get a symmetrical current deviation and to reduce the current ripples[55]. The vectors in state I and IV have half width of the vectors in state II and III. The average voltage applied by the test vectors is still equal to zero. In its neighbouring PWM cycles, V_2 and V_5, V_3 and V_6, are applied respectively in the same way.

The INFORM method is not applicable over the whole speed range. At higher speed the duration of the null vector reduces and becomes not enough to integrate the test vector pairs. The application of the opposite test vectors in the INFORM method needs the switching of two IGBT legs at the same time, and thus inevitably introduces

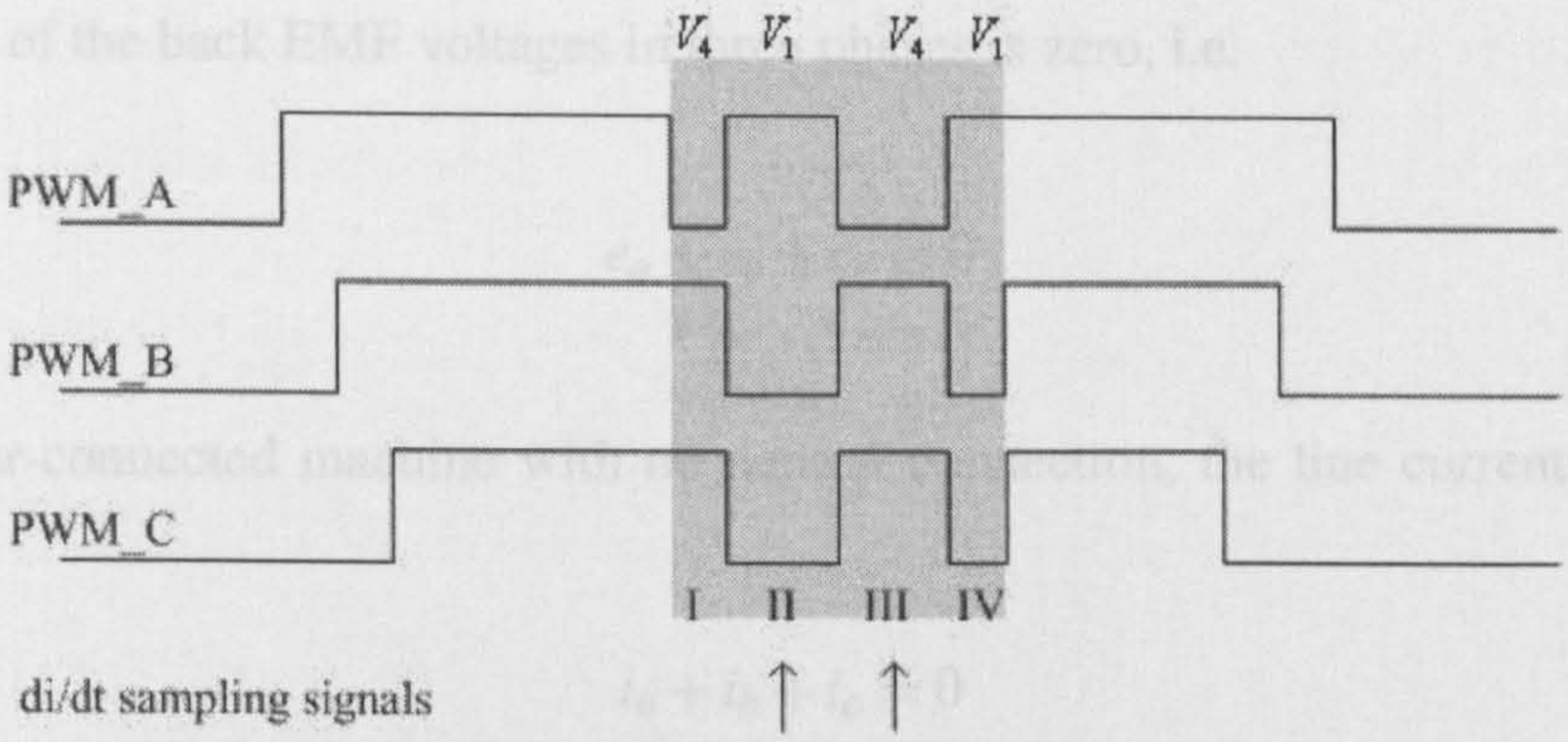

Figure 3.5: PWM sequence of the improved INFORM method

voltage transients of twice the DC-link voltage. This may causes increased common mode currents and puts extra stress on the insulation between the windings of the machine[76].

3.2.2 Position Estimation Using Zero-Sequence Voltage or Current

This inductance imbalance caused by the saliency effect will introduce a zero-sequence component, i.e. a zero-sequence voltage in a star-connected machine or a zero-sequence current in a delta-connected machine, which also provides the information of the rotor/flux position.

3.2.2.1 Position Estimation from Zero-Sequence Voltage in a Star-connected Machine

As discussed above, the stator voltage equation exsits as

$$\mathbf{u_s} = r_s \mathbf{i_s} + \mathbf{l}\frac{d\mathbf{i_s}}{dt} + \mathbf{e} \tag{3.16}$$

The sum of the back EMF voltages in three phases is zero, i.e.

$$e_a + e_b + e_c = 0 \tag{3.17}$$

For a star-connected machine with no neutral connection, the line currents, always satisfy

$$i_a + i_b + i_c = 0 \tag{3.18}$$

and accordingly

$$\frac{di_a}{dt} + \frac{di_b}{dt} + \frac{di_c}{dt} = 0 \tag{3.19}$$

The zero-sequence voltage in a star-connected machine is defined as

$$u_0 = u_a + u_b + u_c \tag{3.20}$$

From (3.16) and (3.18), the zero-sequence voltage can be expressed as

$$u_0 = l_a \frac{di_a}{dt} + l_b \frac{di_b}{dt} + l_c \frac{di_c}{dt} \tag{3.21}$$

To track the saliency position, the method proposed in [43] investigates u_0 when specific switching vector is applied. For example when V_1 is applied, the stator voltage equations are written similar to (3.3):

$$U_{DC} = (i_a^{(1)} r_s + l_a \frac{di_a^{(1)}}{dt} + e_a) - (i_b^{(1)} r_s + l_b \frac{di_b^{(1)}}{dt} + e_b)$$

$$-U_{DC} = (i_c^{(1)} r_s + l_c \frac{di_c^{(1)}}{dt} + e_c) - (i_a^{(1)} r_s + l_a \frac{di_a^{(1)}}{dt} + e_a)$$

$$0 = (i_b^{(1)} r_s + l_b \frac{di_b^{(1)}}{dt} + e_b) - (i_c^{(1)} r_s + l_c \frac{di_c^{(1)}}{dt} + e_c)$$

Using (3.3) and the balanced equations of (3.17), (3.18) and (3.19), the zero-sequence voltage $u_0^{(1)}$ can be written as as

$$\begin{aligned} u_0^{(1)} &= \frac{l_a(l_b+l_c)-2l_bl_c}{l_al_b+l_bl_c+l_cl_a}\cdot U_{DC} \\ &+ 3\frac{l_al_b(e_c^{(1)}+r_si_c^{(1)})+l_bl_c(e_a^{(1)}+r_si_a^{(1)})+l_cl_a(e_a^{(1)}+r_si_a^{(1)})}{l_al_b+l_bl_c+l_cl_a} \end{aligned} \tag{3.22}$$

Similarly, u_0 under the excitation of V_4 can be derived as

$$\begin{aligned} u_0^{(4)} &= \frac{l_a(l_b+l_c)-2l_bl_c}{l_al_b+l_bl_c+l_cl_a}\cdot(-U_{DC}) \\ &+ \frac{l_al_b(e_c^{(4)}+r_si_c^{(4)})+l_bl_c(e_a^{(4)}+r_si_a^{(4)})+l_cl_a(e_a^{(4)}+r_si_a^{(4)})}{l_al_b+l_bl_c+l_cl_a} \end{aligned} \tag{3.23}$$

The equations for $u_0^{(1)}$ and $u_0^{(4)}$ are similar but only with U_{DC} reversed. The second terms of (3.22) and (3.23) represent the effect of the back-EMF and resistance voltage drop on the zero-sequence voltage. These can be eliminated by combining (3.22) and (3.23), and it yields

$$u_{0a} = u_0^{(1)} - u_0^{(4)} = 2U_{DC}\frac{l_al_b+l_cl_a-2l_bl_c}{l_al_b+l_bl_c+l_cl_a} \tag{3.24}$$

where u_{0a} is the zero-sequence voltage obtained from $u_0^{(1)}$ and $u_0^{(4)}$ after eliminating the back-EMF and resistance voltage drop. Considering the inductance equations of 3.1, 3.24 can be finally written as:

$$u_{0a} = \frac{2\triangle lU_{DC}}{l_0}cos(n_{an}\theta_{an}) \tag{3.25}$$

Similar calculations can be carried out when the other two pairs of opposite switching state vectors are applied, i.e.

$$u_{0b} = u_0^{(2)} - u_0^{(5)} = 2U_{DC}\frac{l_a l_b + l_c l_b - 2l_c l_a}{l_a l_b + l_b l_c + l_c l_a}$$
$$= \frac{2\triangle l U_{DC}}{l_0} cos(n_{an}(\theta_{an} - \frac{4\pi}{3})) \quad (3.26)$$

and

$$u_{0c} = u_0^{(3)} - u_0^{(6)} = 2U_{DC}\frac{l_a l_c + l_c l_b - 2l_a l_b}{l_a l_b + l_b l_c + l_c l_a}$$
$$= \frac{2\triangle l U_{DC}}{l_0} cos(n_{an}(\theta_{an} - \frac{2\pi}{3})) \quad (3.27)$$

The three balanced signals, u_{0a}, u_{0b} and u_{0c}, can be combined to give an anisotropy position vector[43]:

$$\overrightarrow{p}(\theta_{an}) = p_a + \alpha p_b + \alpha^2 p_c = u_{0a} + \alpha u_{0b} + \alpha^2 u_{0c} \quad (3.28)$$

Since U_{DC} is regarded as constant, $\overrightarrow{p}$ only changes as a function of the total leakage inductances. The position vector $\overrightarrow{p}$ directly reflects the saliency position angle θ_{an} without any DC offset[43]. As clarified in Fig 3.6, the line-to-line voltages output from the VSI, u_{ab}, u_{bc} and u_{ca}, are three-phase balanced, and the zero-sequence voltage vector $\vec{u}_0$ exists due to the unbalanced three-phase impedances and rotates with the anisotropy position angle θ_{an}.

To implement the position estimation method using the zero-sequence voltage, the opposite test vector pairs are also applied during the null vectors in the fundamental PWM sequence. However, the zero-sequence voltage for estimating the position signal is only available in a star-connected machine, and the star point of the machine must be accessible for measurement.

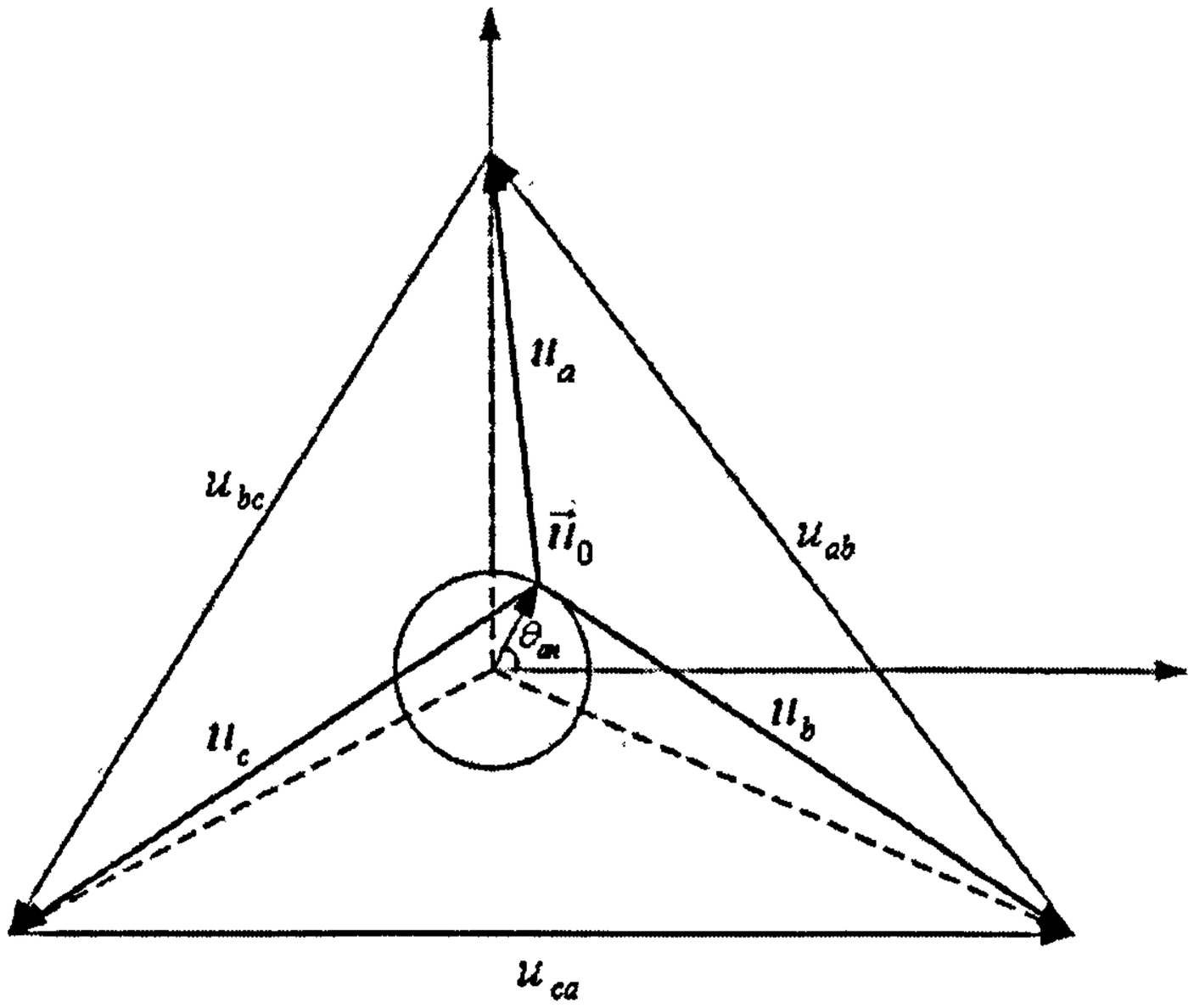

Figure 3.6: Zero-sequence voltage caused by the saliency in the star-connected motor

3.2.2.2 Position Estimation from Zero-Sequence Current in a Delta-connected Machine

As an equivalence to the zero-sequence voltage in a star-connected machine, the zero-sequence current in a delta-connected machine also can be utilized for the estimation of the rotor/flux position[53]. When the switching vector V_1 is applied to a delta-connected machine, as shown in Fig 3.7(a), the stator phase voltage equations are:

$$U_{DC} = i_{ab}^{(1)} r_s + l_a \frac{di_{ab}^{(1)}}{dt} + e_a^{(1)}$$

$$-U_{DC} = i_{ca}^{(1)} r_s + l_c \frac{di_{ca}^{(1)}}{dt} + e_c^{(1)} \tag{3.29}$$

$$0 = i_{bc}^{(1)} r_s + l_b \frac{di_{bc}^{(1)}}{dt} + e_b^{(1)}$$

Under the excitation of V_4, as shown in Fig 3.7(b) there exist similar stator voltage

equations:

$$-U_{DC} = i_{ab}^{(4)} r_s + l_a \frac{di_{ab}^{(4)}}{dt} + e_a^{(4)}$$

$$U_{DC} = i_{ca}^{(4} r_s + l_c \frac{di_{ca}^{(4)}}{dt} + e_c^{(4)} \tag{3.30}$$

$$0 = i_{bc}^{(4)} r_s + l_b \frac{di_{bc}^{(4)}}{dt} + e_b^{(4)}$$

Equation(3.17) still holds true, and the effect of the back EMF and resistance voltage drop can be eliminated by combining (3.29) and (3.30). The zero-sequence current is defined as

$$i_0 = i_{ab} + i_{bc} + i_{ca} \tag{3.31}$$

Therefore, the zero-sequence current derivative during the switching state vector pair of V_1 and V_4,can be derived as:

$$\frac{di_0^{(1)}}{dt} - \frac{di_0^{(4)}}{dt} = U_{DC}(\frac{1}{l_a} - \frac{1}{l_c}) \tag{3.32}$$

Referring to 3.1, this equation can be simplified as:

$$\frac{di_0^{(1)}}{dt} - \frac{di_0^{(4)}}{dt} = \frac{U_{DC}\triangle l}{l_0^2}(cos(n_{an}(\theta_{an} - \frac{4\pi}{3})) - cos(n_{an}\theta_{an}) \tag{3.33}$$

Similarly the zero-sequence current derivative for the other switching vector pairs are:

$$\begin{aligned} \frac{di_0^{(3)}}{dt} - \frac{di_0^{(6)}}{dt} &= U_{DC}(\frac{1}{l_b} - \frac{1}{l_a}) \\ &= \frac{U_{DC}\triangle l}{l_0^2}(cos(n_{an}\theta_{an}) - cos(n_{an}(\theta_{an} - \frac{2\pi}{3}))) \end{aligned} \tag{3.34}$$

and

$$\begin{aligned}\frac{di_0^{(5)}}{dt} - \frac{di_0^{(2)}}{dt} &= U_{DC}(\frac{1}{l_c} - \frac{1}{l_b}) \\ &= \frac{U_{DC}\Delta l}{l_0^2}(cos(n_{an}(\theta_{an} - \frac{2\pi}{3})) - cos(n_{an}(\theta_{an} - \frac{4\pi}{3}))) \quad (3.35)\end{aligned}$$

Thus the position vector is then derived [53] by:

$$\vec{p} = (\frac{di_0^{(1)}}{dt} - \frac{di_0^{(4)}}{dt}) + \alpha(\frac{di_0^{(3)}}{dt} - \frac{di_0^{(6)}}{dt}) + \alpha^2(\frac{di_0^{(5)}}{dt} - \frac{di_0^{(2)}}{dt}) \quad (3.36)$$

from which the anisotropy angle can be estimated as explained.

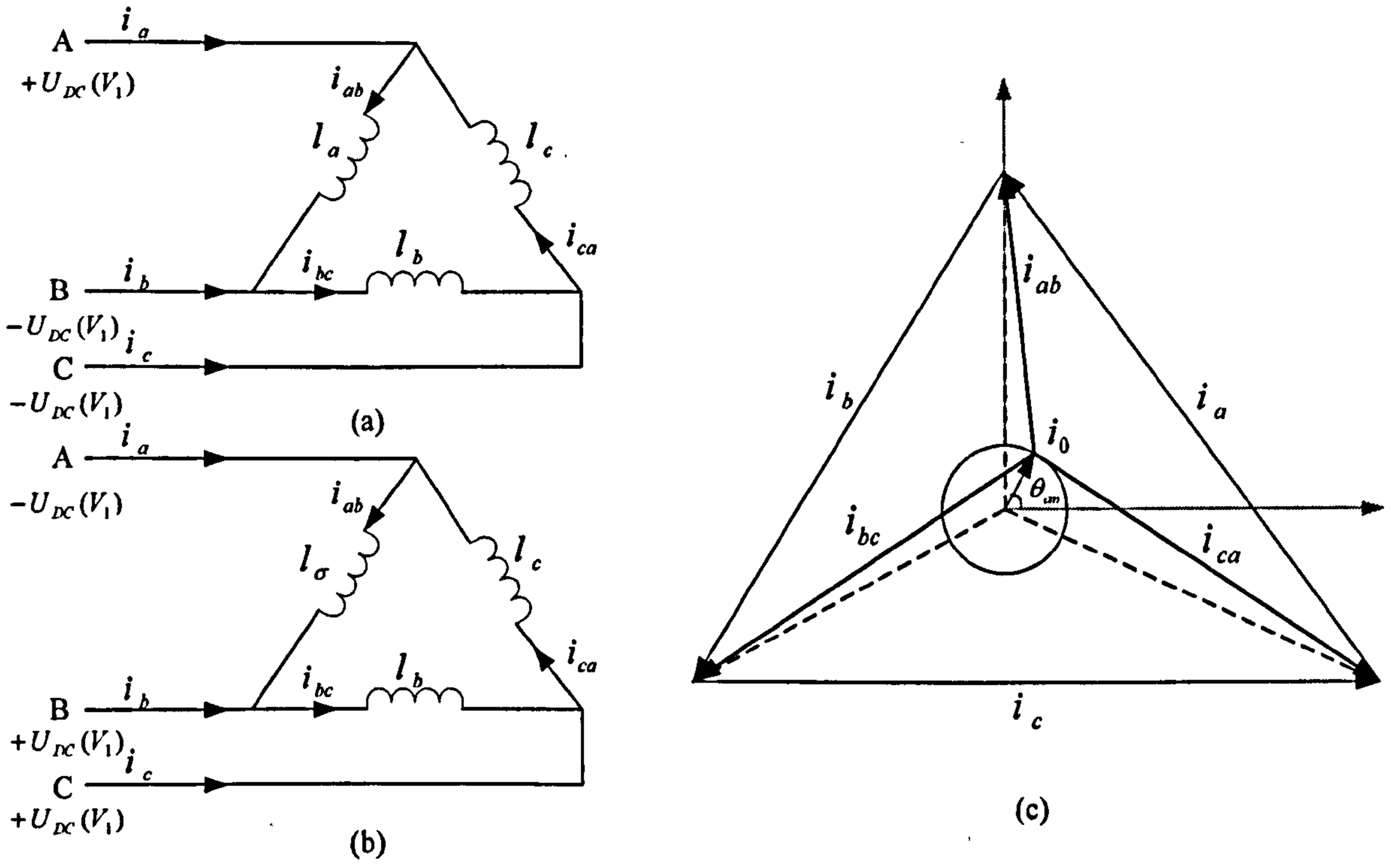

Figure 3.7: (a) Delta-connected machine under the excitation of V_1 and V_4; (b) Zero-sequence current caused by the saliency

The current vectors that exist in the delta-connected machine are shown in Fig 3.7(c).

The zero-sequence current vector is rotating with the anisotropy position angle θ_{an}.

Again, three pairs of opposite test vectors are required to obtain the position vector.

The implementation of the test voltage vectors is similar to that of the INFORM and [43]. However, normally the phase currents are not accessible for the delta-connected machine. In order to estimate the position signal from the zero-sequence current, both terminals of each phase winding should be made available. An external connector may have to be used.

3.2.3 Position Estimation based on the Fundamental PWM Sequence

The INFORM method and its descendant methods have verified that the PWM voltage vectors can be used as the excitation source for saliency tracking, but they all require additional test vectors added in the fundamental PWM sequence [13, 55, 43]. These test vectors can result in additional high frequency noise, extra phase current ripple, and an increased switching frequency for the power devices. Inserting test vectors during the dwelling time of the null vectors is only applicable in the low speed range. Therefore some researchers have attempted to integrate the test vectors within the standard PWM sequence generated by the AC drive controller[14, 60, 57].

3.2.3.1 Main Rules For the Position Estimation from PWM Transient Excitations

It has been claimed that using only the standard PWM sequence is possible in principle to estimate the rotor position [14, 60, 57]. However, the schemes based on PWM voltage vector excitations have to meet some demands proposed by the estimation method and the limitations of the implementation.

1. The transient change of the armature current is determined by the DC link voltage, the phase reactances, the back EMF, and the stator resistance, as related in the stator voltage equation (3.2). The DC link voltage is regarded as a constant. In or-

der to estimate the position signal from the measured three-phase current transient responses, the influence from the back EMF and the stator resistance voltage need to be eliminated. The INFORM method and its descendant methods solve this problem by measuring the current derivatives for a pair of opposite test vectors. Some methods neglecting the resistance voltage drop and the back EMF due to their low values at low speed, can be used only in a quite limited speed range[58][43].

2. The immediate measurement of the current derivatives is impeded by the high frequency switching noise, which arises from the parasitic circuit of the power electronic devices, the electromagnetic interference circuits, the measurement system, the connected machine, etc. The width of the voltage vector used for position estimation should always meet the minimum vector duration t_{dmin}, which causes the difficulty of integrating position estimation within the fundamental PWM sequence.

3. When the position estimation scheme is integrated with the normal fundamental PWM sequence, it should not change the desired output voltage vector. The opposite test vectors in the INFORM method and its descendant methods cancel their additional effect.

4. To obtain one sample of the position estimation, transient currents for more than one active vectors are measured. For one position estimation, the rotor/flux position should be assumed constant over the period when these vectors are applied.

5. No matter which method is applied, the additionally introduced current distortion should be kept as low as possible. The additional current ripple may appear on the torque axis, which can interfere with the smooth operation of the machine. Severe current distortion even brings about adverse effects on the mechanical system. The audible noise also increases when the larger current ripple that present.

3.2.3.2 Principle of the Position Estimation Only Using the Fundamental PWM Sequence

In every fundamental SVPWM period, there exist two non-aligned active vectors and two null vectors being applied symmetrically. Theoretically the voltage vector excitation required by the position estimation schemes can come from the vectors defined by the standard PWM sequence. The method proposed in this research makes a reference to the analysis in [14]. In this section the proposed method will be described by providing the solutions to the rules listed in 3.2.3.1:

1. An effective and simple method is provided in [14] to eliminate the influence from the stator resistance voltage and the back-EMF. Instead of using opposite test voltage vectors, this method takes advantage of the voltage equations established for the null switching vectors applied on the motor. The transient excitations for position estimation are obtained from the active vectors defined by the fundamental PWM sequence. The current derivatives are measured during both active vectors and null vectors.

The proposed method can be explained by taking the example when the the reference voltage vector, $\mathbf{u}_s^*$, is situated in Sector I on the phase plane. The fundamental SVPWM sequence in this case will be $V_0 \rightarrow V_1 \rightarrow V_2 \rightarrow V_7 \rightarrow V_2 \rightarrow V_1 \rightarrow V_0$, with symmetrical width. The following equations are established for the circuit excited under voltage vector V_1, as shown in Fig 3.2(a):

$$U_{DC} = (r_s i_a^{(1)} + l_a \frac{di_a^{(1)}}{dt} + e_a^{(1)}) - (r_s i_b^{(1)} + l_b \frac{di_b^{(1)}}{dt} + e_b^{(1)})$$

$$-U_{DC} = (r_s i_c^{(1)} + l_c \frac{di_c^{(1)}}{dt} + e_c^{(1)}) - (r_s i_a^{(1)} + l_a \frac{di_a^{(1)}}{dt} + e_a^{(1)}) \qquad (3.37)$$

$$0 = (r_s i_b^{(1)} + l_b \frac{di_b^{(1)}}{dt} + e_b^{(1)}) - (r_s i_c^{(1)} + l_c \frac{di_c^{(1)}}{dt} + e_c^{(1)})$$

Similar equations exist during V_0:

$$0 = (r_s i_a^{(0)} + l_a \frac{di_a^{(0)}}{dt} + e_a^{(0)}) - (r_s i_b^{(0)} + l_b \frac{di_b^{(0)}}{dt} + e_b^{(0)})$$

$$0 = (r_s i_c^{(0)} + l_c \frac{di_c^{(0)}}{dt} + e_c^{(0)}) - (r_s i_a^{(0)} + l_a \frac{di_a^{(0)}}{dt} + e_a^{(0)}) \tag{3.38}$$

$$0 = (r_s i_b^{(0)} + l_b \frac{di_b^{(0)}}{dt} + e_b^{(0)}) - (r_s i_c^{(0)} + l_c \frac{di_c^{(0)}}{dt} + e_c^{(0)})$$

If V_0 and V_1 are applied consecutively in one PWM period, it is safe to assume that

$i_a^{(0)} = i_a^{(1)}$, $i_b^{(0)} = i_b^{(1)}$ and $i_c^{(0)} = i_c^{(1)}$,

$e_a^{(0)} = e_a^{(1)}$, $e_b^{(0)} = e_b^{(1)}$ and $e_c^{(0)} = e_c^{(1)}$,

the terms of the back EMF and the resistance voltage drop can then be eliminated by combining (3.37) and (3.38), giving:

$$\frac{di_a^{(1)}}{dt} - \frac{di_a^{(0)}}{dt} = \frac{l_b + l_c}{l_a l_b + l_b l_c + l_c l_a} \cdot U_{DC}$$

$$\frac{di_b^{(1)}}{dt} - \frac{di_b^{(0)}}{dt} = -\frac{l_c}{l_a l_b + l_b l_c + l_c l_a} \cdot U_{DC} \tag{3.39}$$

$$\frac{di_c^{(1)}}{dt} - \frac{di_c^{(0)}}{dt} = -\frac{l_b}{l_a l_b + l_b l_c + l_c l_a} \cdot U_{DC}$$

Substituting (3.1) into (3.39) yields:

$$\frac{di_a^{(1)}}{dt} - \frac{di_a^{(0)}}{dt} = \frac{1}{g}(2 - \frac{\Delta l}{l_0} cosn_{an}\theta_{an})$$

$$\frac{di_b^{(1)}}{dt} - \frac{di_b^{(0)}}{dt} = -\frac{1}{g}(1 + \frac{\Delta l}{l_0} cosn_{an}(\theta_{an} - \frac{4\pi}{3})) \tag{3.40}$$

$$\frac{di_c^{(1)}}{dt} - \frac{di_c^{(0)}}{dt} = -\frac{1}{g}(1 + \frac{\Delta l}{l_0} cosn_{an}(\theta_{an} - \frac{2\pi}{3}))$$

where $g = \dfrac{3l_0(1-(\frac{\Delta l}{2l_0})^2)}{U_{DC}}$.

The balanced position vector can again be defined as:

$$\begin{aligned} \vec{p} &= p_a + \alpha p_b + \alpha^2 p_c \\ &= \frac{\Delta l}{l_0}(cos(n_{an}\theta_{an}) + \alpha cosn_{an}(\theta_{an} - \frac{2\pi}{3}) + \alpha^2 cosn_{an}(\theta_{an} - \frac{4\pi}{3})) \end{aligned} \tag{3.41}$$

and so

$$\begin{aligned} p_a &= 2 - g(\frac{di_a^{(1)}}{dt} - \frac{di_a^{(0)}}{dt}) \\ p_b &= -1 - g(\frac{di_c^{(1)}}{dt} - \frac{di_c^{(0)}}{dt}) \\ p_c &= -1 - g(\frac{di_b^{(1)}}{dt} - \frac{di_b^{(0)}}{dt}) \end{aligned} \tag{3.42}$$

The position angle cannot be achieved from (3.42) alone, because the unknown coefficients in the three phase position scalars cannot be cancelled. Excitation from another active voltage vector, non-aligned with V_1, is required. In sector I, V_2 is the other active vector available. A group of similar position signals can be calculated from the transient currents during V_2 and V_7. The effect of back EMF and stator resistance voltage drop are cancelled in the same way. because V_7 situates closer to V_2 in the fundamental PWM sequence. The three-phase position scalars can be derived as:

$$\begin{aligned} p_a &= -1 + g(\frac{di_b^{(2)}}{dt} - \frac{di_b^{(7)}}{dt}) \\ p_b &= -1 + g(\frac{di_a^{(2)}}{dt} - \frac{di_a^{(7)}}{dt}) \\ p_c &= 2 + g(\frac{di_c^{(2)}}{dt} - \frac{di_c^{(7)}}{dt}) \end{aligned} \tag{3.43}$$

The position vector can be constructed by selecting the position scalars with the cancellable offsets from (3.42) and (3.43). Such as

$$\vec{p} = p_a + \alpha p_b + \alpha^2 p_c$$

$$= (-1 + g(\frac{di_b^{(2)}}{dt} - \frac{di_b^{(7)}}{dt})) + \alpha(-1 - g(\frac{di_c^{(1)}}{dt} - \frac{di_c^{(0)}}{dt})) + \alpha^2(-1 - g(\frac{di_b^{(1)}}{dt} - \frac{di_b^{(0)}}{dt}))$$

where the offset -1 in the position scalar equations can then be eliminated.

The orthogonal components p_α and p_β are derived as:

$$p_\alpha = p_a - \frac{1}{2}(p_b + p_c) = g((\frac{di_b^{(2)}}{dt} - \frac{di_b^{(7)}}{dt}) + \frac{1}{2}(\frac{di_c^{(1)}}{dt} - \frac{di_c^{(0)}}{dt}) - \frac{1}{2}(\frac{di_b^{(1)}}{dt} - \frac{di_b^{(0)}}{dt}))$$

$$p_\beta = \frac{\sqrt{3}}{2}(p_b - p_c) = \frac{\sqrt{3}}{2} g \cdot ((\frac{di_b^{(1)}}{dt} - \frac{di_b^{(0)}}{dt}) - (\frac{di_c^{(1)}}{dt} - \frac{di_c^{(0)}}{dt})) \qquad (3.44)$$

The position angle of the anisotropy can be obtained from (3.15).

Similar derivations and conclusions exist when the reference voltage situates in other sectors. By measuring the three phase current derivatives during the two active vectors and the two null vectors in one PWM sequence, the saliency position can be estimated.

2. The active vectors in the fundamental SVPWM sequence will not meet the requirement of the minimum duration t_{dmin} all the time, especially when the reference voltage vector has a low magnitude or when it is crossing the boundary between two sectors. One or both active vectors may be shorter than t_{dmin}. In these cases, an extension scheme is proposed. If the active voltage vector used for the position estimation is not wide enough, it will be extended to t_{dmin}. In the extended active voltage vector, the current transients can be measured accurately after the high frequency oscillations have died down. The value of the minimum duration t_{dmin} is decided by the transient behaviour of the drive system. Chapter 4 will give a detailed description for the high frequency oscillations after the switching instants.

3. The extension of the active vectors will change the fundamental PWM sequence and thus change the final voltage vector achieved. To keep the voltage time area (VTA) unchanged, i.e. to keep the output voltage vector as the same, a compensation scheme has to be utilized. When one active vector is extended, one of its switching edges is shifted. It is found that, as long as the ON time of each IGBT bridge is kept the same in that PWM period, the total voltage vector applied will not be changed. One case of the extension of V_1 to the minimum duration t_{dmin} is illustrated in Fig 3.8. In Fig 3.8(a), the first switching edge of V_1 on phase A is advanced to make this V_1 long enough to meet the minimum vector duration t_{dmin}. In the second half of this PWM period, the other edge of the phase A is correspondingly shifted in advance the same distance, and thus the turn-on time of phase A, t_a, is unchanged. If the other switching edge of V_1 on phase B is shifted, the PWM sequence is adjusted as shown in Fig 3.8(b).

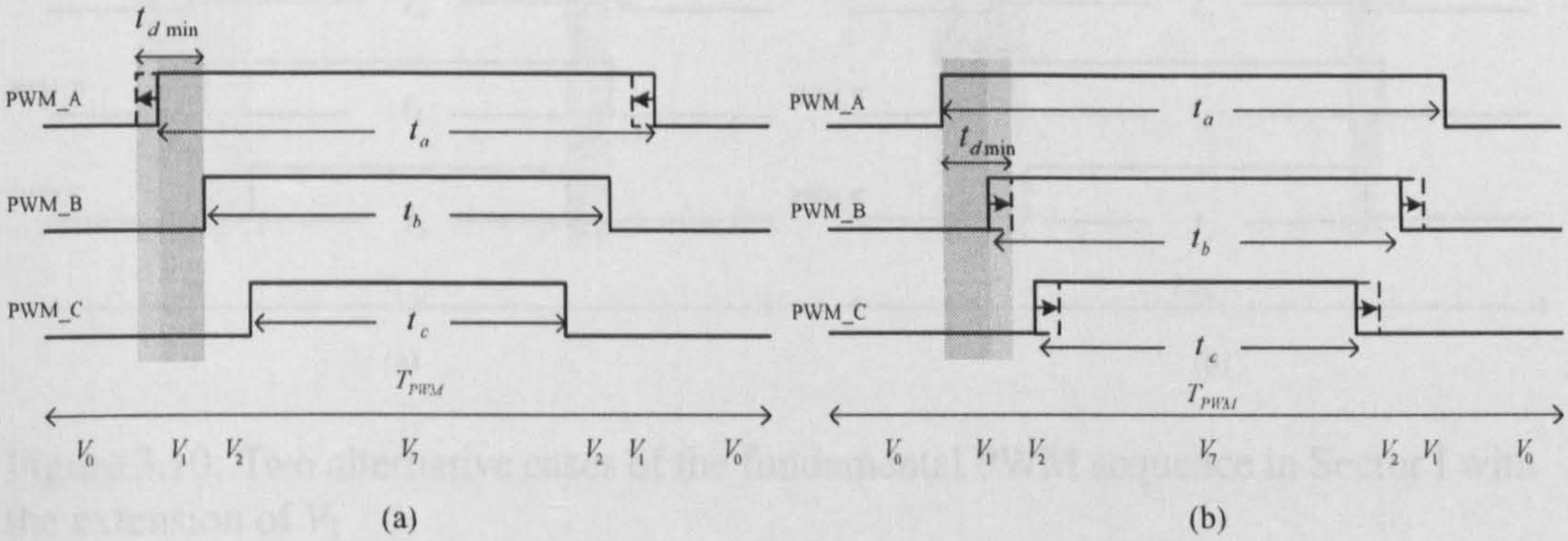

Figure 3.8: Fundamental PWM sequence in sector I with the extension of vector V_1 in two ways

The equivalent effect can be verified by the vector plots in one PWM period as shown in Fig 3.9. The voltage vector plot for a fundamental PWM sequence is shown in Fig 3.9(a). The voltage vectors in the changed PWM sequence are plotted in Fig 3.9(b).

When the reference voltage vector $\vec{u}^*$ is in Sector I, alternative cases are also possible when the switching edges are shifted, as shown in Fig 3.10, which depends on the original widths of V_1 and V_2. But the final output voltage vector is the same, which can be verified by the voltage vector plots in Fig 3.11.

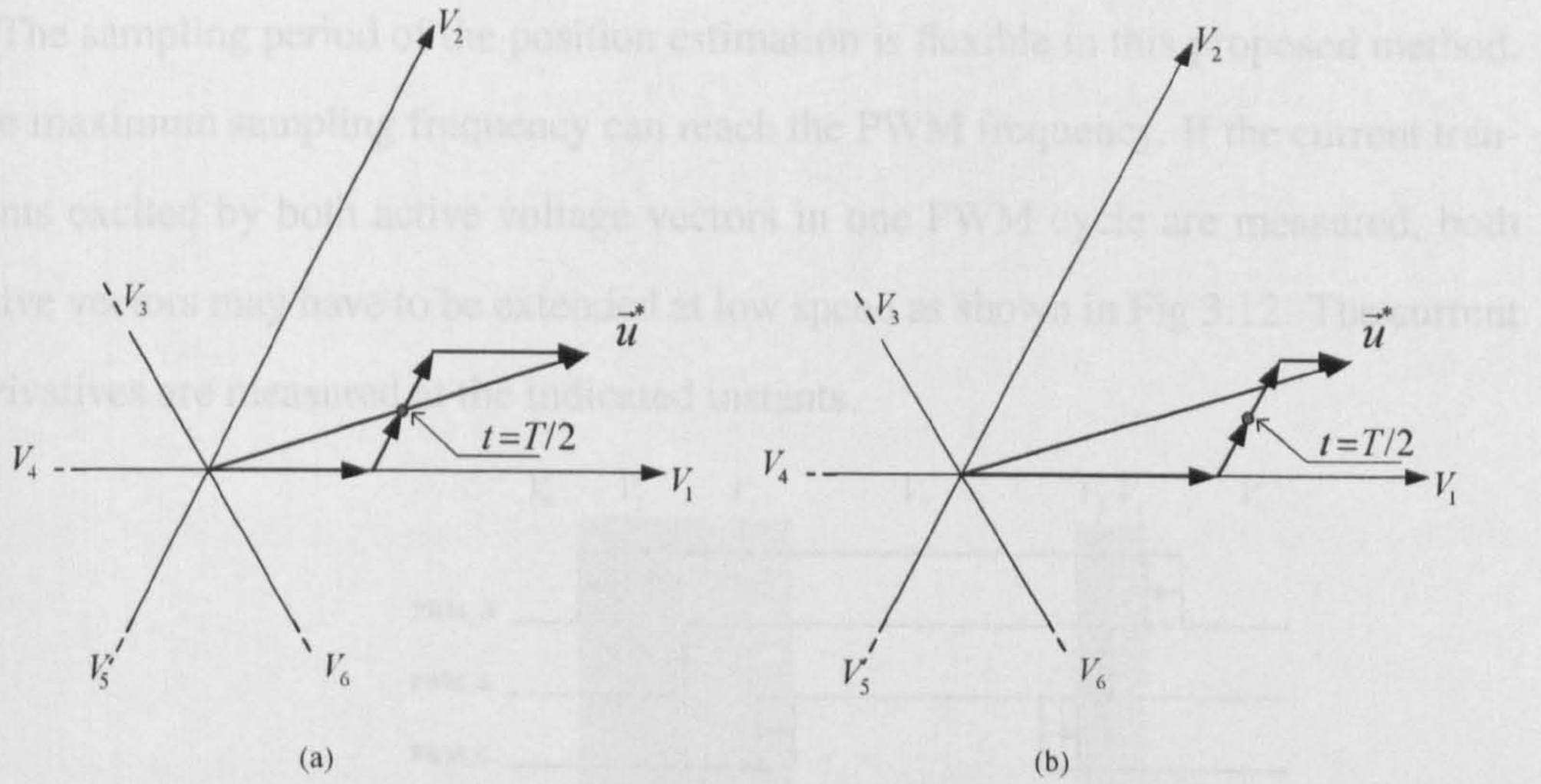

Figure 3.9: Voltage vector plot when $\vec{u}^*$ locates in sector I, (a) without and (b) with the extension of the vector V_1

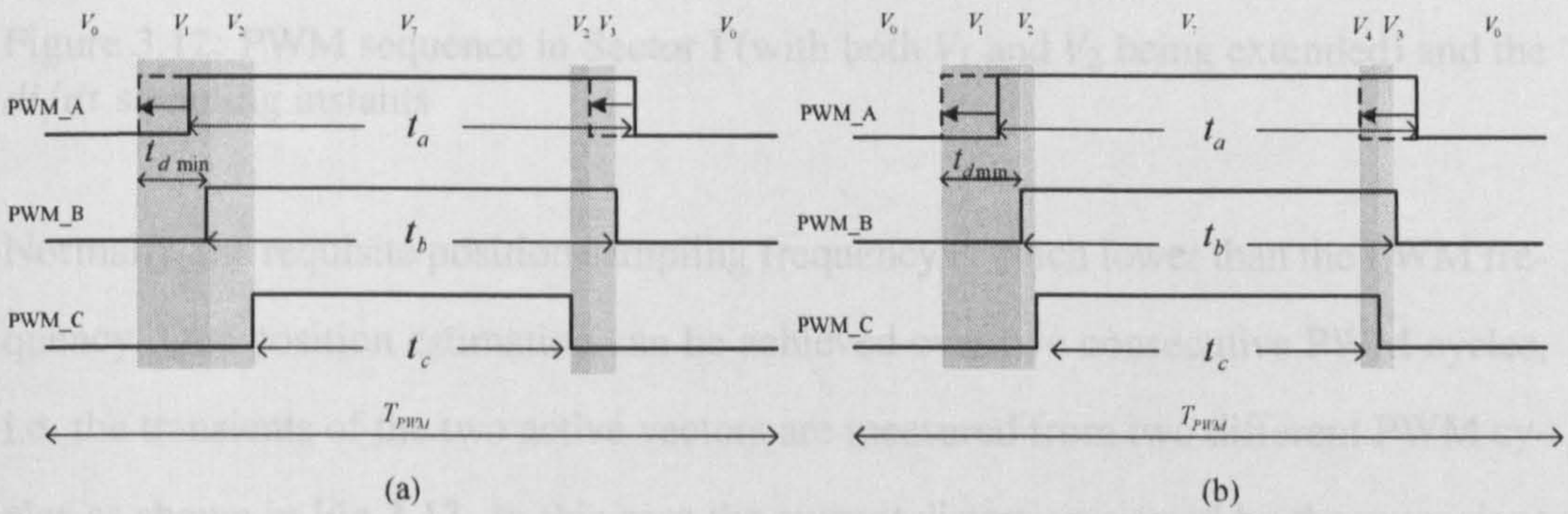

Figure 3.10: Two alternative cases of the fundamental PWM sequence in Sector I with the extension of V_1

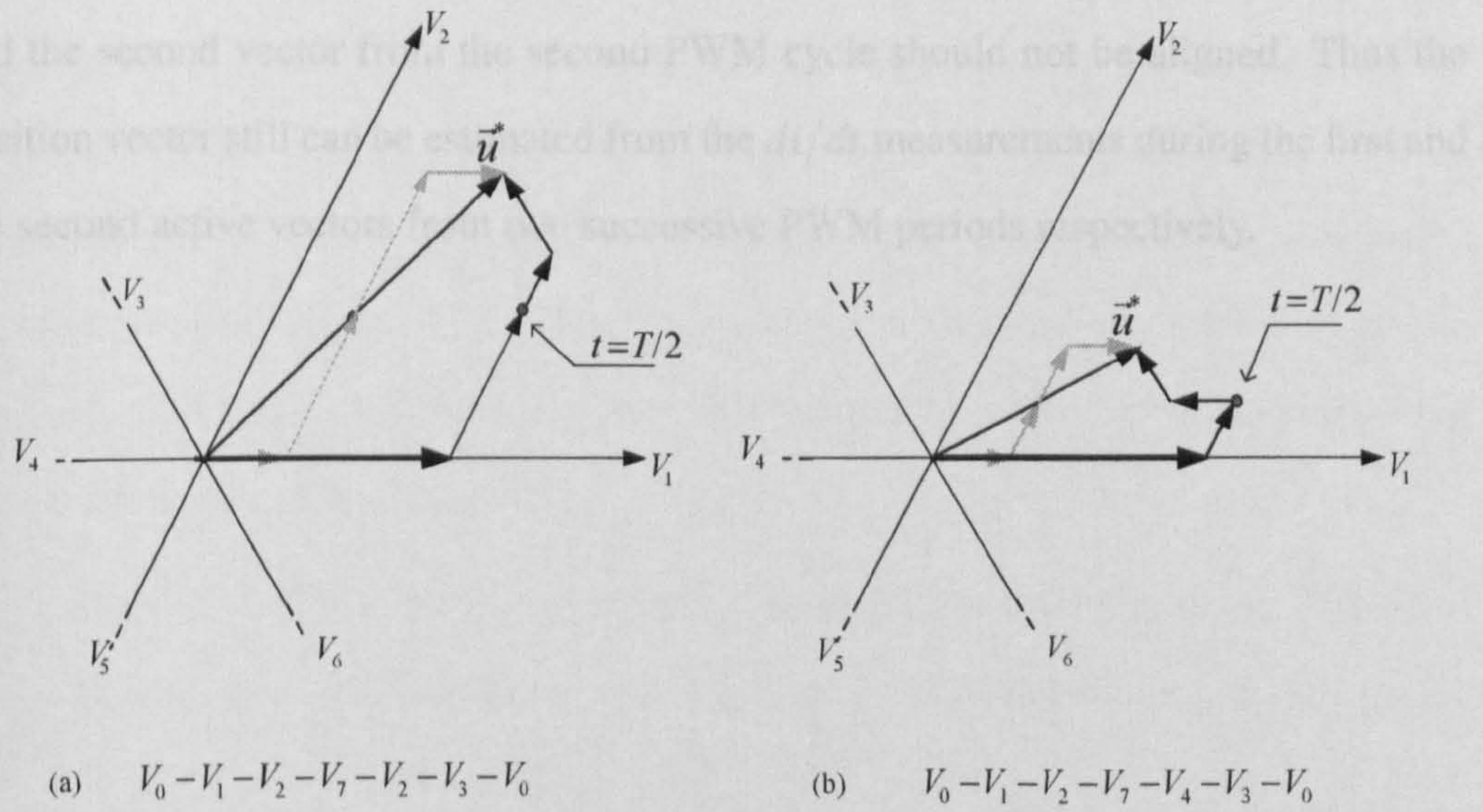

Figure 3.11: Voltage vector plot of the two cases when $\vec{u}_s^*$ locates in sector I with the extension of vector V_1

4. The sampling period of the position estimation is flexible in this proposed method. The maximum sampling frequency can reach the PWM frequency. If the current transients excited by both active voltage vectors in one PWM cycle are measured, both active vectors may have to be extended at low speed as shown in Fig 3.12. The current derivatives are measured at the indicated instants.

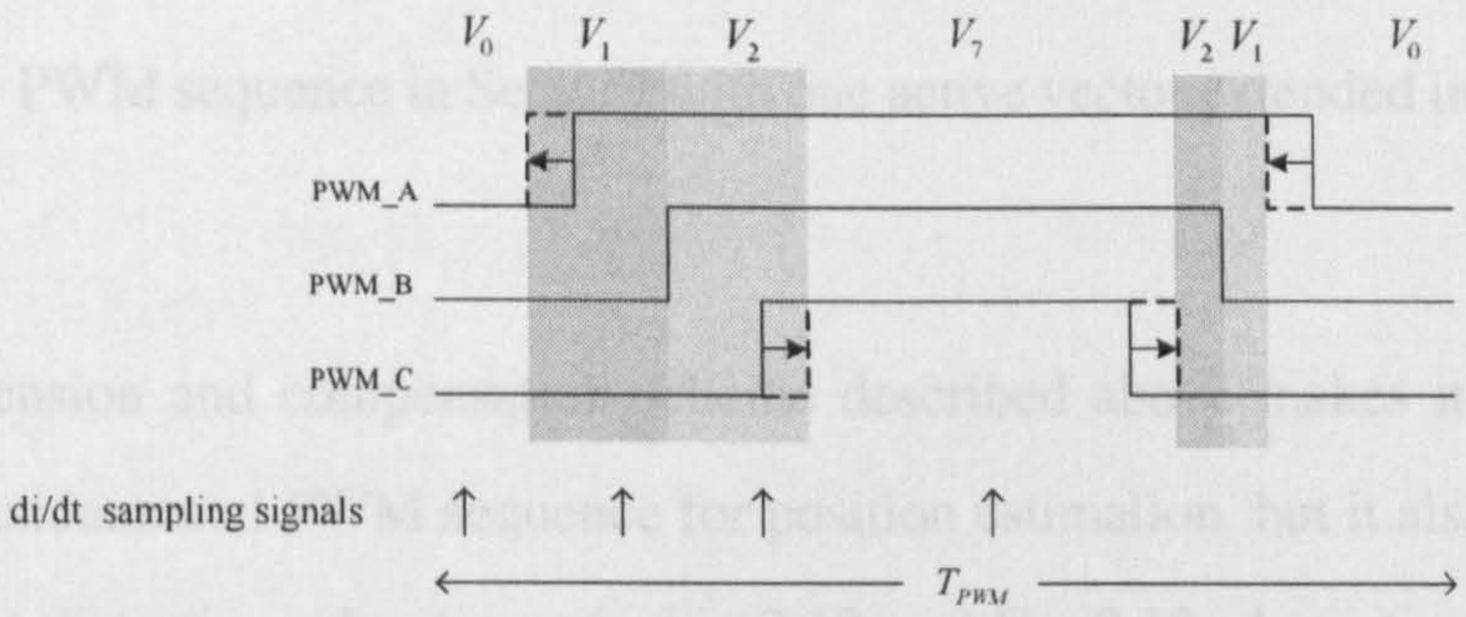

Figure 3.12: PWM sequence in Sector I (with both V_1 and V_2 being extended) and the di/dt sampling instants

Normally, the requisite position sampling frequency is much lower than the PWM frequency. One position estimation can be achieved over two consecutive PWM cycles, i.e. the transients of the two active vectors are measured from two different PWM cycles as shown in Fig 3.13. In this case the current distortion caused by the extensions and compensations will be reduced. Even if the reference voltage vector $\mathbf{u}_s^*$ changes sectors in the two consecutive PWM periods, the first vector from the first PWM cycle and the second vector from the second PWM cycle should not be aligned. Thus the position vector still can be estimated from the di/dt measurements during the first and the second active vectors from two successive PWM periods respectively.

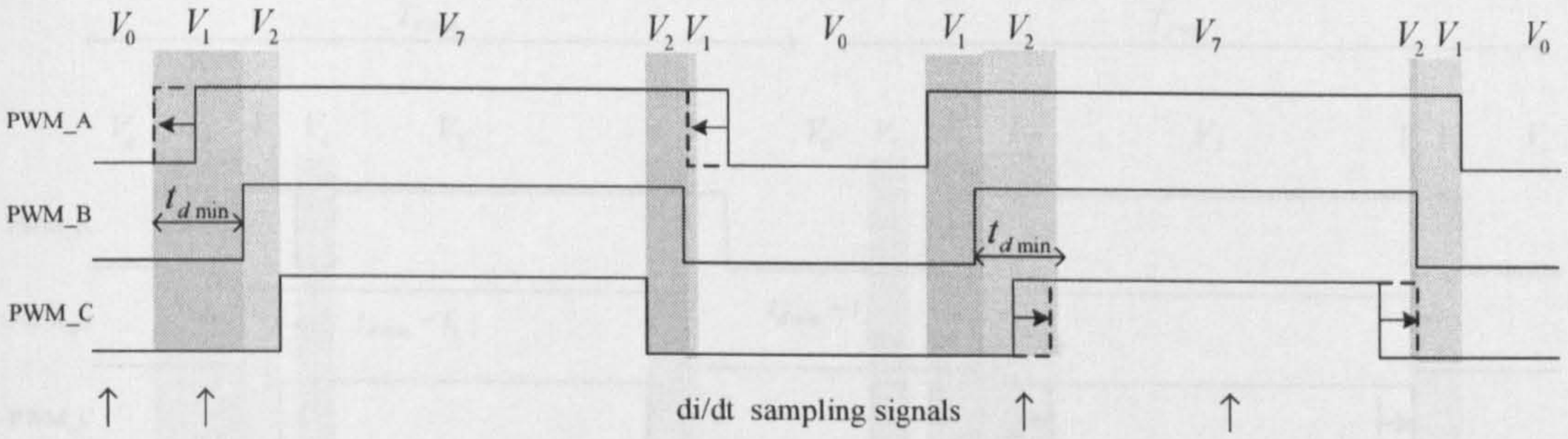

Figure 3.13: PWM sequence in Sector I with one active vector extended in each PWM period

5. The extension and compensation scheme described above makes it possible to utilize the fundamental PWM sequence for position estimation, but it also introduces extra current distortion. As shown in Fig 3.12 and Fig 3.13, the active vectors are extended in the first half PWM period, and then the compensation is made in the second half period. Thus the current deviation caused by the extension will last for the whole dwelling time of V_7.

One possible improvement is to compensate the voltage extension in advance and thus reduce the current deviation. The proposed PWM sequence when $\mathbf{u}_s^*$ is located in Sector I is illustrated in Fig 3.14. In the first half PWM period, V_1 is required for the position estimation and its duration is extended to t_{dmin}. Instead of changing the switching edge of phase A in the second half period, a compensating vector V_4, opposite to V_1, is applied just at the beginning of V_7. It means that the upper IGBT on phase A is turned off for the period of $t_{dmin} - t_1$, cancelling the influence of its extended turn-on period. Similarly, in the second PWM period, when V_2 is extended for the position estimation, its opposite switching state vector V_5 is applied during V_0 for a period of $t_{dmin} - t_2$ as compensation. This sequence can also avoid the switching of two IGBT legs at the same time.

The current distortion with this proposed scheme is less than that of the INFORM method and of [14]. The additional vector is used for current deviation compensation

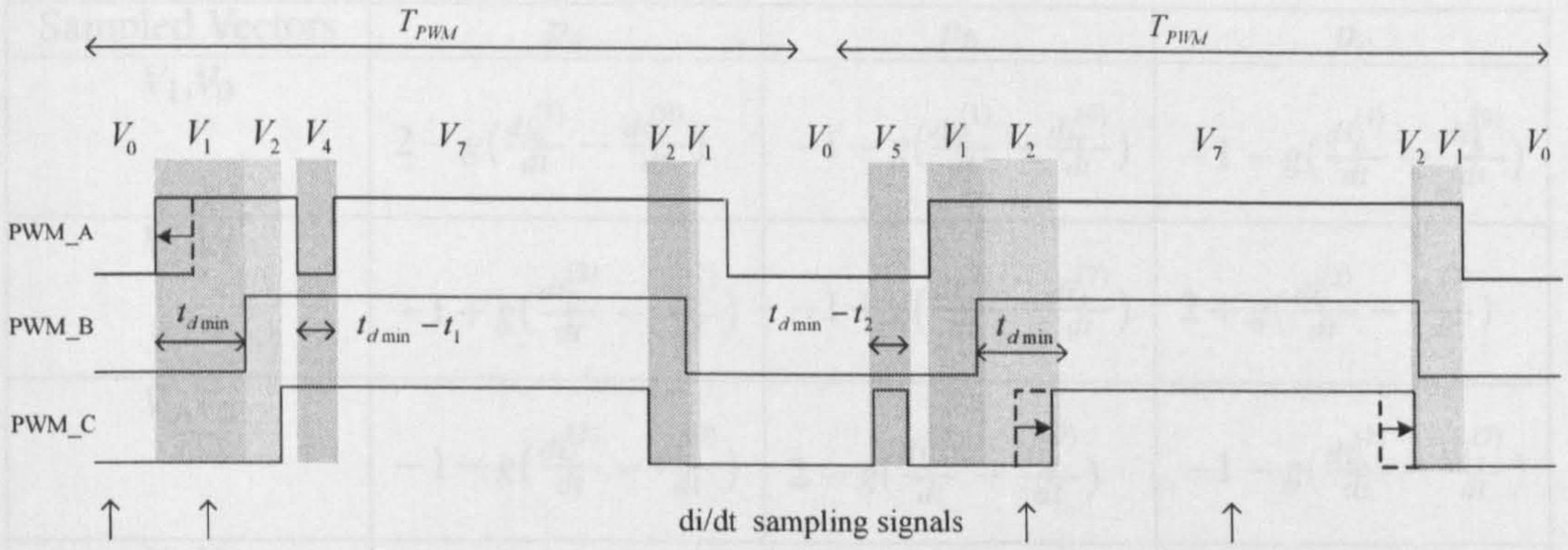

Figure 3.14: PWM sequence with extensions of V_1 in Sector I using the proposed compensation scheme

instead of di/dt sampling. Its width is adaptive to the width of active vector. It will not introduce much additional current ripple and will not restrict the application frequency.

3.2.3.3 Process of Achieving the Estimated Position Angle

Table3.1 and Table3.2 provide the relationship between the position signals (p_a, p_b and p_c) and the di/dt values excitated by the six voltage switching vectors over all sectors, for a star-connected machine and a delta-connected machine respectively[58][14]. The position vector is expressed in terms of the measured current derivatives. In each sector, the estimated position angle can be constructed from the position vector components selected from the tables according to the sector number. The position angle is obtained after the offsets in the position vector components are eliminated .

In these tables, $g = \dfrac{3l_0(1-(\dfrac{\triangle l}{2l_0})^2)}{U_{DC}}$ and $c = l_0/U_{DC}$.

Sampled Vectors	p_a	p_b	p_c
V_1,V_0	$2-g(\frac{di_a^{(1)}}{dt}-\frac{di_a^{(0)}}{dt})$	$-1-g(\frac{di_c^{(1)}}{dt}-\frac{di_c^{(0)}}{dt})$	$-1-g(\frac{di_b^{(1)}}{dt}-\frac{di_b^{(0)}}{dt})$
V_2,V_7	$-1+g(\frac{di_b^{(2)}}{dt}-\frac{di_b^{(7)}}{dt})$	$-1+g(\frac{di_a^{(2)}}{dt}-\frac{di_a^{(7)}}{dt})$	$2+g(\frac{di_c^{(2)}}{dt}-\frac{di_c^{(7)}}{dt})$
V_3,V_0	$-1-g(\frac{di_c^{(3)}}{dt}-\frac{di_c^{(0)}}{dt})$	$2-g(\frac{di_b^{(2)}}{dt}-\frac{di_b^{(7)}}{dt})$	$-1-g(\frac{di_a^{(2)}}{dt}-\frac{di_a^{(7)}}{dt})$
V_4,V_7	$2+g(\frac{di_a^{(4)}}{dt}-\frac{di_a^{(7)}}{dt})$	$-1+g(\frac{di_c^{(4)}}{dt}-\frac{di_c^{(7)}}{dt})$	$-1+g(\frac{di_b^{(4)}}{dt}-\frac{di_b^{(7)}}{dt})$
V_5,V_0	$-1-g(\frac{di_b^{(5)}}{dt}-\frac{di_b^{(0)}}{dt})$	$-1-g(\frac{di_a^{(5)}}{dt}-\frac{di_a^{(0)}}{dt})$	$2-g(\frac{di_c^{(5)}}{dt}-\frac{di_c^{(0)}}{dt})$
V_6,V_7	$-1+g(\frac{di_c^{(6)}}{dt}-\frac{di_c^{(7)}}{dt})$	$2+g(\frac{di_b^{(6)}}{dt}-\frac{di_b^{(7)}}{dt})$	$-1+g(\frac{di_a^{(6)}}{dt}-\frac{di_a^{(7)}}{dt})$

Table 3.1: position vectors calculated for a star-connected machine

Sampled Vectors	p_a	p_b	p_c
V_1,V_0	$1+c(\frac{di_b^{(1)}}{dt}-\frac{di_b^{(0)}}{dt})$	$-2+c(\frac{di_a^{(1)}}{dt}-\frac{di_a^{(0)}}{dt})$	$-1+c(\frac{di_c^{(1)}}{dt}-\frac{di_c^{(0)}}{dt})$
V_2,V_7	$-2-c(\frac{di_c^{(2)}}{dt}-\frac{di_c^{(7)}}{dt})$	$1-c(\frac{di_b^{(2)}}{dt}-\frac{di_b^{(7)}}{dt})$	$1-c(\frac{di_a^{(2)}}{dt}-\frac{di_a^{(7)}}{dt})$
V_3,V_0	$1+c(\frac{di_a^{(3)}}{dt}-\frac{di_a^{(0)}}{dt})$	$1+c(\frac{di_c^{(3)}}{dt}-\frac{di_c^{(0)}}{dt})$	$-2+g(\frac{di_b^{(3)}}{dt}-\frac{di_b^{(0)}}{dt})$
V_4,V_7	$1-c(\frac{di_b^{(4)}}{dt}-\frac{di_b^{(7)}}{dt})$	$-2-c(\frac{di_a^{(4)}}{dt}-\frac{di_a^{(7)}}{dt})$	$1-c(\frac{di_c^{(4)}}{dt}-\frac{di_c^{(7)}}{dt})$
V_5,V_0	$-2-c(\frac{di_c^{(5)}}{dt}-\frac{di_c^{(0)}}{dt})$	$1+c(\frac{di_b^{(5)}}{dt}-\frac{di_b^{(0)}}{dt})$	$1+c(\frac{di_a^{(5)}}{dt}-\frac{di_a^{(0)}}{dt})$
V_6,V_7	$1-c(\frac{di_a^{(6)}}{dt}-\frac{di_a^{(7)}}{dt})$	$1-c(\frac{di_c^{(6)}}{dt}-\frac{di_c^{(7)}}{dt})$	$-2-g(\frac{di_b^{(6)}}{dt}-\frac{di_b^{(7)}}{dt})$

Table 3.2: position vectors calculated for a delta-connected machine

The three-phase current derivatives of a star-connected surface mounted PM synchronous motor are measured when the motor is running at 100rpm (i.e. the stator current fundamental frequency $f_e = 5Hz$). The full details of this motor will be given in 5.4. The three-phase current derivative signals sampled at the first vector of the PWM cycles during two electrical rotations are shown in Fig 3.15(a). The first vector is V_1, V_3 or V_5 depending on the sector in which the voltage reference vector situates. The di/dt signals sampled at the second vectors, which are V_2, V_4 and V_6, are shown in Fig 3.15(b). The offset components in the equations of Table 3.2 can be seen from the di/dt waveforms. The units shown with these di/dt signals have no absolute meaning.

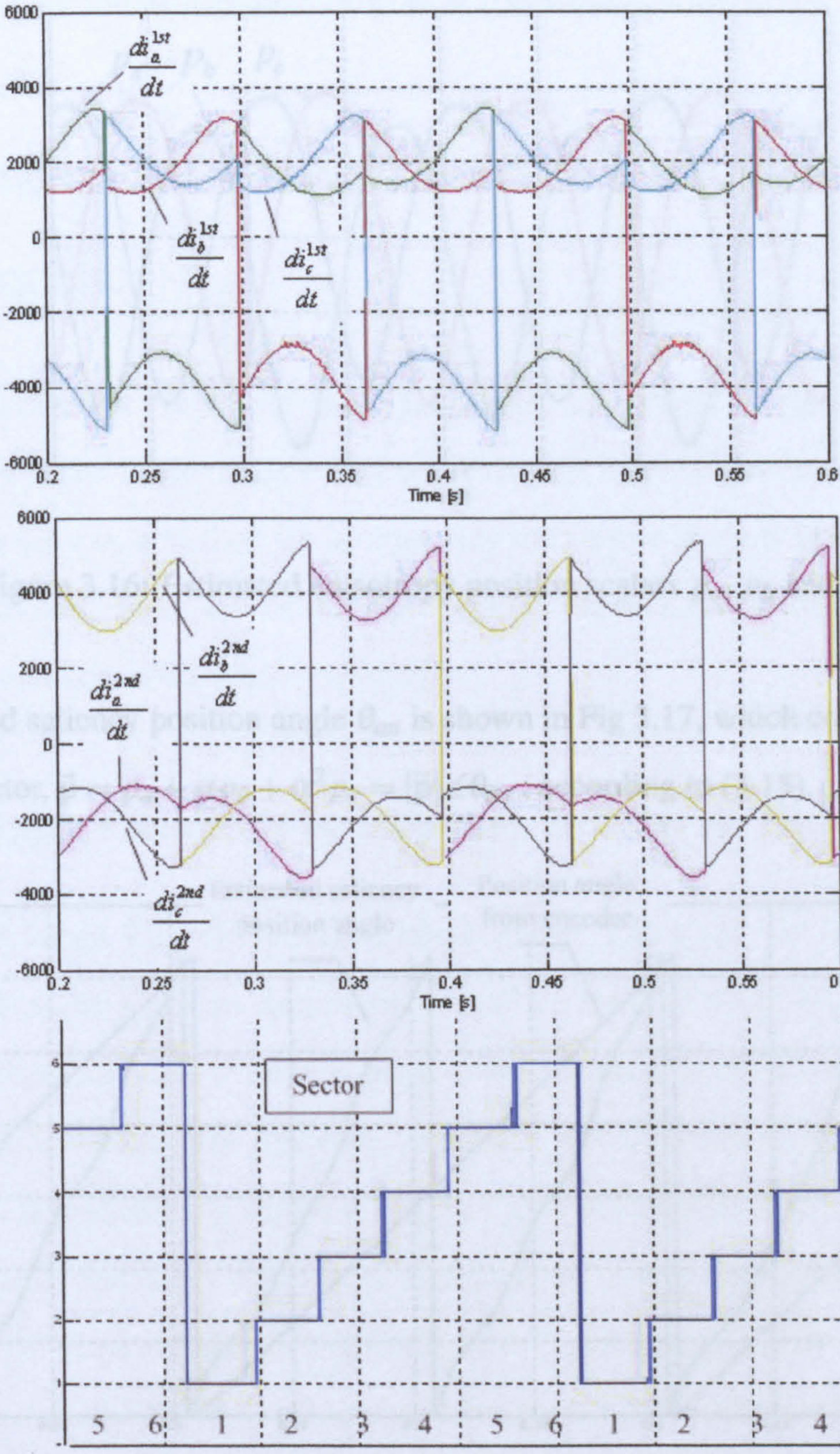

Figure 3.15: Three-phase current derivatives measured at the first (V_1, V_3 and V_5) and second (V_2, V_4 and V_6) vectors in different PWM sectors

Using these measured current derivatives, the position vector is constructed according to the theory explained in 3.2.3.2. The obtained position vector components, p_a, p_b and p_c, are shown in Fig 3.16. The offsets have been eliminated in this process.

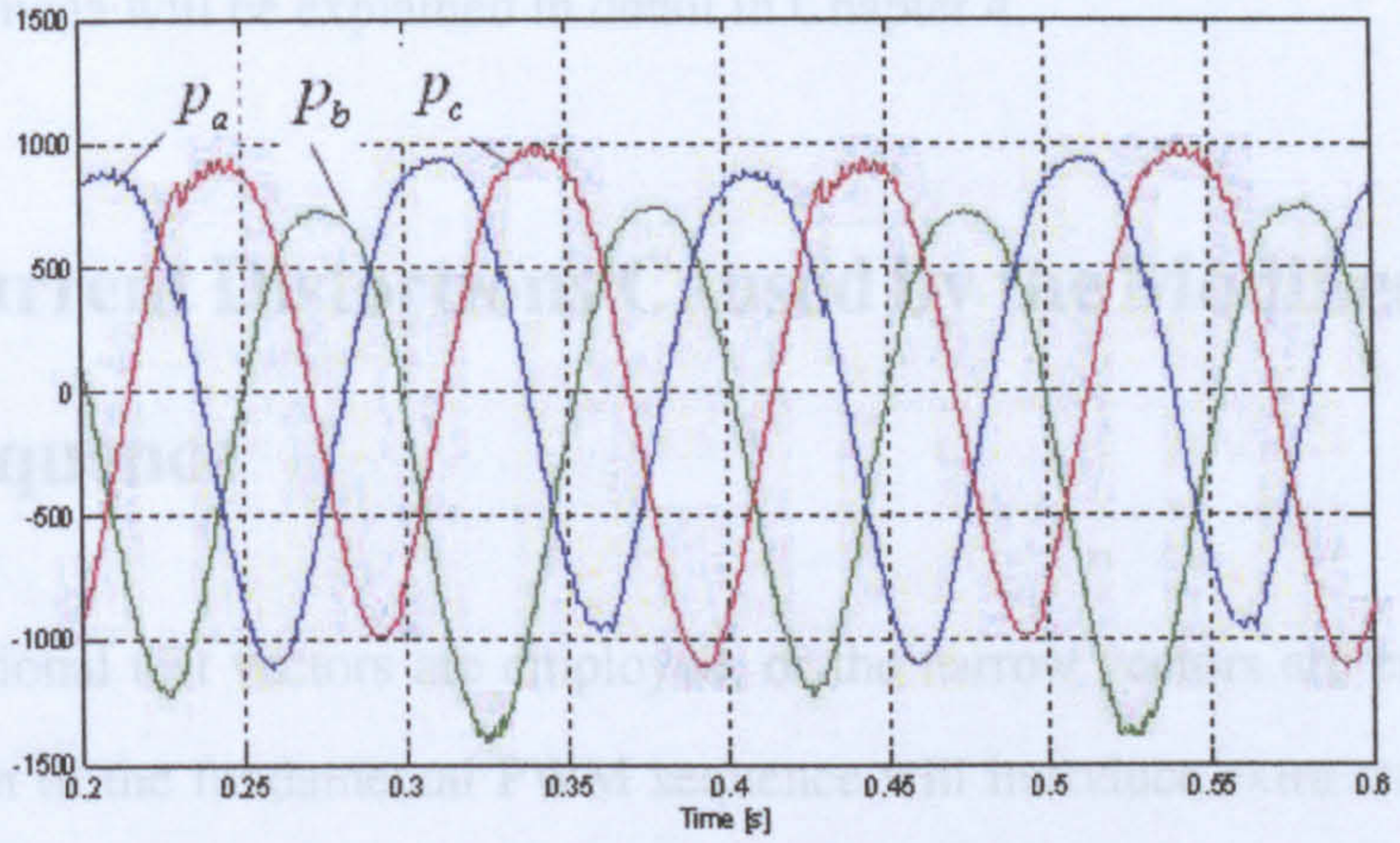

Figure 3.16: Estimated anisotropy position scalars p_a, p_b and p_c

The obtained saliency position angle θ_{an} is shown in Fig 3.17, which comes from the position vector, $\vec{\mathbf{p}} = p_a + \alpha p_b + \alpha^2 p_c = |\vec{\mathbf{p}}| \angle \theta_{an}$, according to (3.15).

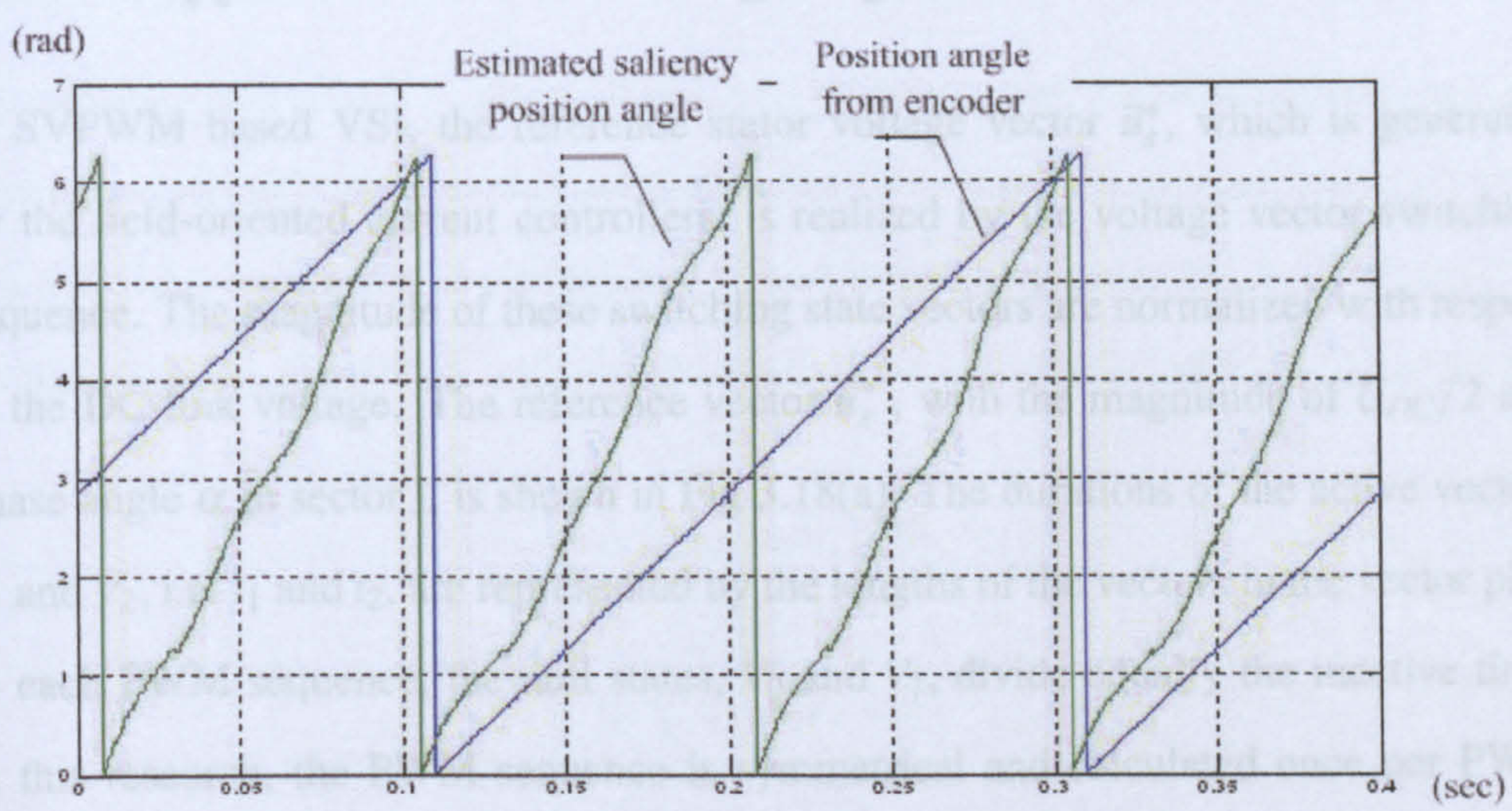

Figure 3.17: Estimated saliency position angle and the encoder measured angle

The saturation saliency position angle has twice frequency of the rotor position which is measured by optical encoder. The phase shift between these two position signals is caused by the flux deviation due to the q-axis current. The distortion appearing in the estimated position angle comes from the harmonic saliencies existing in the machine.

Both phenomena will be explained in detail in Chapter 4.

3.3 Current Distortions Caused by the Modified SVPWM Sequence

When additional test vectors are employed, or the narrow vectors are extended, the modification of the fundamental PWM sequence will introduce extra current distortion. In this section, a method for investigating the current ripple is introduced. The current distortion caused by the different position estimation schemes using PWM voltage vector excitations, are investigated.

3.3.1 Ripple Vectors for Investigating the Current Distortions

In SVPWM based VSI, the reference stator voltage vector $\vec{u}_s^*$, which is generated by the field-oriented current controllers, is realized by the voltage vector switching sequence. The magnitude of these switching state vectors are normalized with respect to the DC-link voltage. The reference vector $\vec{u}_s^*$, with the magnitude of $U_{DC}/2$ and phase angle α in sector I, is shown in Fig 3.18(a). The durations of the active vectors V_1 and V_2, i.e. t_1 and t_2, are represented by the lengths of the vectors in the vector plot. In each PWM sequence, the null states, V_0 and V_7, divide equally the inactive time. In this research, the PWM sequence is symmetrical and calculated once per PWM period.

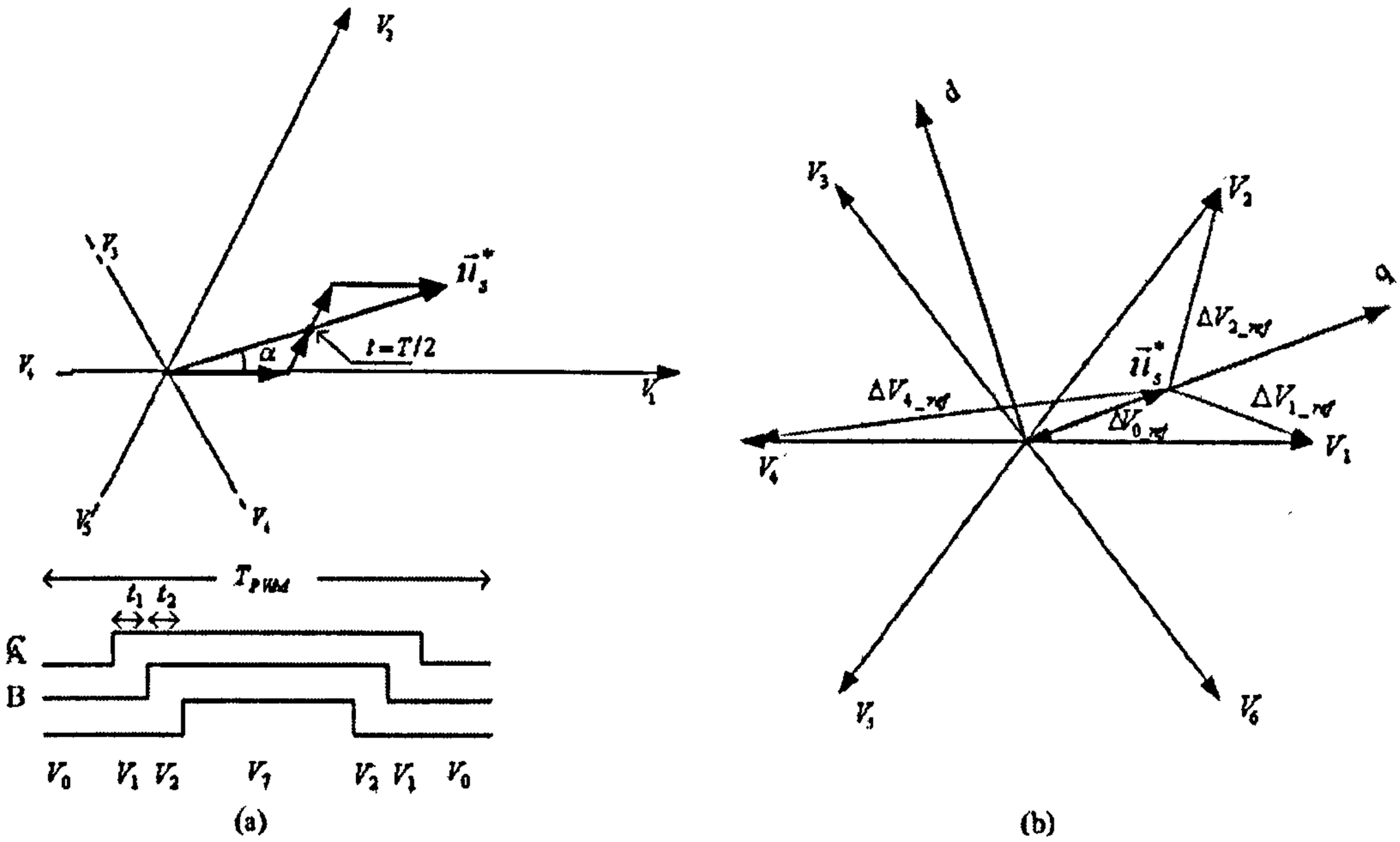

Figure 3.18: Standard SVPWM application (a): fundamental PWM sequence (b): error voltage vectors

For a PWM inverter drive system, there is an error between the instantaneous applied voltage vector and the reference voltage vector [77]. For the reference voltage in this example, the voltage error corresponding to the active vectors V_1, V_2, and the zero vectors, V_0 or V_7, are illustrated in Fig 3.18(b). They are expressed by the vectors as:

$$\Delta V_{1-ref} = V_1 - \vec{u}_s^*$$

$$\Delta V_{2-ref} = V_2 - \vec{u}_s^* \tag{3.45}$$

$$\Delta V_{0-ref} = \Delta V_{7-ref} = -\vec{u}_s^*$$

These voltage errors referred to the reference voltage vector can be defined as "voltage ripple vector", represented by $\mathbf{u}_{ripple}$, because the time integrals of these error voltage vectors can decide the distortion in the output voltage[77]. The voltage errors directly result in the ripple appearing on the stator current. A measure of the phase current ripple can be defined correspondingly as the "current ripple vector", $\mathbf{i}_{ripple}$. If the

resistance voltage drop and the back EMF are neglected, which can be assumed in low speed range, the voltage and current ripple vectors are orthogonal. In the PM motor, these ripple vectors can be resolved along the d-axis and q-axis, in the reference frame synchronized with the rotating reference voltage vector $\vec{u}_s^*$. The q-axis, in accordance with the torque current direction, is aligned with $\vec{u}_s^*$. The d-axis is perpendicular with the q-axis. The voltage ripple vector exists when the switching state vectors are applied, and the current ripple vector is excited by the voltage ripple vector, deriving from the inductive stator circuit.

Figure 3.19(a) illustrates the voltage ripple vector plot for one fundamental PWM cycle. It starts from and ends at the original point. The voltage ripple on d-axis in the first half period and the second half period are symmetrical. The route of the voltage ripple vector is indicated by black lines in the first half cycle and gray in the second half. The d-axis and q-axis voltage and current ripples are derived and plotted in Fig 3.19(b) according to the voltage ripple vector plot. All these ripple waveforms are continuous and piecewise linear functions of time. The voltage ripples on both axes change at the switching instants, and consequently the slopes of the current ripples change at the same time. The total current harmonic distortion can be evaluated by summing the areas confined by the ripple waveforms and the zero axis. The total voltage distortion or the total current distortion over one PWM period is the sum of that on the q-axis and that on the d-axis.

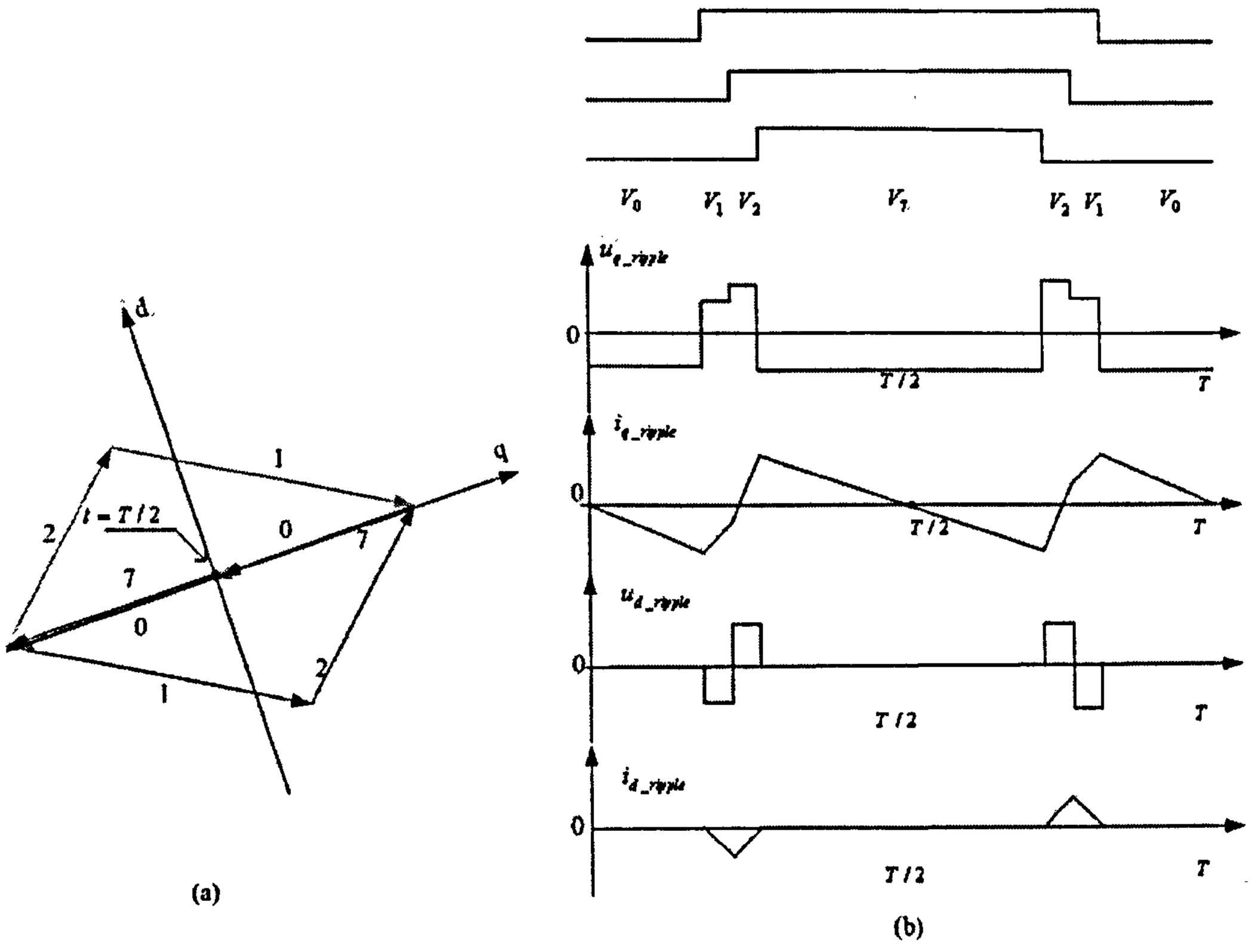

Figure 3.19: Voltage and current ripples of the fundamental SVPWM sequence (a)vector plot of the voltage ripple (b)ripples on the voltages and currents

The magnitudes of both voltage ripple and current ripple over one fundamental PWM period depend on the reference voltage vector and the employed switching sequence.

3.3.2 Current Distortion with the INFORM method

Besides the voltage and current ripple appearing with the fundamental SVPWM sequence, the INFORM method introduces extra distortions due to the added test vectors. The switching sequence of the INFORM method in one PWM period is shown in Fig 3.20, where the reference voltage vector $\mathbf{u}_s^*$ is in Sector I. One pair of test vectors, V_1 and V_4, are inserted during V_7. Both test vectors applied have the width of t_{dmin}. The voltage ripple vectors in this sequence are plotted in Fig 3.20(a). The current distortion can be investigated on the q-axis and d-axis respectively as shown in Fig

3.20(b). The ripple added to the fundamental PWM (same as shown in Fig 3.19) is indicated by the light gray lines for comparison. As can be seen, although the VTA is kept same, the current deviation caused by the added vectors is significant.

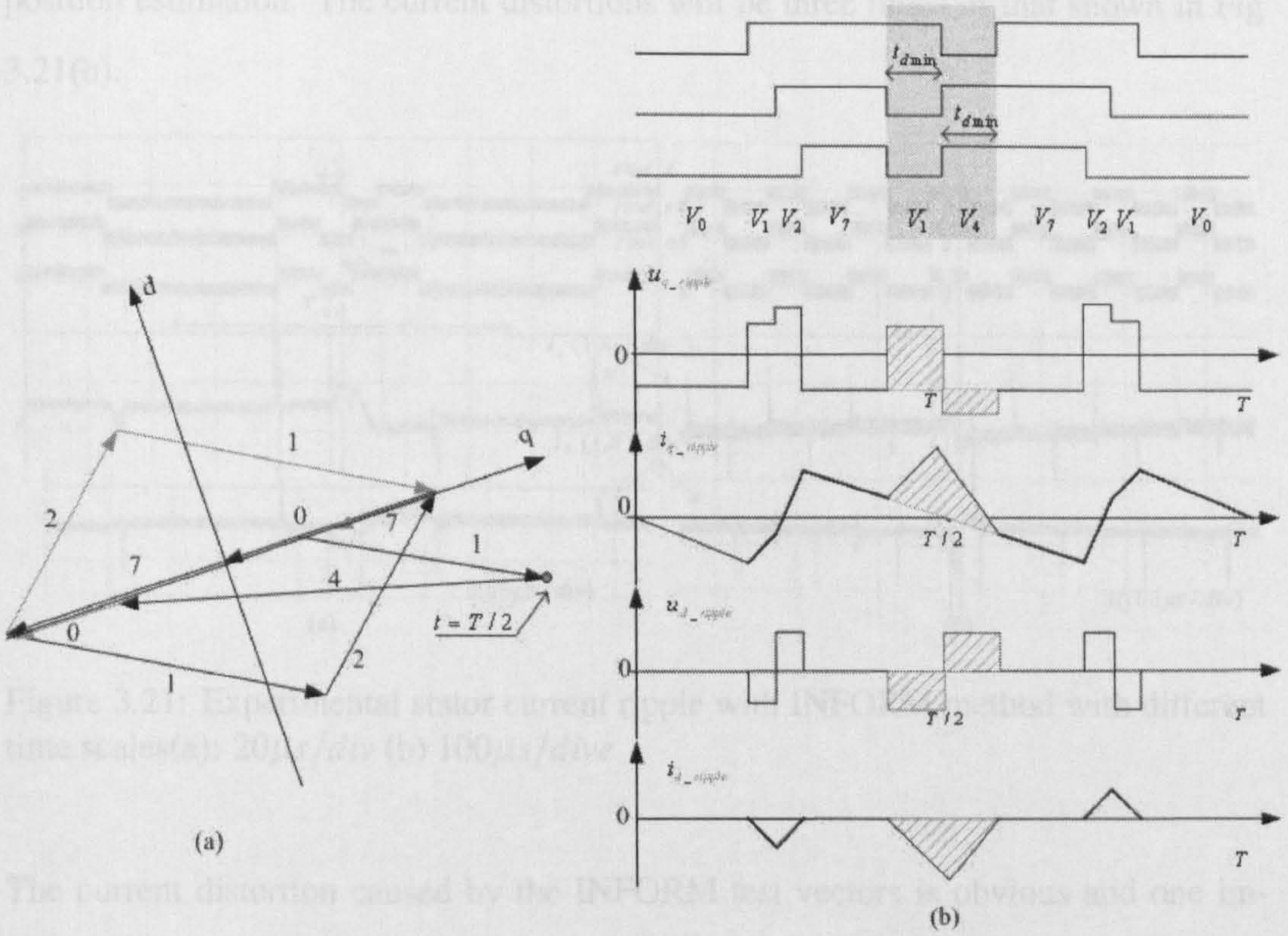

Figure 3.20: Voltage and current ripples of the INFORM method (a):voltage ripple vector plot (b):voltage and current ripple waveforms

To illustrate the current distortion, the stator currents are measured when a surface mounted PMSM is driven using the INFORM scheme. The PM machine is controlled at the speed of $100rpm$ without external load. The symmetrical PWM sequence is updated every $100\mu s$. The minimum duration t_{dmin} are set to be $8\mu s$. For easier comparison between different schemes, the currents shown are all measured when $\mathbf{u}_s^*$ situates in the middle of Sector I. The current ripple caused by the INFORM test vectors can been seen from Fig 3.21. Two phase output currents, i_a and i_b, measured in one PWM cycle are shown in Fig 3.21(a). The test vectors, V_1 and V_4, are added during the dwell time of the null vector V_7. The effect from the deadtime of $3\mu s$ can

also been seen. The influence of this test vector pair on the current waveforms in a longer period is illustrated in Fig 3.21(b). Actually, three pairs of the test vectors should be implenmented in three successive PWM periods for every sample of the position estimation. The current distortions will be three times of that shown in Fig 3.21(b).

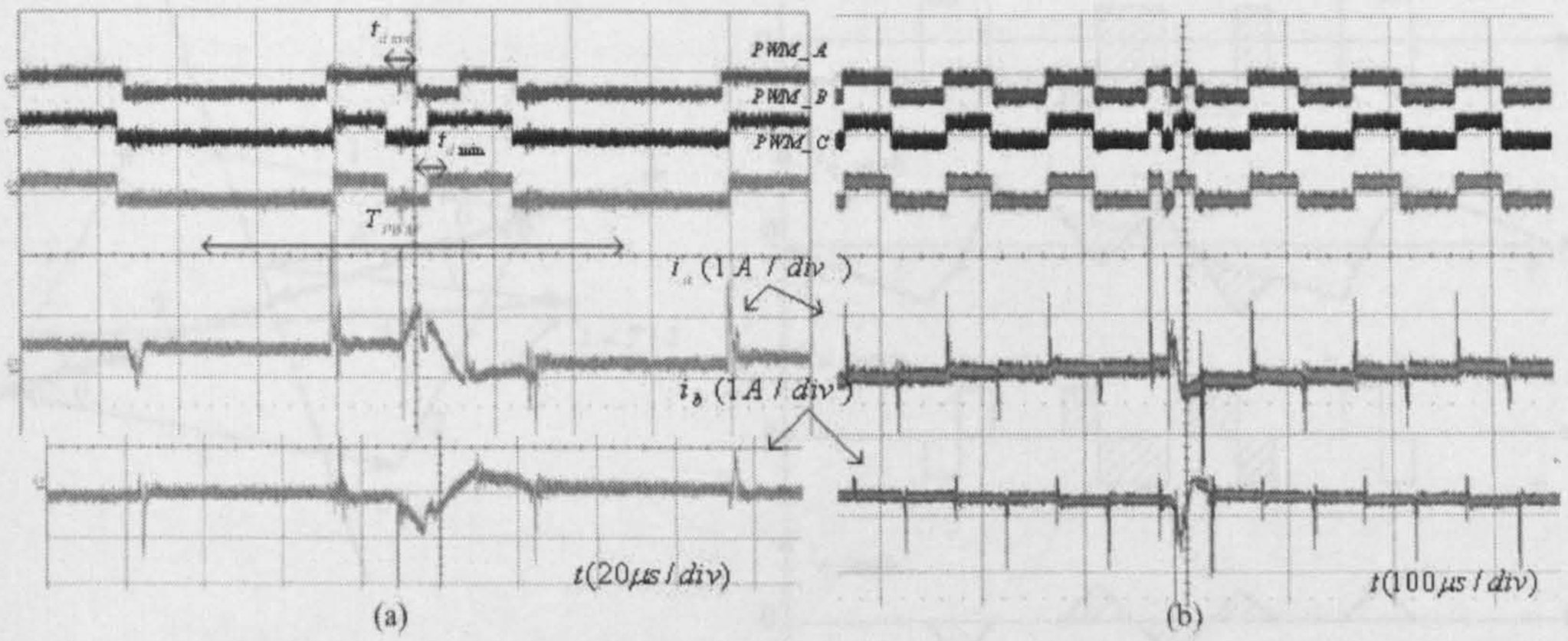

Figure 3.21: Experimental stator current ripple with INFORM method with different time scales(a): $20\mu s/div$ (b) $100\mu s/dive$

The current distortion caused by the INFORM test vectors is obvious and one improvement has been presented in [55]. This scheme adds two more vectors to reduce the current deviations. As shown in Fig 3.22, the test vectors, V_1 and V_4, have the width of t_{dmin}. The other two vectors with the width of $t_{dmin}/2$ are used to reduce the current deviations. For this PWM sequence, the voltage ripple vector route in one PWM period is plotted in Fig 3.22(a) and the ripple waveforms are derived in Fig 3.22(b). Compared with Fig 3.20 the added vectors help to make the current waveforms less distorted as explained in [55]

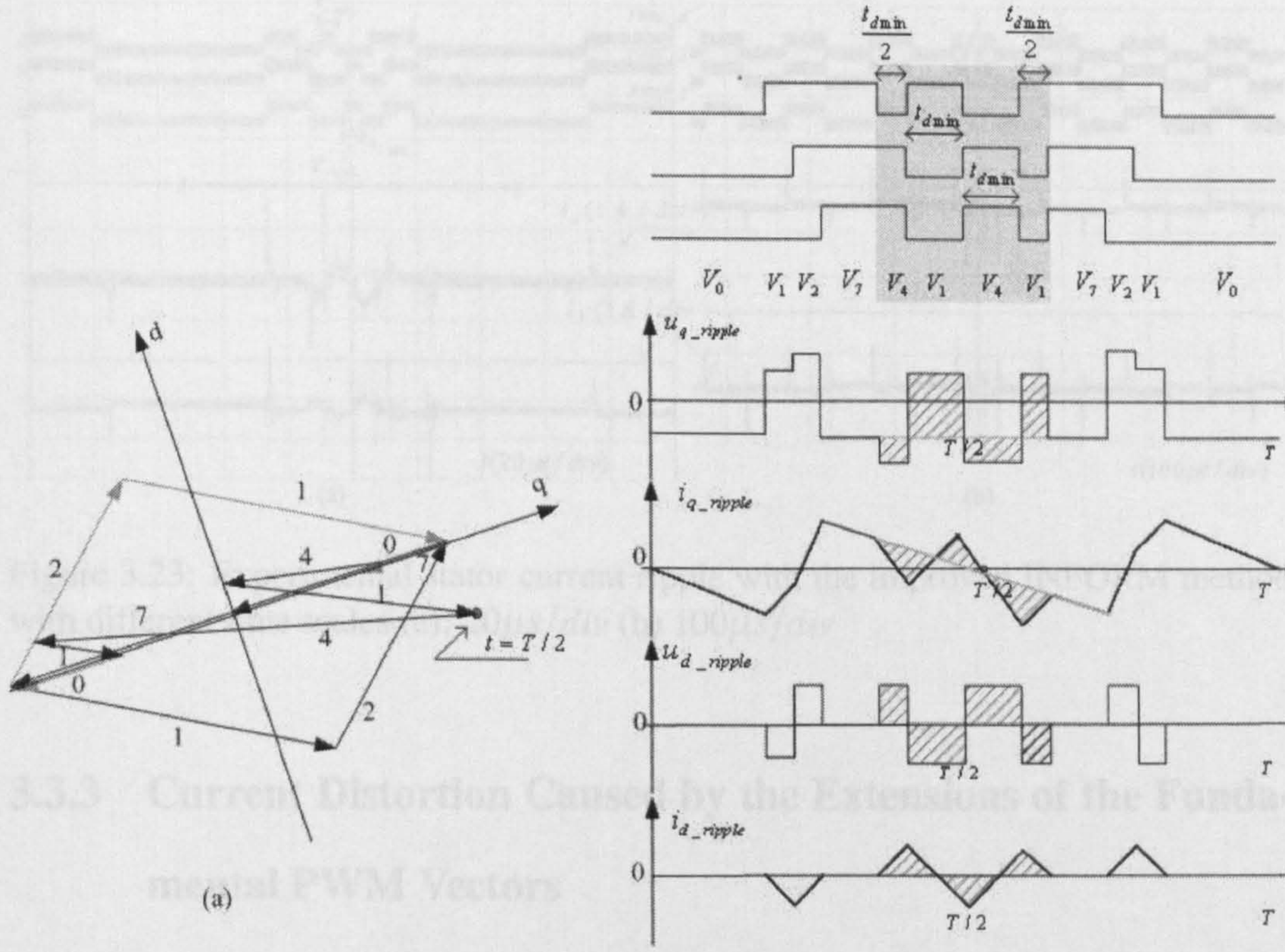

Figure 3.22: Voltage and current ripples of the improved INFORM method (a):voltage ripple vector plot (b):voltage and current ripple waveforms

Experiments are carried out for this improved INFORM switching sequence. The measured two phase currents, under the same experimental conditions as explained for Fig 3.21, are shown in Fig 3.23. Also three times distortion will exist for the position estimation, because three successive PWM cycles are used for the transient measurements. Both of the PWM sequences of the INFORM method, require the null vector to be wide enough for holding all the additional vectors. which can be hard to guarantee at higher speed or with shorter PWM period T_{PWM}.

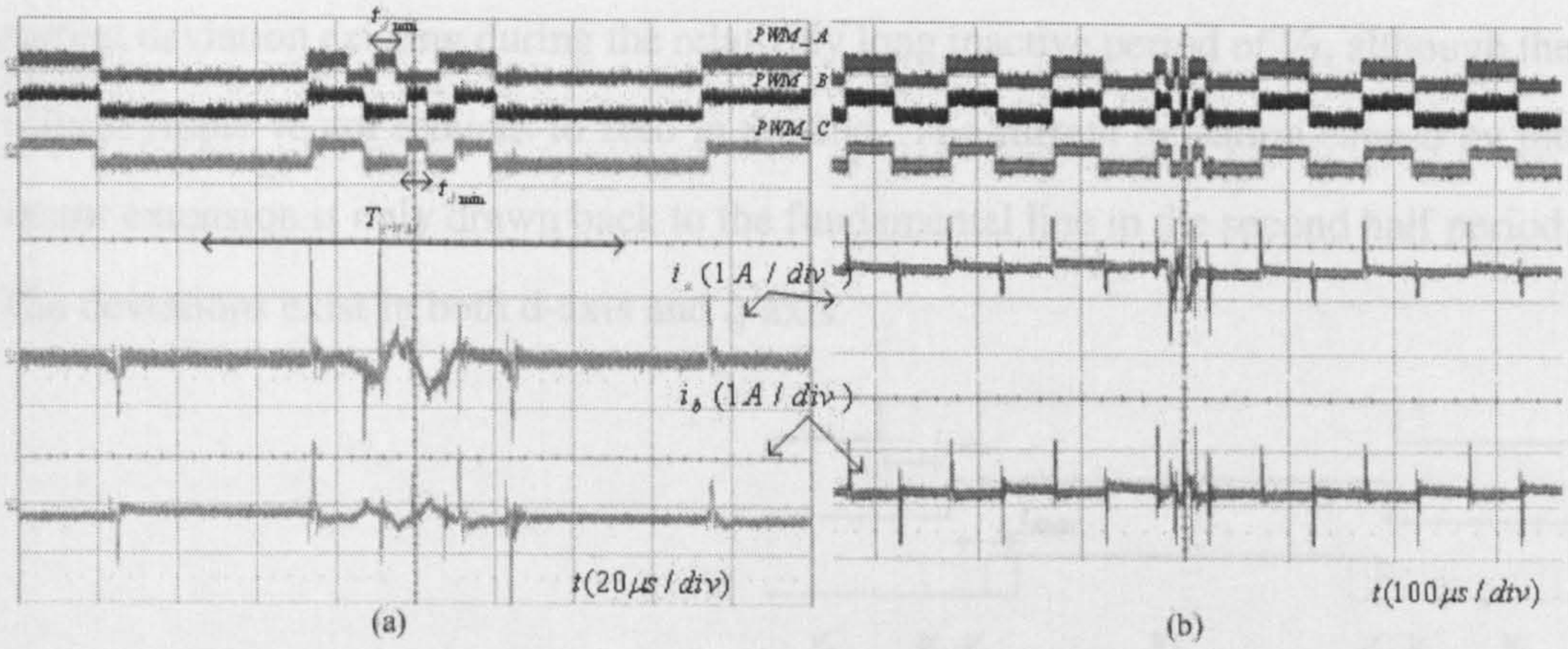

Figure 3.23: Experimental stator current ripple with the improved INFORM method with different time scales (a): $20\mu s/div$ (b) $100\mu s/div$

3.3.3 Current Distortion Caused by the Extensions of the Fundamental PWM Vectors

Instead of using additional test vectors, the active vectors of the fundamental PWM sequence are utilized for position estimation in this research. However, additional current ripple still exists when the narrow vectors are extended to meet the minimum vector width t_{dmin}. The current deviations caused by the extensions and compensations can also be explained by the ripple vectors.

As explained in 3.2.3.2, one sample of the position estimation can be obtained from the two active voltage vectors and the two null vectors in one fundamental PWM cycle. The worst case is that both original active vectors are too narrow and need to be extended in the single PWM cycle. The current ripple in this case is described in Fig 3.24. The voltage ripple vector in one PWM cycle is plotted in Fig 3.24(a). The black and gray solid lines indicate the ripple vector in the first and second half of the PWM period respectively. The dashed line indicates the ripple vector of the fundamental PWM sequence for comparison. The voltage and current ripple waveforms are shown in Fig 3.24(b). As can be seen, one main disadvantage of this scheme is that the big

current deviation existing during the relatively long inactive period of V_7, although the voltage ripple vector reduces to zero in the end. The current deviation caused by the vector extension is only drawn back to the fundamental line in the second half period. The deviations exist in both d-axis and q-axis.

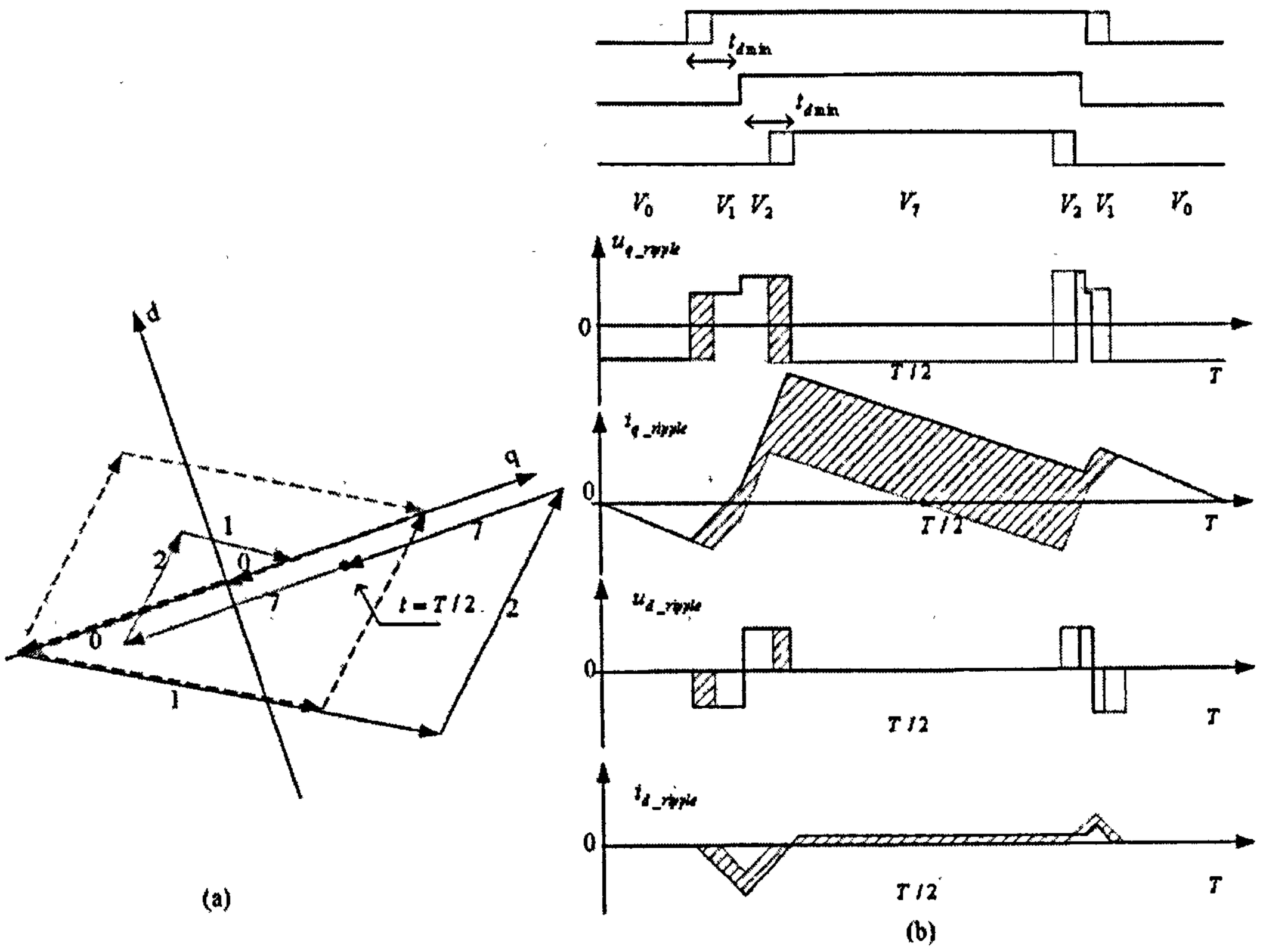

Figure 3.24: Voltage and current ripples of the fundamental PWM with the extensions of the two active vectors (a):voltage ripple vector plot (b):voltage and current ripple waveforms

Experiments under the specified conditions were carried out for this scheme. Two phase stator currents, i_a and i_b , are measured and their deviations in one PWM period can be seen from Fig 3.25(a). Their influence on the stator current waveforms for a longer time is shown in Fig 3.25(b). One point is that one sample of the estimated position can be achieved in only one single PWM period in this method and the current deviation shown here is the worst case.

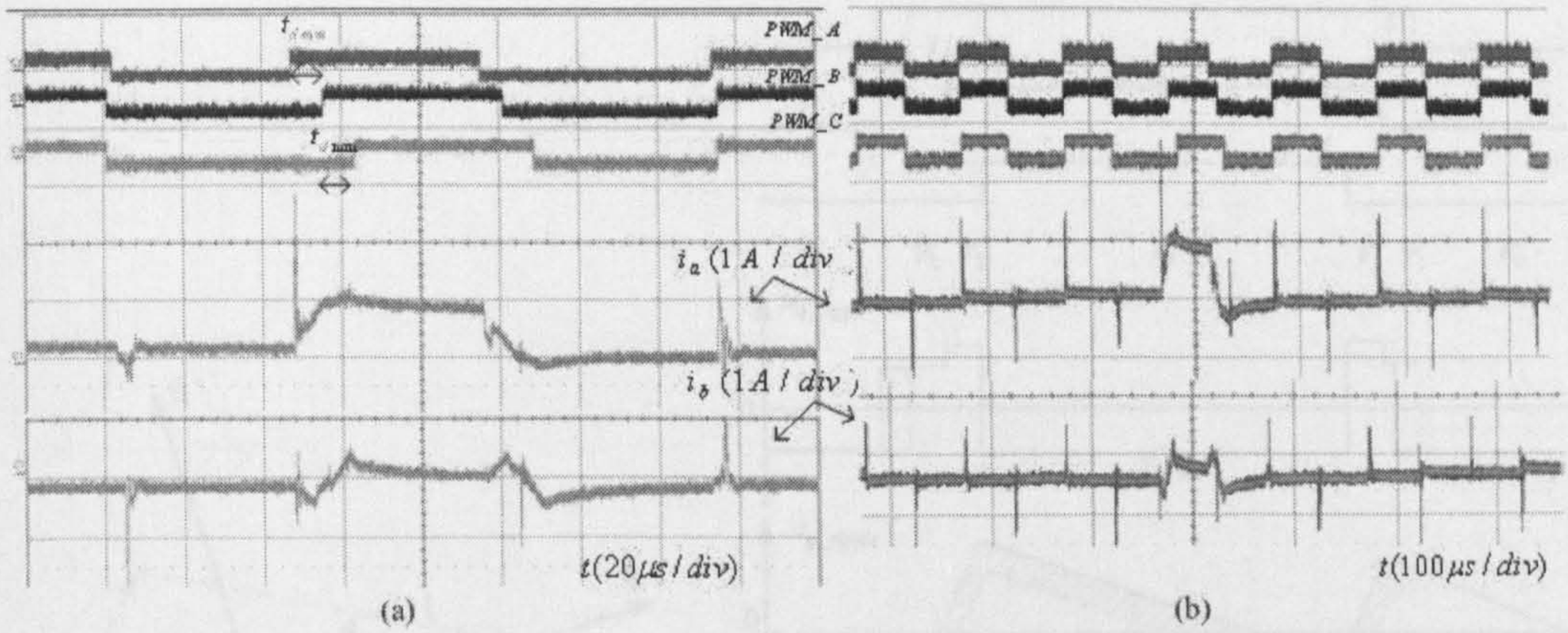

Figure 3.25: Experimental stator current ripples with extensions of both active vectors in one fundamental PWM period with different time scales (a) $20\mu s/div$ (b) $100\mu s/div$

The sampling frequency of the estimated position does not need to be that high. The excitations from two active vectors for one position estimation can be obtained from two successive PWM periods. The current ripple caused by the extensions can then be reduced. The current distortion is drawn in Fig 3.26 for this approach.

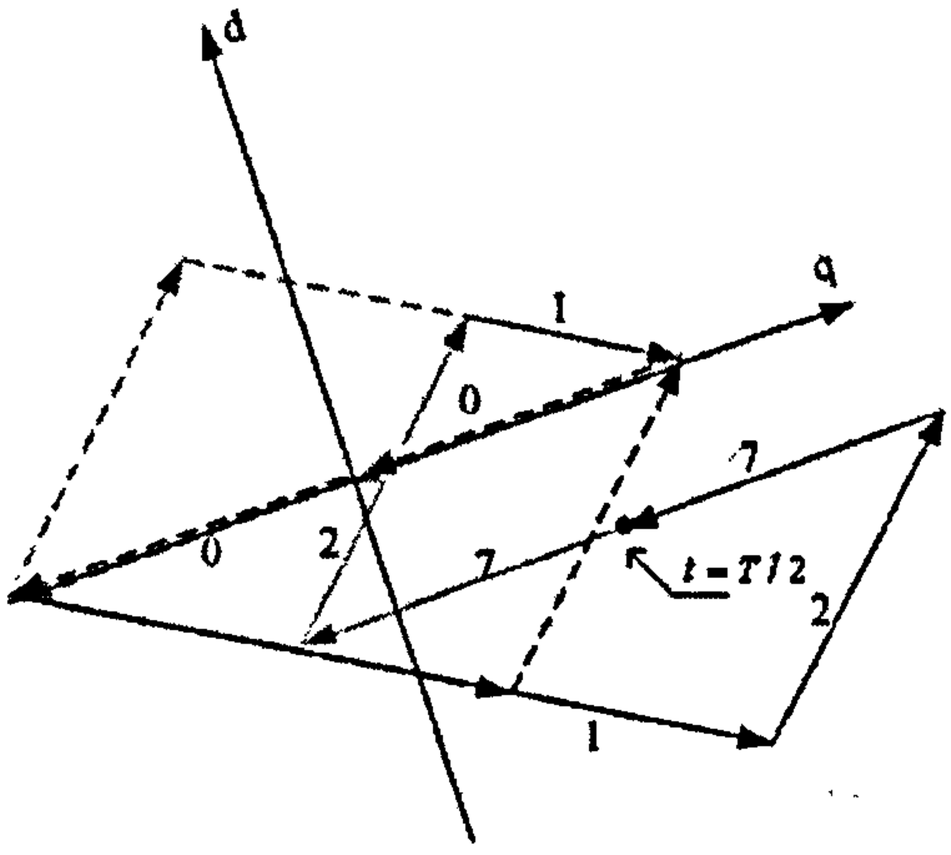

(a)

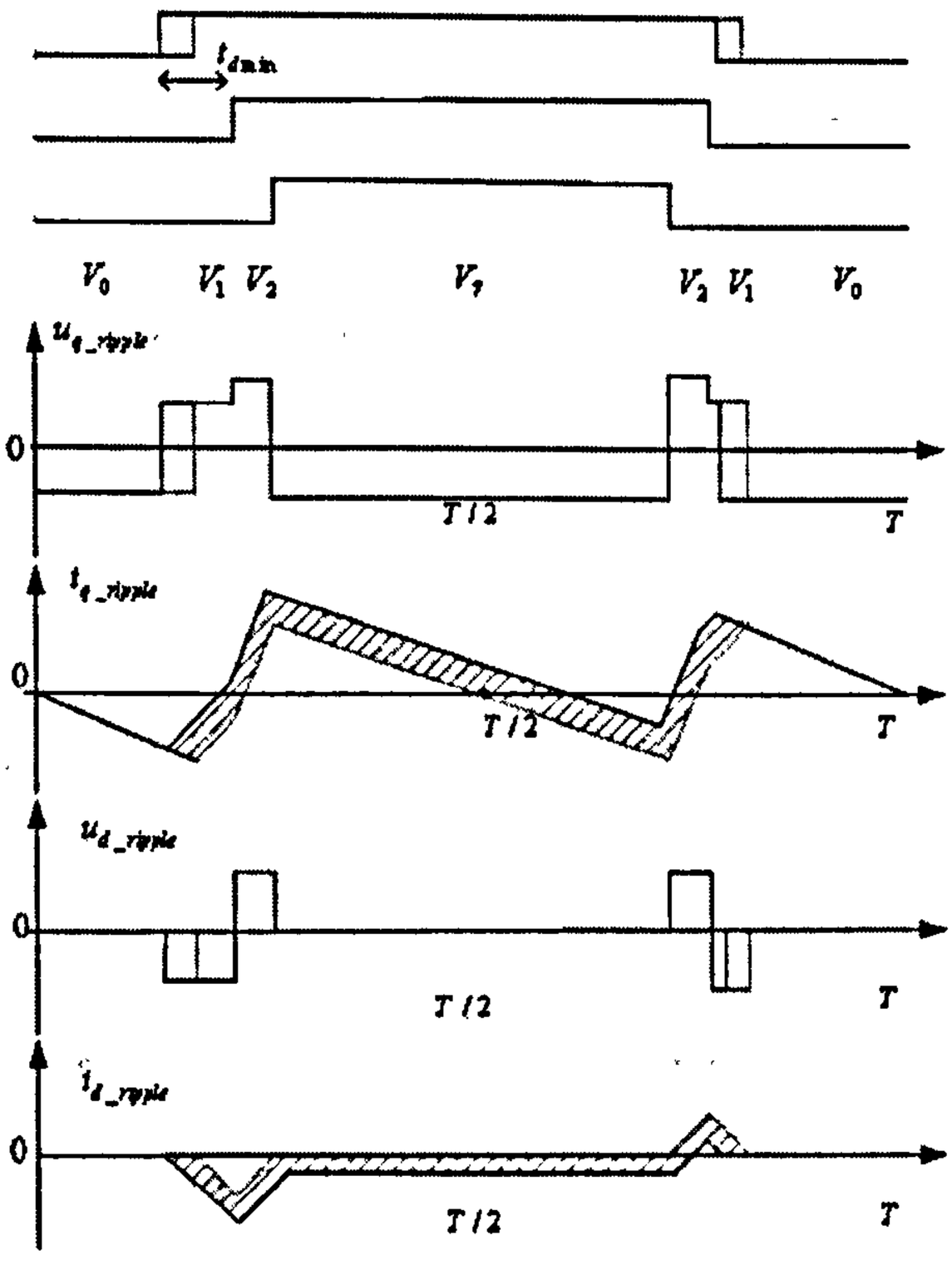

(b)

Figure 3.26: Voltage and current ripples of the fundamental PWM with the extension of one active vector in one PWM period (a):voltage ripple vector plot (b):voltage and current ripple waveforms

The displacement during the inactive vector V_7 still exists in both d-axis and q-axis, but is reduced. The level of the current deviation mainly depends on the degree of extension. Experimental measurements under the conditions specified in this section are shown in Fig 3.27. The main advantage of this method is that no additional vectors are inserted and the extension will occur only when the original vector is not wide enough. This method is applicable in high speed range.

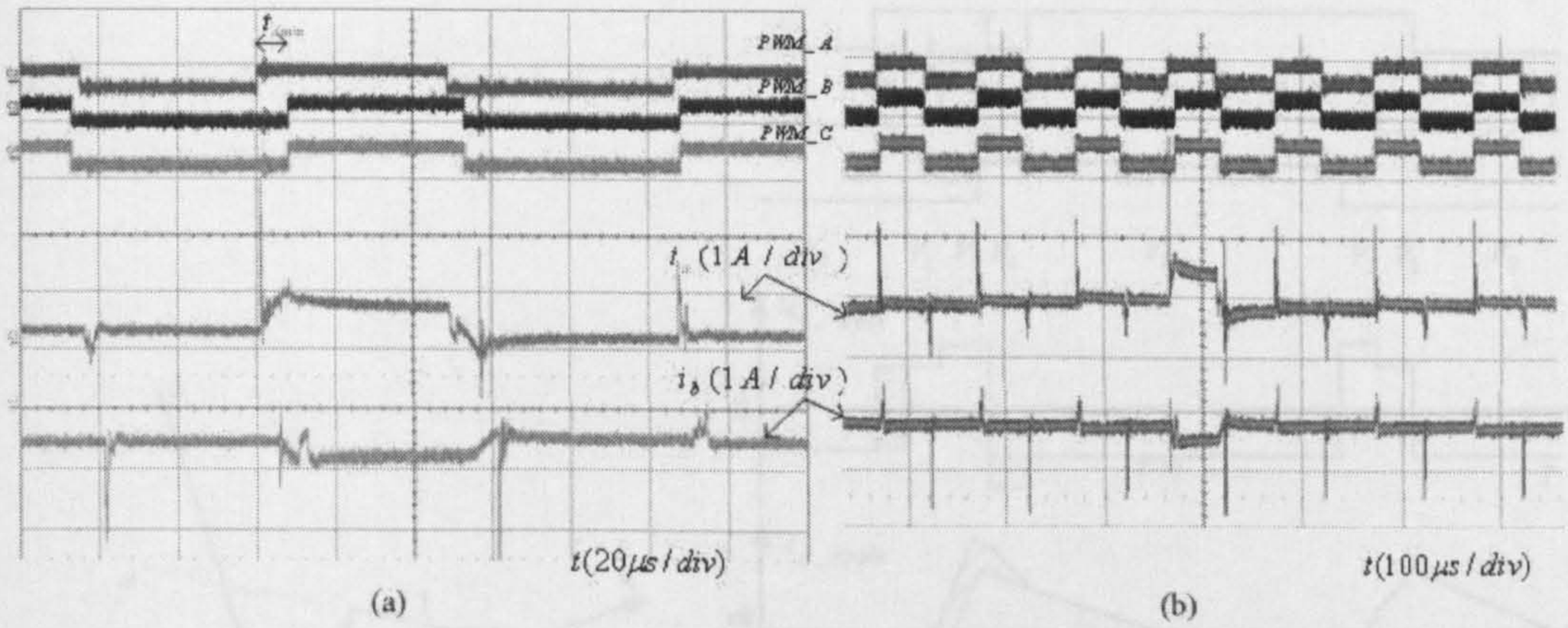

Figure 3.27: Experimental stator current ripple with extensions of one active vector in one fundamental PWM period with different time scales (a): $20\mu s/div$ (b) $100\mu s/div$

3.3.4 Current Distortion with the Improved Compensation Scheme for the Extensions of the Fundamental PWM Vectors

The current distortions discussed in 3.3.3 mainly come from the extensions of the active vectors and the delayed compensations made in the second half period. The current deviation exists during the whole period of the V_7 on both d-axis and q-axis current waveforms.

To reduce this deviation, the compensation can be made in advance, as explained in 3.2.3.2. The improvement scheme is that, when an active voltage vector is extended to t_{dmin} for the position estimation, its opposite voltage vector will be applied during the null vector, with the width equal to the the extended part. For example, the active vector to be extended is V_1 and its original width in the fundamental PWM sequence is $t_1(t_1 < t_{dmin})$. When it is extended to t_{dmin} , its opposite switching state vector V_4, with the width of $t_{dmin} - t_1$, will be inserted at the beginning of the null vector V_7. In this way the current deviation caused by the extension will be drawn back earlier. The current distortion of this improved scheme is illustrated in Fig 3.28.

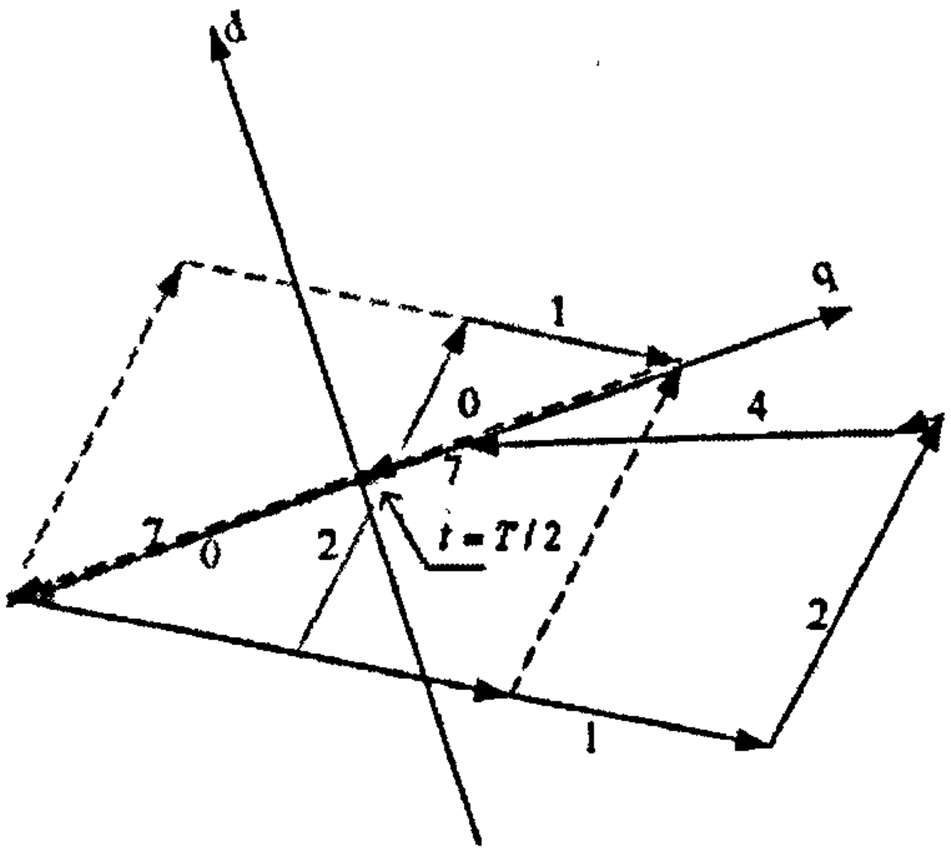

(a)

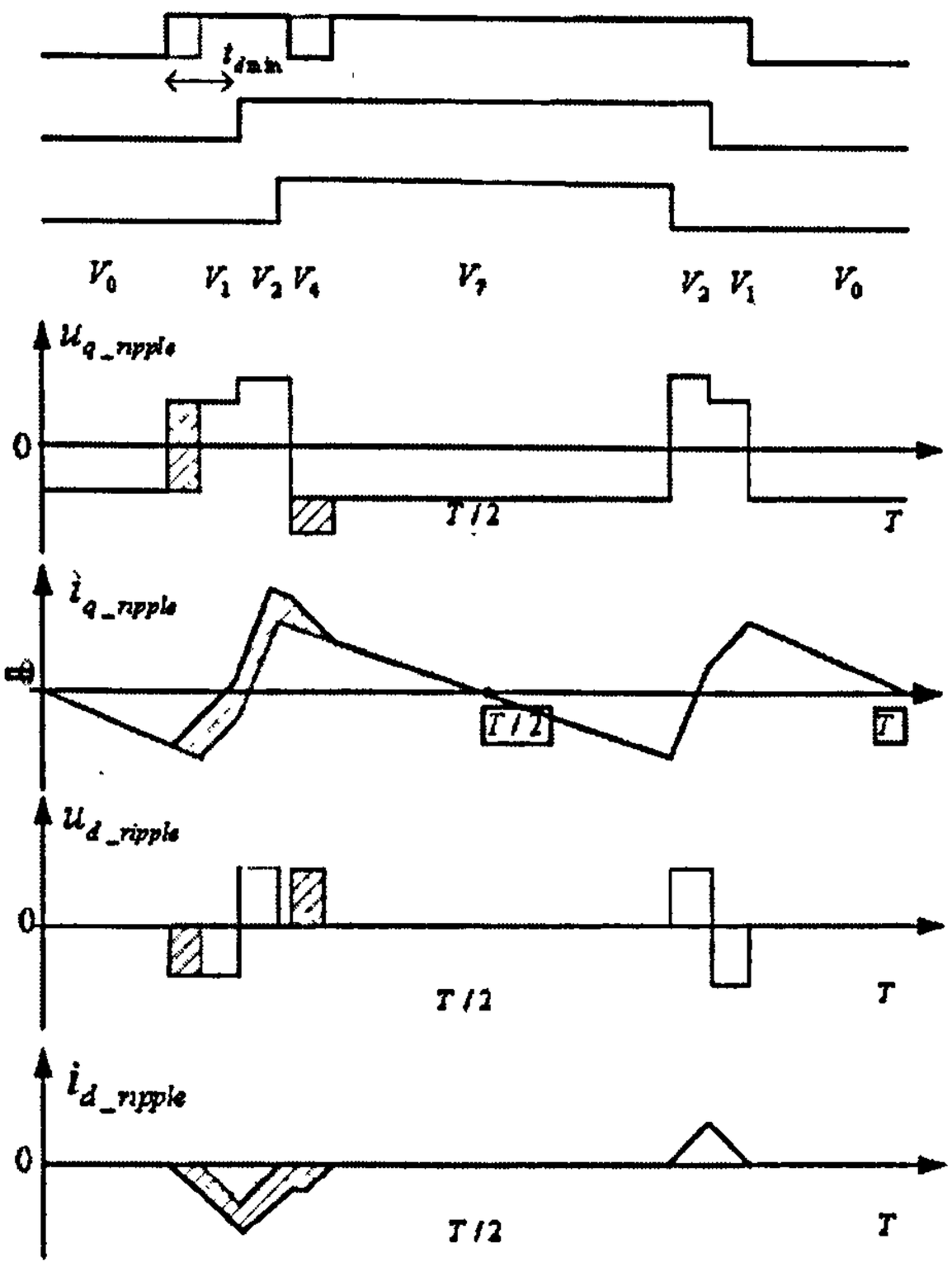

(b)

Figure 3.28: Ripple investigation of the fundamental PWM with improved extension scheme (a):voltage ripple vector plot (b):voltage and current ripple waveforms

The current waveforms measured under the specified experimental conditions are shown in Fig 3.29. As can be seen, the deviation in the current waveforms are reduced compared with Fig 3.25 and Fig 3.27. Although an additional voltage vector is inserted, it only works for the cancellation of the current deviation, and does not provide the transient excitation for position estimation. One sample of the estimated position can be achieved from two or one PWM period, similar to the schemes explained in 3.3.3. If only one active voltage vector is utilized as shown in Fig 3.29, one position estimation can be achieved from two successive PWM cycles.

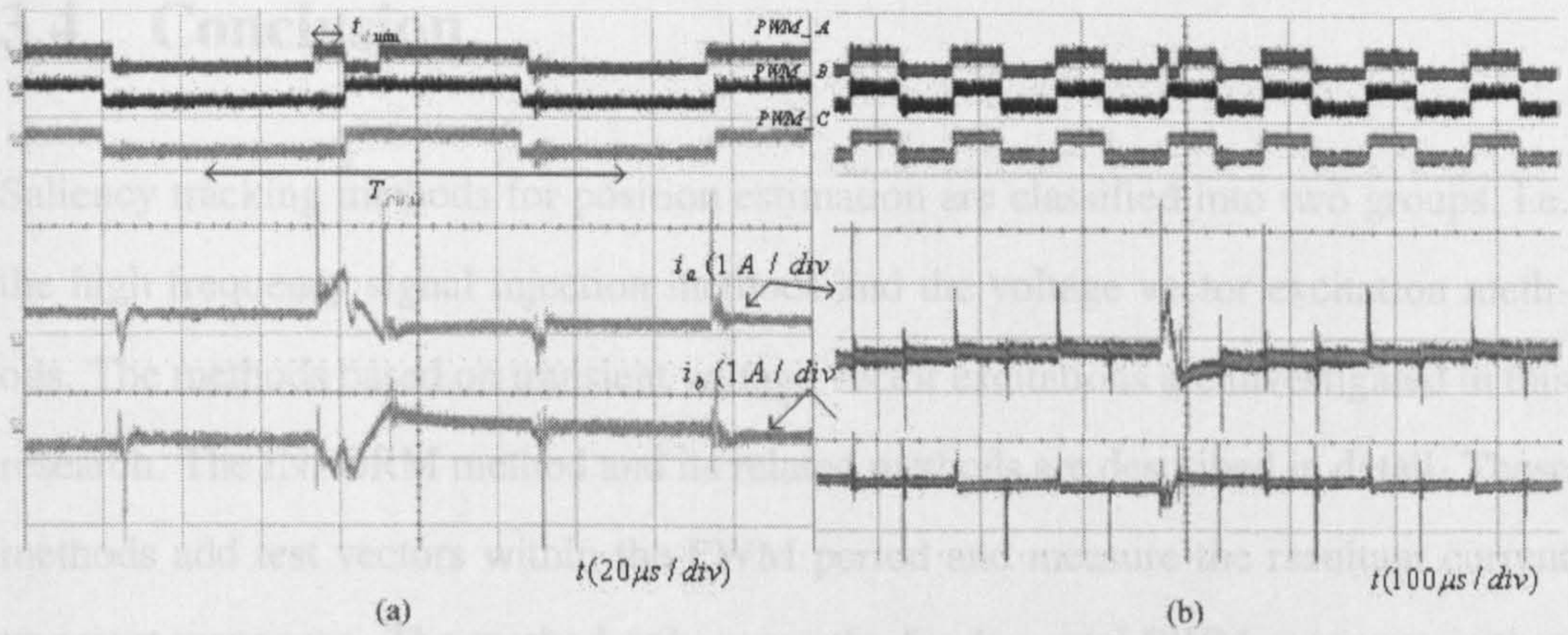

Figure 3.29: Experimental current ripple of the fundamental PWM with the improved extension and compensation scheme (a): current ripple in one PWM cycle (b) current distortions

In order to compare quantitatively the current ripple with different PWM modifictions in these position estimation schemes, the machine is controlled to output 20% torque consistently with these different schemes being applied. The total harmonic distortion (THD) of one phase current is calculated, as the results listed in Table 3.3. In this test the minimum vector time duration or the test vector width is set to be $5\mu s$. The position estimation method using fundamental PWM sequence with the improved compensation scheme, exhibits the least current distortion.

Position Estimation Schemes	Fundamental PWM	INFORM	Optimized INFORM	Scheme using Fundamental PWM Sequence	Scheme using Fundamental PWM with Improved Compensation
THD(%)	4.98	11.56	9.62	10.06	8.19

Table 3.3: THD of stator currents with different position estimation schemes

3.4 Conclusion

Saliency tracking methods for position estimation are classified into two groups, i.e. the high frequency signal injection methods and the voltage vector excitation methods. The methods based on transient voltage vector excitations are investigated in this research. The INFORM method and its related methods are described in detail. These methods add test vectors within the PWM period and measure the resultant current transient responses. The method only using the fundamental PWM sequence is then introduced. The principle of this method is modified to address the difficulties and solutions of integrating the position estimation within the fundamental PWM sequence. Position estimation results are provided to verify its effectiveness.

The current distortion caused by the test vectors or the vector extensions is one disadvantage for these methods. The added test vectors of the INFORM and its related methods cause significant current distortion. For the method only using the fundamental PWM sequence, the extension of the active vector leads to obvious current deviation. If just the switching instants of each phase are shifted to make these extensions, the current deviation will last the whole inactive period of the vector V_7, and thus the current distortion is high. One possible improvement is proposed to bring forward the compensation and thus the current deviations are suppressed. These position estimation approaches, i.e. the INFORM method, method using only the fundamental PWM sequence and the improved compensation scheme, are all applied to a surface mounted PMSM. The experimental stator currents are measured under the same operating conditions. Different current distortions are observed, with the improved compensation scheme providing the lowest distortion.

Chapter 4

Acquisition of di/dt Signals

As described in Chapter 3, the stator di/dt signals are measured during the voltage vectors applied to the AC motor in order to estimate the flux/rotor position. However, there are a lot of high frequency oscillations introduced by the IGBT switching actions, which can make the sampling difficult and inaccurate. A waiting time is required to allow these high frequency current oscillations to damp down, i.e. the voltage vectors need to be wide enough for the position estimation to work. The high frequency switching oscillations will be analyzed in this chapter. The measures required to reduce this switching noise will be investigated.

4.1 Conducted Electromagnetic Interference (EMI) in the PWM AC Drive System

The high dv/dt caused by the power device switching in a voltage source PWM inverter is the main source of the conducted electromagnetic interference in the AC drive system. Due to the parasitic capacitances and stray inductances distributed in the system, the high dv/dt causes high frequency switching noise at the inverter output, the power supply and the ground cables. The electromagnetic interference in an AC drive

system is complicated, because it includes the connections to the motor and the supply, the power electronic circuits, and the machine's complex properties in the high frequency range, etc.

4.1.1 High Frequency Models of the Main Power Components

The high-frequency behaviour of a star-connected AC motor can be represented by a 3-phase network as shown in Fig 4.1 [78]. It comprises the distributed leakage inductances of the windings L_d, the stray capacitances between the windings and the machine's frame C_s, and the damping resistances R_d and R_s. At very high frequencies (MHz and above) there will be very little current penetrating into the windings and then the machine can be represented by a constant terminal capacitor C_{hf_motor}. The stray capacitance and inductance between two phases can be ignored due to the stator winding structure[79].

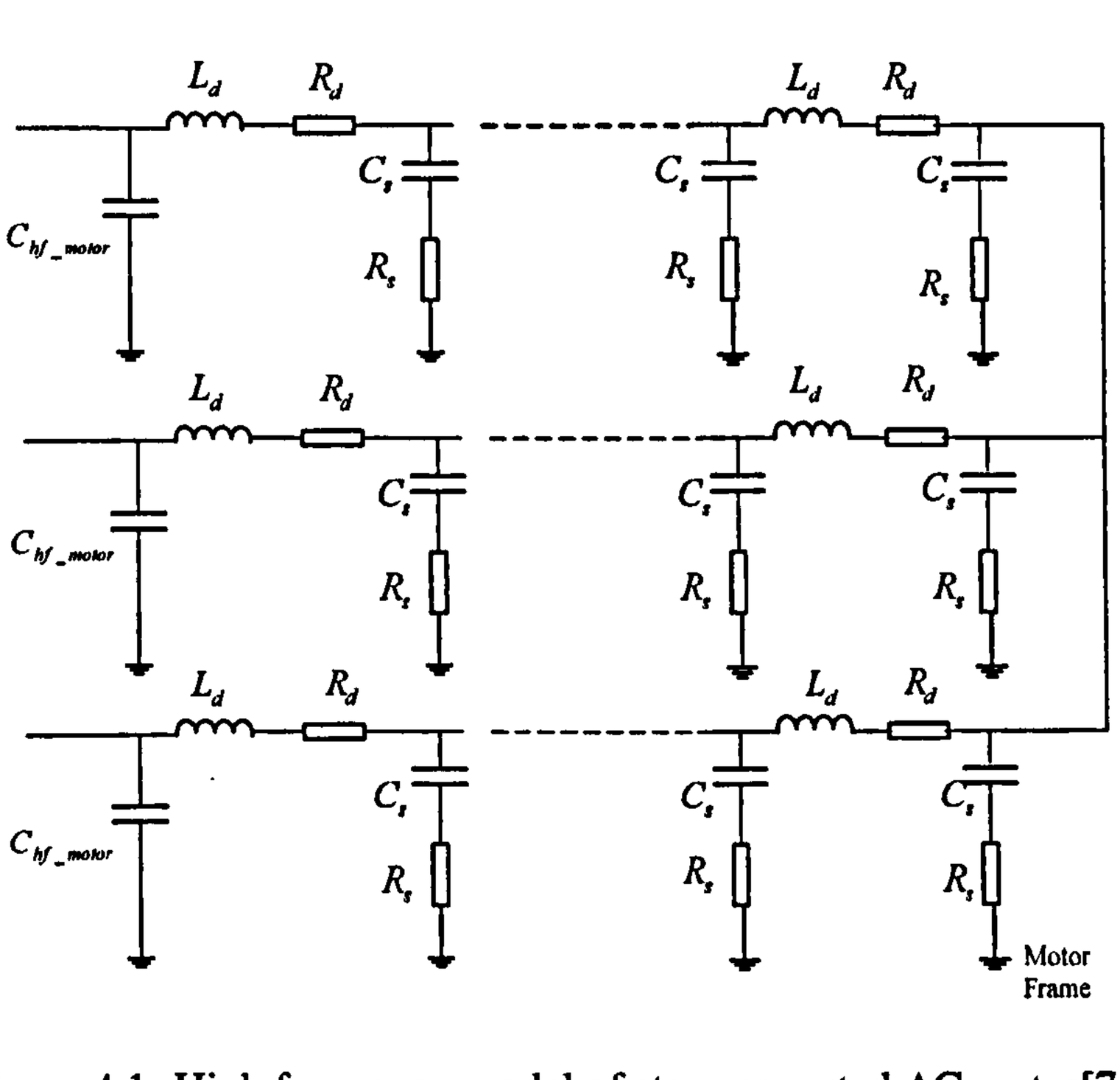

Figure 4.1: High frequency model of star-connected AC motor[78]

The cables used in this research, connecting the power converter with the power supply

and with the machine, are four-core unshielded copper-conductor cable. They can be represented by the lumped parameter π structure as shown in Fig 4.2[78][80]. The parameters of these conducting cores are symmetrical. The earth conductor in the supply cable is directly connected to the heatsink underneath the rectifier module. The earth conductor in the machine cable is connected to the heatsink underneath the IGBT modules. Both heatsinks are linked with the system's ground. For the common mode noise, the three phase conductors are modelled in parallel with the earth conductor and connected to the ground through the parasitic capacitors. For the differential mode noise, three phase conductors are coupled through their interactive stray capacitors.

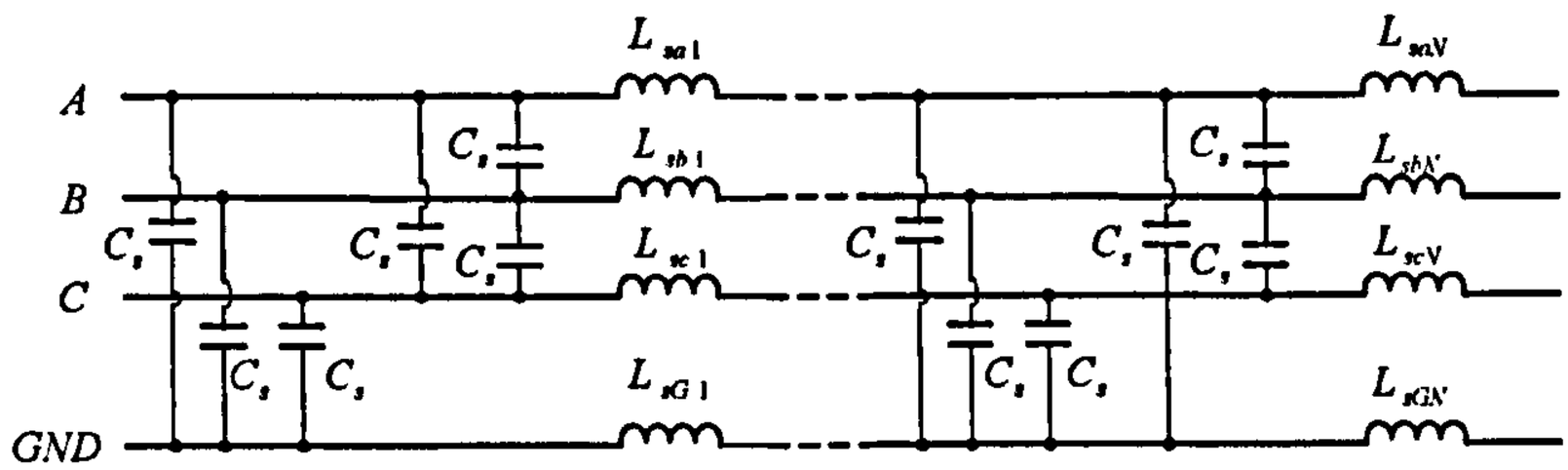

Figure 4.2: High frequency model for the four core cable

Each IGBT module, used as one inverter leg in this research, consists of two IGBTs, two free-wheeling diodes, and three power terminals connecting with the positive DC link, the negative DC link and the output lead respectively, as shown in Fig 4.3(a). The high frequency characteristics of one IGBT module are illustrated in Fig 4.3(b) [81] [78]. The IGBT and diode are modelled by its internal stray inductances and parasitic time-varying capacitances during the switching transition. The stray capacitances between the module terminals and the heatsink also present.

4.1.2 Common Mode Noise

The common mode noise is caused by the currents flowing between the inverter phase circuits and the system ground[82]. Figure4.4 illustrates the common mode equiv-

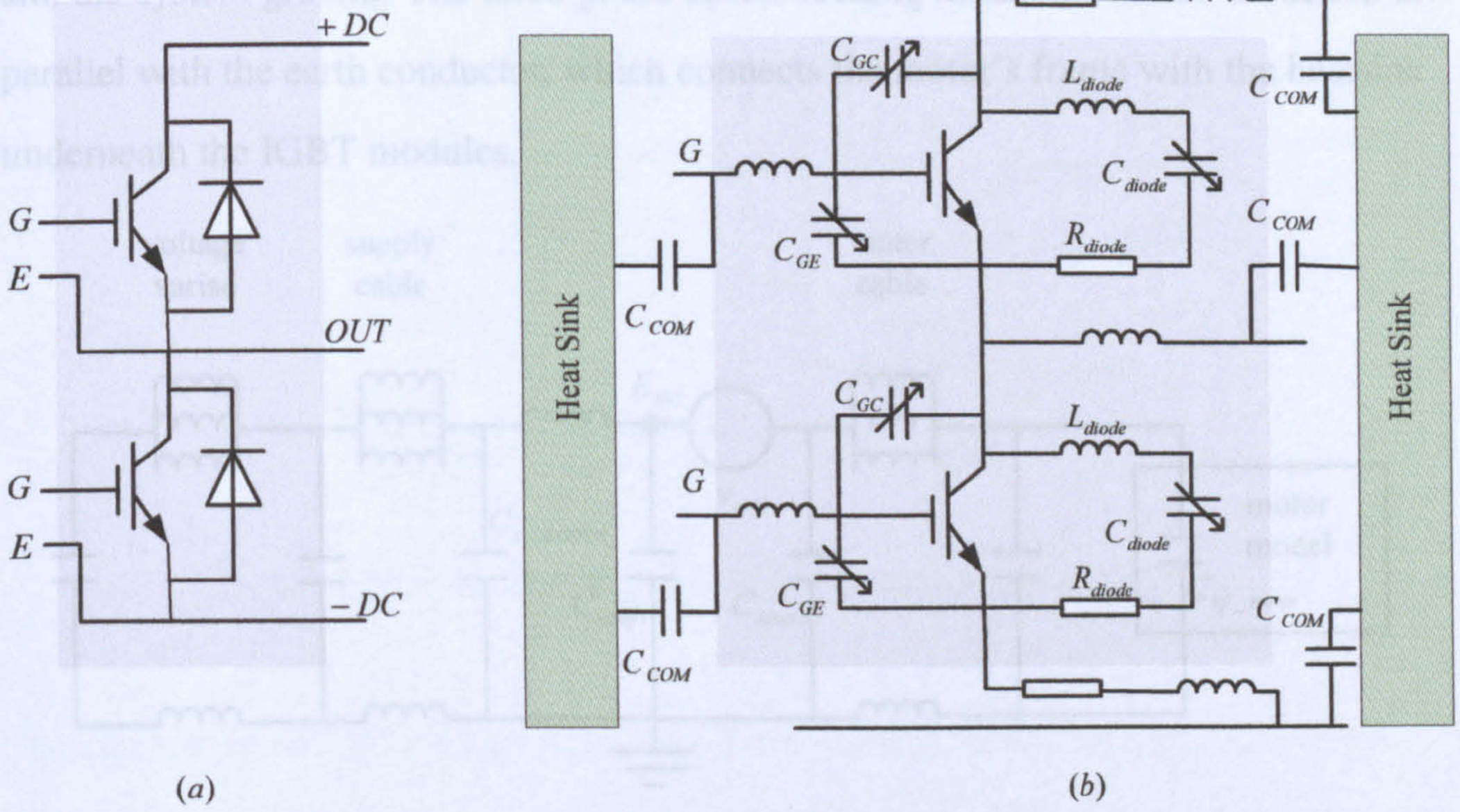

Figure 4.3: High frequency model of one IGBT module

alent circuit of the AC drive system. For the common mode currents, the positive and the negative DC buses, which are connected through the large electrolytic capacitors, can be considered as a single potential point E_{DC} in the high frequency circuit. The voltage between this DC link equal potential point and the star point of the motor is identified as the common mode noise source v_{com} [78]. v_{com} is decided by the DC-link voltage and the PWM switching state. Switching events of the PWM inverter excite the common mode circuit. On the input side of the system, three phase supply conductors are connected in parallel with the ground. Because the rectifier module always provides two diodes conducting the input current, its high frequency behaviour is represented by its equivalent series inductance (ESL) and its stray capacitance $C_{s-rectifier}$ connected to the ground via the heatsink. The ground conductor in the power supply cable is connected to the heatsink underneath the rectifier module, providing a return path for the common mode current. On the side of the inverter, the stray capacitors,C_{stray1} and C_{stray2}, between the IGBT modules and the heatsink underneath, conduct the common mode currents between the DC link equipotential point

and the system ground. The three-phase cables feeding the motor is also modelled in parallel with the earth conductor, which connects the motor's frame with the heatsink underneath the IGBT modules.

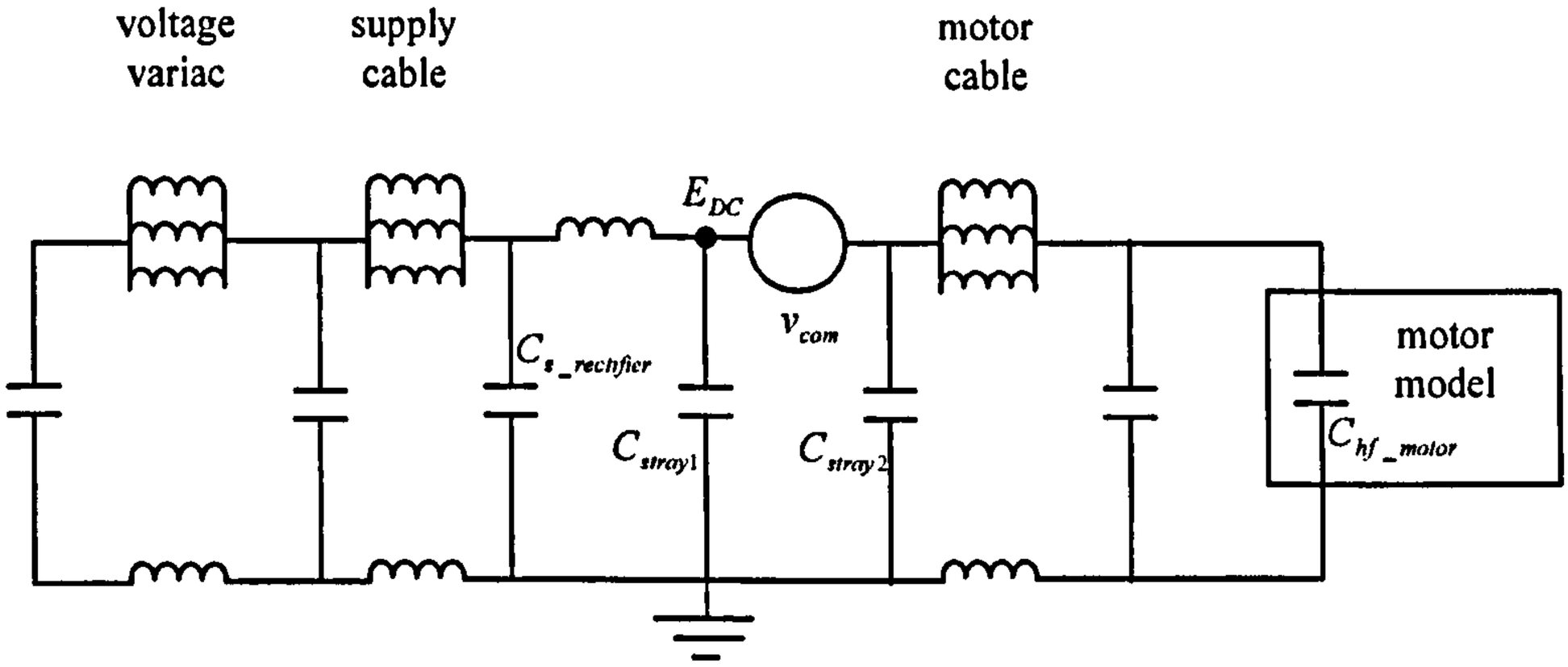

Figure 4.4: Equivalent circuit for the common mode current in the AC drive system

When the common mode noise is investigated by measuring the earth currents, components from two different frequency ranges are found, which is in accordance with the analysis in [78]. The first current component is the slower fluctuation with a frequency around $100 \sim 200kHz$. At this frequency the currents can penetrate into the stator windings and flow through the supply viariac inductors. Thus this component exists in the earth conductor of both the supply cable and the machine cable. The other component is the small oscillation with a higher frequency above $2MHz$. This oscillation only shows up at the grounding point on the inverter's output side. It is because the currents at this frequency are blocked by the impedance of the viariac's inductances and the machine's stator windings. In this frequency range, the machine is just simply represented by its terminal capacitance $C_{hf-motor}$. Figure4.5 shows the propagation paths of these two common mode currents.

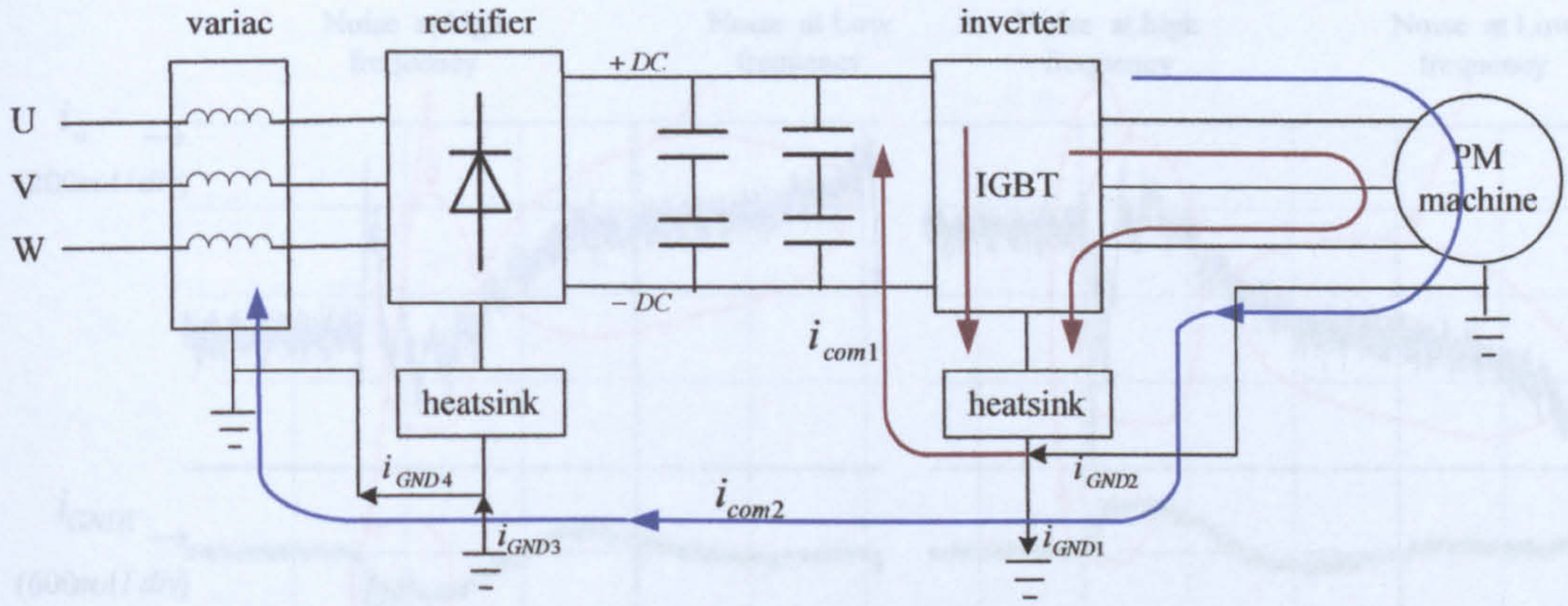

Figure 4.5: propagation paths of the common mode currents

The currents in the grounding conductors are measured in this research. Their waveforms are used to identify the common mode noise in the measured output currents. In Fig4.6, the measured waveforms of one phase output current, the ground current on the inverter's output side i_{GND1}, and the ground current on the supply side i_{GND3}, during two independant switching instants, are shown. The switching oscillations from the two different frequency ranges as mentioned above can be observed. The low frequency noise in the output current has the same profile as that in the ground currents, which verifies this low frequency switching oscillation comes from the common mode noise. Besides, a much higher frequency component appears in i_{GND1} at about $3 \sim 4MHz$, but it has a very small amplitude and dies off quickly. This component cannot be found in i_{GND3} as being analyzed. The other high frequency component at about $2 \sim 3MHz$, with high spike amplitude and only appearing in the output current, is thought to be from the differential mode currents.

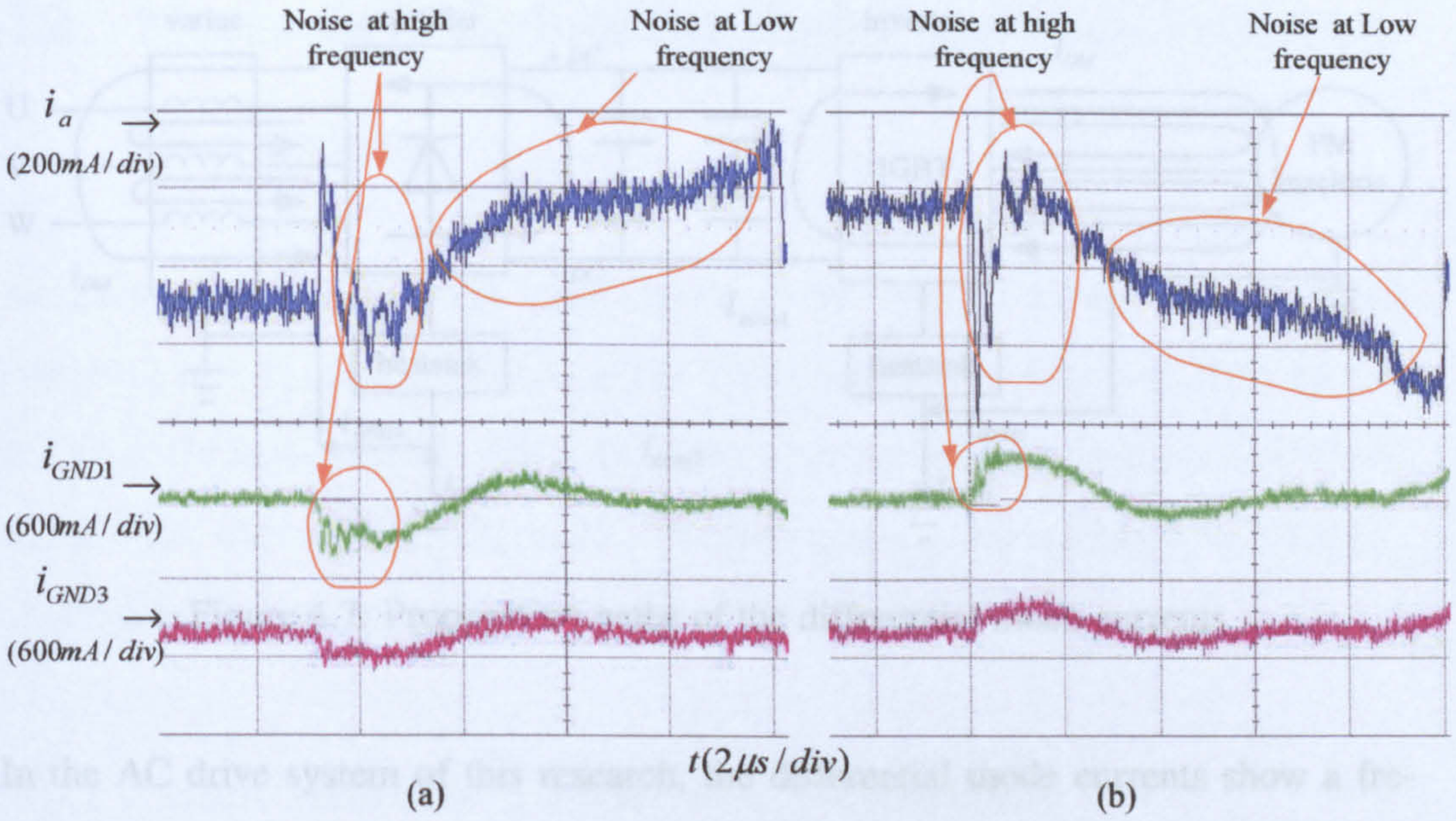

Figure 4.6: Current wavefroms at two switching instants (a) and (b):
blue: the output current i_a; green: the ground current at the inverter's output side i_{GND1}; purple: the ground current at the power supply side i_{GND3}

4.1.3 Differential Mode Noise

On the output side of the inverter, when one phase is switched on or off, a resonant circuit is excited between the switched phase and the other two unswitched phases. This results in the differential mode oscillations on the output terminal voltages and currents. The differential mode current paths between phases are indicated in Fig 4.7. On the input side, the differential mode electromagnetic emissions are excited by the high frequency voltage drop across the DC link, which is caused by the differential mode currents flowing through the DC link capacitors to the output phases[82].

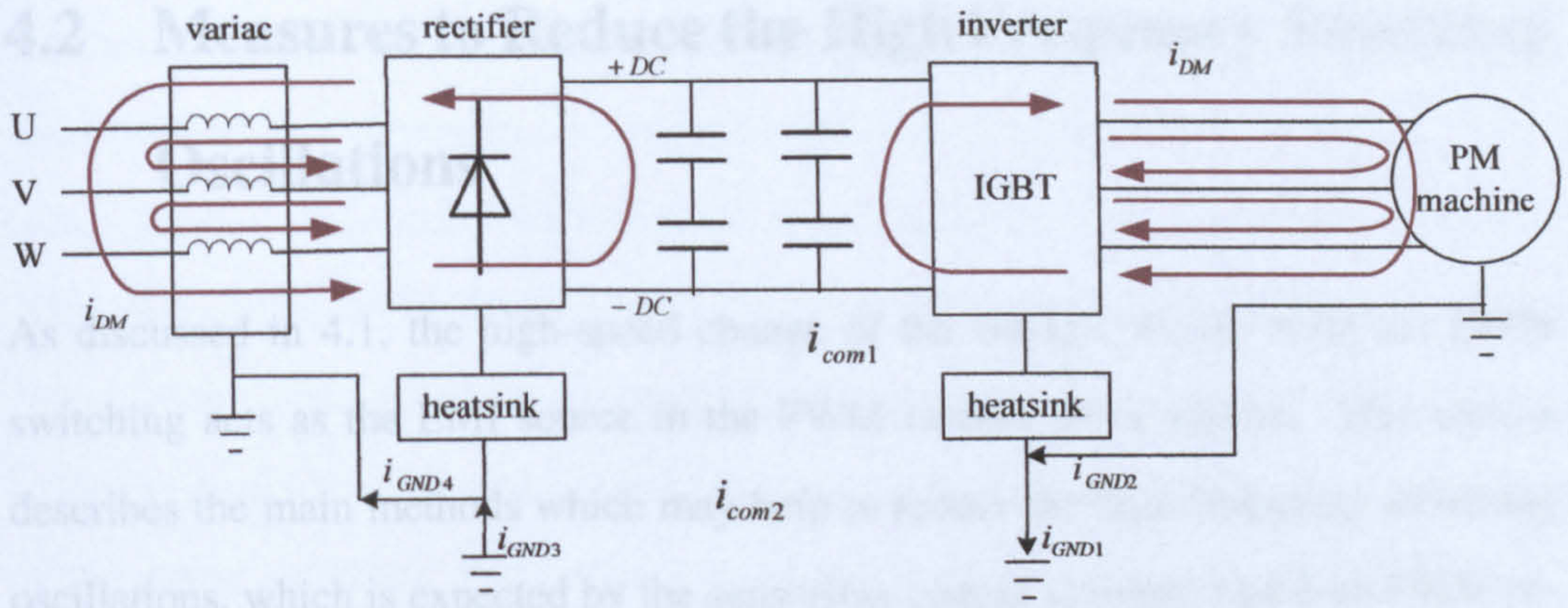

Figure 4.7: Propagation paths of the differential mode currents

In the AC drive system of this research, the differential mode currents show a frequency around $2 \sim 3MHz$. The motor is only modelled by its terminal capacitance at this frequency range. On the inverter output side, the differential mode equivalent circuit between two phases is shown in Fig 4.8. The switching events are the noise source for this circuit and the coupling stray parameters provide the propagation paths. The behaviour of the differential mode noise mainly depends on the stray capacitances C_{spp} between the phases and equivalent series inductance L_{cable} of each phase. In Fig 4.6, the differential mode noise appearing in the output current can be seen clearly.

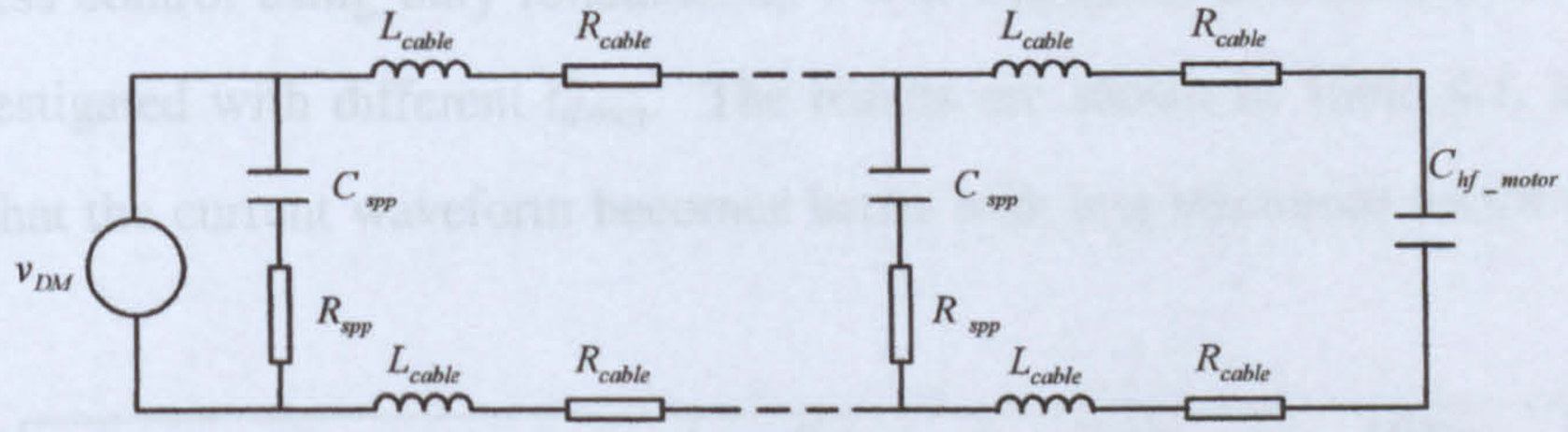

Figure 4.8: Equivalent circuit for the differential mode noise between two phases

4.2 Measures to Reduce the High Frequency Switching Oscillations

As discussed in 4.1, the high-speed change of the voltage, dv/dt, from the PWM switching acts as the EMI source in the PWM inverter drive system. This section describes the main methods which may help to reduce the high frequency switching oscillations, which is expected by the sensorless control schemes based on PWM excitations explained in Chapter 3.

4.2.1 Main Measures Used for EMI Suppression

The minimum vector duration t_{dmin} is decided by the EMI properties of the system, which cause the high frequency oscillations occurring at each switching instant. If the high frequency oscillations can be suppressed, the minimum vector duration t_{dmin} can thus be reduced. With reduced t_{dmin}, the position estimation schemes based on PWM vector excitation will make less modification of the fundamental PWM waveforms and thus bring about less current distortions. The stator current waveforms of the sensorless control using only fundamental PWM sequence, as described in 3.2.3.2, are investigated with different t_{dmin}. The results are shown in Table 4.1, and they verify that the current waveform becomes better with less minimum vector duration t_{dmin}.

t_{dmin}	$0\mu s$	$5\mu s$	$10\mu s$
THD (of stator current)	4.98%	8.19%	11.68%

Table 4.1: THD of current waveforms with different minimum duration for sensorless control

The first group of methods reducing EMI noise aim to change the noise propagation paths. Compactly and carefully designed layout of the power circuits is one effective way. The stay capacitance and inductance can be reduced if the designer avoids

redundant paths, evenly arranges the three phases, and shortens the connections between the main components. In commercial inverters, laminated busbars are widely used. Busbars have many advantages over wiring harness in the terms of the reliability and compactness. But they still introduce considerable stray inductance in the loop circuit consisting of the switching power devices[83]. In this research, an integrated Printed Circuit Board (PCB) is developed to integrate all the main components of the power converter. The compact layout and use of PCB tracks help to reduce the conducted EMI.

Insertion of a filter network between the inverter and the motor is another method to change the EMI noise propagation path. Different filter networks and methods to decide the filter parameters are proposed in[84][80][85][86].It is noticed that the overvoltage and high frequency ringing are caused by the distributed nature of the long cable leakage inductance and stray capacitance. The output filters are used to shunt the high frequency currents, preventing them from entering the motor. The topology of a commonly used RLC filter is shown in Fig 4.9. Harmonic currents above the designed cut-off frequency are largely passed through the RC branch of the output filter.

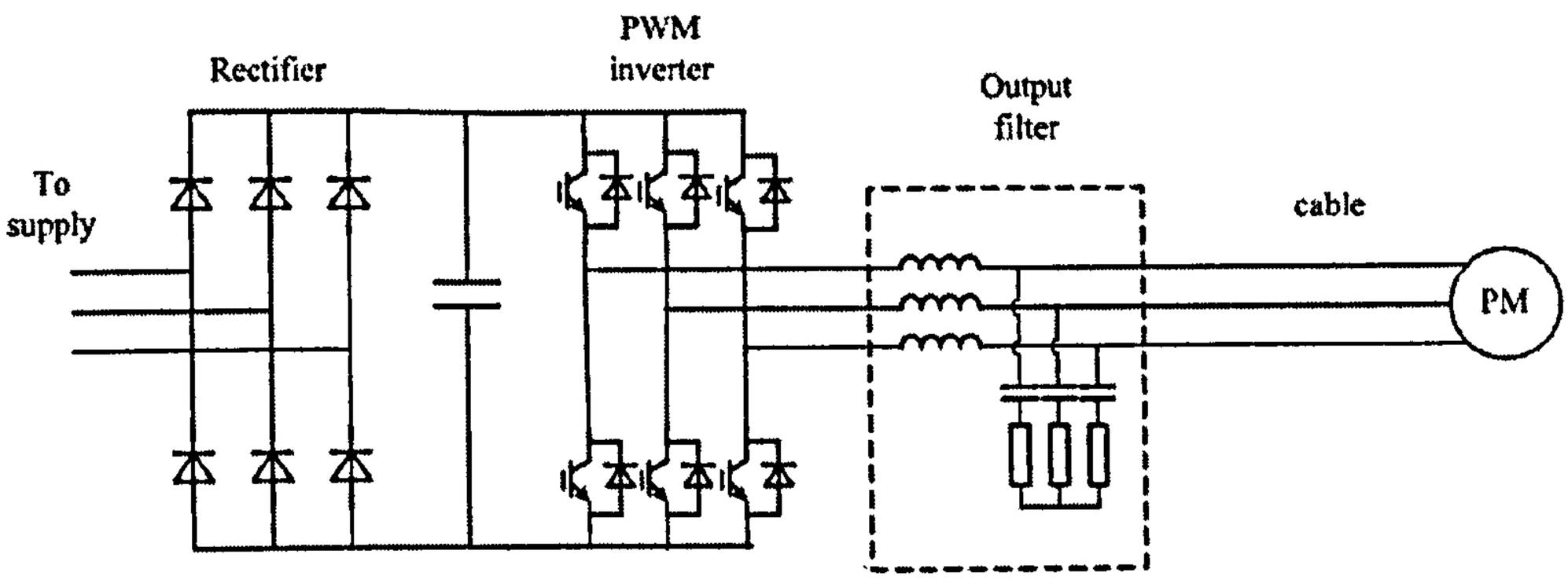

Figure 4.9: PWM inverter driving system with RLC output filter

However, this method is not suitable for this research. Firstly, if the high frequency part of output voltage applied to the motor has been filtered out, its excitation on the machine cannot generate large enough di/dt signals for the position estimation.

Secondly, the output filter normally works well for reducing the strong ringing with the long feeding cable, but does not show as much effect for suppressing the relatively low oscillations appearing in the output currents as in this research. The filter network adds to the cost and makes the system bulky.

Instead of focusing on the EMI noise propagation paths, the other kind of method tries to reduce the noise emissions at its source. The PWM output voltages of the power switch devices normally exhibit steep rising and falling edges, which bring about a large amount of strong excitations in the high frequency spectrum. The idea of this group of methods is to lessen the noise by reducing the slope of the rising edge and falling edge of the voltage outputs. One method is to add a snubber circuit[87]. Snubber circuits can reduce dv/dt by transferring the high frequency switching energy from the IGBT output to an energy storage element. The other way to slow down the switching is to increase the gate resistance of the IGBTs. A larger gate resistor can limit the charging and discharging speed of the gate capacitor, thus reducing the rate of building up the gate voltage v_{GE}[87]. However, both methods add complexity and increase power losses. Both of them are investigated in this research and these drawbacks are accepted as the cost of reduced conducted emissions and improved sensorless control results.

4.2.2 Suppression of the Conducted EMI by Increasing the IGBT Gate Resistance

Selecting the proper gate resistor for the IGBT gate drive is important. The value of the gate resistor has a significant impact on the dynamic performance of the IGBT. The IGBT is turned on and off by charging and discharging the gate capacitance. A smaller gate resistor will charge and discharge the gate capacitance faster, reducing the switching time and switching losses. However, smaller gate resistors may cause high dv/dt and increase surge voltage during the free-wheeling diode recovery process.

The high dv/dt may lead to oscillation problems in conjunction with any parasitic inductance in the output circuit. In this research, a gate drive circuit providing a changeable gate resistor is developed and applied. During normal operation periods, the nominated gate resistance is connected in the circuit. When the di/dt signals are to be measured for position estimation, the gate resistance is increased to reduce the high frequency oscillations appearing in the output current waveforms.

The turn-on waveforms of the gate driving voltage v_{GE}, the output voltage v_{CE} and the output current i_o of the lower IGBT in one IGBT bridge module, during one switching instant, are shown in Fig 4.10. When the lower IGBT is switched on, its collector-emitter voltage v_{CE} falls from U_{+DC} to U_{-DC}, and so the output current is driven to the negative DC link. A level period during the rising of v_{GE} is due to the Miller effect[88]. That is the decreasing v_{CE} causes current to flow through the Miller capacitance C_{GC}, and this current is drawn from the gate circuit and diminishes the current available to charge the gate-emitter capacitance.

The IGBT used for this work is SKM 50GB 123D, described in [89]. The effect of the value of gate resistance is shown in 4.10. The recommended gate resistance $R_g = 28\Omega$ and the twice resistance $R_g = 56\Omega$ are used and compared. It can be seen that, with larger gate resistance, the high frequency oscillations, both on the output current i_o and on the voltage v_{CE}, are much reduced. When $R_g = 28\Omega$, v_{CE} falls from $620V$ to $0V$ within less than $0.5\mu s$. There exists a period of current oscillation lasting about $5\mu s$. When $R_g = 56\Omega$, v_{CE} reaches and settles at its steady state in about $1\mu s$. The current settling time is reduced from about $5\mu s$ to less than $3\mu s$. That means, the di/dt sampling can be made with less waiting time as explained in Chapter 3.

Similarly, the waveforms during the turn-off switching are shown in Fig 4.11. The negative gate signal is applied, and v_{GE} decreases in a linear fashion. Once v_{GE} drops below the threshold voltage, v_{CE} starts increasing linearly. When v_{CE} reaches the DC link voltage, the clamp diode starts conducting and the IGBT current falls linearly. In

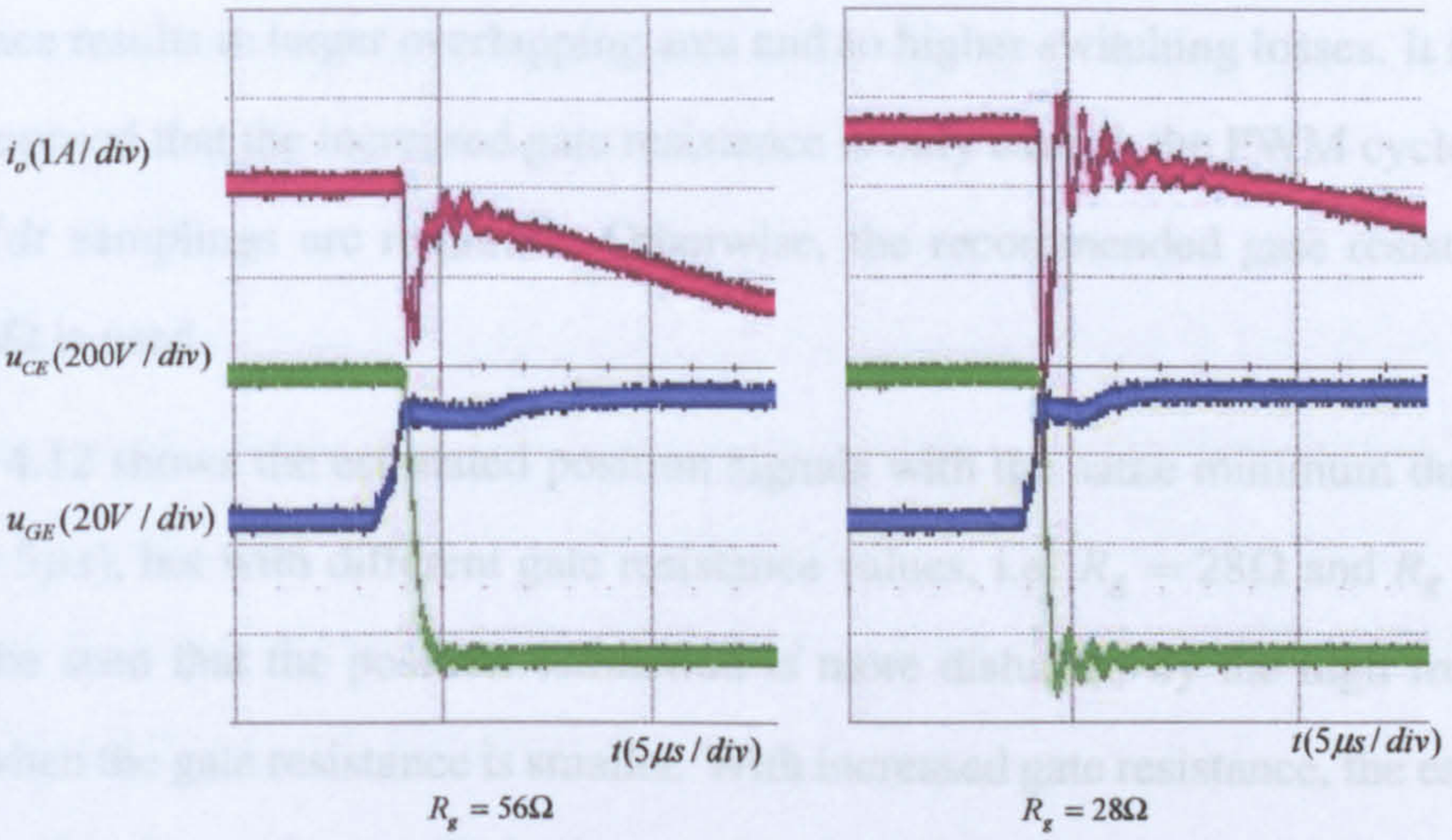

Figure 4.10: IGBT turn-on waveforms with different R_g

the turn-off switching, different gate resistances do not show as big a difference on the output currents, as that shown for the turn-on switching in Fig 4.10. Also the dv/dt is almost the same with different R_g, which is $dv_{CE}/dt \approx 620V/2\mu s = 310MV/s$.

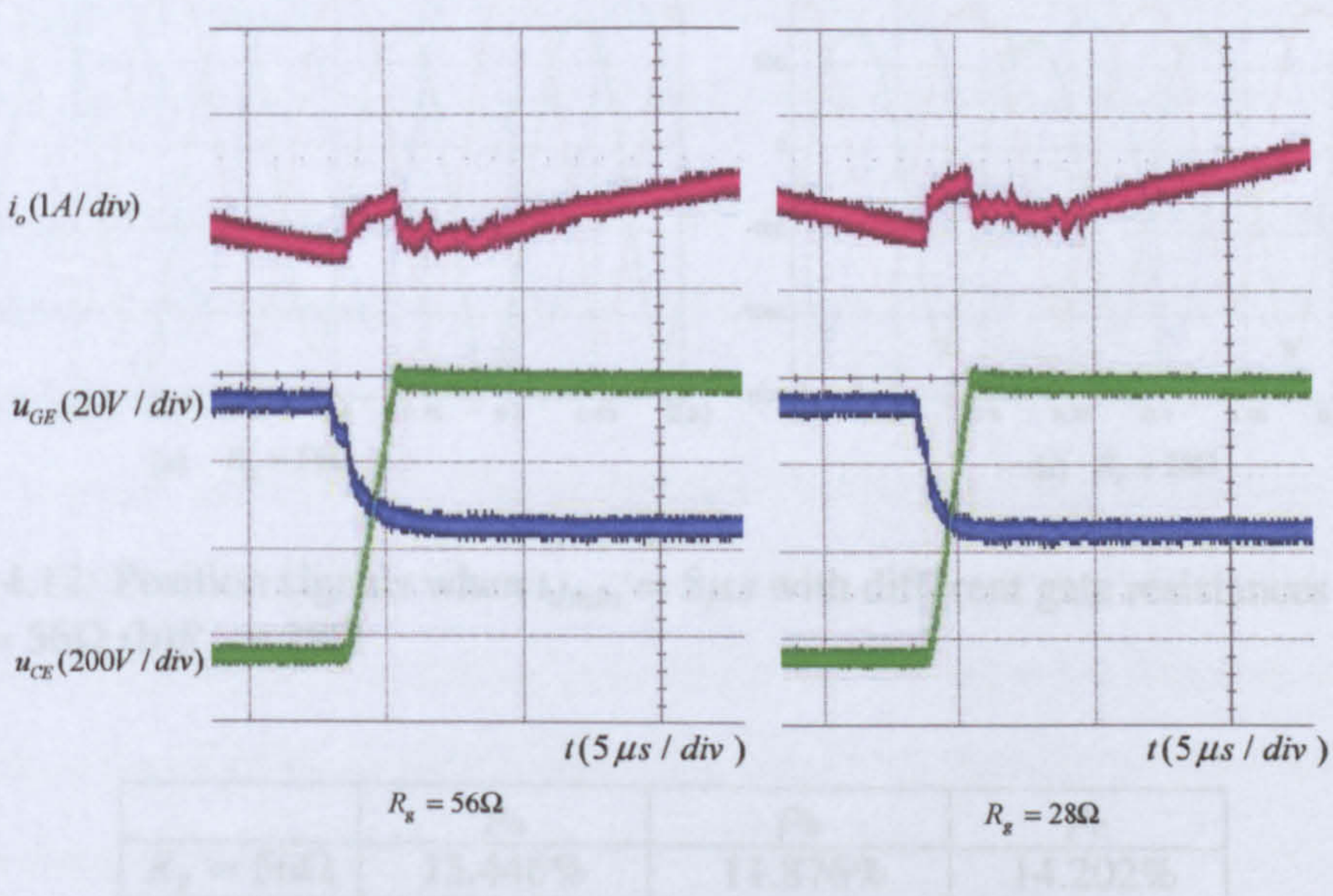

Figure 4.11: IGBT turn-off waveforms with different R_g

The switching losses are directly related to the overlap of the IGBT current and voltage waveforms during turn-on and turn-off. They are influenced by the magnitude and time duration of the current and voltage during the switching. The larger gate

resistance results in larger overlapping area and so higher switching losses. It is therefore proposed that the increased gate resistance is only used in the PWM cycles when the di/dt samplings are required. Otherwise, the recommended gate resistance of $R = 28\Omega$ is used.

Figure 4.12 shows the estimated position signals with the same minimum duration ($t_{dmin} = 5\mu s$), but with different gate resistance values, i.e. $R_g = 28\Omega$ and $R_g = 56\Omega$. It can be seen that the position estimation is more disturbed by the high frequency noise when the gate resistance is smaller. With increased gate resistance, the estimated position signals are cleaner. To further verify this, the total harmonic distortion (THD) of the position signals are calculated for these two cases, and the results are listed in Table 4.2.

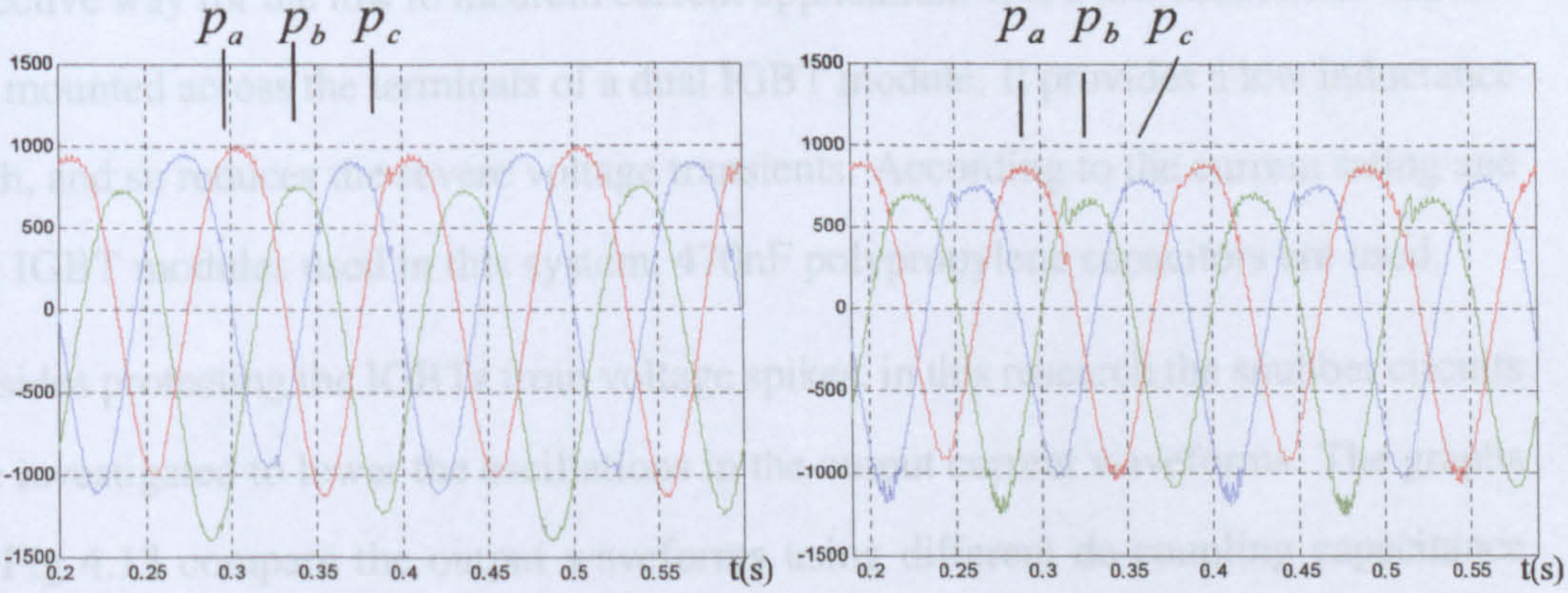

(a) $R_g = 56\Omega$ (b) $R_g = 28\Omega$

Figure 4.12: Position signals when $t_{dmin} = 5\mu s$ with different gate resistances (a)$R_g = 56\Omega$ (b)$R_g = 28\Omega$

	p_a	p_b	p_c
$R_g = 56\Omega$	13.446%	11.876%	14.202%
$R_g = 28\Omega$	17.476%	15.376%	15.819%

Table 4.2: THD of the estimated position signals with different gate resistance values

4.2.3 Suppression of Conducted EMI by Increasing the Snubber Capacitor

When a power device is abruptly turned off, the trapped energy in the circuit's stray inductance is dissipated in the switching device, causing a voltage overshoot across the device. The magnitude of the transient voltage spike is decided by the trapped energy in the circuit stray inductance[90]. Snubber circuits are always needed to protect the device from the high voltage transients.

There are different types of snubber circuits for IGBT applications[91], such as de-coupling capacitors, RCD snubber clamp circuits, RCD charging and discharging circuit, etc. The de-coupling capacitor is adopted in this research, as it is a simple and effective way for the low to medium current application. It is a low inductance capacitor mounted across the terminals of a dual IGBT module. It provides a low inductance path, and so reduces the severe voltage transients. According to the current rating and the IGBT modules used in this system, 470nF polypropylene capacitors are used.

Besides protecting the IGBTs from voltage spikes, in this research the snubber circuits are investigated to lower the oscillations in the output current waveforms. The graphs in Fig 4.13 compare the output waveforms using different de-coupling capacitance values, $0.94\mu F$ and $0.47\mu F$. The collector-emitter voltage v_{CE} of the lower IGBT and the output current of one phase i_o are measured at one turn-off switching instant. From the experimental waveforms, it is found that the larger de-coupling capacitor can reduce the oscillations appearing on the output voltage, but do not significantly change the current transients.

4.2.4 Software Cancellation of the Common Mode Noise

The common mode equivalent circuit shown in Fig 4.4 actually exists for each phase. A simplified common mode circuit on the inverter's output side is shown in Fig 4.14.

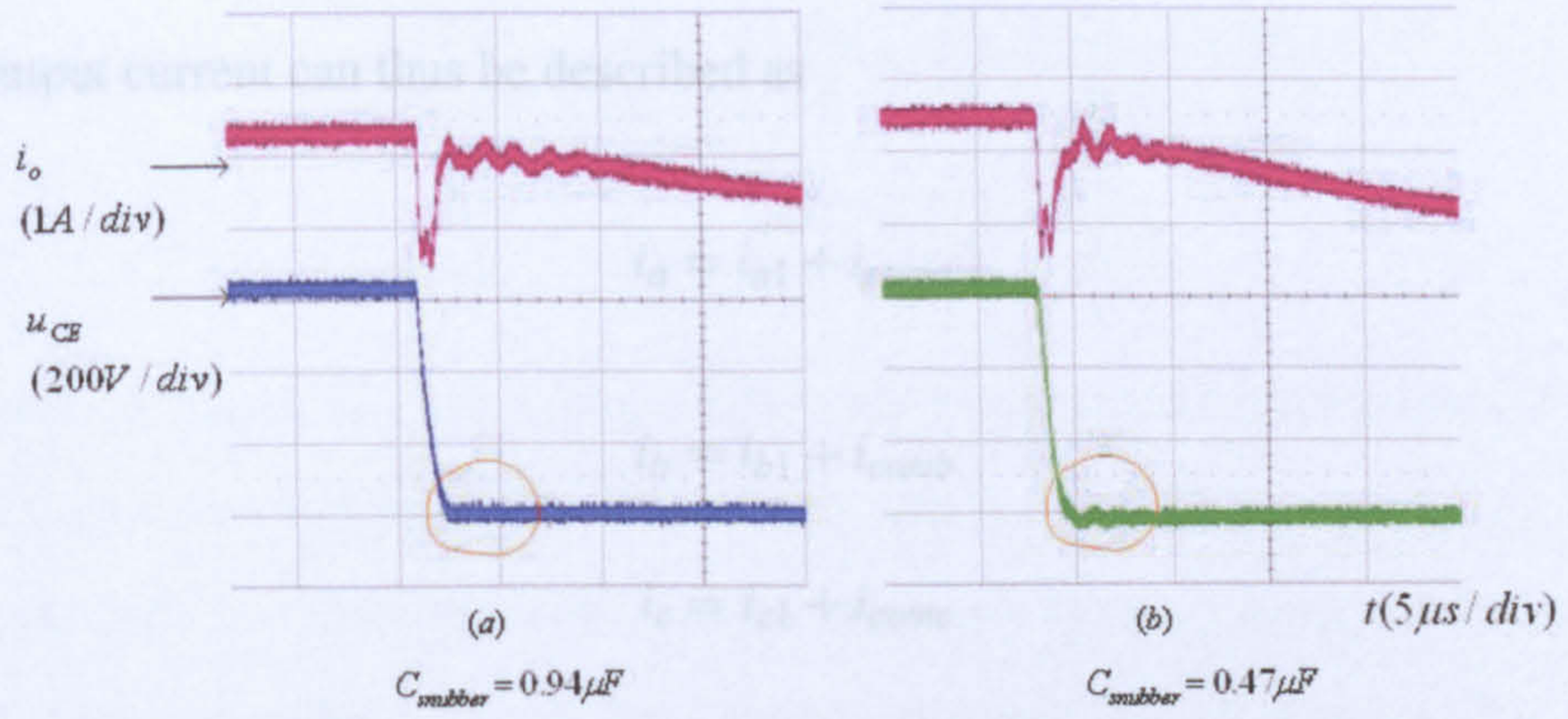

Figure 4.13: IGBT turn-on waveforms with different snubber capacitors

Normally, if the layout is balanced and the cable used is symmetrical, the parameters in the three phase circuits should be the same. The common mode currents flow equally through the three phases. The ground current is the sum of them.

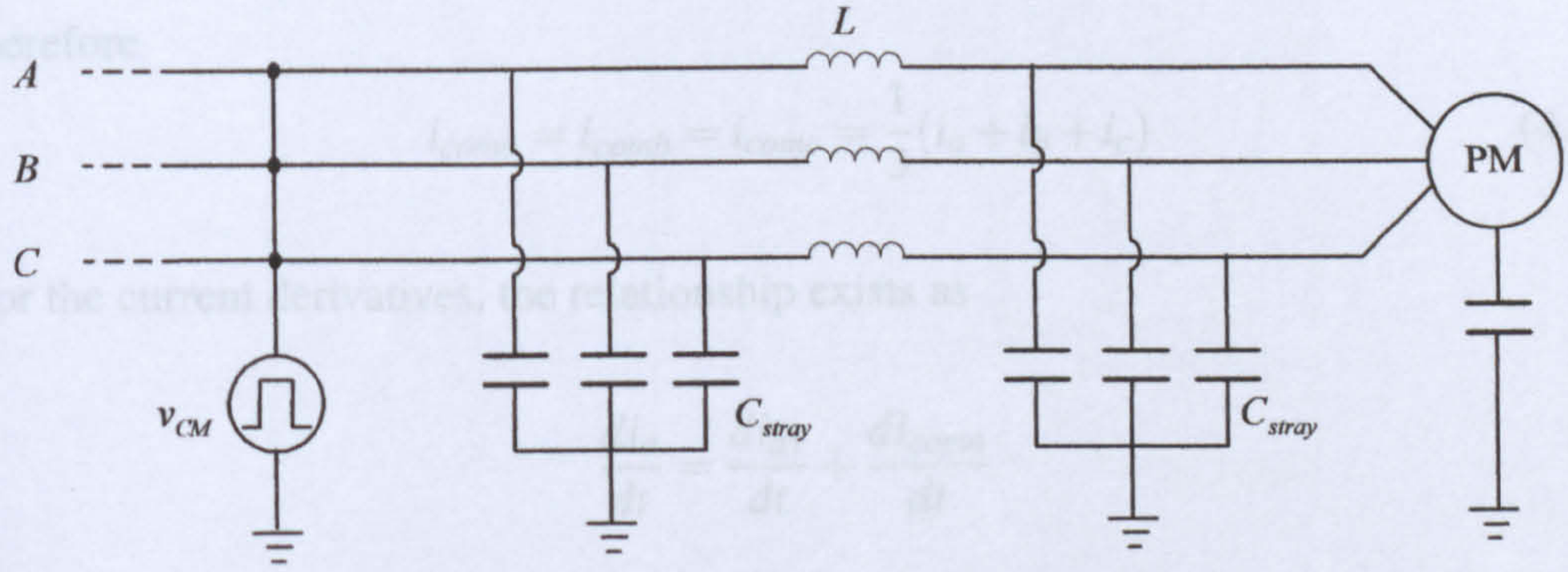

Figure 4.14: Simplified three-phase common mode circuit on the Inverter's output side

The common mode currents appear in the output currents transients. Thus the position estimation from the measured di/dt will be influenced. Its effect on the di/dt measurements can be simply cancelled by software. The inaccurate part in the sampled di/dt signals caused by the common mode noise can be eliminated by programming. Because of the symmetrical parameters of the three phases in Fig 4.14, the common mode currents through three phases are the same, that is

$$i_{coma} = i_{comb} = i_{comc} \tag{4.1}$$

The output current can thus be described as

$$i_a = i_{a1} + i_{coma}$$

$$i_b = i_{b1} + i_{comb} \tag{4.2}$$

$$i_c = i_{c1} + i_{comc}$$

where i_a,i_b,i_c are the stator currents output from the inverter, and i_{a1},i_{b1},i_{c1} are the current components without common mode noise. Because

$$i_{a1} + i_{b1} + i_{c1} = 0 \tag{4.3}$$

therefore

$$i_{coma} = i_{comb} = i_{comc} = \frac{1}{3}(i_a + i_b + i_c) \tag{4.4}$$

For the current derivatives, the relationship exists as

$$\frac{di_a}{dt} = \frac{di_{a1}}{dt} + \frac{di_{coma}}{dt}$$

$$\frac{di_b}{dt} = \frac{di_{b1}}{dt} + \frac{di_{comb}}{dt} \tag{4.5}$$

$$\frac{di_c}{dt} = \frac{di_{c1}}{dt} + \frac{di_{comc}}{dt}$$

and

$$\frac{di_{coma}}{dt} = \frac{di_{comb}}{dt} = \frac{di_{comc}}{dt} = \frac{1}{3}\left(\frac{di_a}{dt} + \frac{di_b}{dt} + \frac{di_c}{dt}\right) \tag{4.6}$$

In this system, di/dt sensors are used to measure the current derivatives at the inverter's output. From the above equations, the common mode noise can be removed by

$$\frac{di_{a1}}{dt} = \frac{di_a}{dt} - \frac{1}{3}\left(\frac{di_a}{dt} + \frac{di_b}{dt} + \frac{di_c}{dt}\right)$$

$$\frac{di_{b1}}{dt} = \frac{di_b}{dt} - \frac{1}{3}(\frac{di_a}{dt} + \frac{di_b}{dt} + \frac{di_c}{dt}) \tag{4.7}$$

$$\frac{di_{c1}}{dt} = \frac{di_c}{dt} - \frac{1}{3}(\frac{di_a}{dt} + \frac{di_b}{dt} + \frac{di_c}{dt})$$

The position vector, $\overrightarrow{p} = p_a + \alpha p_b + \alpha^2 p_c$, can be obtained from the current derivatives as discussed in Chapter 3. Figure 4.15 shows the position signals, p_a, p_b and p_c, estimated from the current derivatives. A comparison is carried out between the results with and without the common mode compensation, as shown in Fig 4.15(a) and (b) respectively. The units of these signals have no specific meanings. It can been seen that much noise in the estimated position signals has been removed by software compensation.

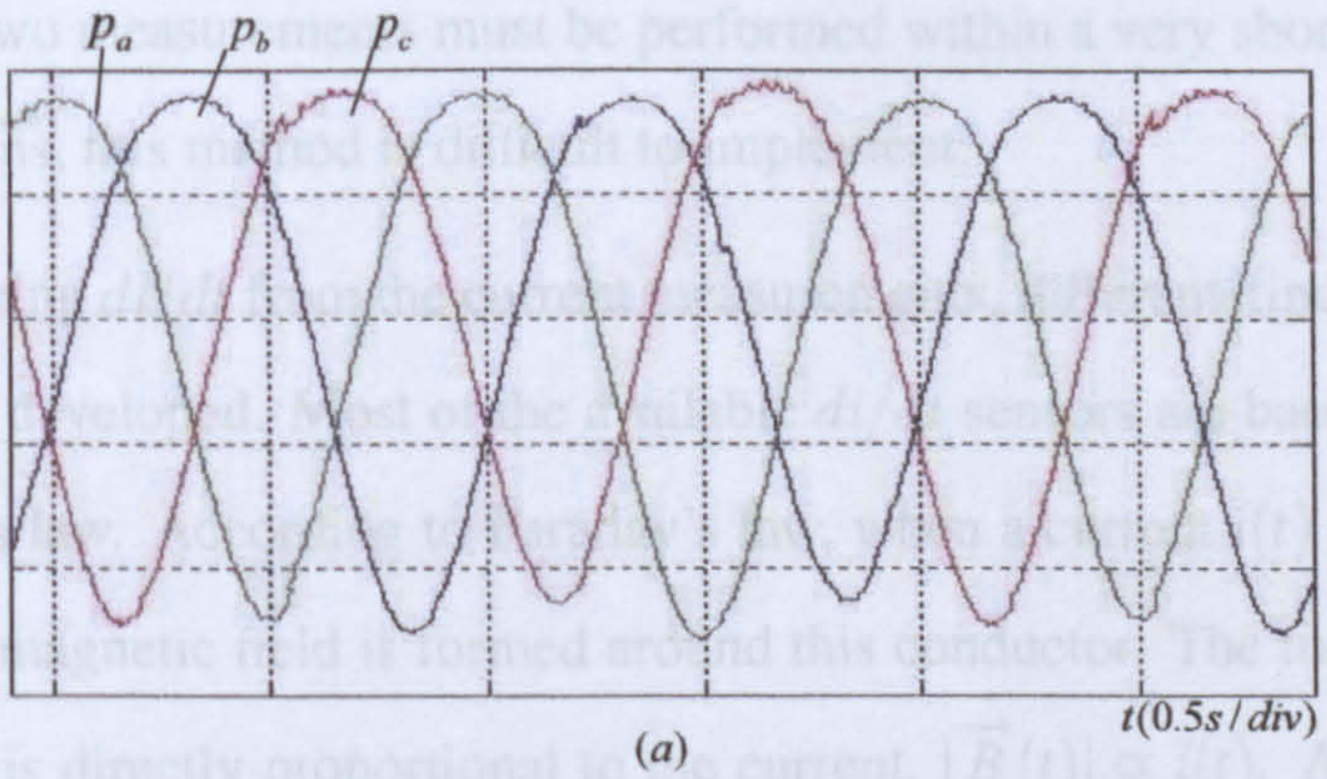

Figure 4.15: Estimated position signals (a)with and (b)without cancellation of the common mode noise

4.3 Measurement of the Current Derivative Signals

4.3.1 Current Derivative Sensors

To measure the di/dt signals after the switching instants, several methods were proposed by researchers. One method is based on the differentiation process of the current measurements during a short period. It takes the difference of two current samples with a time interval Δt, and calculates the current derivative value taking advantage of the near linearity, $di/dt = \Delta i/\Delta t$. Although this method is direct and requires no special sensors, the noise appearing in the current signals is amplified and can easily corrupt the calculation result. To use this method, the system must have enough sampling ability. Two measurements must be performed within a very short time interval. For these reasons, this method is difficult to implement.

Instead of deriving di/dt from the current measurements, different kinds of di/dt sensors have been developed. Most of the available di/dt sensors are based on the Faraday's induction law. According to Faraday's law, when a current $i(t)$ passes through a conductor, a magnetic field is formed around this conductor. The magnitude of the magnetic field is directly proportional to the current, $|\vec{B}(t)| \propto i(t)$. Also the change of the magnetic field induces an electromotive force (EMF) within a wire loop which is located perpendicular to it. This EMF appears as a voltage signal proportional to the change of the magnitude field of the wire loop, as $E(t) \propto d|\vec{B}(t)|/dt$. Combining these two relationship, the output voltage of the wire loop is therefore proportional to the time-differentiation of the current, $E(t) \propto di(t)/dt$.

One kind of di/dt sensor is the Rogowski Coil[92]. It is a closely and evenly wound coil of N turns/m on a non-magnetic former of constant cross sectional area Am^2, wrapping around the power line where the current is to be measured, as shown in Fig 4.16. The induced output voltage is calculated by the formula[93]:

$$v_{sensor} = \frac{\mu_0 NL}{2\pi} ln(\frac{c}{b}) \frac{di}{dt} \tag{4.8}$$

where *c*,*b* are the distance from the coil to the wire, *L* is the size of the coil, and μ_0 is the permeability of the air.

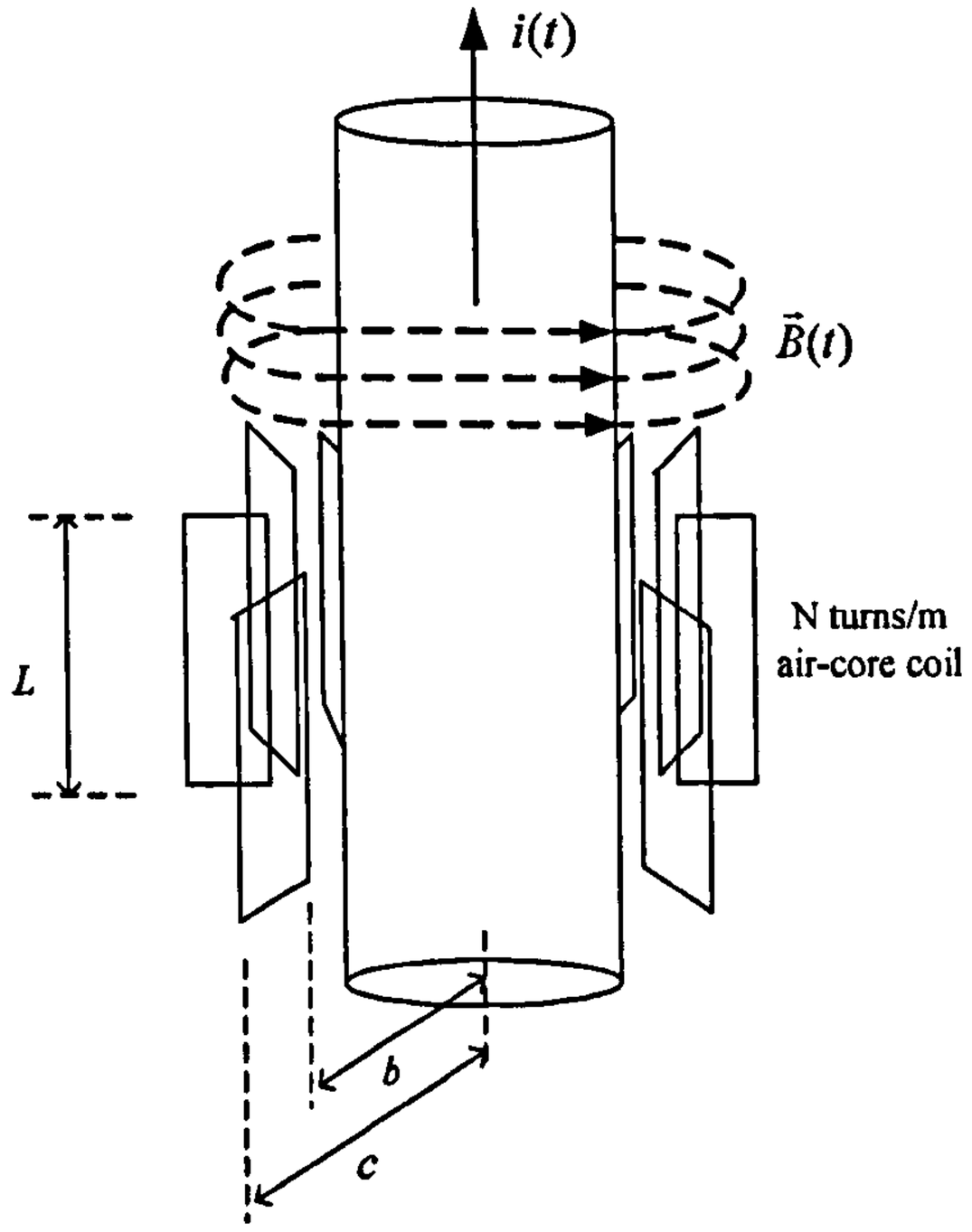

Figure 4.16: General structure of the Rogowski *di/dt* Sensor

The main advantages of the Rogowski Coil can be summarized as[94]:

- The sensor is electrically isolated from the measured conductor
- The saturation point of the air is extremely high and so no DC or high current saturation.
- Air core gives linear phase response.
- The sensor is able to measure high current.
- No significant power consumption is needed.

- The sensor has a wide bandwidth allowing for harmonic analysis.
- The output varies very little with the changes in temperature.

The other kind of di/dt sensor is a highly coupled air-core mutual inductor as shown in Fig 4.17[58]. Its primary winding is connected in series with the line cable, and the output voltage is obtained from the ends of the secondary winding, as

$$v_{sensor} = N_2 \frac{d\Phi}{dt} \propto \frac{N_2}{N_1} \frac{di}{dt} \tag{4.9}$$

where N_1, N_2 are the number of turns in the primary and secondary coils, V_{sensor} is the induced voltage, Φ is the magnetic flux through one turn of the coil, and i is the primary current to be measured.

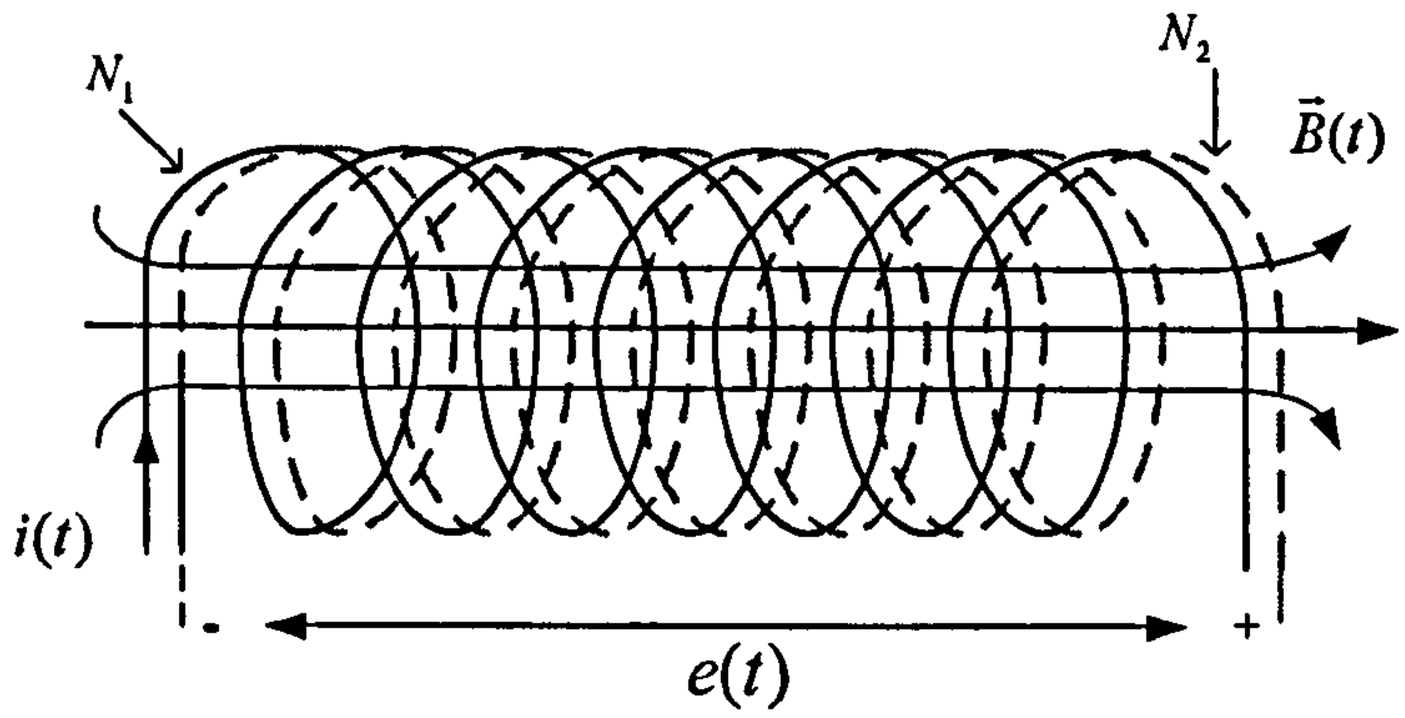

Figure 4.17: Structure of the air-core mutual inductor di/dt sensor

The advantages of the Rogowski Coil as a di/dt sensor also apply to the air-core mutual inductor. The main current goes through the primary winding. The secondary winding for measurement is electrically isolated from the main power circuit. Compared with the Rogowski Coil, the highly coupled design of the mutual inductor results in lower parasitic inductance and capacitance, and so lower parasitic oscillations. In addition, the behaviour of the Rogowski Coils is significantly influenced by whether or not the geometry is symmetrical, i.e. the current centrally situated and perpendicular to the plane of the coil, and there are no other external magnetic loops coupled

with the coil[58]. By comparison, the air-core mutual inductor can be easily made and installed by hand to achieve stable measuring characteristics.

The sensitivity of this current derivative sensor will be influenced by the structure and dimensions of the mutual inductor. The sensor used in [58, 14] uses the shielded signal cable to make the coils. The cable and the sensor design is shown in Fig 4.18(a). The primary current goes through the outlayer wires of the cable. The inner signal core is connected to measure the induced voltage signal, which is proportional to di/dt value. In this design, the primary winding and the secondary winding are set compactly and have the same turn numbers.

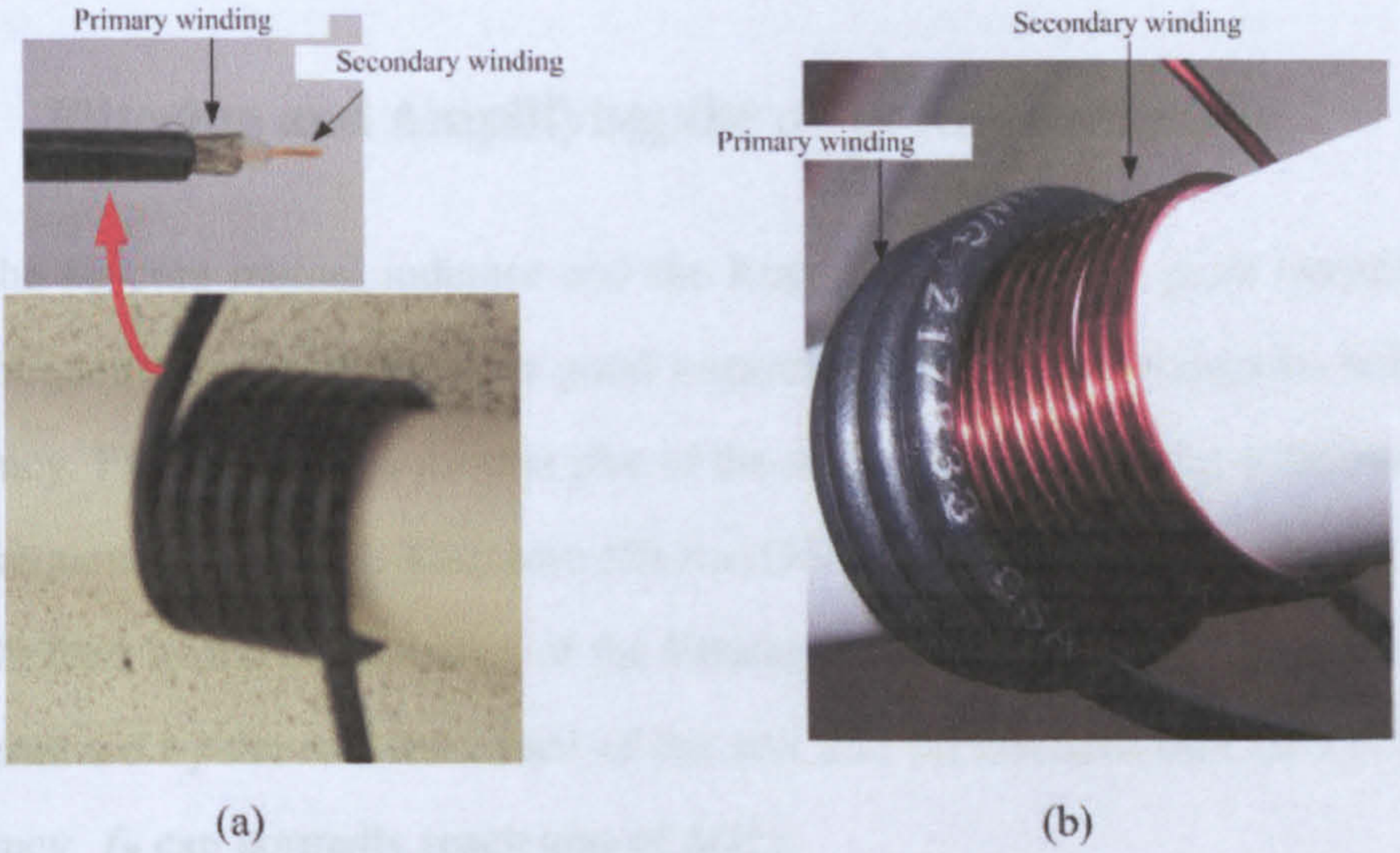

(a) (b)

Figure 4.18: Air-core mutual inductor for di/dt measurement (a): single layer design (b): double layer design

In this research, the primary coil and the secondary coil are put in two separately but closely placed layers, as indicated by Fig(b) (the figure is just an indication of the windings). The main advantage is the increased measurement gain. Each sensor has 19 turns winding for the primary winding and 40 turns for the secondary winding based on the dimensions of the windings and core used. Increasing the number of turn ratio between the primary and the secondary windings, can effectively enhance the amplitude of the output. In addition, between these two layers of windings, a layer

of metal foil connected to the ground is inserted, which helps to eliminate the stray capacitance between the two layer windings. The two coils are coupled well in the compact design and installation. For the sensor used in this research, its logically defined current derivative sensitivity [65] is calibrated as:

$$S = \frac{v_{sensor}}{di/dt} = 7.6\mu V \cdot s/A \tag{4.10}$$

where v_{sensor} is the output induced voltage of the sensor, and di/dt is the input current transient changing.

4.3.2 Filtering and Amplifying the di/dt Measurements

Both the air-core mutual inductor and the Rogowski Coil show good linearity in a wide frequency range and exhibit good response to the current transients with high frequency. Figure 4.19 is a general plot of the sensitivity of this kind of sensor in the wide frequency range[95]. They lose effect at DC and very low frequency range below f_A as limited by the basic theory of the Faraday's Law. The high-frequency limit f_B is determined by the self-resonance of the coil and the inherent time delays at high frequency. f_B can normally reach tens of MHz.

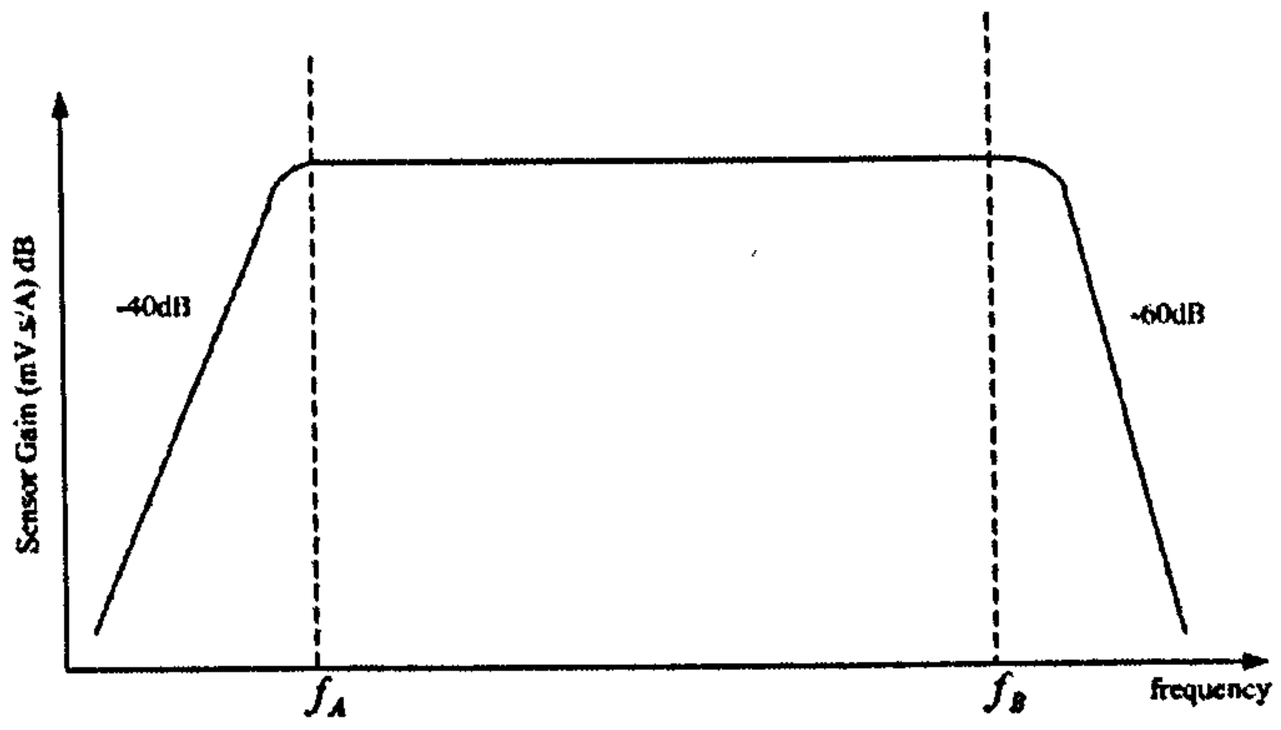

Figure 4.19: Sensor sensitivity vs. frequency relationship

During the PWM switching, due to the steep output voltage, there exist very high fre-

quency noise in the current transient signals. Although the high frequency noise does not have a large influence on the current waveform, it will become the dominant component in the output voltage of the di/dt sensor due to the differentiation operation. In this research, the current transients about several hundreds kHz are of interest because they are the resultant current response to the implementations of PWM voltage vectors via the stator circuit and contain the information of the saliency position. However, the switching oscillations resulting from the electrical magnetic interference (EMI) as discussed in 4.1, are much more amplified than the signal of concern and impair the precise sampling of the di/dt signals. For this reason, a signal processing circuit is added to suppress the high frequency noise. The circuit and parameters are shown in Fig 4.20. A RC low pass filter is used to filter out the high frequency noise and an amplifying circuit is used to improve the sensitivity.

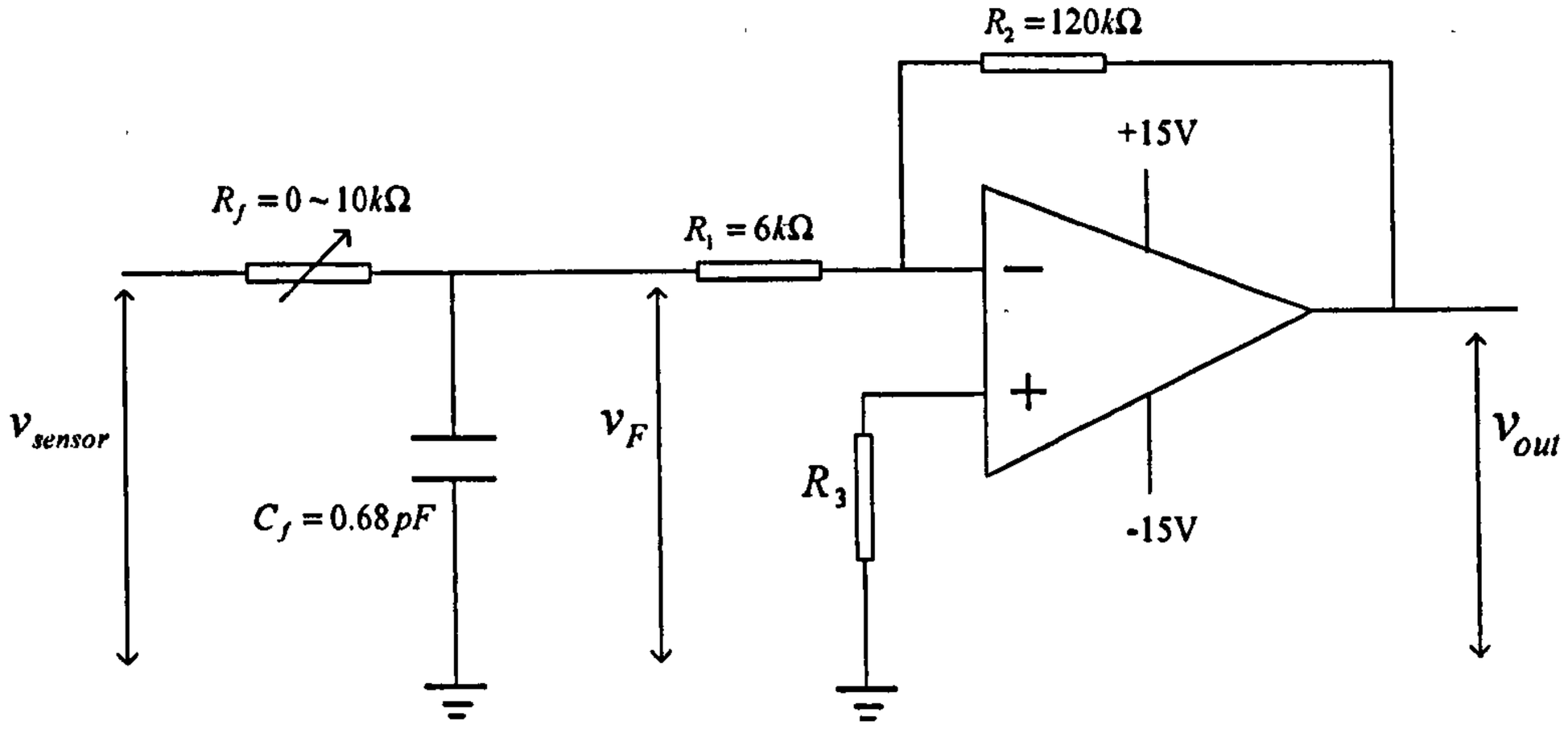

Figure 4.20: di/dt signal processing circuit

The RC low pass filter is designed with the cut-off frequency f_F at about $250kHz$, which is tunable by changing the resistance value. An inverting amplifier based on the operational amplifier is used to improve the sensitivity by introducing a fixed gain. However, with the design of most circuits with operational amplifier, a consideration of its bandwidth is required. The highest frequency and the fastest edge that the selected operational amplifier can process should be known. As a rule of thumb,

the gain and the bandwidth of a closed-loop operational amplifier circuit are always compromised, based on the principle that the product of the closed-loop gain and the bandwidth (GBP) is constant[96]. A good design should provide adequate bandwidth to support the signal and also function as an active filter at the noise frequencies.

For the inverting amplifier shown in Fig 4.20, the amplifying gain is $G = -R_2/R_1$. The selected operational amplifier, AD711, provides a unity gain bandwidth of $GPB = 3MHz$[97]. For the parameters of $R_1 = 6k\Omega$ and $R_2 = 36k\Omega$, the inverting amplifier has an inverting gain of $G = -6$. The closed-loop bandwidth of this amplifier circuit is about $f_{AMP} = GBP/G_{CLN} = 500kHz$.

4.3.3 Transfer Function of the di/dt Measurement Circuit

The transfer function of the full measurement circuit can be derived, taking the current i as the input and the final voltage signal from the amplifier as the output. The sensor is ideally a derivative element, with the spectrum performance shown in Fig 4.19 added. f_A ($f_A < 1Hz$) and f_B are decided by the sensor's design characteristics and located far away from the frequency range of interest. The low pass filter's transfer function is

$$\frac{V_{LPF}}{V_{in}} = \frac{1}{1+RCs} = \frac{\omega_F}{1+\omega_F s} \tag{4.11}$$

where ω_F is the low pass filter's cut-off frequency, $\omega_F = 2\pi f_F = 1/RC$. f_F is around $250kHz$ in this research. The inverting amplifier can be expressed as a fixed negative gain with a low pass filter.

$$\frac{V_{out}}{V_{LPF}} = A \cdot \frac{\omega_{AMP}}{1+\omega_{AMP}s} \tag{4.12}$$

where $\omega_{AMP} = 2\pi f_{AMP}$ is the bandwidth of the inverting amplifier. f_{AMP} is around

$500kHz$ as a result of the compromise with the amplification gain $A = -6$. As shown by the bode plot, the current components with frequency higher than f_{AMP} can be suppressed by this measuring circuit. For the lower frequency range, the output voltage is proportional to the current derivative value, as the system requires. The signal with the frequency of interest should be located in this range. The bode plot for the complete system is shown in Fig 4.21.

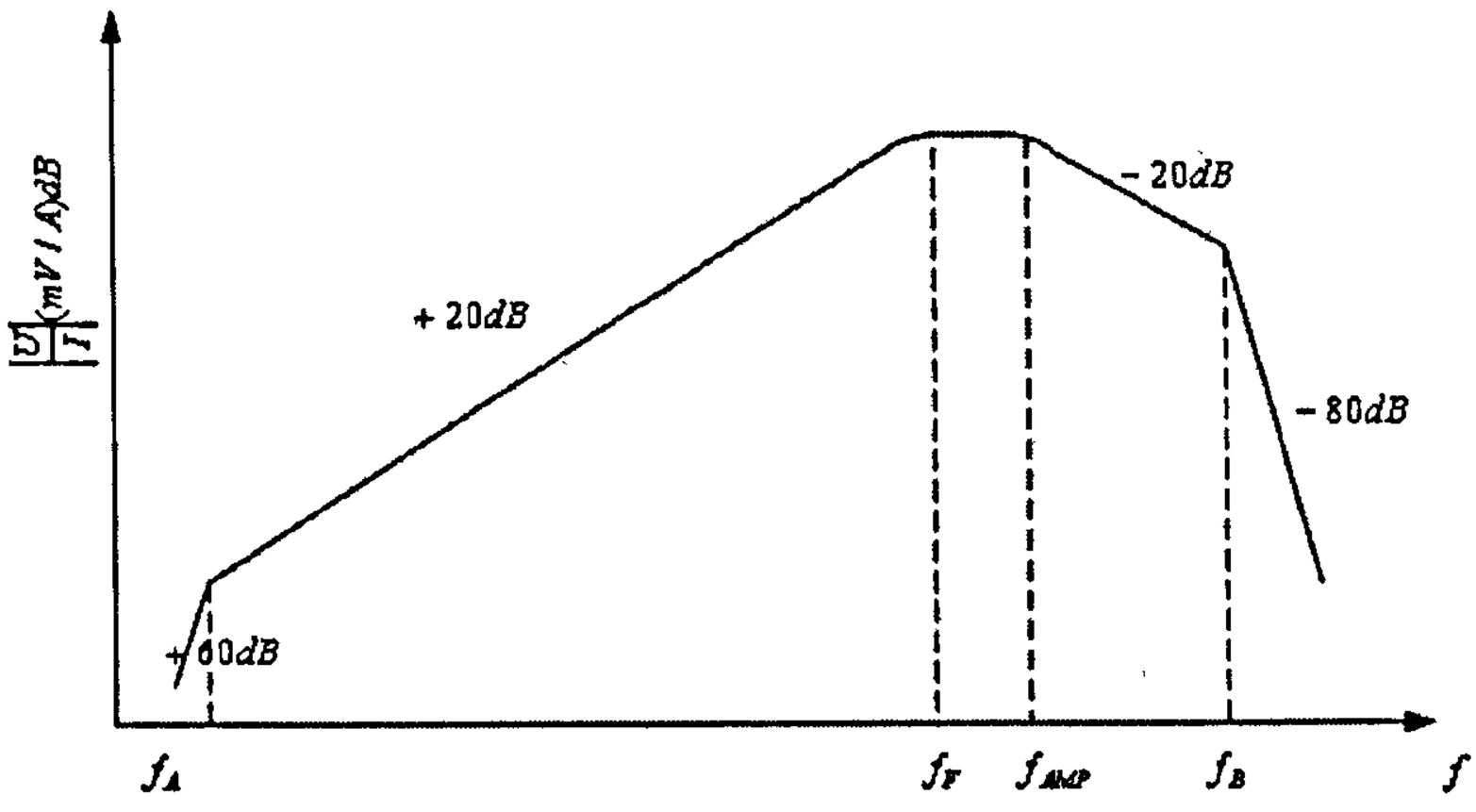

Figure 4.21: Gain-frequency relationship for the di/dt measurement circuit

4.3.4 Experimental Results for the di/dt Measurement

Figure 4.22 shows the voltage signals measured at different points of the di/dt measurement circuit. Figure 4.22(a) and (b) are measured in two different switching periods.

v_{sensor} is the output voltage of the air-core mutual inductor di/dt sensor. It is seen that the current derivative waveform has been overwhelmed by the enlarged high frequency switching noise. v_F is the output voltage of the RC low-pass filter. The noise has been much suppressed and the current response to the applied voltage vector can be recognized. But v_F has a very low amplitude which is difficult to be sampled by the analog to digital converter. The output of the amplifier circuit v_{out} is shown, which will be sent to the analogue to digital converter. As seen from the waveforms of v_F

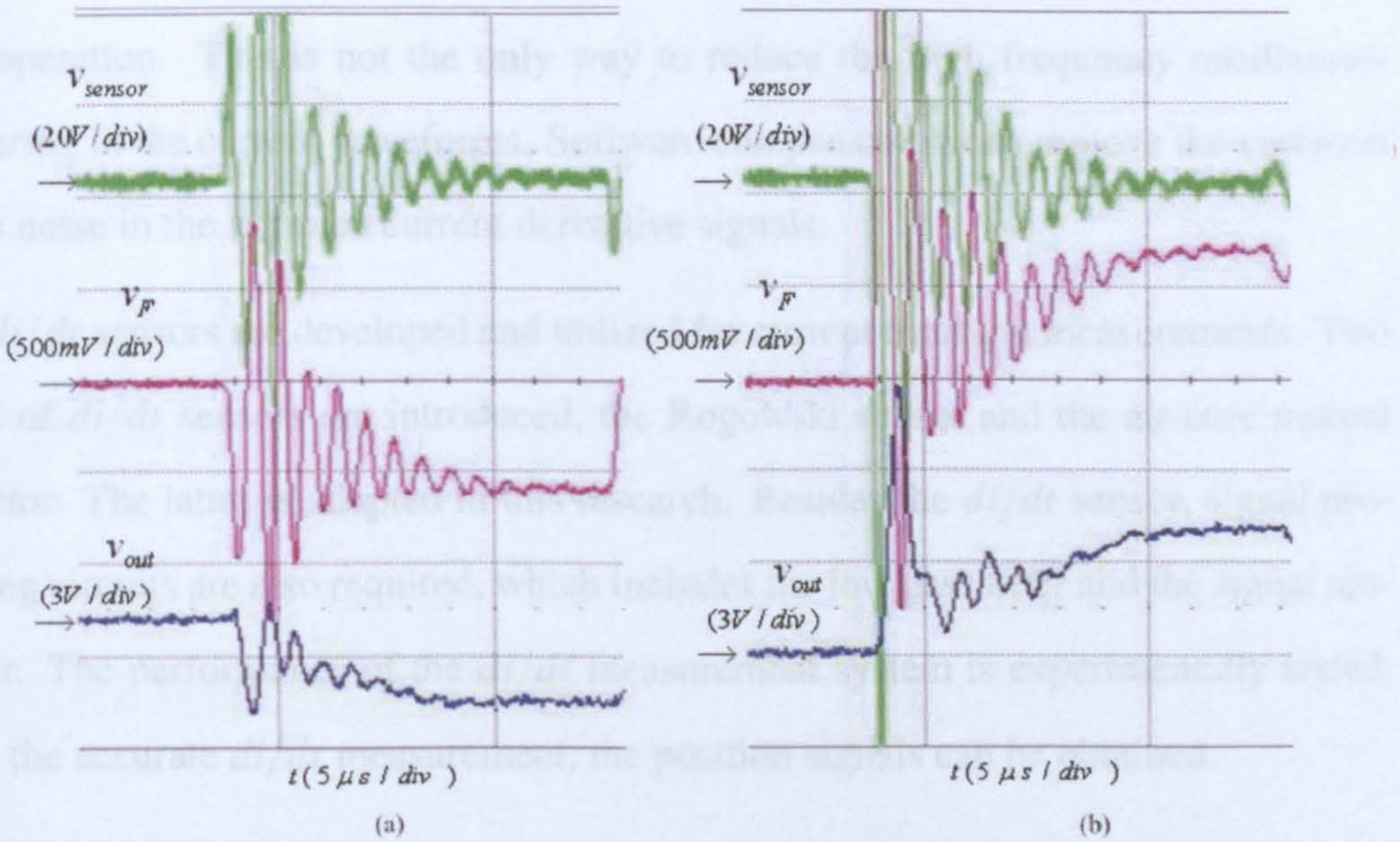

Figure 4.22: Measured di/dt signals: air-core mutual inductor output signal v_{sensor}; low-pass filter output signal v_F; amplifier circuit output signal v_{out}

and v_{out}, the amplifier not only enlarges the signal, but also provides further filtering of the noise. Finally precise and sufficient di/dt signals can be obtained.

4.4 Conclusions

Position estimation schemes based on PWM voltage vector transient excitation require the current transient values to be measured. However, the high frequency switching oscillations in the stator current waveforms make the di/dt sampling difficult. In this chapter, the high frequency switching oscillations in the AC drive system are firstly analyzed. Common mode and differential mode noise are recognized and described from their sources, paths and influence on the output currents. The possible measures are presented for reducing the switching noise. The increased gate resistance of the IGBT shows effect on suppressing the high frequency noise in the output current, which then reduces the required minimum voltage vector width for di/dt sampling. The added snubber capacitor eliminates the voltage spikes and thus ensures IGBT's

safe operation. This is not the only way to reduce the high frequency oscillations appearing in the current waveforms. Software compensation can remove the common mode noise in the sampled current derivative signals.

The di/dt sensors are developed and utilized for current transient measurements. Two kinds of di/dt sensors are introduced, the Rogowski sensor and the air-core mutual inductor. The latter is adopted in this research. Besides the di/dt sensor, signal processing circuits are also required, which includes the low pass filter and the signal amplifier. The performance of the di/dt measurement system is experimentally tested. With the accurate di/dt measurement, the position signals can be obtained.

Chapter 5

Experimental Rig

In this research, a three-phase PWM AC drive system has been designed and constructed, in order to implement and investigate the sensorless strategies discussed in Chapter 3 and Chapter 4. The design considerations of the hardware and software of the whole system will be presented in this chapter.

5.1 Overall System

Figure 5.1 shows the overview of the entire system structure. The power circuit incorporates the rectifier, the DC link, the inverter, and the PM motor. The gate drive boards transform the switching control signals into the inverter device gate signals. The digital control system, including the FPGA (field-programmable gate array) subsystem and the DSP (digital signal processor) subsystem, provides the control platform and produces the user interface.

The whole power circuit is fully assembled on one PCB, and connected with the AC power source and PM motor. The power rating of this system is designed to be less than 15kW. Highly precise current and voltage measurements and effective protection are achieved by using advanced sensors and signal processing. Current derivative

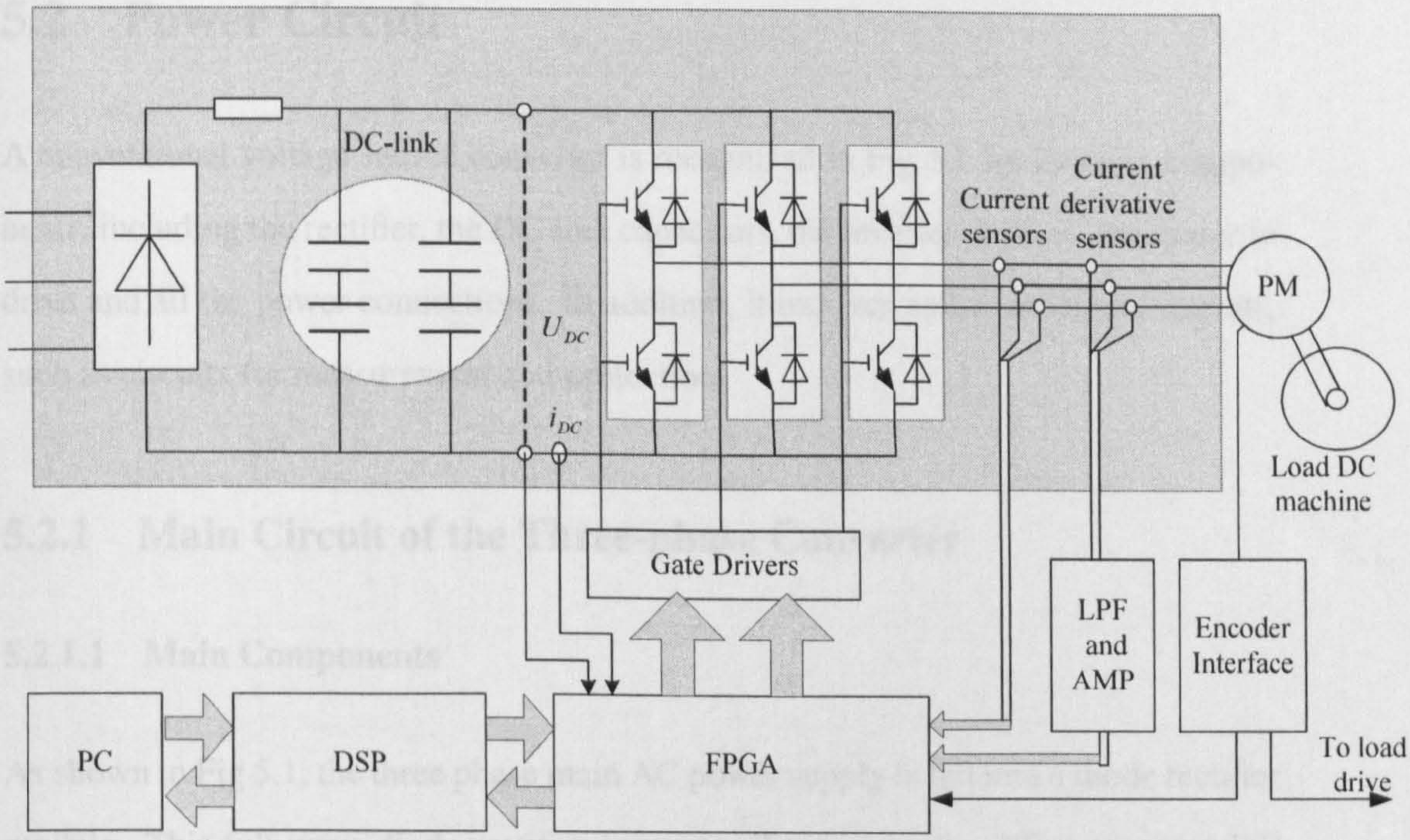

Figure 5.1: Overall block diagram of the AC drive system

measurements are obtained by specially designed sensors for the sensorless control scheme. The encoder is still used in this system for comparison only and for the DC load driving system. Electro-magnetic interference (EMI) are minimized in this system, not only through the compact layout and the snubber circuits, but also by the special design of the gate drivers which provide the capability for a higher gate resistance.

Vector control, or field-oriented control, is applied, which keeps the rotor magnetic field amplitude constant and controls the motor speed or position by applying appropriate torque. SVPWM (Space Vector Pulse Width Modulation) is used for the continuous voltage modulation with symmetric switching cycles and maximum DC link voltage utilization[74]. Position estimation is based on the excitation from the fundamental PWM switching with the measurement of the current derivative, as di/dt, signals.

5.2 Power Circuit

A conventional voltage source converter is recognized in Fig 5.1 by its main components, including the rectifier, the DC link capacitors, the inverter devices, the motor to drive and all the power connections. In addition, it requires some peripheral circuits, such as circuits for measurement and protection.

5.2.1 Main Circuit of the Three-phase Converter

5.2.1.1 Main Components

As shown in Fig 5.1, the three phase main AC power supply is fed into a diode rectifier module. This full-wave diode rectifier converts all the incoming AC power to a DC form which is further smoothed by the DC link capacitors. One pre-charge circuit is required between the diode rectifier module and the DC link capacitors, which limits the rate of change of the voltage across the DC link capacitors and the inrush current. The simplest pre-charge circuit can be a NTC (negative temperature coefficient) thermistor. When cold, its high resistance allows a small current to pre-charge the DC link capacitor, but after it warms up, it changes to a low resistance to efficiently pass the full load currents. However, in this system, a variable AC transformer (variac) is used to feed this system and so the in-rush current is naturally avoided.

Electrolytic capacitors are commonly used as the DC link capacitors in power electronic converters due to their high capacitance density. Electrolytic capacitors use electric properties of aluminum oxide. When the capacitor is charged and discharged electrons are stored in the dielectric. When the discharge mechanism is removed these electrons build up a DC voltage. Figure 5.2(a) is a commonly used electric equivalent circuit of one electrolytic capacitor, including the equivalent series resistance (ESR), the equivalent series inductance (ESL), the capacitance (C) and the parallel resistance

for the leakage current (R_{leak})[98]. The current through the electrolytic capacitor will cause a power loss in it, mainly due to the ESR.

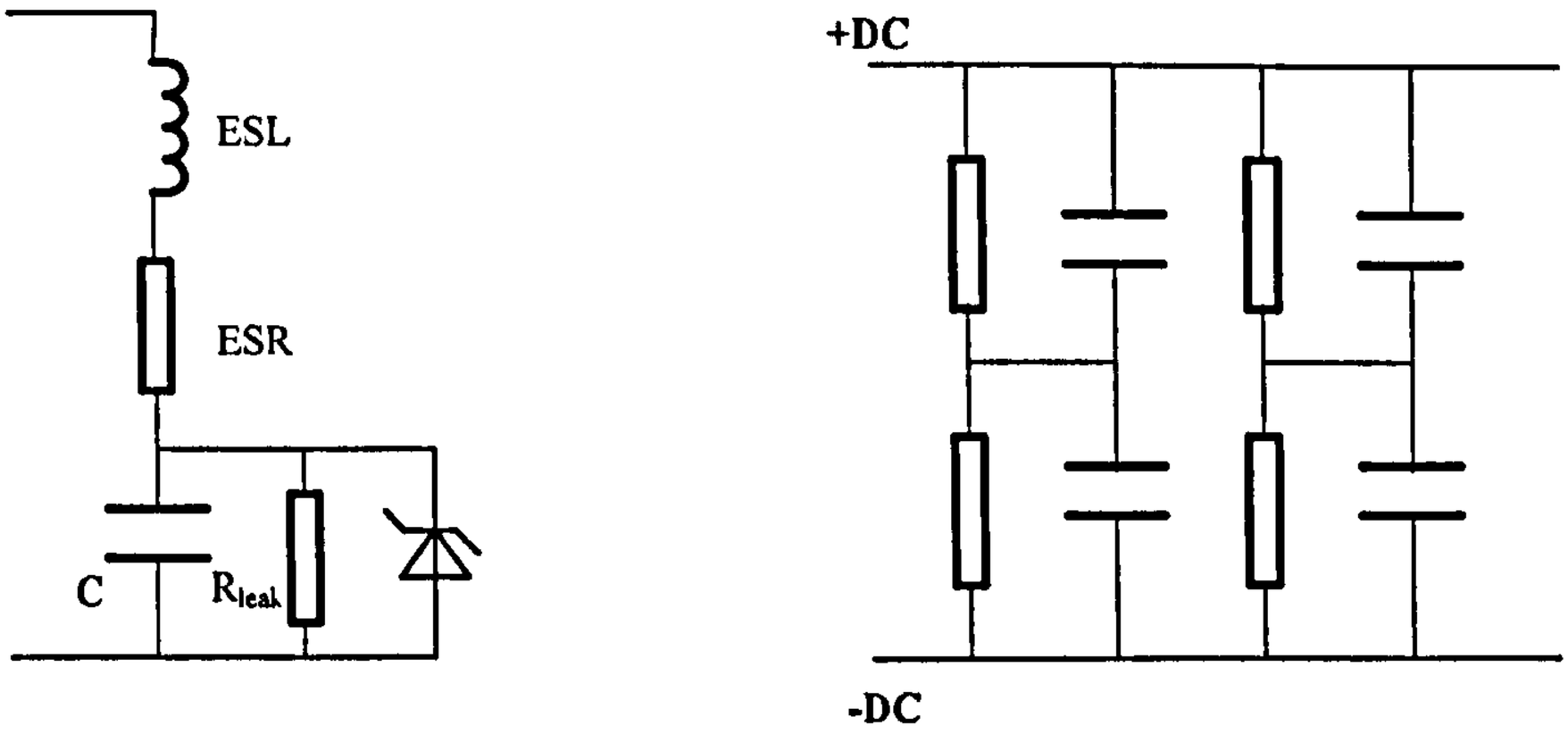

(a) Equivalent circuit of an electrolytic capacitor

(b) Connection of DC link capacitors

Figure 5.2: DC link capacitor

The DC link capacitors are used to smooth the voltage after the diode rectifier. The capacitance needed can be calculated from the required level of the voltage ripple by[99]:

$$C = \frac{2 \times P}{(U_{max}^2 - U_{min}^2) \times f_{rectifier}} \tag{5.1}$$

or

$$C = \frac{P}{U_{ripple} \times (U_{max} - U_{ripple}/2) \times f_{rectifier}} \tag{5.2}$$

where P is the load power in watts, U_{max} is the highest value of the output voltage from the diode rectifier, and U_{min} is the lowest value of the output voltage from the diode rectifier, and $f_{rectifier}$ is the frequency of the output voltage ripple.

In this research, the output voltage of the 3 phase, 6 diode rectifier gives a frequency $f_{rectifier}$ as $300Hz$. If the ripple is limited to within 40 volts, with the load power rated at $15kW$, the required DC link capacitance can be roughly calculated to be $2016\mu F$.

According to the technology of the electrolytic capacitor, the maximum nominal volt-

age of electrolytic capacitors is absolutely limited, practically to between 500 and 600 Volts [100]. Therefore, as in most drive systems, several capacitors in series or parallel are used to meet the requirements of capacitance and voltage rating. The resistances of the capacitors in series may vary from one to the other, and therefore high value resistors must be connected to each capacitor to balance the voltage. In this research, four capacitors, with ratings as 400V and $2200\mu F$, are paralleled in two branches of dual series capacitors as shown in Fig 5.2(b).

Many different types of IGBT modules are available in current market, discrete IGBT chips, IGBT bridge or three-phase IGBT package, etc. Proper selection of an IGBT involves two key points. The first is that the peak collector current during operation including any required overload current is less than the device rated current. The second criterion is that the IGBT operating junction temperature must always be kept lower than $T_{j(max)}$. It is preferred to use a higher current rated module if less cooling is employed. In this research SKM 50GB 123D is adopted, which consist of two IGBTs in series[89]. The free-wheeling diodes are also mounted inside for easy assembling and minimum lead inductance. The maximum current through the IGBT can reach 50A, with sufficient tolerance for the operation in this research. Three of these IGBT bridge modules are mounted on a bonded fin aluminum heatsink.

5.2.1.2 PCB tracks

All the power components in this system are integrated onto a two-layer PCB, providing more compact and more powerful connections than if conventional cables or busbars are used. Large copper tracks are embedded on both layers of the PCB for the main power current. The PCB layout accommodates all the modules and the surface mounted components of the power stage in the inverter. Instead of using the busbar or power cable, the PCB integration can also greatly reduce the EMI introduced by the connecting elements, because the PCB track or copper layer has much lower

impedance than that of a cable or busbar.

The PCB track will heat up as the current flows through it due to its resistance, and the amount of resistive heating is governed by the width of the track, the thickness of the copper, and the resistivity of the copper. The resistivity of the copper is generally a fixed standard value. According to the generic standard of the PCB design IPC-2221[101], the diagram shown in Fig 5.3, is the widely used, informative and indicative method to decide the width of the PCB track according to its current capacity, or to estimate the temperature rise due to an electrical current[102]. Firstly according to the current requirement, find the cross-section area needed for the track to allow for a certain degree of temperature rise. Secondly, in the lower diagram determine the track width for the track thickness utilized. Conversely, if the track width and thickness are known, the temperature rise for a given current goes can be estimated from this figure.

By consulting this graph, as an example for this research, a standard copper PCB track with 1oz. thickness, capable of carrying a current up to 20 Amps with a 50°C temperature rise, would need to be 300 mils wide. The minimum width of the power traces the PCB developed for this research is 360mil.

Enough spacing should be kept between the tracks with high voltages to prevent arcing. In this research, the DC link voltage is about 620V under the normal operation, and to prevent creepage gap of more than 5mm is kept between the tracks with +DC and -DC voltages. The main tracks of the +DC bus and the -DC bus are placed respectively on the surfaces of the two sides of the PCB board, which optimizes the design space and improves the safety.

5.2.2 Protection Circuits

The protection circuit is very important for the safe and reliable operation of the whole system. The most common faults of an AC drive system are recognized[103] and

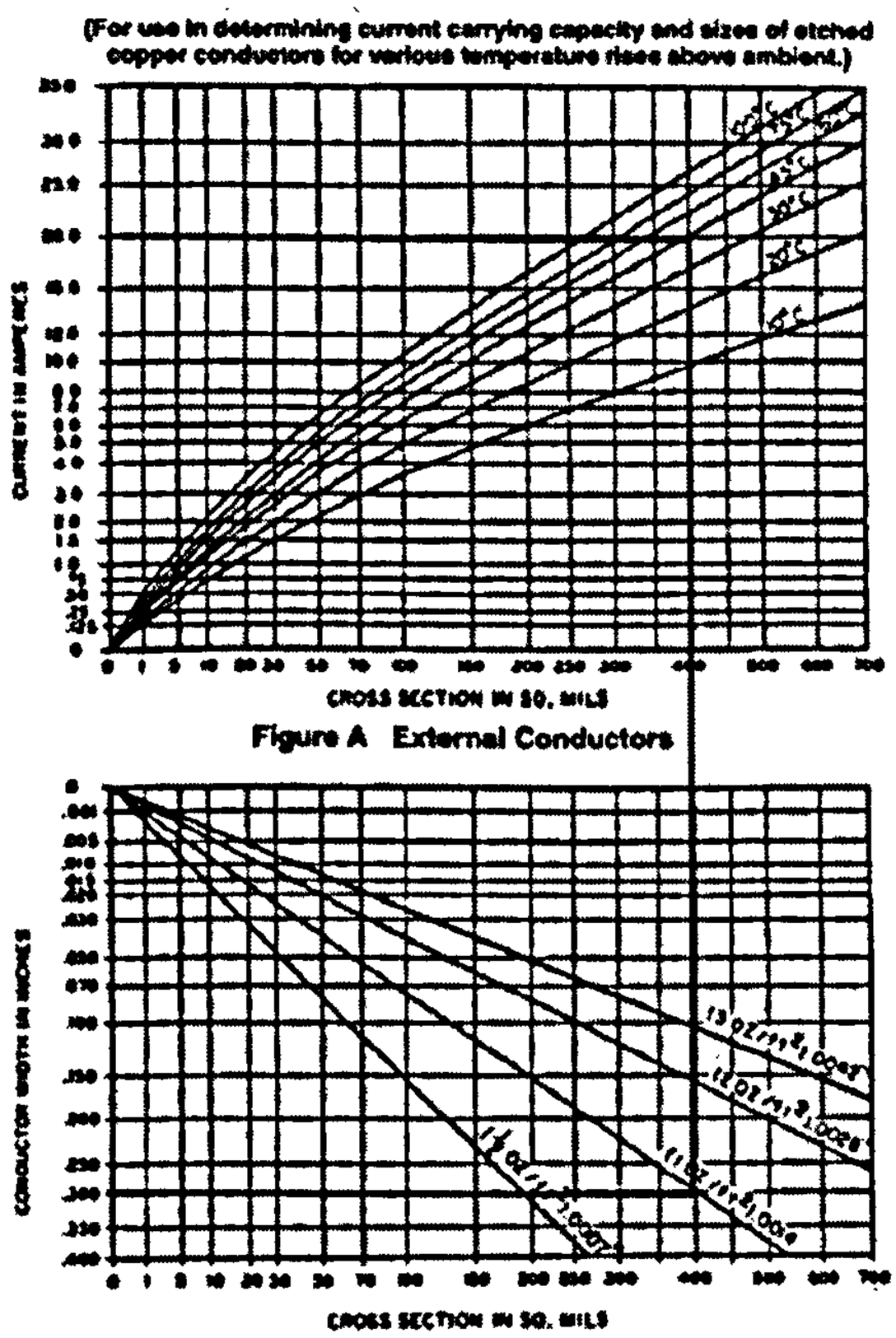

Figure 5.3: Diagram from IPC-2221 for deciding current carrying ability of external PCB traces

many reasonable solutions are provided with the rapid development of power electronic technology. The main protection schemes can be categorized as the over-current protection, the over-voltage protection and the over-temperature protection.

5.2.2.1 Over-current Protection

Over-current problems are usually caused by short circuit conditions, and therefore the causes and the circuits of the possible fault conditions are analyzed to investigate effective over-current protection[103]. Three types of short-circuit fault conditions exist, indicated by Fig 5.4:

a. Shoot-through fault. The short circuit current flows through one IGBT bridge mod-

ule. This may be caused by IGBT or diode destruction, or incorrect control, or a noise induced malfunction.

b. Line to line fault. The short circuit occurs between two output lines. Miswiring or phase-to-phase insulation destruction can lead to this kind of short circuit.

c. Ground fault. The short circuit current flows from the inverter to the ground point. The reason can be motor phase-ground dielectric breakdown or the incorrect wiring.

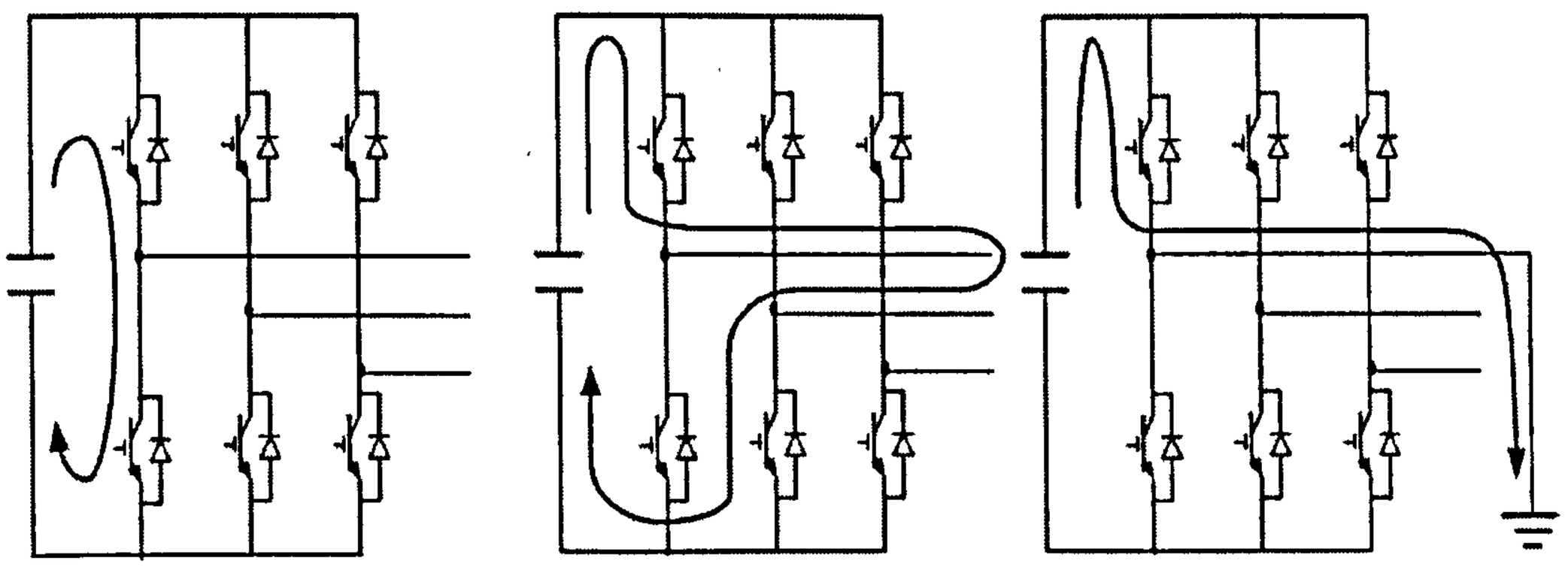

(a) shoot through fault (b) line to line fault (c) ground fault

Figure 5.4: Short circuit faults for a 3-phase inverter

Over-current detectors can be inserted at specific places for effective protection of the drive system. In the event of a short circuit, the over-current is detected and then the IGBTs are disabled as soon as possible. The period from the over-current detection to the complete turn-off of the IGBTs must be very short. In this research, Hall effect current sensors are installed to measure the output currents and the current flowing through the -DC bus. The utilized current transducer has fast response, with the reaction time less than 500ns[104]. By measuring three phase output currents and the current going through -DC bus, over current is prohibited and thus the inverter is protected from the above short circuit faults. Fast hardware overcurrent protection is provided on the FPGA board by comparing the analogue transducer measurement

with a value set by a potential divider. If any of the three phase currents or the -DC bus current exceeds the preset threshold, a logic signal is created which can be used to trip the circuit.

5.2.2.2 Over-voltage Protection

The first type of over voltage protection is achieved by measuring the voltage across the DC link, and comparing it with a predetermined threshold value. This ensures that the DC link capacitors are not over-charged.

However, due to the high speed switching of the IGBTs, the stray inductance in the circuit can cause high surge voltages at the terminals of IGBTs, especially during turn-off periods. The commonly used method is to add snubber circuits across the IGBTs. Different kinds of snubber circuits have been proposed, which can be RC or RCD, individual or lumped[103]. In this research, the easiest but still effective method adopted is to place a polypropylene capacitor of 470nF close to and across each IGBT module. Thus the high frequency surge currents are passed to the snubber capacitors, $C_{snubber}$, as shown in Fig 5.5 and the high voltage spikes are then considerably reduced.

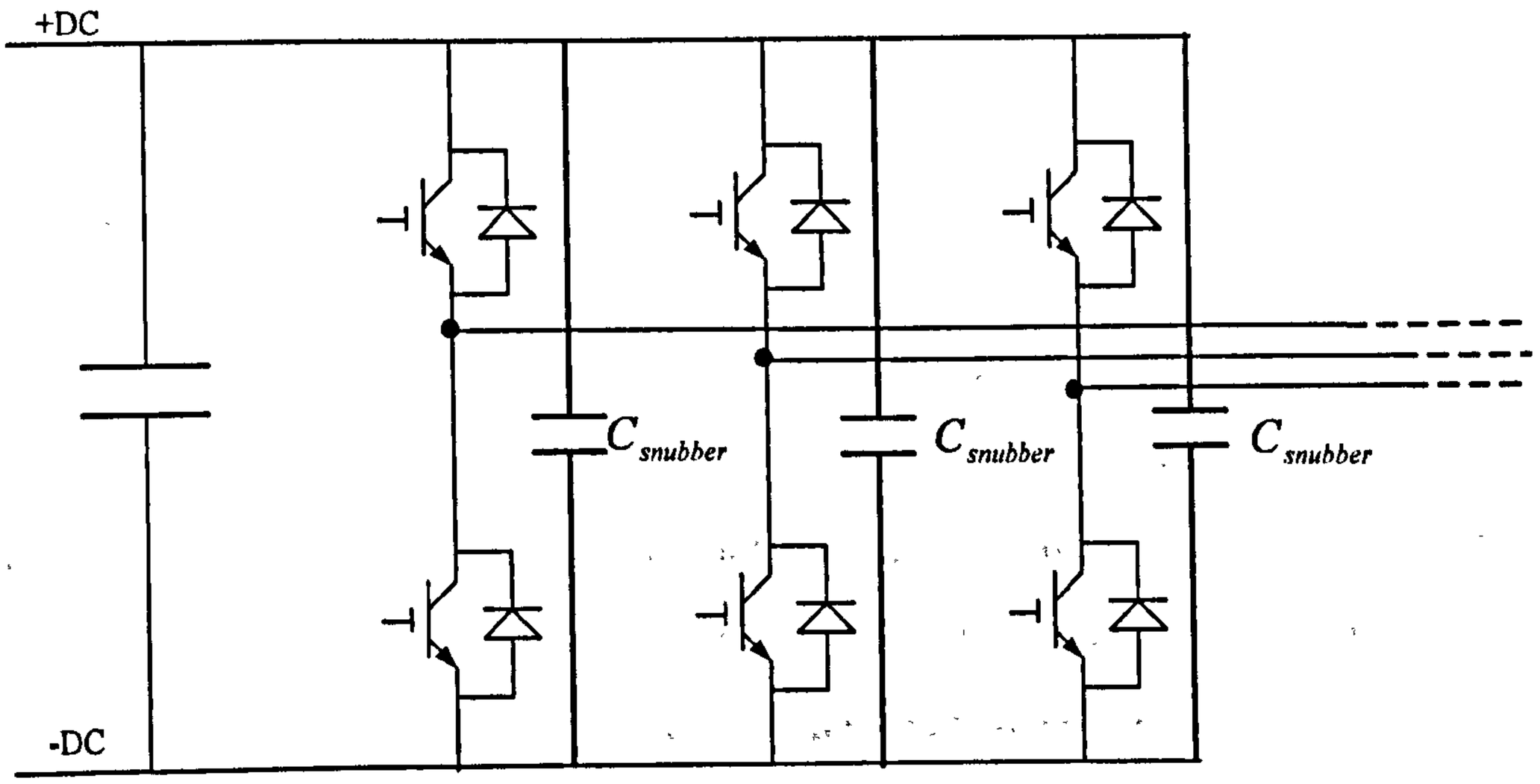

Figure 5.5: 3-phase IGBT bridges with snubber capacitors

5.2.3 Measurement Circuits

5.2.3.1 Current and Voltage Measurement

The current transducers and the voltage transducers are all mounted on the main PCB. All of the three phase inverter output currents and the -DC bus current are measured by LEM current transducers (LAH 50-P[104]). This Hall Effect device provides precise and linear measurement, and also electrical isolation. The range of its AC measurement is $\pm 50A$. The DC link voltage and also two phase line-to-line voltages are measured by the LEM voltage transducers (LV 25-P[105]), which is also based on Hall Effect and characterized by its high bandwidth and low common mode disturbance.

For both kinds of transducers, the output is a current signal proportional to the measured current or voltage. This is then transformed to a voltage signal by passing through a selected high precision resistor. Because the current signal shows higher noise immunity than the voltage signal in transmission, these resistors are placed on the FPGA board. The resultant voltage signal passes through analogue comparators preset with the trip threshold values. These comparators provide "instantaneous" over-current trip in hardware. The signals are then digitalized by the Analogue-to-Digital converters.

5.2.3.2 Current Derivative Measurement

The three phase current derivatives at the inverter's output side need to be measured for the position estimation scheme in this system. As described in Chapter 4, three handmade air-core transformers are built for the di/dt measurements. The output current of the inverter flows through the primary coils, while the induced voltages of the inner secondary coils are detected. The induced voltage across the secondary coil is proportional to the output current derivative value.

These three di/dt sensors are placed at the output side of the PCB. Their output volt-

age are fed into a small PCB for signal processing, including lowpass filtering and amplifying circuits. The signals are then sent to the FPGA board, where they are sampled and digitalized.

5.2.3.3 Rotor Position and Speed Measurement

An optical quadrature encoder is fitted on the PM machine shaft to measure the rotor position. The output of the encoder, an incremental quadrature signals of 1024 pulses per revolution, is transformed to an absolute position signal by an encoder interface board. The encoder signal can be used not only for the position measurement of the PM machine, but also for the feedback required by the load drive. Thus an encoder board is built to split the signal and isolate both resultant signals, for use by the two drives. On the side of the PM machine drive, the output signal of the encoder is sent to the FPGA board, where the FPGA program detects the quadrature pulse edges and calculates the rotor position. The rotor speed can be obtained in the DSP program from the rate of change of the position signal. The key component of the encoder interface board is the quadrature decoder/counter IC HCTL2016[106]. This IC counts the positive and negative edges of both the encoder quadrature signals, which quadruples the resolution to 4096 pulses per revolution. The 16-bit counter is incremented or decremented depending on the direction of the rotation, and it is reset by the zero signal output from the encoder to yield the absolute position measurement.

5.3 IGBT Gate Driver

IGBTs are voltage controlled devices and require a proper gate voltage to establish the collector-to-emitter conduction. The safe operation and good dynamic characteristics of the IGBT depend on the design of its gate drive circuit.

5.3.1 Gate drive circuit

The primary function of the gate drive circuit is to convert logic level control signals into the appropriate voltage and current signals for the efficient and reliable switching of the IGBT module. An IGBT is turned on when a positive voltage of typically 15V is applied across its gate and emitter. Although the IGBT can also be turned off when there is no potential difference between the gate and emitter at steady state, a negative voltage bias is preferred to turn off the IGBT, in order to improve the IGBT immunity to the collector-to-emitter dv/dt injected noise, especially for the IGBT bridge application[107]. Also, the turn off losses can be reduced by choosing an appropriate negative bias voltage.

For most high power IGBT modules, it is desirable to use completely electrically isolated gate drive circuits. That means the logic level control signal is isolated from the power supply for each gate driver. The advantages include: (1) Stable ON/OFF driving voltage level independent from the power device switching. (2) Possible high current output for the large IGBT modules. (3) Isolation of the control circuit from the power circuit switching noise and high voltage potential. The proposed components providing this electrical isolation can be discrete transistors, pulse transformers, optocouplers, or the optical fiber waveguides. Most discrete transistor designs do not provide sufficient safety and noise immunity. The pulse transformer is a traditional and simple solution but suffers from potential core saturation. The optical waveguide is only used for very high powers and where longer lines are required between the control and power stages. The gate driver optocoupler IC integrates the LED light source and optical receiver for safe isolation, and the transistor for sufficient drive ability. The compact optocoupler IC can reduce power dissipation and save space on the gate drive board. In the gate drive board developed in this research, the HCPL-315J is adopted[108], which incorporates two separate channels of optocoupler circuits, suitable for the dual-IGBT module used in this research.

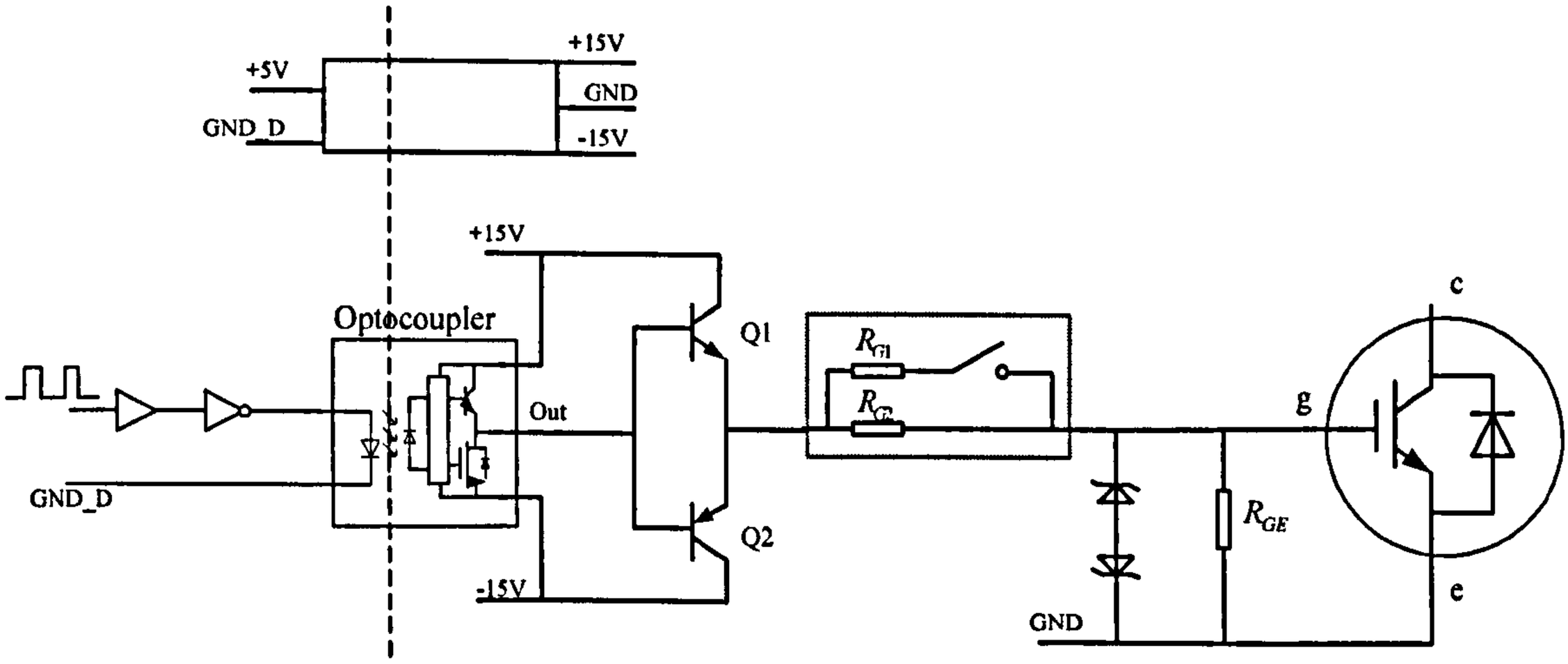

Figure 5.6: Gate drive circuit for one IGBT switch

The proper operation of the IGBT depends not only on the proper gate voltage, but also sufficient gate current i_G which flows out from or into the gate for charging or discharging. According to the charge required, it may be necessary to amplify the power by using a push-pull circuit, as shown in Fig 5.6, after the optocoupler. Isolated power supplies are used to supply the push-pull circuit and thus amplify the output signal of the optocoupler. This gate drive power supply should have high voltage insulation capability. The DC-DC converter block NMH0515DC[109] is used which has a nominal input as +5V and outputs of both +15V and -15V with a power rating up to 2W. The capacitance between each output and in the logic circuits is designed to minimize dv/dt induced noise.

During switching or short circuit operation, the miller effect current[110] may cause voltage across the gate resistor and voltage through the gate parasitic inductance. These voltages are added to the normal control state voltage causing surge voltage on the gate. In order to limit the gate voltage surges, it is desirable to implement gate voltage clamping. The simplest form is two back-to-back zener diodes connected from gate to emitter as shown in Fig 5.6. The zener break down voltage is 18V in this research. A $10k\Omega$ resistor R_{GE} is placed between the gate and emitter close to the

IGBT, in order to prevent the possible destruction caused by the voltage applied to the power circuit when the gate circuit has failed.

The gate resistance has a significant impact on the dynamic performance of the IGBT. In this research, the gate resistance is made changeable by programming, instead of using a constant value as is usual.

5.3.2 Changeable Gate Resistance

Normally the IGBT utilized has a recommended gate resistance value, which is set according to the specific dynamic performance. One influence from R_G is that, a smaller gate resistance charges and discharges the IGBT input capacitance faster, and so reduces the switching time and the switching loss. However, a small R_G can lead to high oscillations between the IGBT input capacitance and the parasitic lead inductance, which introduces oscillations in the IGBT output voltages and currents. The dv/dt shoot through current can also be avoided by increasing R_G. The surge voltage during switching becomes smaller when R_G increases.

In this research, as discussed in Chapter 3, the output current derivatives are to be measured during a specific vector of the PWM switching. In order to measure the di/dt values precisely within a short period after the desired switching instants, the high frequency switching oscillations must be reduced. One effective method is to increase the gate resistance R_G. The gate driver is thus expected to provide different gate resistance values, one for the normal operation cycles and one for the di/dt measurement cycles, which should be chosen by the program.

For this purpose, two gate resistors, R_{G1} and R_{G2}, are paralleled and placed between the output of the optocoupler and the gate of the IGBT. R_{G2} is in series with a circuit functioning as a bi-directional switch. The switch is realized by two MOSFET modules in series with opposite directions as shown in Fig 5.7. The two MOSFETs are switched ON/OFF at the same time. When the ON signal is sent to them, part of

the gate current i_G will go through one of the MOSFETs and the free-wheel diode of the other MOSFET, depending on its direction, or say, depending on if it is charging or discharging the gate of the IGBT. When the OFF signal is recieved, both MOSFETs are blocked and no current goes through the branch of R_{G2}. One point is, the control signal of the MOSFETs should be electrically isolated from the other part of the gate drive power circuit. The optocoupler and the isolated power supplies are also applicable, with the 0V potential floating with the main gate drive circuit.

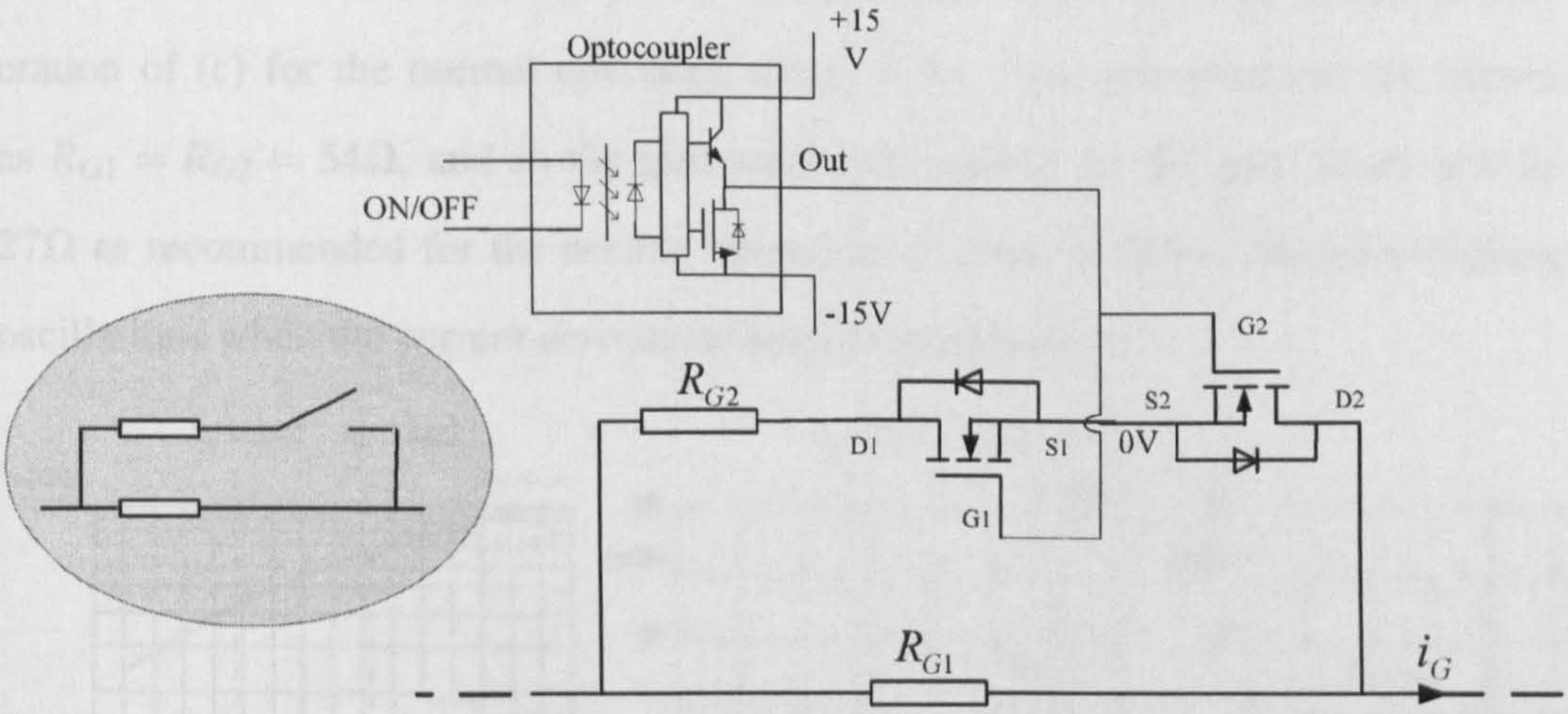

Figure 5.7: Changeable gate resistance utilizing MOSFET bi-directional switch

During normal operation, the bi-directional switch is kept ON, and the gate current i_G goes through both gate resistors. The equivalent gate resistance is decided by the paralleled R_{G1} and R_{G2}. When the motor current derivatives are to be measured, the bi-directional switch is turned off, and the gate resistance is equal to R_{G1}. No gate current goes through the branch of R_{G2} and the MOSFETs. The gate resistance signals are sent out from the DSP program.

As discussed before, the gate resistance value is a compromise between the switching noise and the switching loss. R_{G1} and R_{G2} need to be selected according to the IGBT characteristic diagrams, as shown in Fig 5.8, from its datasheet[89]. Figure 5.8(a) and (b) show the tendency of the switching time and the switching loss chang-

ing with the gate resistance. Because these plots are obtained under the conditions when the collector current $I_C = 40A$, which is much higher than the current about $10A$ in the normal operation of this research, Fig 5.8(c) is also provided for understanding the relationship between the switching energy and the collector current. The recommended gate resistance value is 27Ω. If setting $R_G = 54\Omega$, twice of the recommended value, the turn-on time will be extended from 420ns to about 700ns, and the turn-off time extended from 80ns to about 120ns, according to the plot in (a). The switching loss will be increased but is acceptable by checking (b) and making relevant consideration of (c) for the normal operating range of I_C. Two gate resistors are chosen as $R_{G1} = R_{G2} = 54\Omega$, and so the gate resistance applied on the gate driver will be 27Ω as recommended for the normal operation, or 54Ω with the reduced switching oscillations when the current derivatives need to be measured.

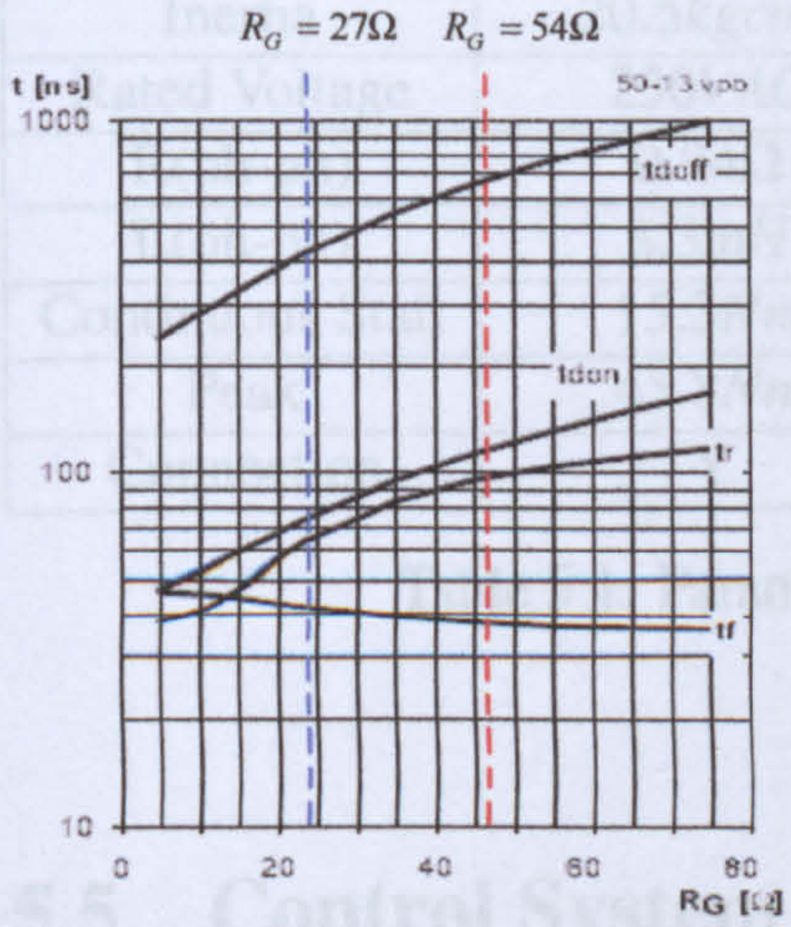

(a) switching time vs. gate resistance
(V_{CE} =600V, V_{GE} =+/-15V, I_C =40A)

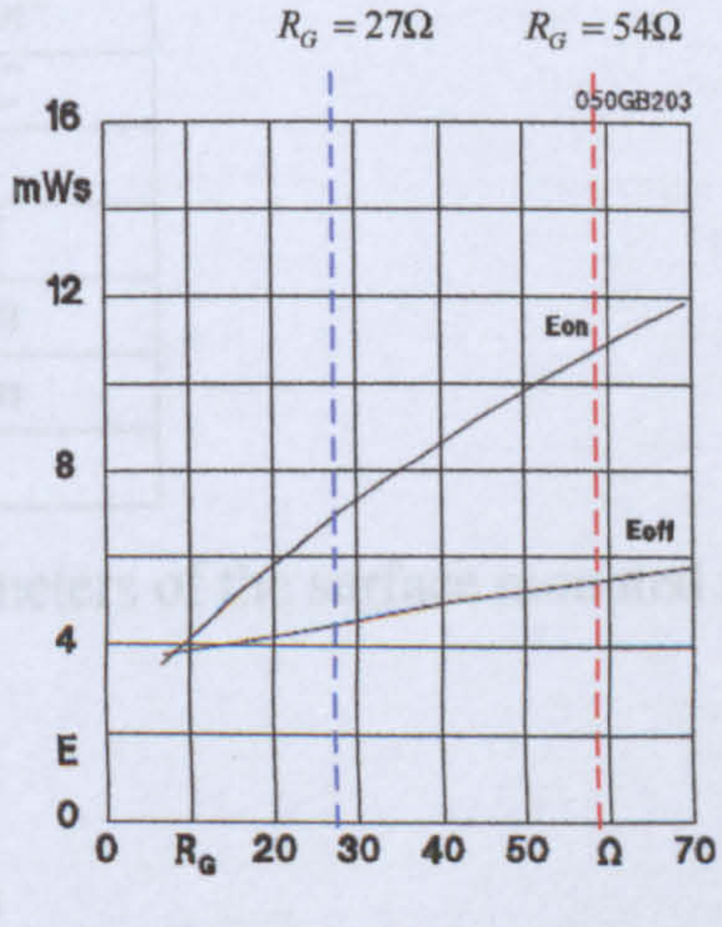

(b) turn on/off energy vs. gate resistance
(V_{CE} =600V, V_{GE} =+/-15V, I_C =40A)

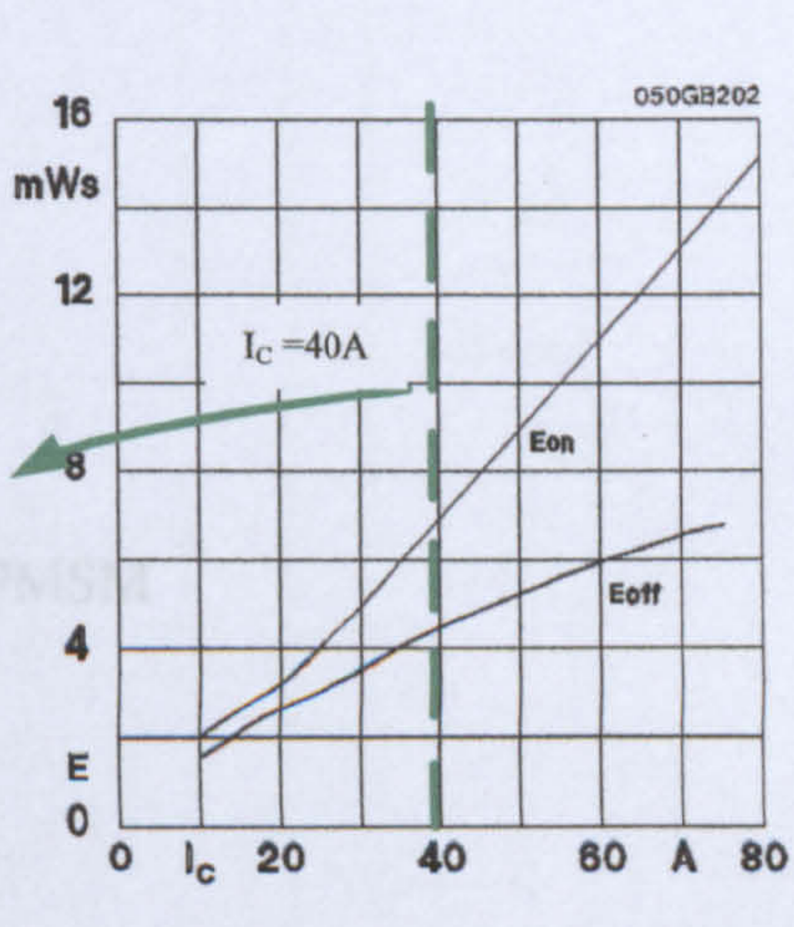

(c) turn on/off energy vs. collector current
(V_{CE} =600V, V_{GE} =+/-15V, R_G=27ohm)

Figure 5.8: Selecting gate resistance according to IGBT characteristic diagrams

5.4 PM Motor

The motor to drive in this system is a surface mounted permanent magnet synchronous AC servomotor, provided by *Control Techniques* with the serial number as 142UMC30.

It is a 6 pole machine of power rating as 3.82kW. The machine parameters are listed in Table 5.1. The rated torque is 12.2Nm and thus the rated torque current in the vector control scheme can be calculated as 7.625A. To load this surface mounted PMSM, an DC machine drive system is used. A torsionally rigid coupling directly connects the shafts of both machines. The DC motor used for the load drive is rated at *5.6kW*, allowing operation up to the nominal speed of PM machine. It is supplied from a four quadrant controlled rectifier.

Model	142UMC30
Number of Poles	6
Rated Speed	$3000rpm$
Rated Torque	$12.2Nm$
Rated Power	$3.82kW$
Kt	$1.6Nm/A$
Ke	$98.0Vrms/krpm$
Inertia	$20.5kgcm^2$
Rated Voltage	$230VAC$
R(ph-ph)	0.94Ω
L(ph-ph)	$8.3mH$
Continuous Stall	$15.3Nm$
Peak	$45.8Nm$
Connection	Y

Table 5.1: Parameters of the surface mounted PMSM

5.5 Control System

The control system in this research is a general-purpose advanced digital system, developed by Dr Lee Empringham and Dr Maurice Apap for the PEMC Group of the University of Nottingham. The control system is programmed using a field programmable gate array (FPGA) chip and a 32-bit float-point digital signal processor (DSP). The FPGA and DSP cooperate to realize the signal interfacing, data processing and command implementing.

5.5.1 FPGA Subsystem

A ProASIC3, the third-generation family of Actel Flash FPGAs, is chosen due to its good features in power, price, performance and density. The ProASIC A500K050 used in this research is based on nonvolatile flash technology and support 100k system gates and up to 204 high-performance user I/Os. Centred with the FPGA chip, the A/D channels, LED fault display, D/A converter, user inputs and ouputs, etc, are incorporated for use on the board as shown in Fig 5.9.

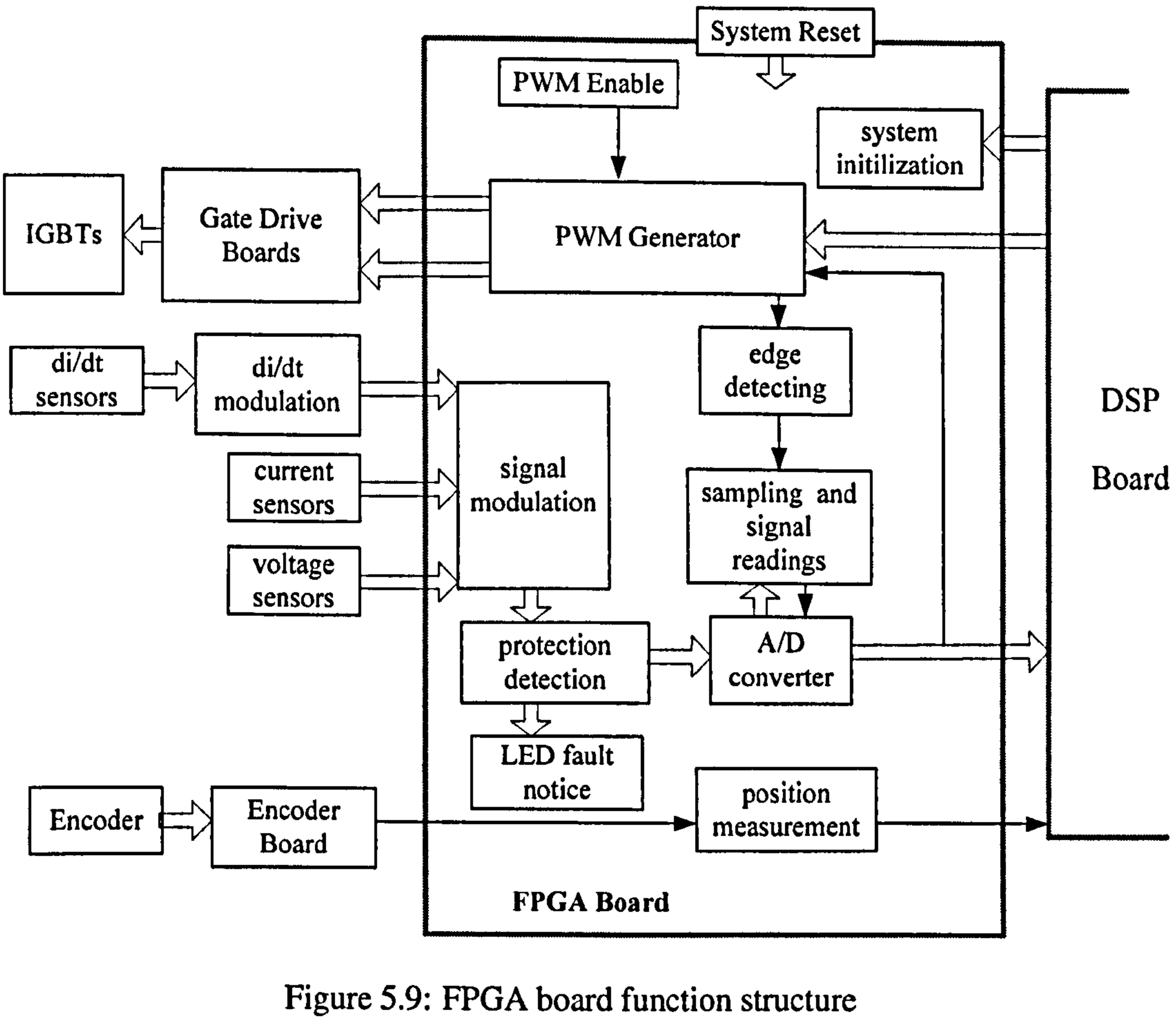

Figure 5.9: FPGA board function structure

Nine A/D channels are available for sampling the data of three phase currents, three phase current derivatives, 2 phase line-to-line voltages, and the DC link voltage. Each channel has its own potentiometer and comparator to set the trip level for protection. For the precise timing of di/dt measurements, edges of the PWM signals need to be

detected based on the control scheme. All the A/D results are kept in the registers of FPGA for the use of DSP control program. The quadrature signals from the encoder board are processed in the FPGA to obtain the real position in time. The PWM block recieves the command vector sequence generated by the DSP program and generates the three-phase six IGBT switching voltage levels with the designed deadtime of $3\mu s$.

5.5.2 DSK Subsystem

The C67XX DSP Study Kit (DSK) [111] is a standalone development platform that enables the users to evaluate and develop applications for the TI C67XX DSP family. The DSK comes with a full compliment of on-board devices that suit a wide variety of application environments. On the DSK board, a DSP TMS320C6713 operating at 225MHz interfaces to the on-board peripherals through a 32-bit wide EMIF (External Memory Interface). The SDRAM, Flash and CPLD are all connected to the bus.

The DSK provides three expansion connectors that accept plug-in daughter cards, which are for memory, peripherals, and the Host Port Interface respectively. The memory connector provides access to DSP asynchronous EMIF signals to interface with memories. The peripheral connector brings out the DSP's peripheral signals, such as clocks, timers. These two connectors are used to communicate with FPGA board in this research. And thus the DSP only focuses on mathematical calculations and the control scheme. The peripheral tasks and the logical operations are implemented by FPGA. The HPI connector is a high speed interface and brings out specific control signals. It is used for communicating with the user in this research, through an added extension card and USB connection, for sending the command signals and monitoring the system parameters.

The DSP is programmed by a standard procedure, which performs in a clocked and periodic interruption service routine. The PWM period, equal to the interruption period, is set and maintained by a clock in the FPGA. The main work done by the DSP

includes, processing the measured data, estimating the position and speed signals, implementing three drive control loops, communicating with host program, all the initialization settings and the software protections.

5.6 Conclusions

One AC drive system has been designed and built in this research. Its design has been described in this chapter, including the power circuits, the analog circuits and the digital control system. The designed voltage-type power converter was presented, whose main circuit is integrated on a large PCB board, including the diode rectifier, the DC-link capacitors, the IGBT inverter, etc. The PCB tracks are designed to safely carry the currents flowing through the converter. The measurement system and the protection system were then explained. Gate drivers of the IGBTs send the control signals to the power devices. Their circuits are described in detail. A Special feature of this research is that the gate resistors are made changeable for the investigation of improvements to the sensorless control. The control algorithm works as the brain of the drive system. It is programmed through a DSP-FPGA control system. The logic coordination and the main interfacing tasks are implemented by the FPGA subsystem. DSP carries out the complicated mathematical calculations and control algorithms.

Chapter 6

Enhanced Position Estimation

The process to obtain the position signal by measuring the transient currents under PWM voltage vector excitation, has been described in Chapter 3. However the estimated saliency position angle does not represent the rotor position angle directly. As the saturation saliency position is tracked to get the position signal in this research, the disturbances caused by other saliency harmonics should be eliminated. The saturation saliency is orientated with the air-gap flux position, and thus the angle shift between the estimated position angle and the rotor position should be compensated. Other noise should also be filtered out in order to achieve acceptable position or speed signals. The schemes used to obtain the enhanced position estimation will be described in this chapter.

6.1 Harmonic Disturbance Elimination

The effectiveness of the saliency tracking methods depends on the assumption that only one single sinusoidally distributed spatial saliency is present in the motor. In this research, the leakage inductance modulation caused by the flux saturation is the dominant exploitable saliency for a surface mounted PMSM. Besides the dominant

saliency to be tracked, other anisotropic properties behave as disturbances, which may impair the estimated position and speed signals. Their effect must be eliminated or reduced.

6.1.1 Harmonics Existing in the Estimated Position Signals

When a high frequency voltage excitation is applied to the motor, which can be the injected continuous high frequency signal, or the transient excitations of the PWM voltage vectors, the saliency position residing in the motor can be detected from the measurements of the motor current responses. However, the obtained saliency position signal contains many other harmonics. The two orthogonal estimated position signals, p_α and p_β , obtained using the method described in 3.1 are shown in Fig 6.1(a). The SMPM machine is controlled at 100rpm, i.e. the stator current fundamental frequency $f_e = 5Hz$. The frequency spectrum of p_α and p_β, obtained using the MATLAB FFT routine, are shown in Fig 6.1(b).

As can be seen from Fig 6.1, the flux saturation causes the dominant saliency with a frequency of $2f_e$ due to the symmetrical structure of the rotor magnet. Other saliencies have a minor influence. Although they do not prevent the position estimation scheme from working, they can make the estimated position and speed signals inaccurate and noisy. For the surface mounted PMSM used in this research, the main harmonics appear at f_e, $4f_e$ and DC.

6.1.2 Main Methods of Compensating the Harmonic Disturbances

The harmonic disturbance in the position estimation needs to be eliminated. Several methods have been proposed to compensate or reduce their disturbing effect.

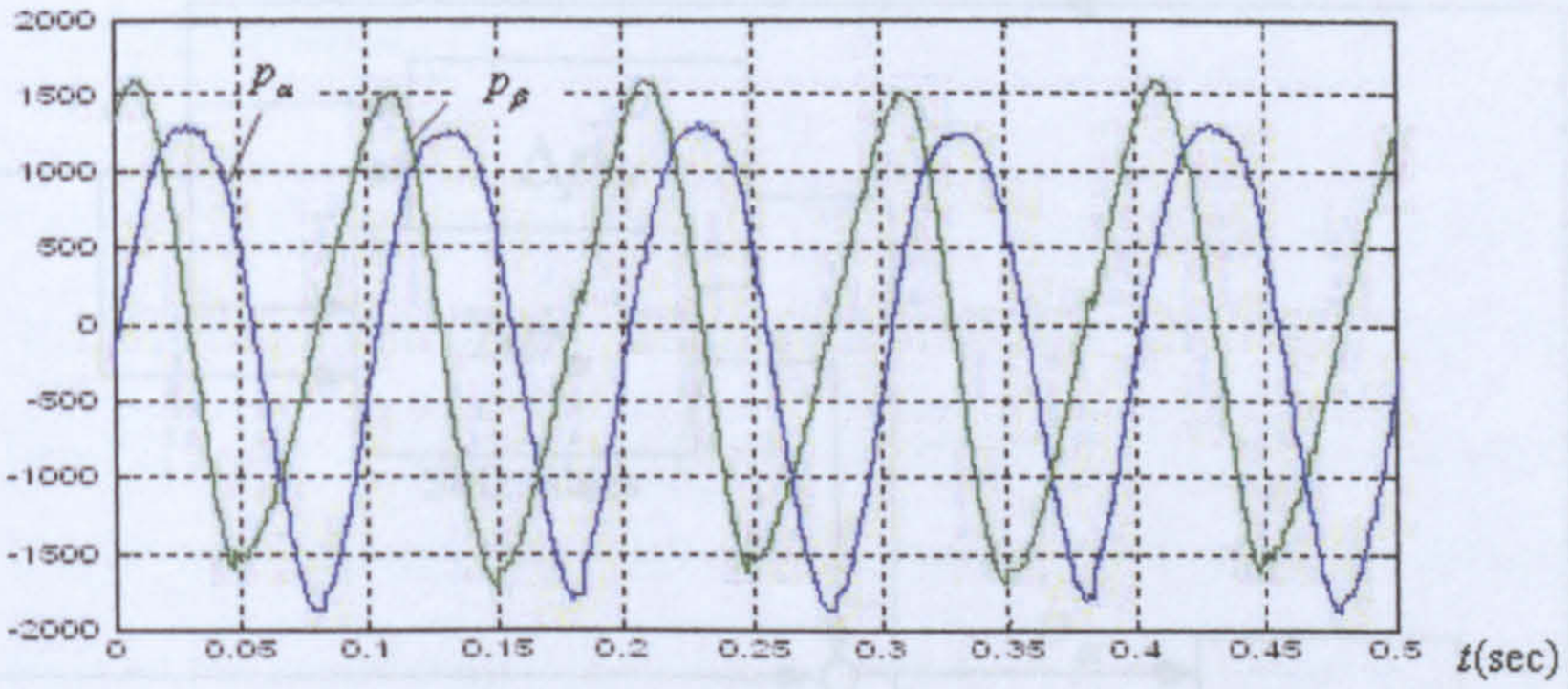

Figure 6.1: Estimated position signals from the PWM transient excitations and their frequency spectrum

6.1.2.1 Space Modulation Profiling

The space modulation profiling (SMP) technique is to characterize the general harmonic waveforms in a large look-up table [112]. It is found that the disturbance signals vary with the stator current angle and the load level, and have a very weak relationship with the speed. In this method, one fundamental rotation is discretized into a series of cells. The motor operates under different load levels in the sensored mode. The ideal position signals, p_α and p_β, can be derived from the encoder measurements and therefore the disturbance signal is calculated and stored in a two-dimensional look-up table as $\triangle\mathbf{p}(i_{sq}, \theta_r)$. For accurate profiling, the dimensions of this table should be large. Once the SMP table is established, the online compensation can be done by accessing this table with index of the estimated position angle $\hat{\theta}_r$ and the torque current i_{sq}. The obtained disturbance signals $\triangle p_{\alpha,\beta}$ are then eliminated from the estimated position signal. The process is shown in Fig 6.2.

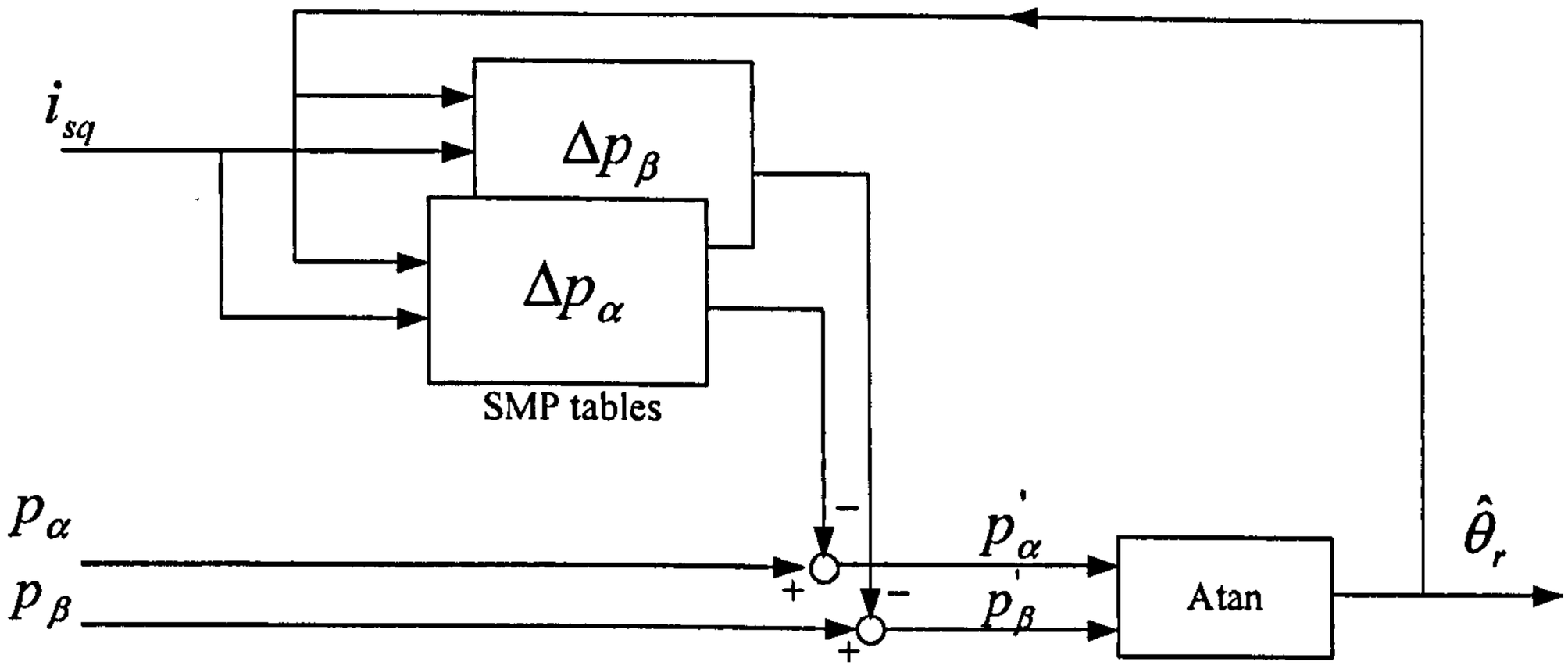

Figure 6.2: Compensation diagram by SMP

Good rotor position estimation with the SMP has been demonstrated in [68, 112]. The SMP is suitable to compensate for the disturbances appearing over a wide spectrum. However, the SMP table has to be created offline in a sensored commissioning process, operating at different individual load conditions. The amount of information that should be stored needs to be investigated for different machines. A large memory is required for storing these disturbance data.

[41] proposes an approach termed as spatial filtering, which is used to eliminate the saturation harmonics which for an induction motor are well separated from the position signal. The approach is similar, but simpler than the SMP described previously. A single lookup table is used, accessed by estimated rotor position and load level (i_{sq}). The lookup table provides the instantaneous value of the main saturation harmonic, and this is subtracted from the raw position signal to clean up the estimate. This lookup table can be commissioned using sensored control and a first order low pass filter operating the drive at various load levels. This technique is not applicable to derive the saturation saliency from other harmonics around the fundamental frequency as the case in this research.

6.1.2.2 Neural Network

[113] utilizes an artificial neural network (ANN) for removing the flux/load dependence of the position estimated by the INFORM method in an induction motor. The input to the ANN should be the load current and the output is the disturbance component. Under sensored mode the ANN is trained through the back propagation algorithm at different load levels. The training has to be done offline in a separate data processing system. By comparing the estimated position with the real rotor position angle, the weighting factors in the ANN are tuned. After training, the resultant weighting factors of the ANN are then used for the online compensation of the estimated position signals. The neural network technique makes the commissioning process much easier than that of the SMP table.

[114] proposes a structured neural network to decouple both saturation induced and intermodulation saliency components, as a feasible alternative to the random neural network in [113]. The proposed structure is based on the physical representation. There is a clear criterion for arranging the layers and neurons. Each harmonic component is estimated from its own subnetwork, which consists of organized layers particularly performing cosinusoidal/sinusoidal function, multiplications, or addition. Advantages with respect to the random neural network include the significantly reduced training time, less size and complexity, and the decoupling ability for as many harmonics as needed.

[115] proposes a structure combining an FFT and a neural network, to eliminate the saturation induced harmonic from the slotting modulation position signal to be tracked. The ANN is trained using the amplitudes and angles of the disturbance signal obtained from FFT analysis at different load levels. Only three layers and a few neurons are required. This technique also enables the separation of different harmonic components. This paper shows a reliable separation of the slotting signal at very low fundamental frequency even with high load.

6.1.2.3 Synchronous Reference Frame Filter

The saliency position signal obtained from the PM machine with more than a single sinusoidally distributed saliency can be represented through the Fourier series as[10]:

$$p_{(\alpha,\beta)} = \sum_k p_{(\alpha,\beta)k} e^{j(k\omega_r t + \theta_k)} \tag{6.1}$$

where $p_{(\alpha,\beta)}$ is the total saliency position signal, $k = ..., -2, -1, 0, 1, 2, ...$, is the harmonic number of the saliency, $p(\alpha,\beta)_k$ is the magnitude of the kth harmonic saliency signal, θ_k is the initial phase angle of the kth harmonic component. In the PMSM, the stator current fundamental frequency f_e is equal to the rotor operating frequency $f_r = \frac{\omega_r}{2\pi}$. For $k = 2$, it is the saliency signal caused by the magnetic saturation, which is to be tracked in this research.

The synchronous filter is used to extract a harmonic at a specific frequency using a low pass filter implemented in the reference frame rotating synchronously with that harmonic signal[10]. The block diagram of the synchronous filter which extracts the k_ith harmonic signal is shown in Fig 6.3. It firstly transforms the original estimated position signal onto the synchronous reference frame rotating at $k_i\omega_r$, which results in

$$p^{k_i}_{(\alpha.\beta)} = p_{(\alpha,\beta)k_i} e^{j\theta_{k_i}} + \sum_{k \neq k_i} p_{(\alpha,\beta)k} e^{j((k-k_i)\omega_r t + \theta_k)} \tag{6.2}$$

The DC components in $p^{k_i}_{(\alpha,\beta)}$ is retained by the low-pass filters, and these contain the information of the k_ith harmonic existing in the original position signals $p_{(\alpha,\beta)}$. This DC component can then be transformed back to its original waveform in the static reference frame by a reverse transformation. Thus $p_{(\alpha,\beta)k_i} e^{j(k_i\omega_r t + \theta_{k_i})}$ is separated out from the estimated position signals.

Using the synchronous filters, the unwanted harmonic components in the estimated position signals can be extracted separately. Each synchronous filter branch behaves

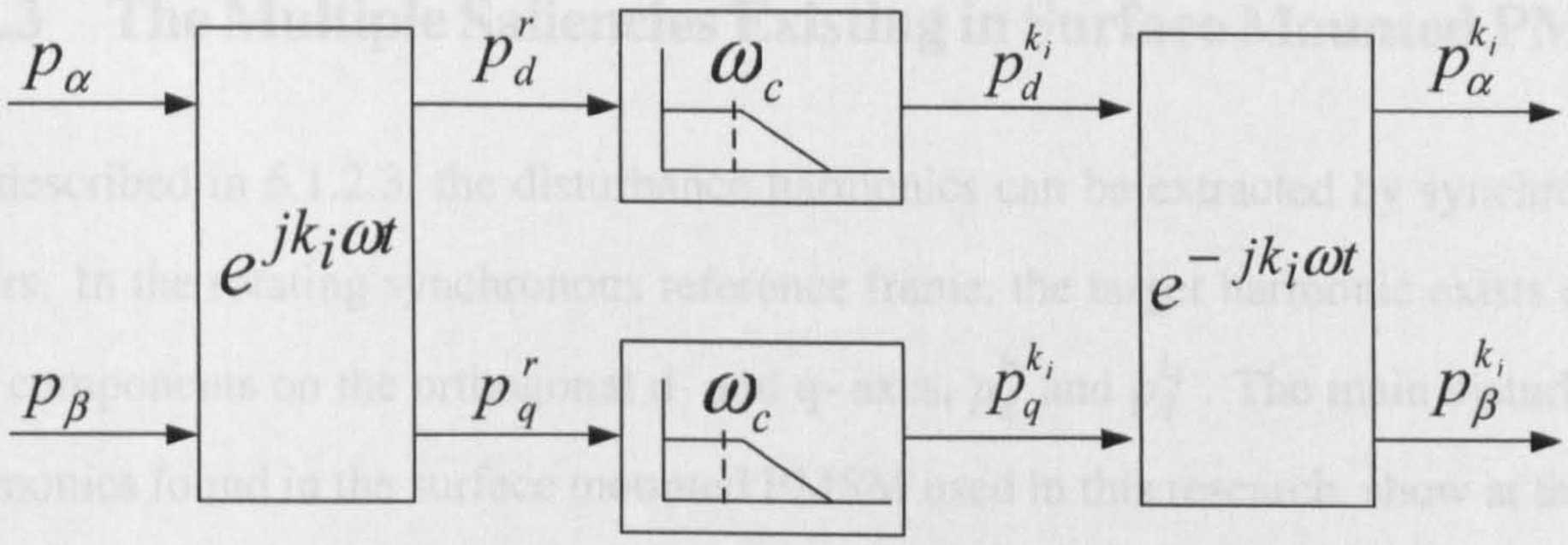

(a)

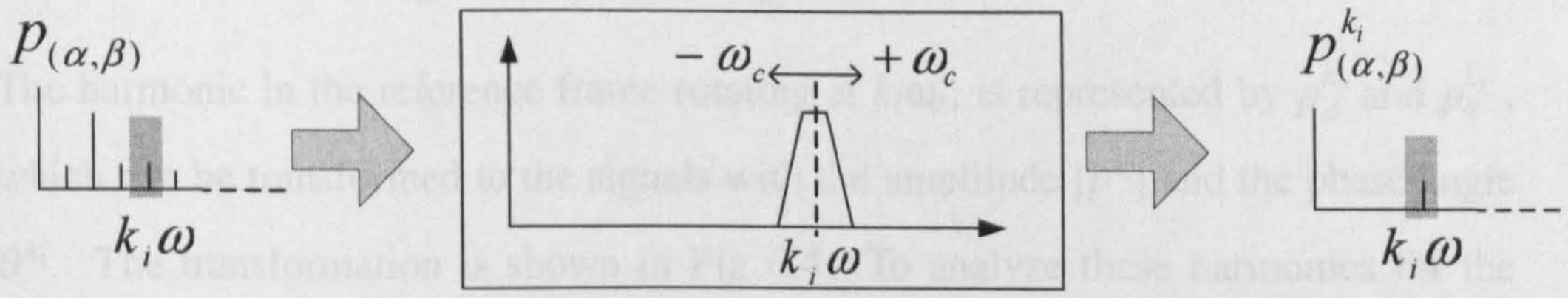

(b)

Figure 6.3: Structure (a) and filtering effect (b) of the synchronous filter branch

like a bandpass filter with its passband centred at its rotating transformation frequency $k_i\omega_r$, as shown in Fig 6.3(b). The bandwidth of the equivalent bandpass filter is determined by the bandwidth of the low pass filter within the synchronous filter branch. This can be explained by the transfer function of the kth filtering branch as

$$Y(s) = \left(I(s + jk_i\omega_r) \cdot \frac{\omega_c}{s + \omega_c} \right) |_{s=s-jk_i\omega_r} = I(s) \cdot \frac{\omega_c}{(s - jk_i\omega_r) + \omega_c} \tag{6.3}$$

where $I(s)$, $Y(s)$ are the input and output of the synchronous filter branch, ω_c is the cutoff frequency of the lowpass filter.

To achieve a position signal without harmonic disturbance, the unwanted harmonics are extracted using the synchronous filters and then removed from the estimated position signals. This filtering process is carried out online. It does not introduce a time delay. The resultant position signals are always synchronous with the original estimated position signals.

6.1.3 The Multiple Saliencies Existing in Surface Mounted PMSM

As described in 6.1.2.3, the disturbance harmonics can be extracted by synchronous filters. In the rotating synchronous reference frame, the target harmonic exists as the DC components on the orthogonal d- and q- axes, $p_d^{k_i}$ and $p_q^{k_i}$. The main disturbance harmonics found in the surface mounted PMSM used in this research, show at the frequencies of DC, f_e and $4f_e$. These harmonics can be extracted separately at different load levels and their origins will be investigated.

The harmonic in the reference frame rotating at $k_i\omega_r$, is represented by $p_d^{k_i}$ and $p_q^{k_i}$, which can be transformed to the signals with the amplitude $|p^{k_i}|$ and the phase angle θ^{k_i}. The transformation is shown in Fig 6.4. To analyze these harmonics for the machine used here, the surface mounted PMSM was operated under different load conditions. The values of $|p^{k_i}|$ and θ^{k_i} are recorded when the torque current i_{sq} varies between $-7A$ and $+7A$.

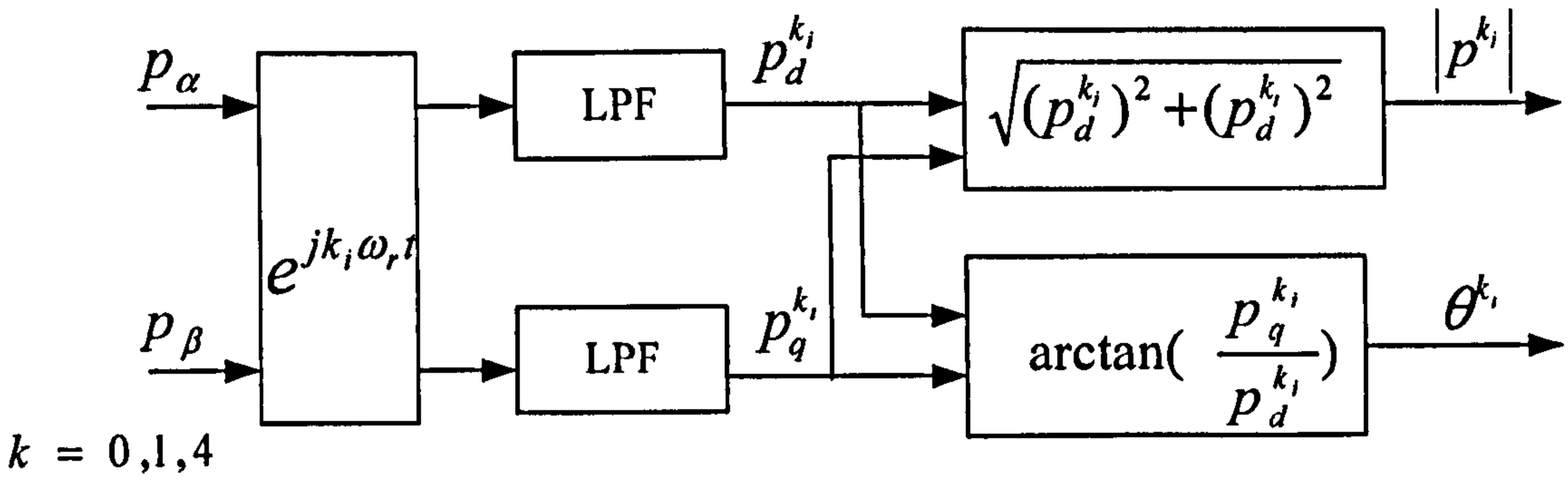

Figure 6.4: Synchronous branch for analyzing the harmonic vectors

The extracted DC harmonic components are shown in Fig 6.5. As i_{sq} changes, the DC harmonic amplitude $|p^0|$ and phase angle θ^0 show symmetrical and linear distribution. Its spatial angle follows that of the the air-gap flux instead of the rotor position. Its magnitude changes linearly and proportional to the torque current i_{sq}.

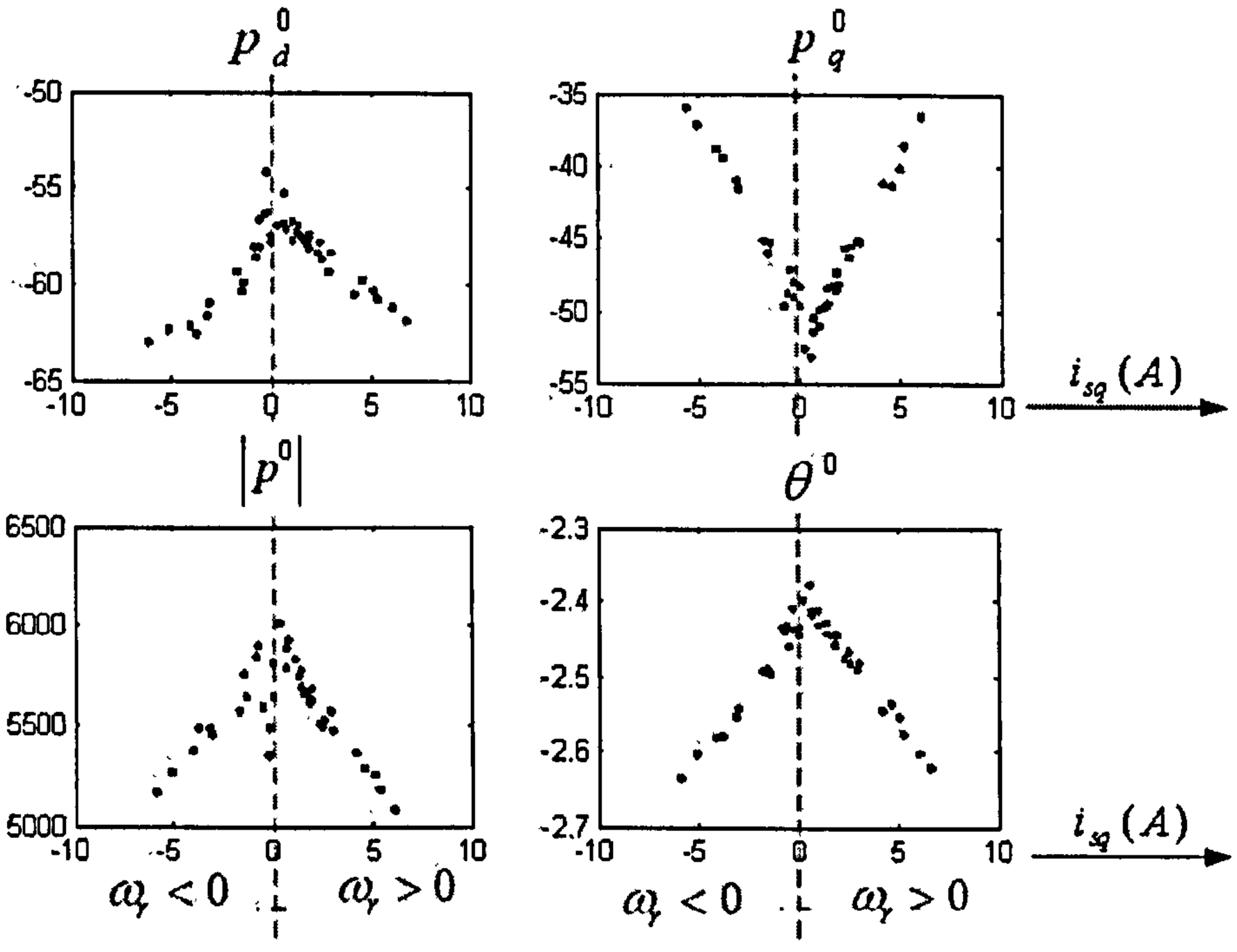

Figure 6.5: Experimental measurements of the DC harmonic component changing with the load current i_{sq}

One cause of the DC component may be unbalance in the di/dt measurements due to the imbalanced sensors or signal processing circuits. It is not the main reason in this case because of the dependence on the torque current. Another possible reason for the DC harmonic in Fig 6.5, is the intermodulation from two different saturation effects. As is known, the rotor magnet establishes a flux density of approximately sinusoidal distribution in the air gap with its maximum in the rotor d-axis direction. Under no load, that is $i_{sq} = 0$, the stator iron directs and concentrates this flux producing stator tooth saturation in the d-axis direction, as shown in Fig 6.6. This effect produces an increased equivalent air-gap length for the main d-axis flux resulting in a reduction of the main flux inductance on the d-axis. Due to the orthogonal position between the stator windings and their magnetic axes, this main flux also affects the stator leakage flux path, causing a spatial modulation of the leakage inductance. The reduction of the permeance of the leakage flux path causes a reduction of the q-axis

leakage inductance. These two saturation effects work in opposite directions. Thus the magnetizing inductance variation from the saturation effect is dominant, which is the saliency tracked for position estimation in this research.

When the motor is loaded, that is i_{sq} increases positively or negatively, the q-axis stator current creates a flux termed as $L_q i_{sq}$. A shift of the air-gap flux distribution towards the q-axis appears. The maximum flux density will not be aligned with the d-axis, which makes the air-gap flux direction dependent on the load current i_{sq}. Both of these two kinds of saturation effects are influenced by the torque current. As these two saturation effects possess the same frequency and opposite directions, their possible interaction effect may give rise to the harmonics at DC and $4f_e$.

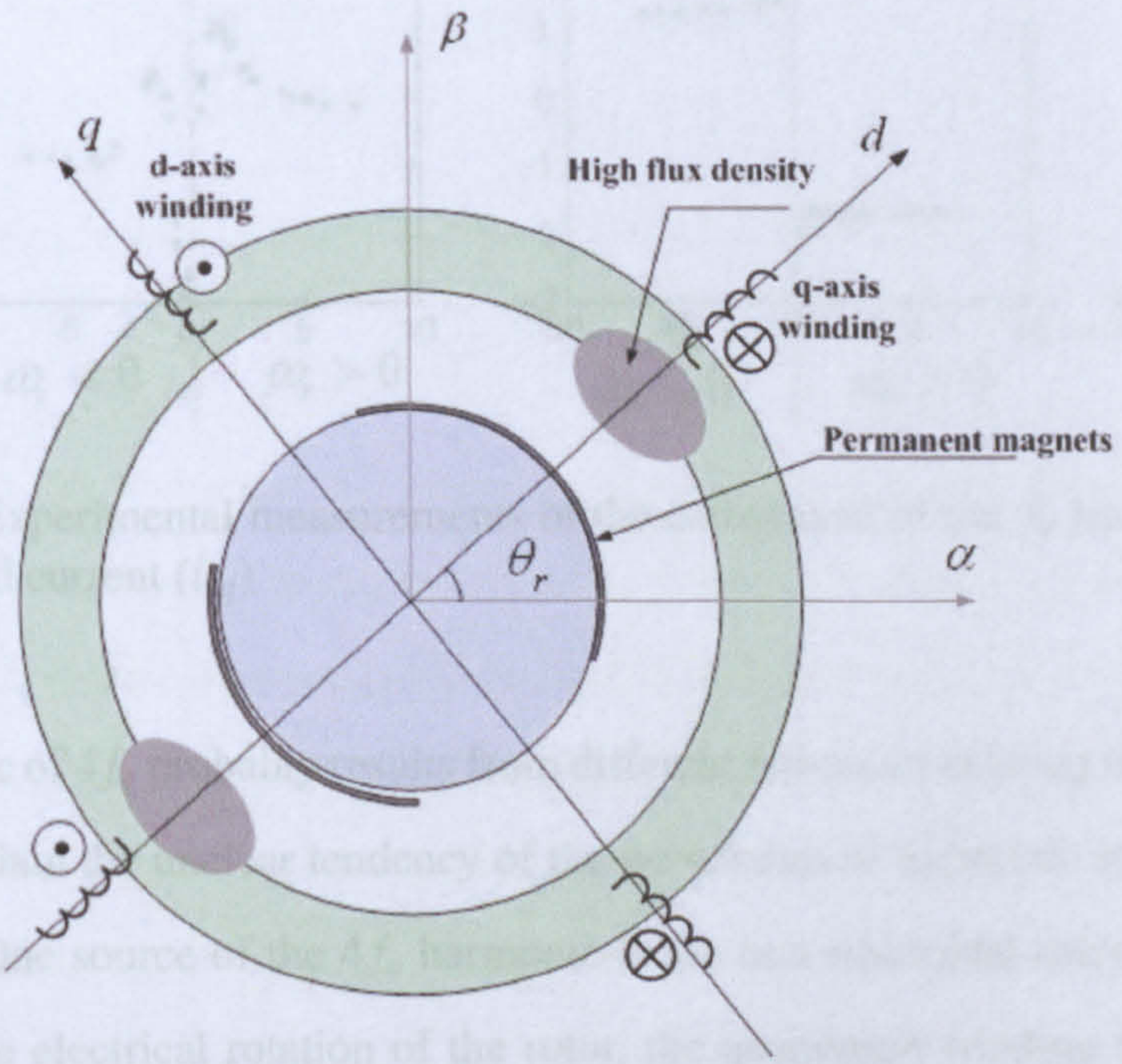

Figure 6.6: Saturation effects in SMPM machine with concentrated d-q windings

The harmonic with the fundamental frequency f_e is generated by the physical asymmetries in the AC motor, which can be the engineering imbalance of the stator windings, the rotor magnetics, or any kind of non-smooth design. Because it comes from the physical construction of the machine, the fundamental harmonic vector should

not be influenced by the torque current. This is verified by the experimental results shown in Fig 6.7, which shows that the magnitude $|p^1|$ and phase angle θ^1 have little variation with load except the direction.

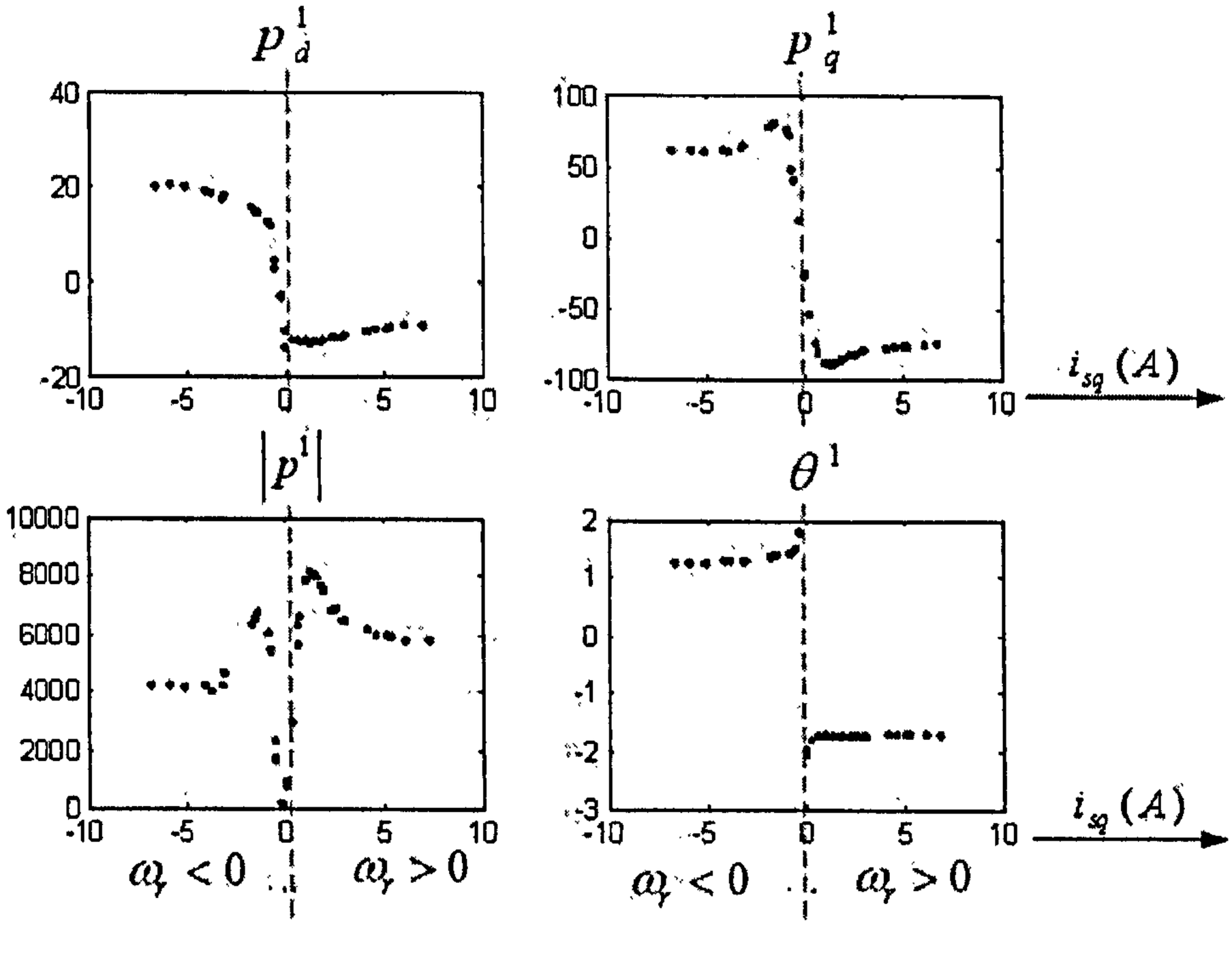

Figure 6.7: Experimental measurements of the component of the f_e harmonic distortion with load current (i_{sq})

The harmonic of $4f_e$ probably results from different saliencies existing in the machine. This can explain the unclear tendency of the waveforms of harmonic at $4f_e$ as shown in Fig 6.8. One source of the $4f_e$ harmonic is the non-sinusoidal rotor flux distribution. For one electrical rotation of the rotor, the quadrature winding locates at four quadrature positions as shown in Fig 6.6. The leakage flux caused by the winding currents, if not ideally sinusoidally distributed, can give rise to a saliency of $4f_e$. This saliency is not influenced by the load level. Additionally, as with the DC harmonic, it may arise from the intermodulation of two opposite saturation effects.

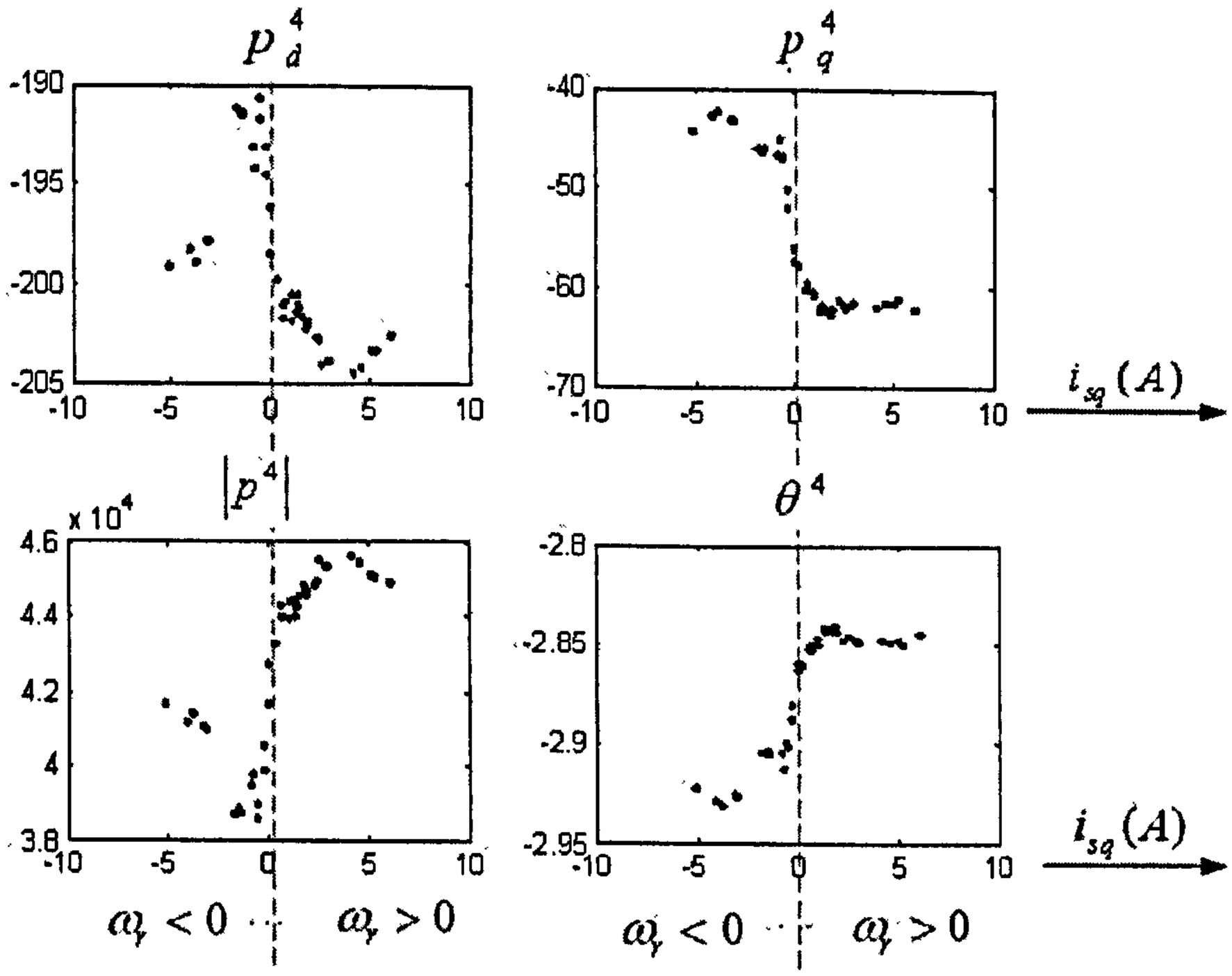

Figure 6.8: Experimental measurements of the component of the $4f_e$ harmonic distortion with load current i_{sq}

The saliencies existing in the AC motor are complicated and may vary from motor to motor. They are not easy to explain clearly. Using a frequency spectrum to define the harmonics in the estimated position signals and removing separately the influential harmonics, is an easy and effective way to improve the quality of the estimated position signals. This improved position signal can be used for high performance sensorless control system.

6.1.4 Adaptive Disturbance Identifier

Although the synchronous filter theoretically works well to extract the target harmonics, its effect is limited in the low frequency range. As discussed in 6.1.2.3, each synchronous filter behaves like a bandpass filter centred at its target frequency with the bandwidth of the low pass filter. When the machine is running at very low speed,

the disturbing harmonics and the saturation saliency to be tracked locate very close to each other in the frequency spectrum. The passband of these synchronous filters can not be too narrow because their induced time delay should be acceptable. This causes difficulty for separating and filtering these harmonics using synchronous filters alone in the low speed range.

In this research a small look-up table is utilized to solve the problem of the synchronous filter at low speed. Because these harmonic disturbances have weak dependence on the rotor speed, if the torque current is constant, each harmonic vector should have constant magnitude and phase angle in the reference frame rotating at its frequency. Figure 6.9 shows an adaptive disturbance identifier scheme, combining the synchronous filters with the look-up table. When the motor speed is above the threshold value ($20rpm$ in this research), under different load levels, the synchronous filters work as normal. The measured DC components of the harmonic signals in each synchronous reference frame, p_d^{ki} and p_q^{ki}, are recorded in the table with index of the torque current i_{sq}. When the speed is lower than the threshold value, these data can be accessed using the torque current at that time, and the data are used to rebuild the harmonic waveforms for the disturbance compensation. This avoids the filtering difficulty due to the filter bandwidth in the low speed range. Depending on the speed, the switch $S_{1k}(k = 0,1,4)$ decides if the harmonic signals should be extracted from the synchronous filter or from the value stored in the memory. At higher speed, the synchronous filters work normally to extract the harmonics and compensate the disturbances. The switch $S_{2k}(k = 0,1,4)$ controls the learning process.

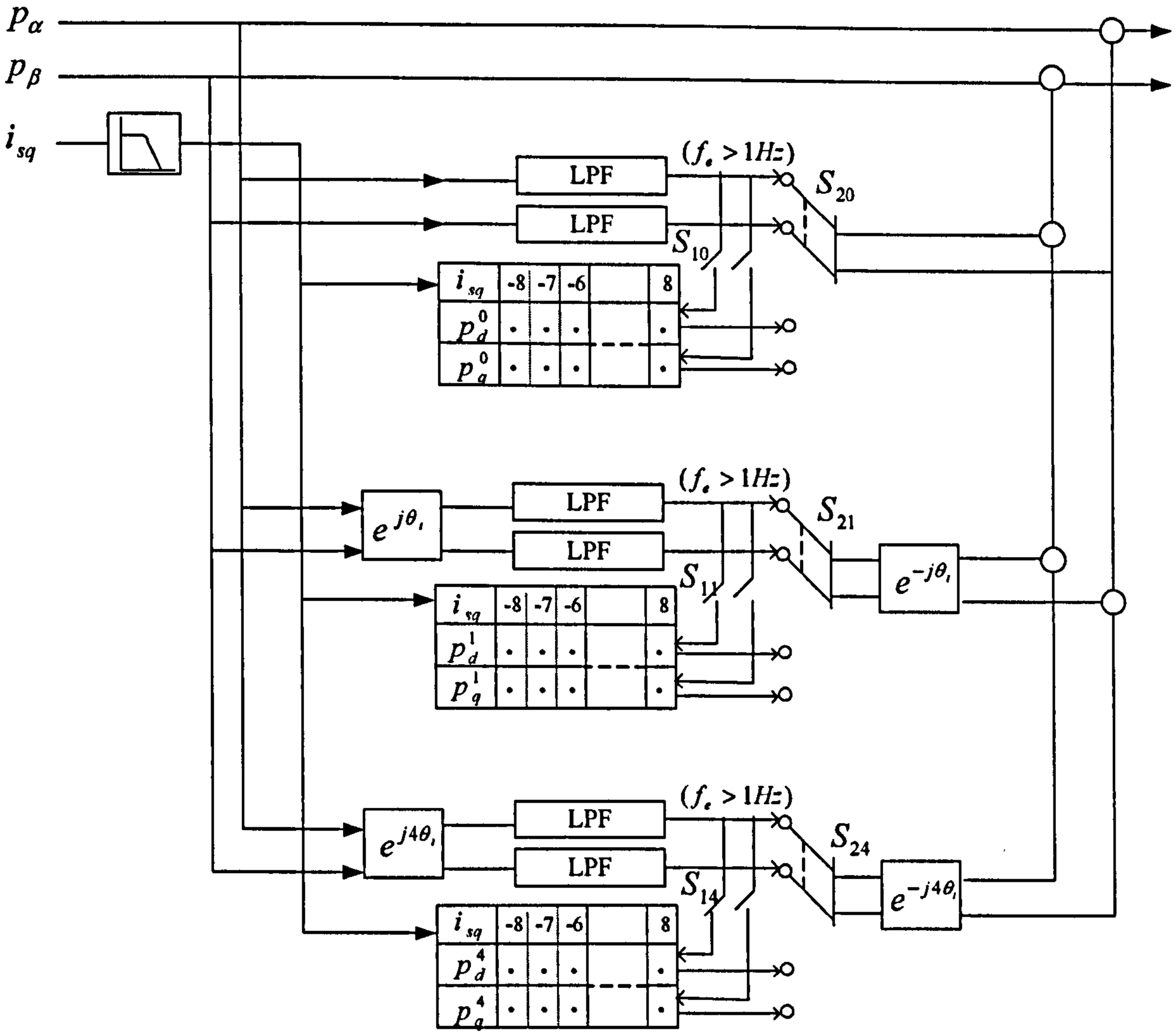

Figure 6.9: Structure of the adaptive disturbance identifier for removing DC, f_e and $4f_e$ harmonics

6.1.5 Experimental Results for the ADI

The performance of the proposed ADI for eliminating the harmonic disturbances from the estimated position signals is satisfactory. Results at two different operating frequencies are shown. The estimated position signals before and after the ADI is used are shown in Fig 6.10, when the machine is running at 5rpm, i.e. the stator current fundamental frequency f_e is 0.25Hz. The upper plots in Fig 6.10 shows the waveforms

of p_α and p_β , before and after compensating the harmonics of DC, f_e and $4f_e$. The lower plots show their frequency spectra. It can be seen that these harmonics are much reduced. At this frequency, the harmonic information is obtained from using the look up table.

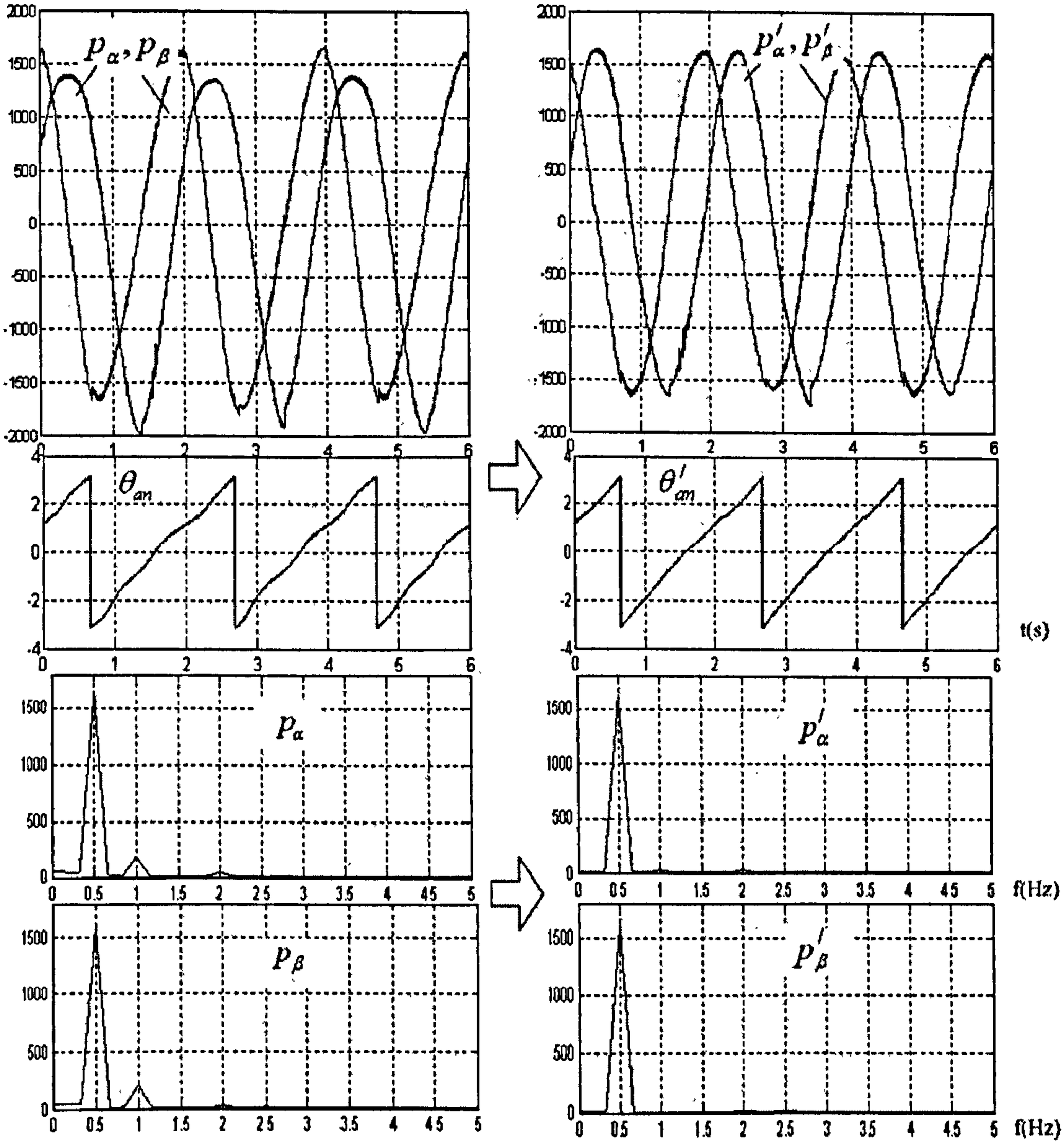

(a) Estimated position signals before ADI (b) Estimated position signals after ADI

Figure 6.10: Elimination of the main harmonics by the ADI with $f_e = 0.5Hz$

Similar experimental results at 100rpm, that is $f_e = 5Hz$, are shown in Fig 6.11. The estimated position signals before and after the disturbance compensation are com-

pared. The effectiveness of the ADI can be seen. At this frequency, the harmonic components are extracted online by the synchronous filters.

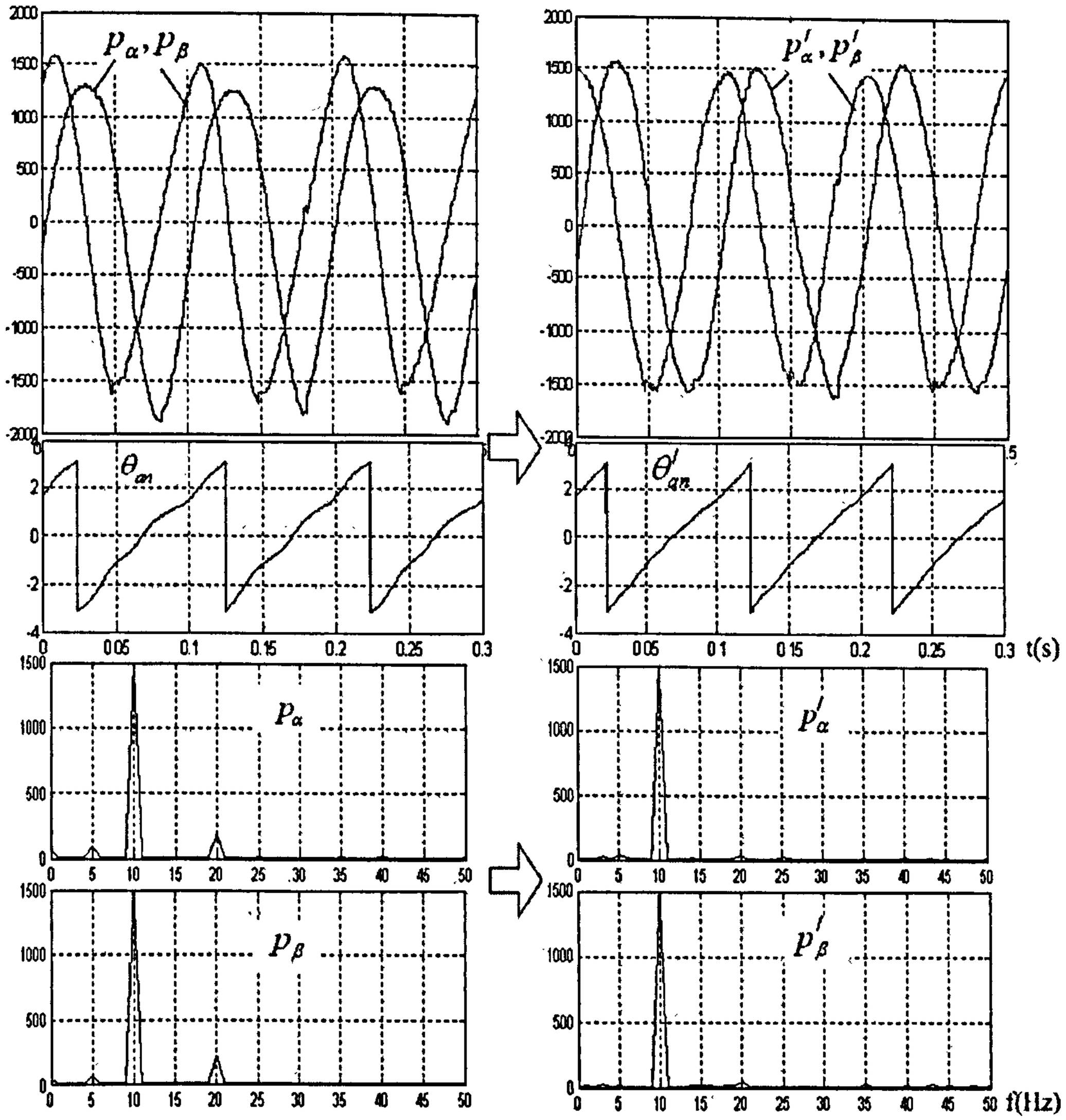

(a) Estimated position signals before ADI (b) Estimated position signals after ADI

Figure 6.11: Elimination of the main harmonics by the ADI with $f_e = 10Hz$

The memory required by the ADI scheme is much less than other compensation schemes of [68][41], because only the DC components are required for each harmonic at any load level. The look-up tables can be updated during normal operation. However the compensation will not be exact under transient conditions.

6.2 Position Phase Shift Compensation

The saturation saliency is oriented with the air-gap flux position, instead of the rotor position. The current in the q-axis stator windings creates an additional flux, which deviates the air-gap flux distribution towards the q-axis. The saturation saliency is misaligned from the rotor direction indicated by the d-axis. To obtain the actual rotor position, this angular difference should be compensated. The compensation method used in this research is realized by a look up table. This table is built up through a pre-commissioning process with sensored control and is accessed by the torque current i_{sq}. This commissioning process records the angle difference between the measured rotor position and the estimated saliency position under different load levels. The resulting curves commissioned at different speeds are shown in Fig 6.12. The phase shift is only influenced by the torque current, not the operating speed, as expected.

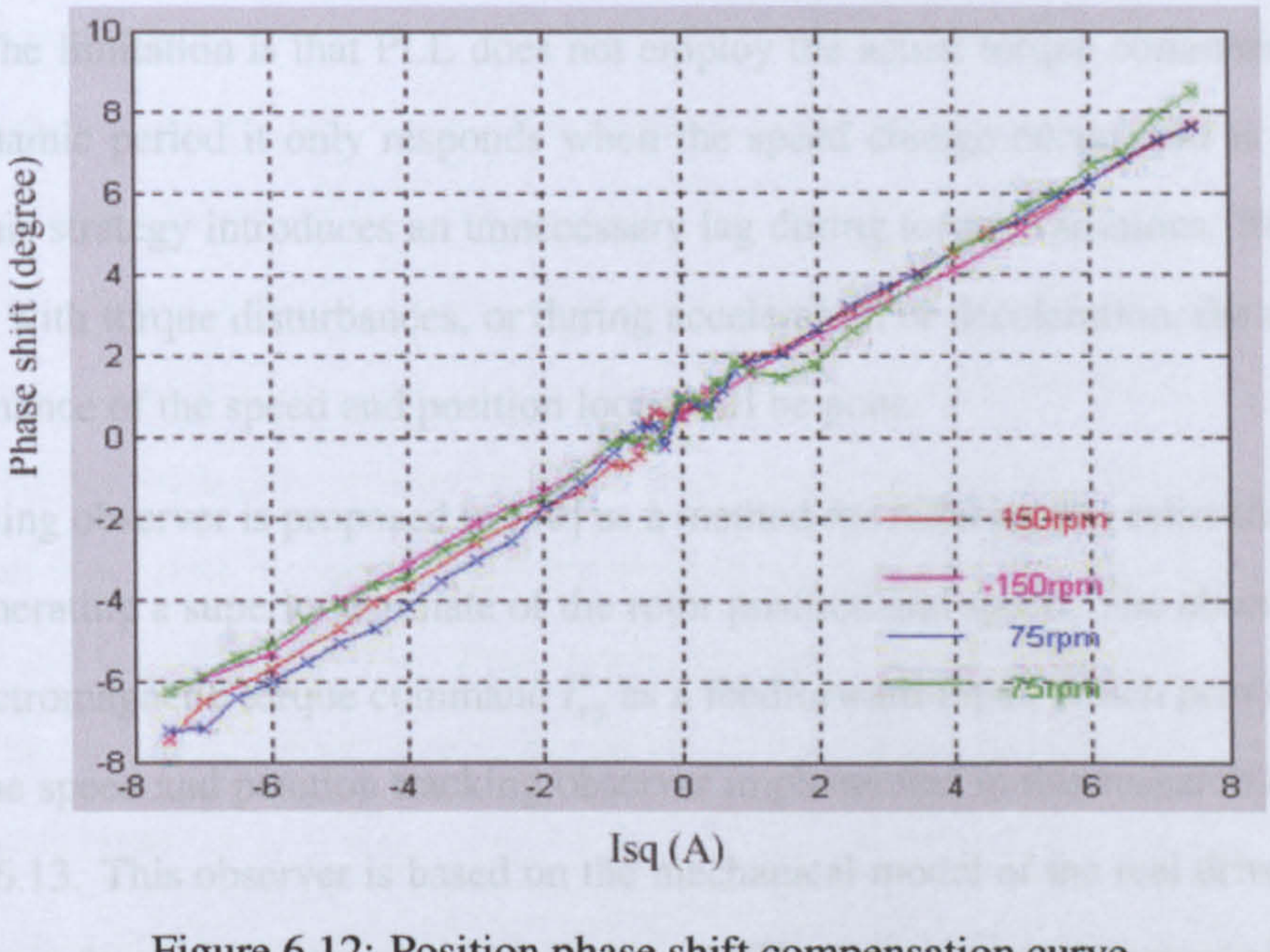

Figure 6.12: Position phase shift compensation curve

6.3 Mechanical Observer

Besides the harmonics appearing at specific frequencies, some high frequency disturbance also exist in the estimated position signals. These mainly come from the random noise and other high order harmonics. These noise components have small magnitudes compared with those of the saliency signals. However, because the speed signal is derived from the differentiation of the position signal, the high frequency noise will be amplified in this process due to their high frequency property and will appear on the estimated speed.

Filtering of the estimated position signal is not an acceptable ripple reduction solution, because the lag associated with the filter can degrade the closed-loop performance. The phase shift caused by the filter will make the estimated position signals unacceptable to use as feedback. The strategy of the phase-locked loop (PLL) is proposed in [68]. The limitation is that PLL does not employ the actual torque command and in the dynamic period it only responds when the speed change occurs and is deleted. Thus this strategy introduces an unnecessary lag during torque variations. For applications with torque disturbances, or during acceleration or deceleration, the dynamic performance of the speed and position loops will be poor.

A tracking observer is proposed in [10] as a method for reducing the estimation noise and generating a superior estimate of the rotor position and speed. The observer uses the electromagnetic torque command i_{sq}^* as a feedforward input, which provides zero lag. The speed and position tracking observer implemented in this research is shown in Fig 6.13. This observer is based on the mechanical model of the real drive system and thus referred to as "mechanical observer". The torque current command i_{sq}^* acts as the feedforward input to the observer. The original estimated position signals, p_α and p_β , obtained from the saliency tracking scheme are fed to the observer as the command input. The rotor position signal derived by this observer $\hat{\theta}_r$ is fed back to be compared with the command input, making it a closed-loop observer. The phase error

is obtained from the cross-product between the input estimated position signals, p_α and p_β , and the observer output position signals, p'_α and p'_β . The gains k_{op}, k_{oi}, and k_{od} determine how rapidly the closed-loop observer will converge to the real system.

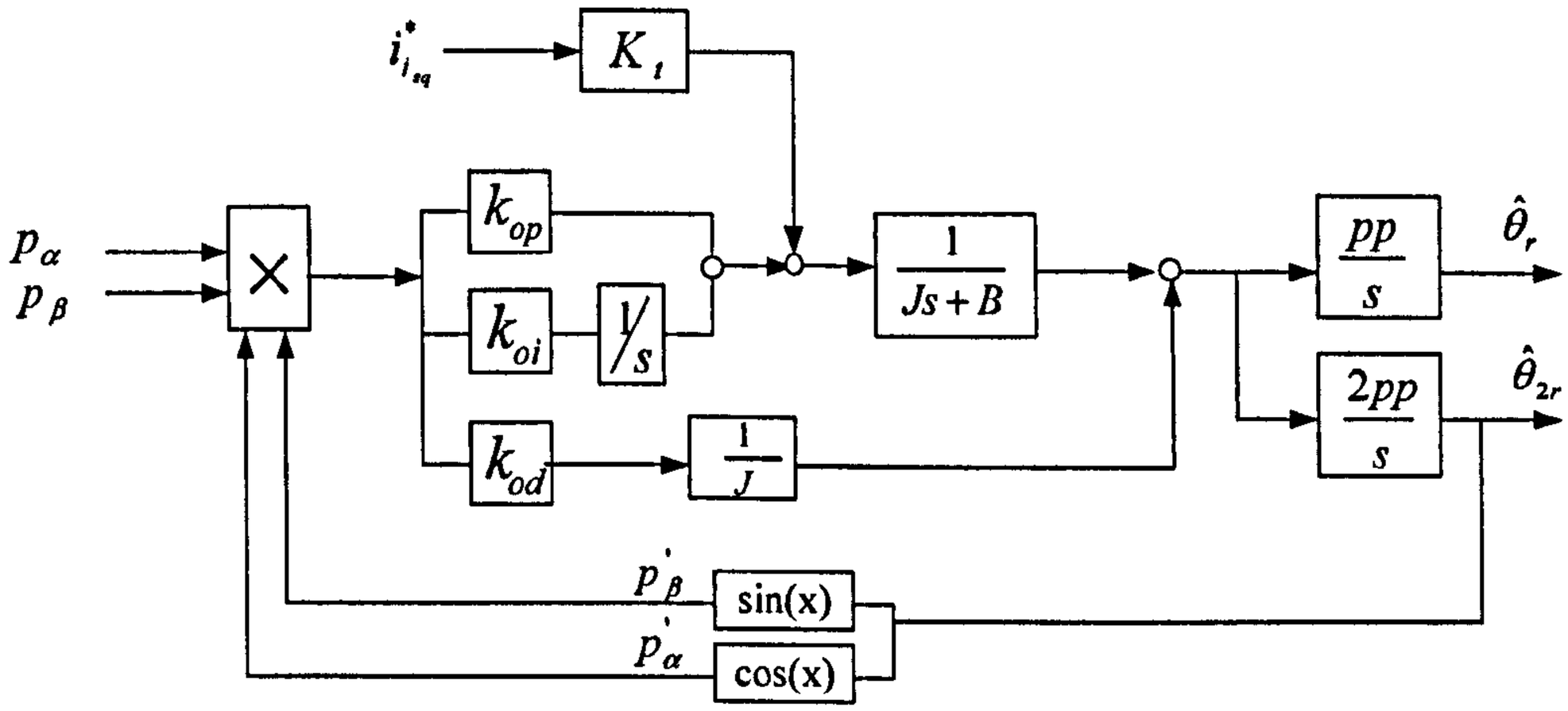

Figure 6.13: Diagram of the mechanical observer

The mechanical observer can be designed independently from the other parts of the drive system[116]. If there is significant measurement noise in the estimated position signals, the parameters of the observer controller should be kept low to avoid amplifying the noise, which also limits the observer response time. However one important design consideration is that, in order to provide acceptable feedback the observer should be fast enough compared with the dynamics of the physical system. One rule of thumb that exists is that the observer should converge 5 to 10 times faster than the closed-loop system does[117]. When tuning the observer controller, the trade-off between the dynamic performance of the observer and the amount of noise suppression is the main issue.

In this research, the mechanical observer is designed to have a bandwidth of 36Hz, providing both acceptable position and speed estimation and satisfactory dynamic response. Using the method of root-locus, the PID controller of the mechanical observer as shown in Fig 6.13 is designed as:

$$G_c(s) = 7.57 \times 10^3 \times \frac{(1+0.033s)(1+0.017s)}{s} \tag{6.4}$$

Thus the parameters in Fig 6.13 are:

$k_{op} = 378.5$, $k_{oi} = 7.57 \times 10^3$, $k_{0d} = 4.247$

The experimental results in Fig 6.14 and Fig 6.15 show the output of the mechanical observer, when the PMSM is controlled at 10rpm and 100rpm respectively. It can be seen that the position signals obtained by the mechanical observer are free from the high frequency disturbances. The estimated speed signal $\hat{\omega}_r$ is acceptable at both speed range.

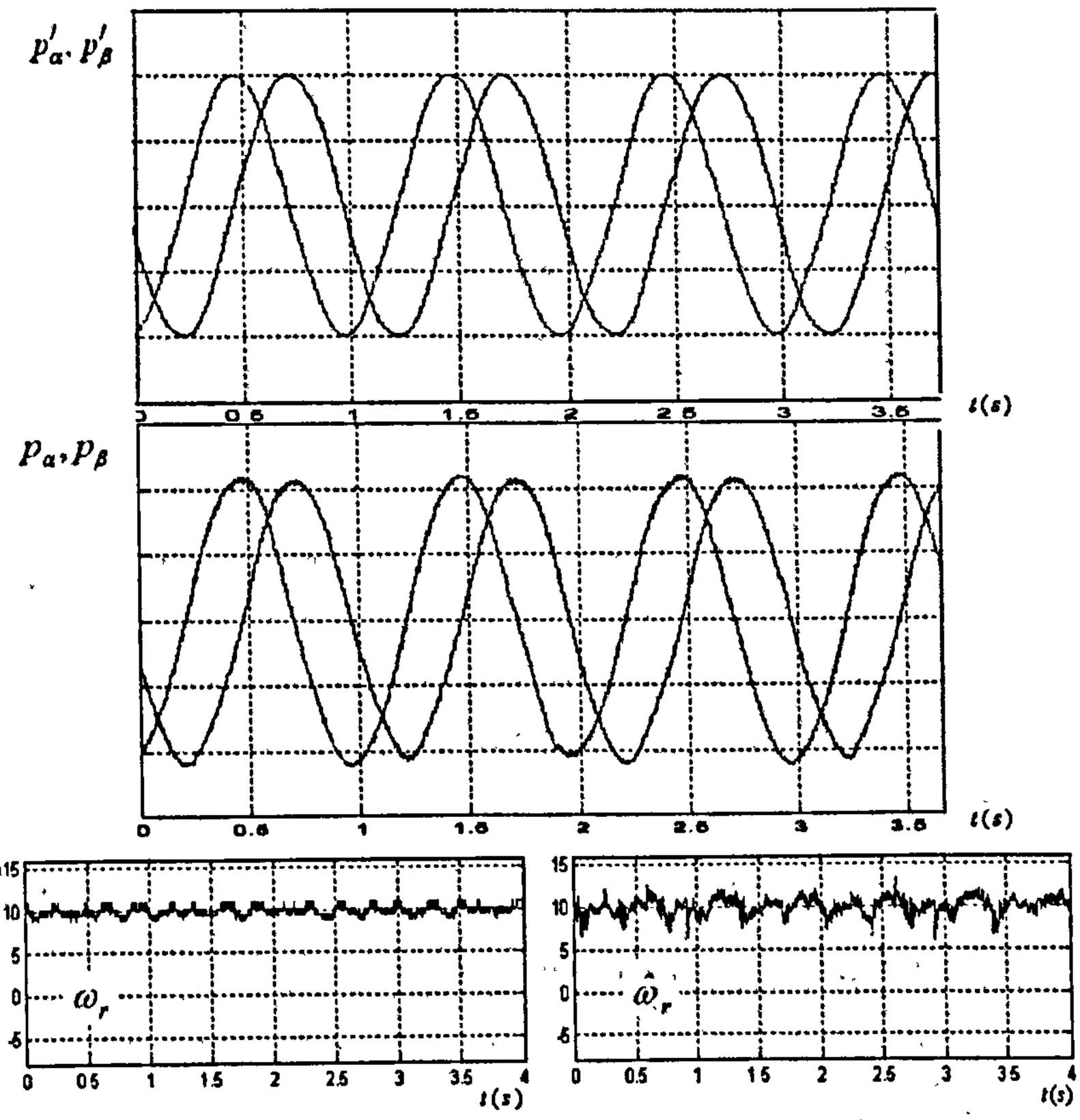

Figure 6.14: Experimental outputs from the mechanical observer at 10rpm

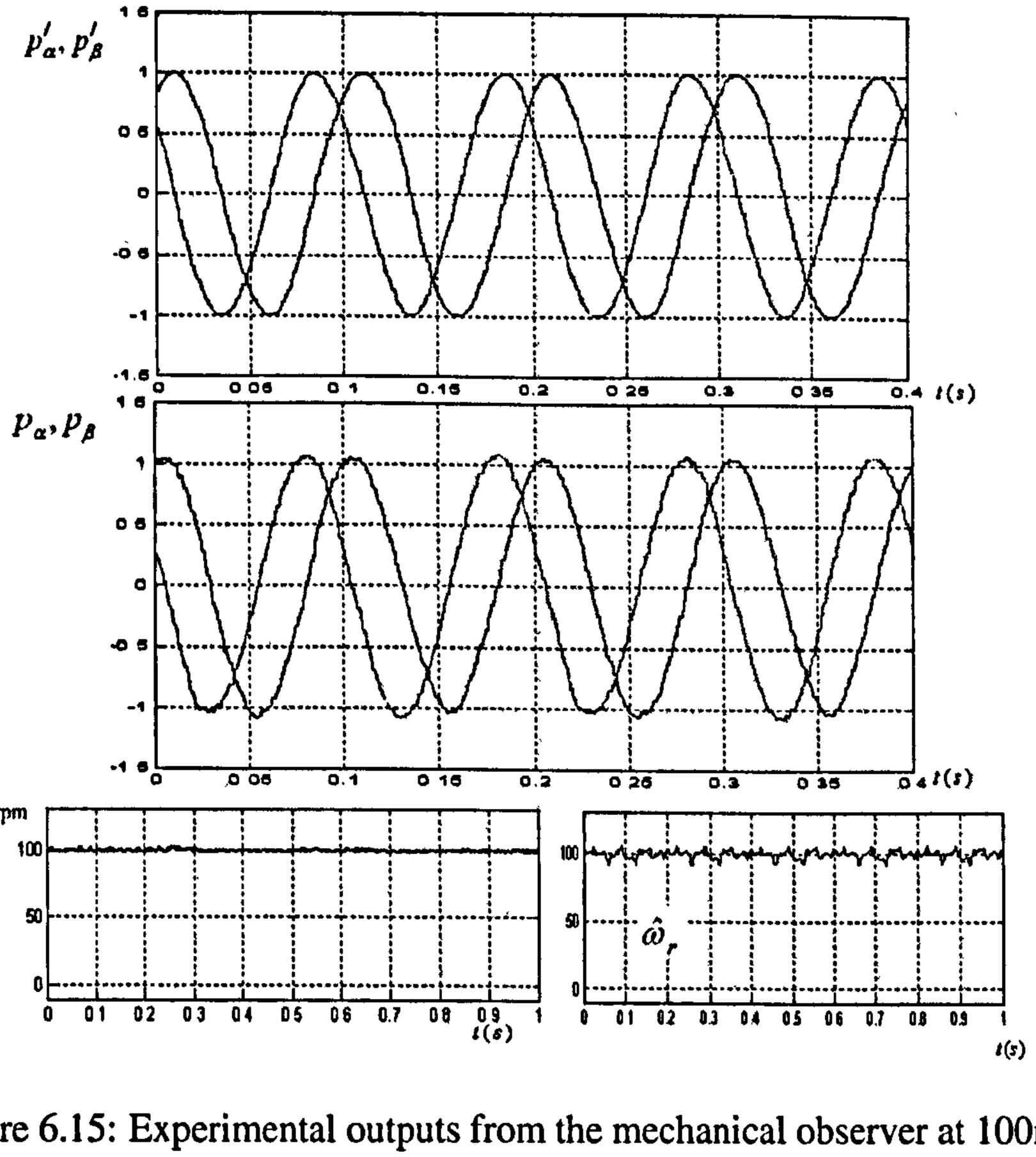

Figure 6.15: Experimental outputs from the mechanical observer at 100rpm

6.4 Conclusion

The estimated saliency position signal needs to be enhanced for sensorless control. In this chapter schemes have been introduced to improve the position signals estimated from the saturation saliency tracking. The disturbances caused by other harmonic saliencies appear as a series of components rotating at the frequencies at kf_e. An Adaptive Disturbance Identifier, which combines a group of synchronous filters with a small look-up table, is used to eliminate the harmonic disturbances. When the motor is running above a threshold speed, the targeted harmonics can be extracted by the synchronous filters and then compensated in the estimated position signals. The harmonic information is also stored in the look-up table, which is used when the motor

is running below the threshold speed. Compared with other disturbance elimination methods, the ADI scheme shows advantages, such as low memory requirement, easy pre-commissioning process, identification of the harmonics, and online memory updating ability.

The phase error between the air-gap flux position and the rotor position is compensated online by a look up table. The table is build up during a commissioning process. After the harmonic disturbance elimination and the phase error compensation, a tracking observer based on the motor mechanical model is developed. The mechanical observer is a good solution to reduce the random noise in the estimated position signals, and provides the improved position and speed signals for the high performance sensorless control system.

Chapter 7

Closed-loop Sensorless Position and Speed Control

In this chapter, the position estimation scheme only using the fundamental PWM excitation as explained in Chapter 3 and the techniques to improve the position and speed estimated signals as detailed in Chapter 6, are implemented on the experimental rig described in Chapter 5, in order to achieve high performance full sensorless control of a surface mounted PMSM. The design procedure of a cascaded control system will be described in this chapter. Then the full sensorless position control and speed control are investigated.

7.1 Overall Structure

The overall structure of both the control system and the power converter is shown in Fig 7.1.

The motor parameters have been described in 5.4. The power converter includes the rectifier, the DC link capacitors, the IGBT inverter, the measurement circuits and the protection circuits as described in Chapter 5. The control schemes are realized through

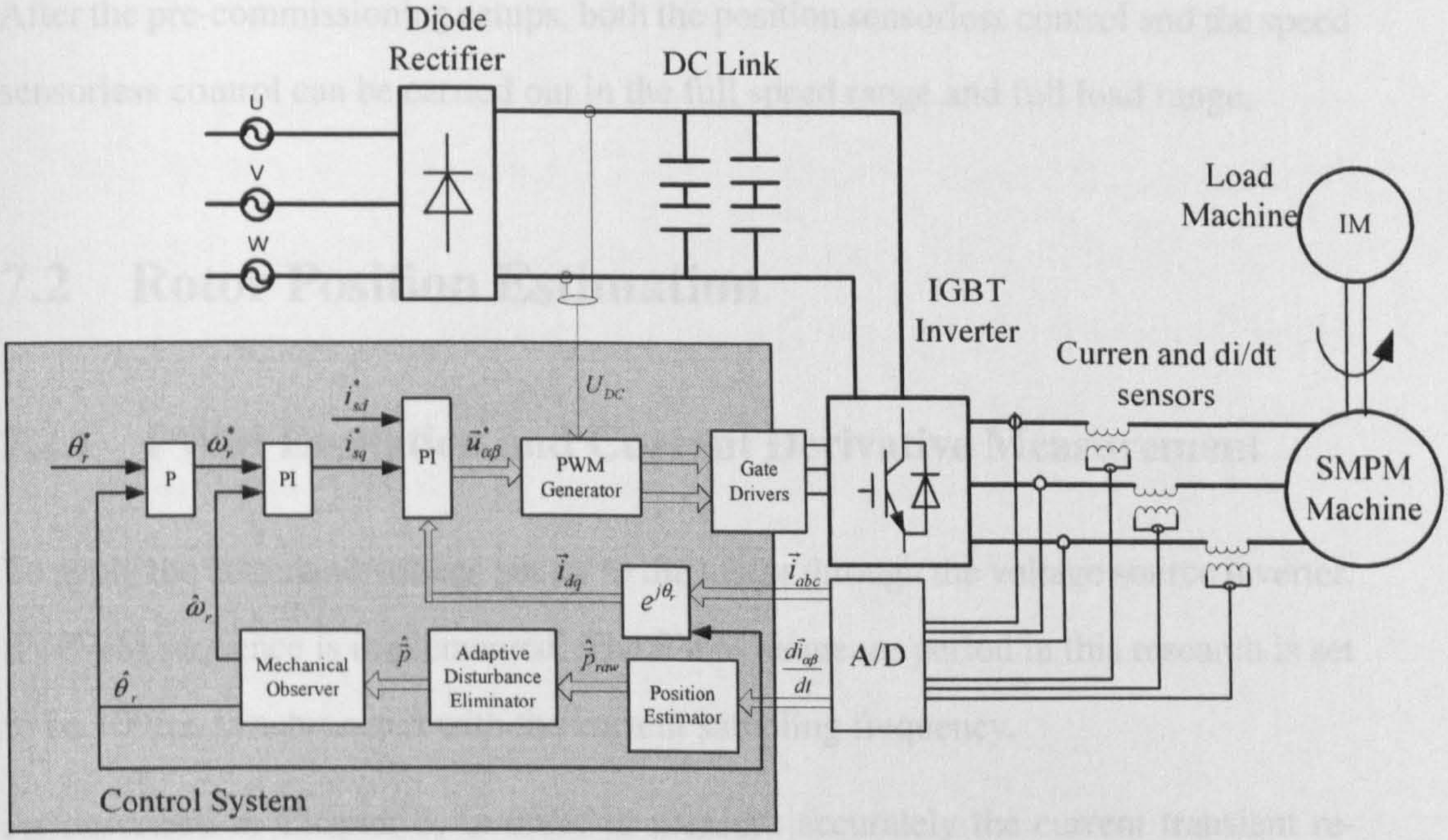

Figure 7.1: overall structure of the sensorless vector control system

a DSP-FPGA coordinated platform, where the DSP system performs the main part of the controlling algorithm and the FPGA system deals with almost all of the logical operations. A human plant interface (HPI) board is used for the communication between the converter and the PC for the data acquisition and program loading.

In a sensorless control system, the speed and position signals are obtained by the position estimation schemes. One optical encoder is installed for control of the loading system. All the signals being measured include the three-phase currents for the vector control, the three-phase current derivatives for the position estimation, and the DC link voltage for PWM signal generation. The position signals are estimated from the current derivative signal using the scheme introduced in Chapter 3. The adaptive disturbance identifier and the mechanical observer are designed according to the quality of the estimated position signals, in order to get accurate rotor position and speed signal. The estimated rotor speed and position will be used for the flux orientation and control feedback. Three control loops, namely the current loop, the speed loop and the position loop, are designed in sequence.

After the pre-commissioning setups, both the position sensorless control and the speed sensorless control can be carried out in the full speed range and full load range.

7.2 Rotor Position Estimation

7.2.1 PWM Excitation and Current Derivative Measurement

To apply the command voltage vector to the motor through the voltage source inverter, SVPWM sequence is implemented. The PWM sequence period in this research is set to be $100\mu s$, synchronized with the current sampling frequency.

As described in Chapter 3, in order to measure accurately the current transient responses resulting from the voltage vectors applied to the motor, the voltage vectors are required be wide enough, so that any high frequency noise caused by the IGBT switching can be avoided from the di/dt sampling. However, the vectors in the fundamental PWM sequence may not satisfy this requirement especially under low speed operation or during sector crossings of the rotating voltage vector. Narrow PWM active vectors have to be extended for correct di/dt measurement. The extension effects should be compensated to ensure the basic vector control scheme unchanged. Different schemes have been described in Chapter 3. In this chapter the sensorless control system uses the method as described in 3.1, because it results in the lowest current disturbance and lowest audible noise.

Three handmade air-cored mutual inductors are connected in series with the inverter's three-phase outputs and are used as the di/dt sensors. The structure and dimensions of the di/dt sensors in this research have been illustrated in Chapter 4. In this research the position estimation is carried out once every 8 PWM cycles. This means that the position signal sampling frequency is 1.25kHz, which is high enough for flux orientation and position feedback. The active vectors where the di/dt samplings occur, are

guaranteed to be wide enough. Note also that, the gate resistance of the IGBTs, in the gate drive circuits, are doubled during these sampled vectors. This is realized through the dual-MOSFET bi-way switching circuit described in Chapter 5. It is controlled by a signal which indicates if the di/dt sampling will happen in a particular PWM period or not. The enlarged gate resistance helps to suppress the high frequency switching noise and reduce the requirement for the minimum period of the active vectors t_{dmin}. In the experiments of this chapter, the threshold is set as $t_{dmin} = 5\mu s$. This means, for the active vectors which are initially less than $5\mu s$ and their current transient responses are to be measured, they will be extended to $5\mu s$.

7.2.2 Derivation of the Rotor Position

The estimated position vector obtained from the di/dt measurements actually reflects the total saliency position in the motor, which is a combination effect of the saturation saliency to be tracked and various other harmonic saliencies. The ADI as discussed in Chapter 6 is used to extract and eliminate the harmonic disturbances at DC, f_e, $4f_e$, and $8f_e$. There is a difference between the rotor position and the saturation saliency position, which is caused by the q-axis flux generated by the torque current. This difference is compensated by a lookup table, which is addressed by the torque current value as shown in 6.9. There is also high frequency noise appearing in the estimated position signals ranging from several kHz to hundreds of Mhz. This noise will be highly amplified in the estimated speed when differentiation is performed on the estimated position. The mechanical observer is then designed to create acceptable position and speed outputs. The observer design is a compromise between its noise suppression ability and the dynamic response. In this research, the bandwidth of the mechanical observer is set to be $36Hz$, as has been explained in 6.3.

7.3 Sensorless Vector Control Design

7.3.1 Current Control Loop

In the inner layer of the cascaded vector control system shown in Fig 7.1, there are two independent fast current control loops, the flux current i_{sd} loop and the torque current i_{sq} loop. Due to the symmetry of the surface mounted PM machine, these two loops have identical design. The mathematical model for the electrical quantities of the surface mounted PMSM, in the synchronously rotating reference frame aligned with the rotor flux linkage, can be expressed as[19]:

$$v_{sd} = r_s i_{sd} + \omega_r \lambda_{sq} + \frac{d\lambda_{sd}}{dt}$$

$$v_{sq} = r_s i_{sq} + \omega_r \lambda_{sd} + \frac{d\lambda_{sq}}{dt} \tag{7.1}$$

$$\lambda_{sd} = L_s i_{sd} + \lambda_m$$

$$\lambda_{sq} = L_s i_{sq}$$

where λ_{sd} and λ_{sq} are the stator flux linkages in the d- and q- axis; v_{sd} and v_{sq} are the stator voltages in d- and q- axis; λ_m is the permanent magnet flux linkage; ω_r is the rotor speed. After cancelling out the cross-coupled terms, the resultant dynamic equations can be simplified to

$$v_{sd} = R_s i_{sd} + L_s \frac{d}{dt} i_{sd}$$

$$v_{sq} = R_s i_{sq} + L_s \frac{d}{dt} i_{sq} \tag{7.2}$$

The transfer functions from the command voltages to the stator currents are then given by

$$\frac{v_{sd}(s)}{i_{sd}(s)} = \frac{v_{sq}(s)}{i_{sq}(s)} = \frac{1}{L_s s + R_s} \tag{7.3}$$

and with the machine parameters given in Table 5.1, they yield

$$\frac{v_{sd}(s)}{i_{sd}(s)} = \frac{v_{sq}(s)}{i_{sq}(s)} = \frac{1}{4.15 \times 10^{-3} s + 0.47} \tag{7.4}$$

The current loop controllers are designed as PI regulators to achieve the zero error closed-loop tracking response. Using the root locus method, the PI parameters are designed with a closed-loop cut-off frequency of $\omega_c = 500Hz$ and a damping factor of $\xi = 0.7$. It yields

$$G_{cd}(s) = G_{cq}(s) = \frac{9.49s + 9.49 \times 10^3}{s} \tag{7.5}$$

Given the sampling frequency of the stator currents, $f_{sample} = 10kHz$, the controller can be easily digitalized as

$$G_{cd}(z) = G_{cq}(z) = \frac{10.439\,(z - 0.9091)}{z - 1} \tag{7.6}$$

It should be noted that, in sensorless control, the position orientation is carried out every 8 PWM periods. It does not influence the current controller design and the dynamic response of the current loop, because the current sampling frequency is much higher than the rotor's operation speed.

The torque current command i_{sq}^* is the output of the PI regulator in the speed loop as shown in Fig 7.1. The speed loop has a much lower sampling frequency than the current loop. Therefore steps will appear in i_{sq}^*. Due to the high bandwidth of the current loop, sharp changes in the command current will result in sharp changes with overshoot in the stator currents. Smooth operation is desired. For this reason, both of the current commands, i_{sd}^* and i_{sq}^*, are prefiltered. The prefilter is designed as (7.7) to eliminate the overshoot caused by the zero $z = 0.9091$ in the current controllers closed loop transfer function:

$$G_{cpf} = \frac{0.0909}{z - 0.9091} \tag{7.7}$$

Figure 7.2(a) shows the response of the current control loop to a step change of the torque current command, while the flux current is controlled at zero as is usual. The effect of the prefilter can been seen from the enlarged plot in Fig 7.2(b), where no overshoot exists.

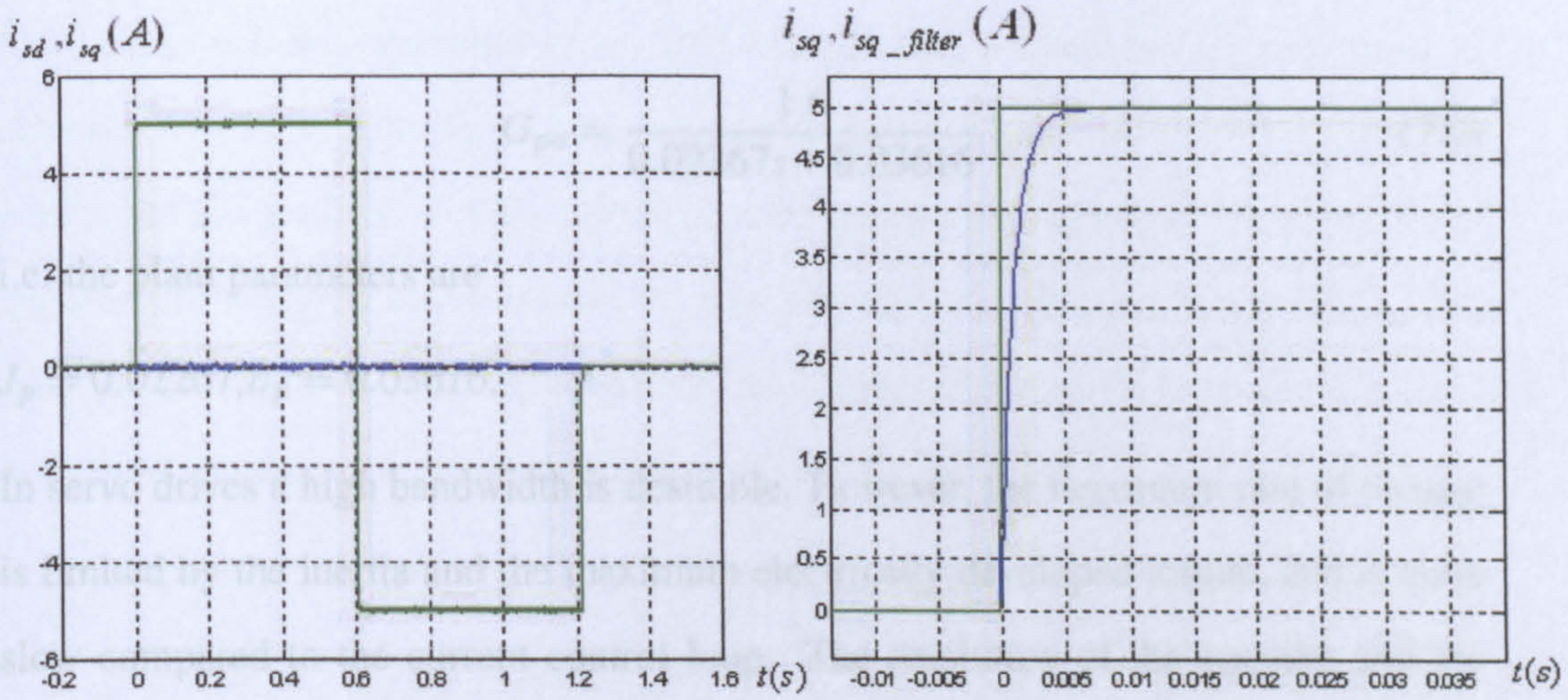

Figure 7.2: current control response to step changes in i^*_{sq} (left: i_{sd} and i_{sq}; right: $i^*_{sq}$and i_{sq})

7.3.2 Speed Control Loop

The high bandwidth of the current loops allows their closed-loop dynamics to be neglected when designing the speed loop. Hence the dynamic response for the speed loop is dominated by the mechanical system. As the SMPM machine in this research is also connected to a DC drive to obtain controllable loading, the shaft coupling changes the inertia and friction of the system from the nominal values in the datasheet of the PM machine. The transfer function of the mechanical system, as the control object, has to be identified.

The mechanical system of the plant is modeled as

$$G_{po} = \frac{\omega_r}{i_{sq}} = \frac{K_t}{Js+B} \tag{7.8}$$

A step command is applied to the torque current i_{sq} loop, with the flux current i_{sd} kept zero, and the speed response is recorded. Using a curve fitting method, the response curve can be identified as a transfer function of:

$$G_{po} = \frac{1.6}{0.02267s+0.03616} \tag{7.9}$$

i.e. the plant parameters are

$J_p = 0.02267, B_p = 0.03616.$

In servo drives a high bandwidth is desirable. However, the maximum rate of change is limited by the inertia and the maximum electrically developed torque, and is quite slow compared to the current control loop. The resolution of the encoder and the speed sampling time also have an influence on the sensored system. For the sensorless control system in this research, the speed control response is limited by the dynamic response of the mechanical observer. As described in Chapter 6, the mechanical observer cannot be designed with a high bandwidth due to the noisy characteristics of the estimated position signals. The speed loop should have a bandwidth of about $5 \sim 10$ times lower than that of the mechanical observer. The control loop is designed separately from the estimation subsystem. In this research, the compromise is made as that the bandwidth of the mechanical observer is about $40Hz$, and the bandwidth of the speed loop is about $8Hz$. Based on the plant transfer function we can derive the speed loop PI controller as (7.9):

$$G_c = \frac{0.6 \times (s+17.857)}{s} \tag{7.10}$$

Due to the large mechanical time constant compared with the bandwidth of the current loops, the speed controller can operate at its limit for a relatively long period of time. Therefore an anti-windup algorithm should be used.

7.3.3 Position Control Loop

The outermost loop of the cascaded system shown in Fig 7.1 is the position loop. Only a proportional controller is required for this loop, because the inherent integral relationship in the plant, $\theta_r = \int \omega_r$, can guarantee zero steady state error of both the speed and the position to their reference commands. The dynamic response of the speed loop designed above should be considered when deciding the position loop gain. In this research, with the bandwidth of the speed loop as 8Hz, the position loop gain is set to be $k_p = 2$, which produces a bandwidth of 4Hz.

For the position control, the motor is required to rotate from one specific position angle to the other angle instantaneously. However, if the motor does this with a square or trapezoidal position profile, its velocity will show a sudden change from 0 to the maximum and then back to zero suddenly. The sharp corner in the position profile produces not only the sudden change of the speed, but also abrupt surge, actually infinitely impulse, with the torque. Sudden acceleration or deceleration tends to reduce the life of the mechanical components, or even damage the application. To avoid this phenomenon, the transition to a new position needs to occur smoothly by slowly reaching a target acceleration or deceleration. The S-curve function defines a smooth response yet still maintains a high acceleration. The effect of the S-curve position profile on the speed profile and the torque profile is shown in Fig 7.3. Smoothing out the corners of the position command using the S-curve reduces the abrupt change in the speed and also the torque impulses.

Due to the relatively low bandwidth of both the position loop and the speed loop as designed above, the servo lag phenomena exists and influences the tracking dynamic

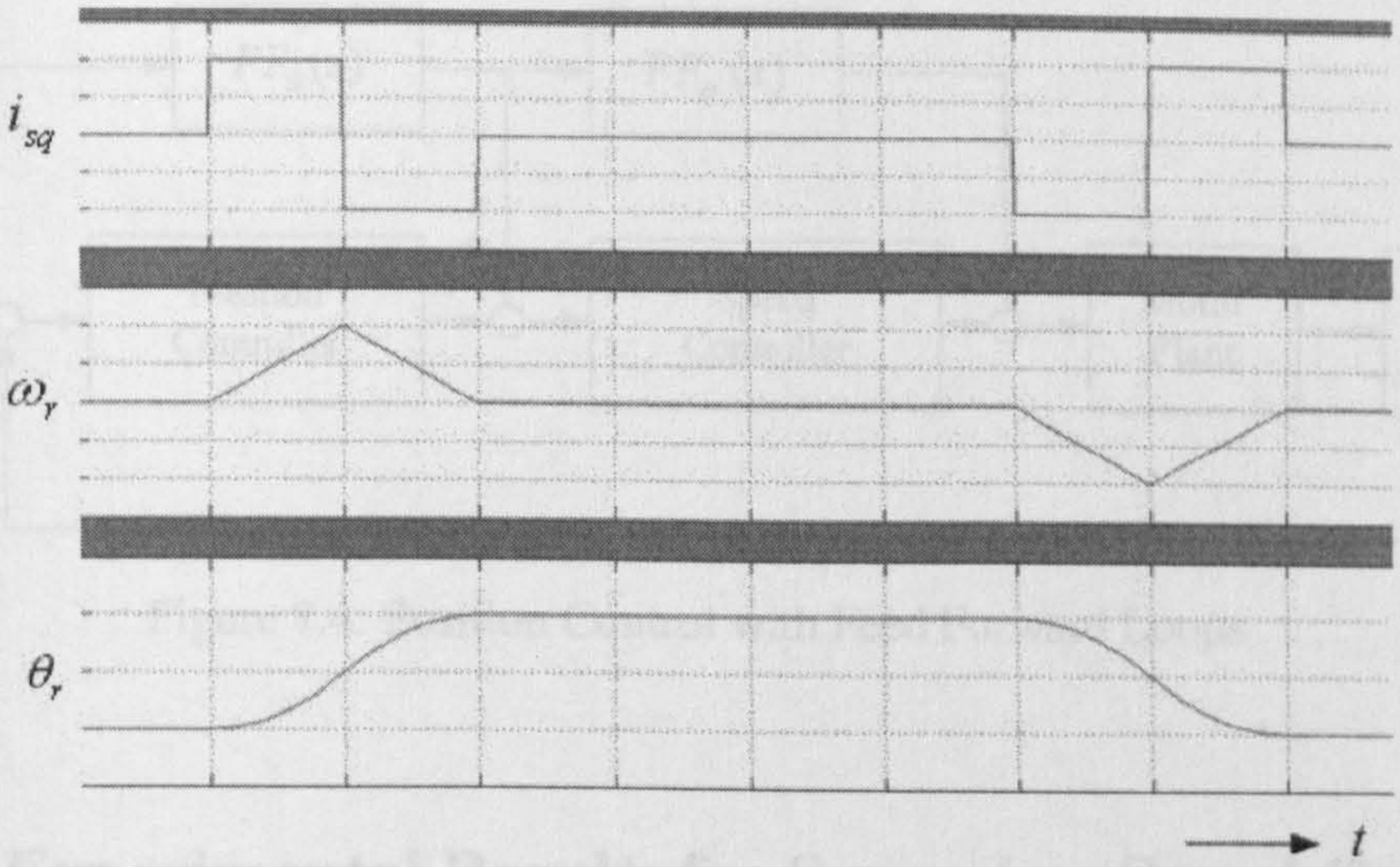

Figure 7.3: S curve profiles for the position angle θ_r, the speed ω_r and the torque current i_{sq}

performance. One approach to improve the response is to place the feed forward controller at the system's inputs. As shown in Fig 7.4, the speed command value and the torque command value can be predicted from the position command θ_r^*, because the relationships between these variables are precisely known. The command feed forward compensation has the advantage that its design is independent of the parameters of the position loop controller and the speed loop controller. In this machine drive system, the feed forward algorithm is

$$FF_\theta(s) = s \tag{7.11}$$

and

$$FF_\omega(s) = Js + B \tag{7.12}$$

The predicted commands are added to the loop controllers' output for compensating the delay due to the control lag. The internal feedback loops are used to suppress the effects due to the system's uncertainty and the feed forward control loops are used to improve tracking performance.

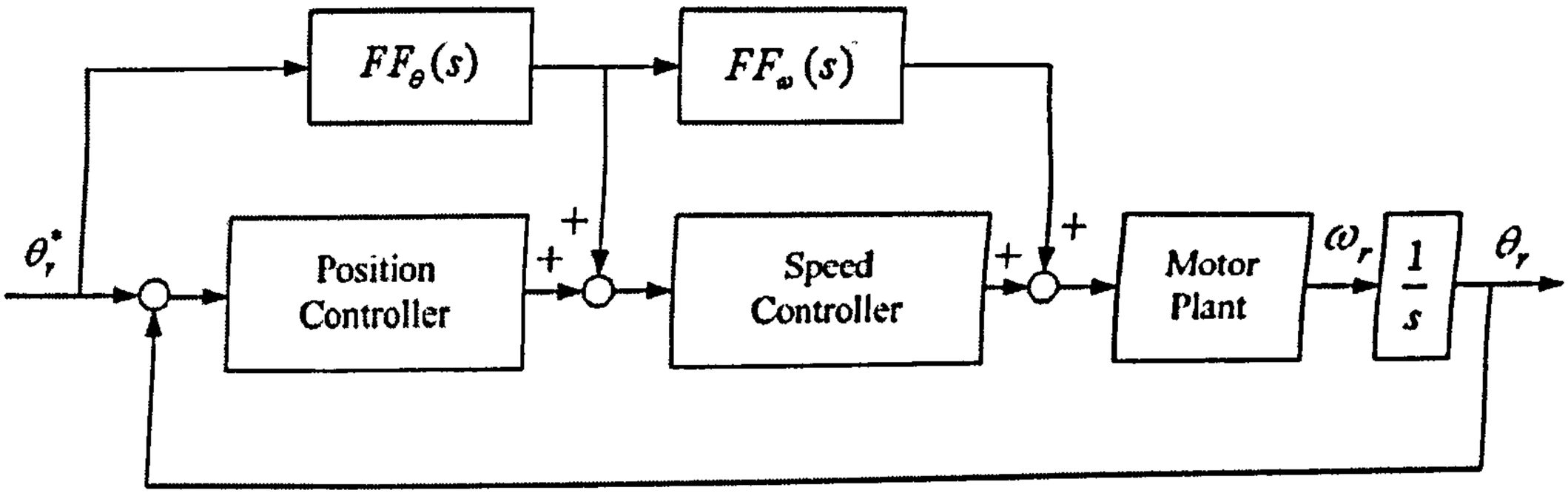

Figure 7.4: Position Control with Feed Forward Loops

7.4 Experimental Results for Sensorless Speed Control

7.4.1 Speed Reversal Operation

The ability of the sensorless control at low speed is firstly assessed by speed reversals from 10rpm to -10rpm (i.e. the stator fundamental frequency from 0.5Hz to -0.5Hz). This experiment is repeated under zero and heavy load conditions.

7.4.1.1 Low Speed Reversal With no Load

The speed and position response when no external load is applied are shown in Fig 7.5 and Fig 7.6, for the sensored and sensorless control respectively. The machine is accelerated to $10rpm$, speed reversed to $-10rpm$, and then stopped. The $6f_e$ periodic disturbance, appearing in both sensored and sensorless control results, is probably produced by the cogging of the PM machine. The sensorless speed control does not show a big difference from the sensored control. Both the steady state performance and the dynamic response are good.

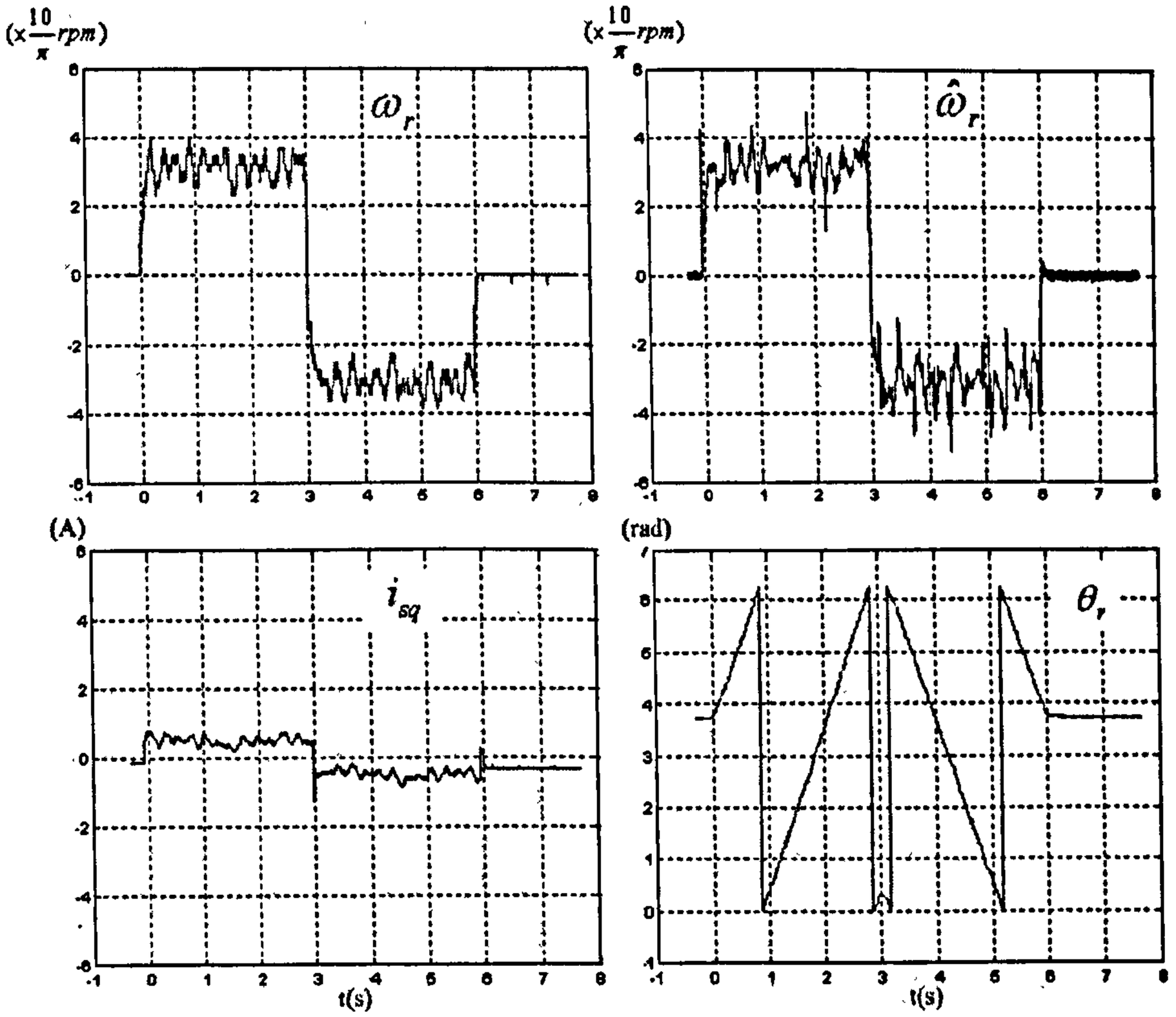

Figure 7.5: Sensored control for low speed reversal without added load

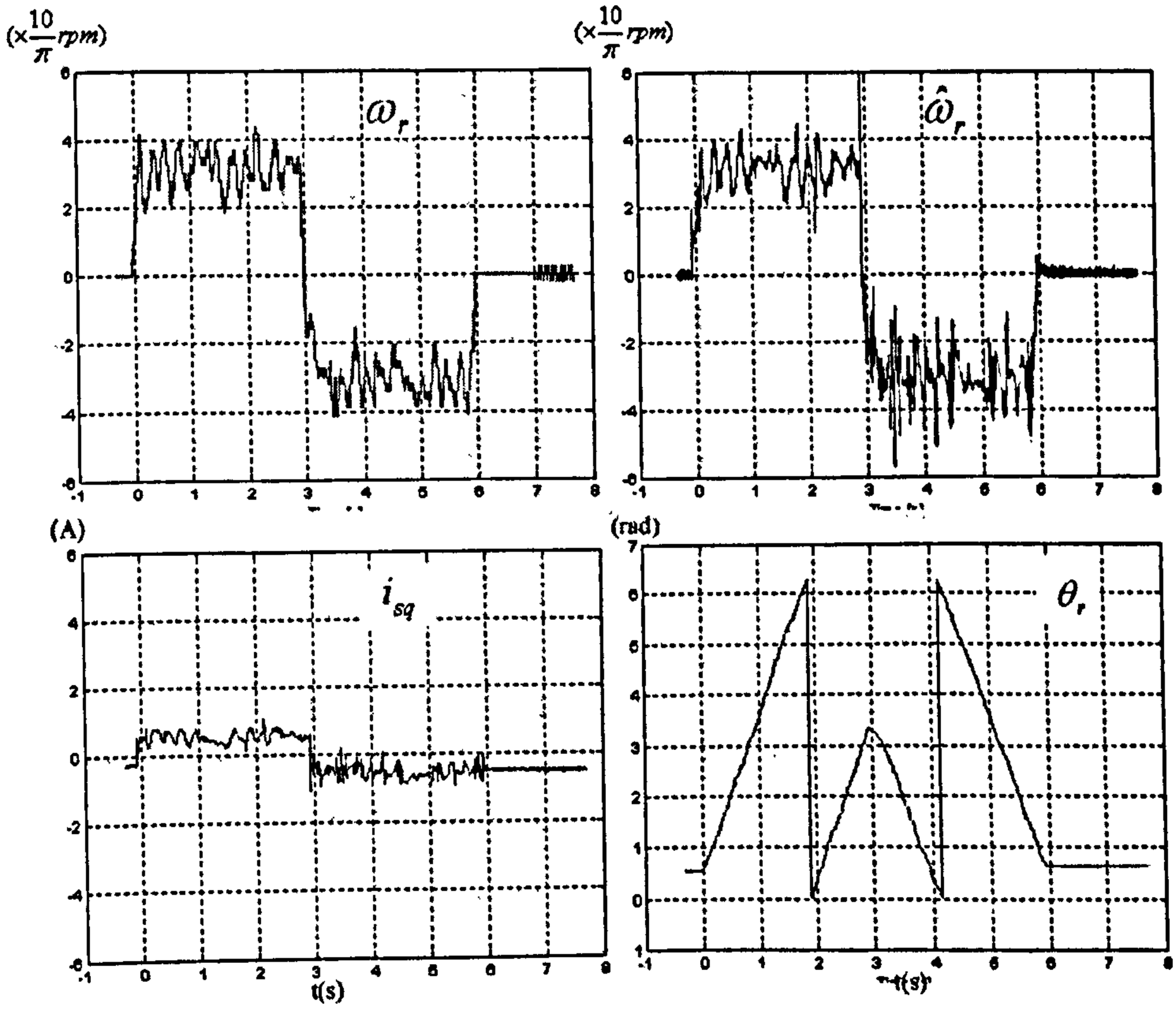

Figure 7.6: Sensorless control results for low speed reversal without added load

7.4.1.2 Low Speed Reversal With Full Load

The low speed reversal results under the rated load (i.e. the torqure current is around 7.6*A*) are shown in Fig 7.7 and Fig 7.8 for the sensored and sensorless control respectively. The load machine is controlled to keep a constant torque output in the negative direction. Compared with the sensored control, the sensorless control at low speed shows satisfactory results.

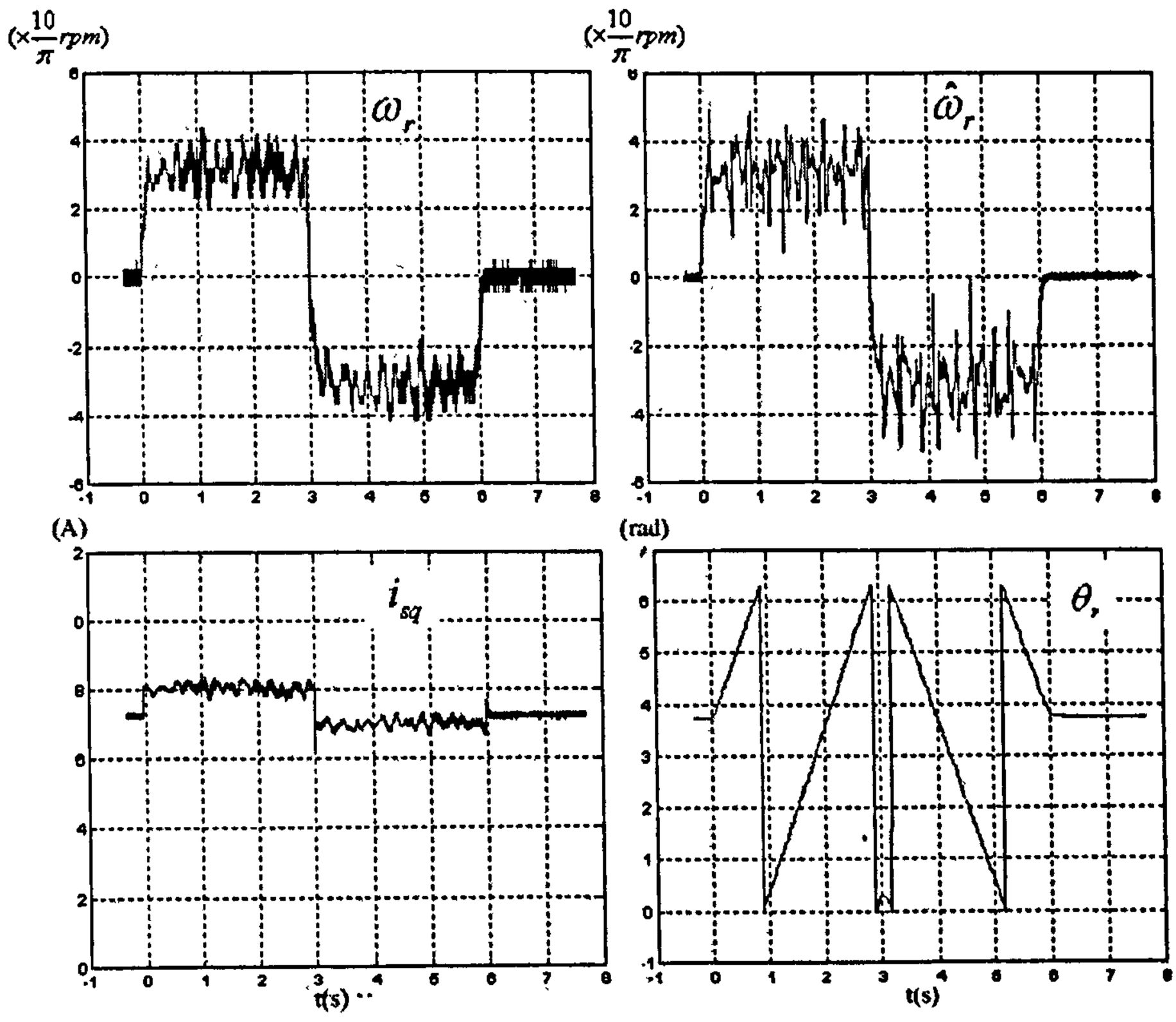

Figure 7.7: Sensored control for low speed reversal with full load

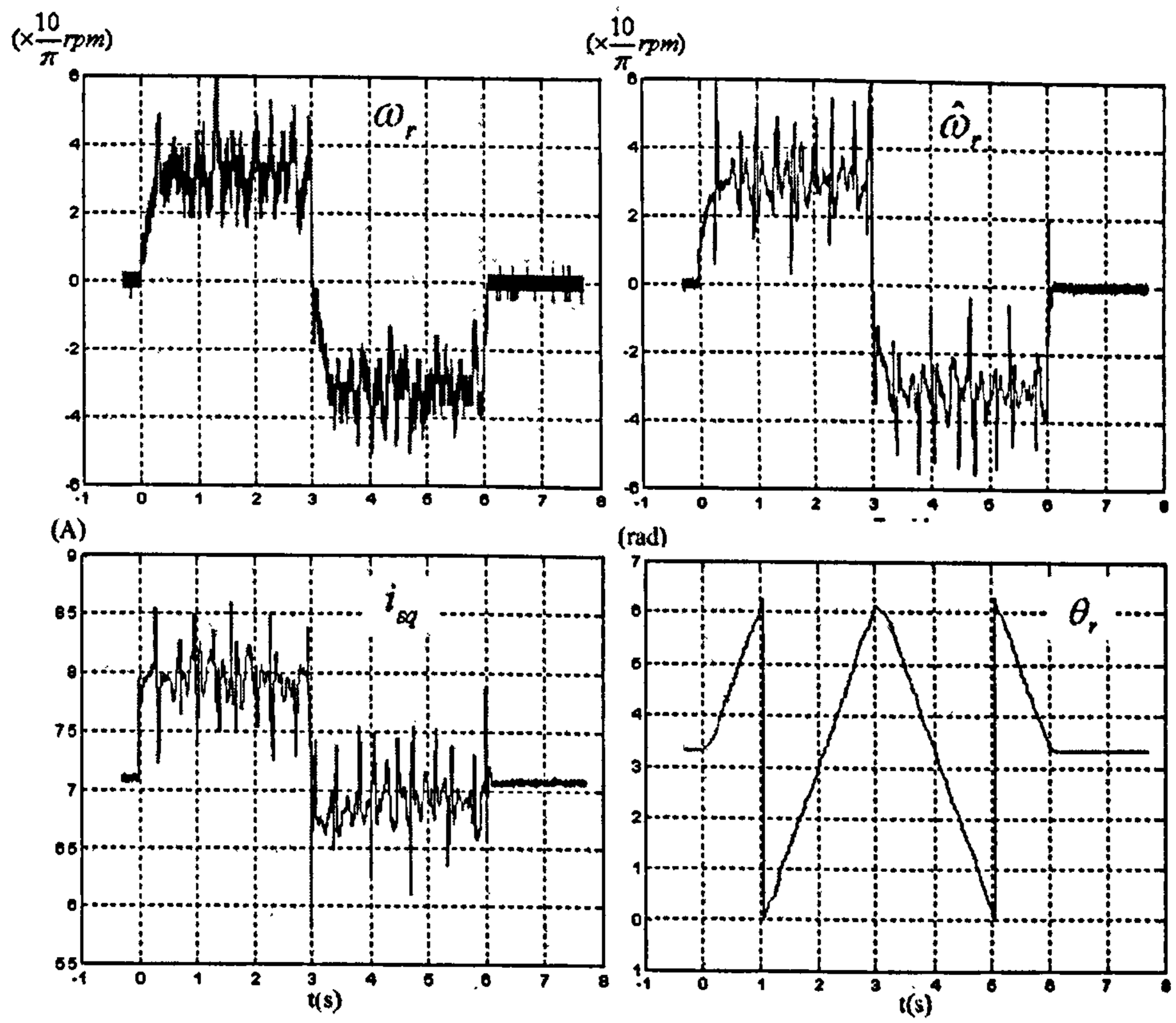

Figure 7.8: Sensorless control for low speed reversal with full load

7.4.1.3 Higher Speed Reversal With No load

Similar speed reversal experiments are carried out at higher speed. The PM machine is accelerated up to 300rpm (i.e. the fundamental frequency $f_e = 15Hz$), reversed to -300rpm, and then stopped. This experiment is repeated without and with external loads.

The measured and estimated speed responses of the sensorless controlled system are shown in Fig 7.9. The measured torque current and rotor position signals are also plotted. These results show good dynamic response and controllability of this sensorless control system. At steady state, the position estimation error is very small and the speed estimation error is within $\pm 15rpm$, that is within 5% of the running speed.

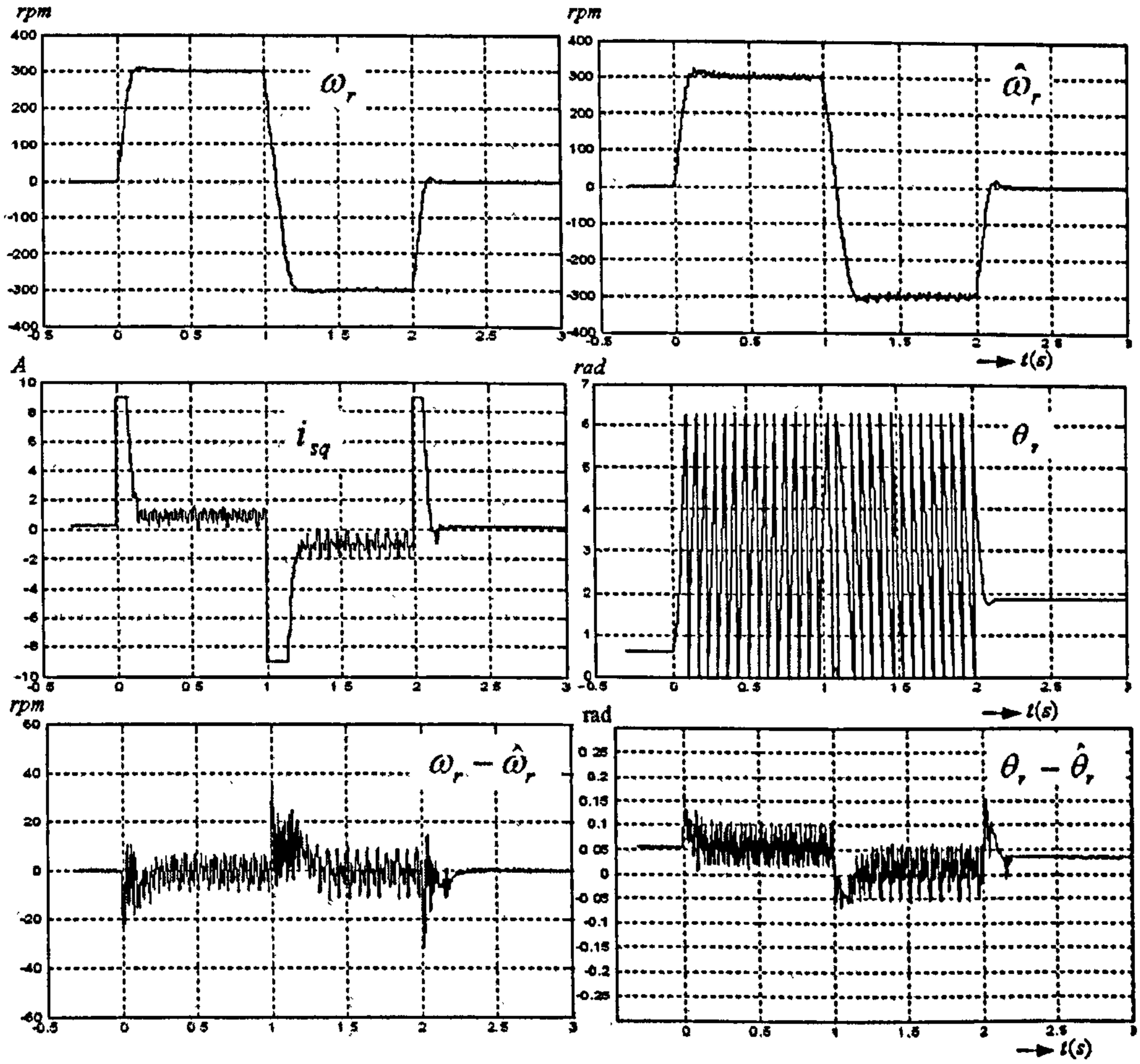

Figure 7.9: Sensorless control results for speed reversal from 300rpm to -300rpm without load

7.4.1.4 Higher Speed Reversal With Full Load

The experimental results for a sensorless speed reversal from 300rpm to -300rpm with external load are shown in Fig 7.10. The full load is applied, which is achieved by controlling the output torque of the load drive.

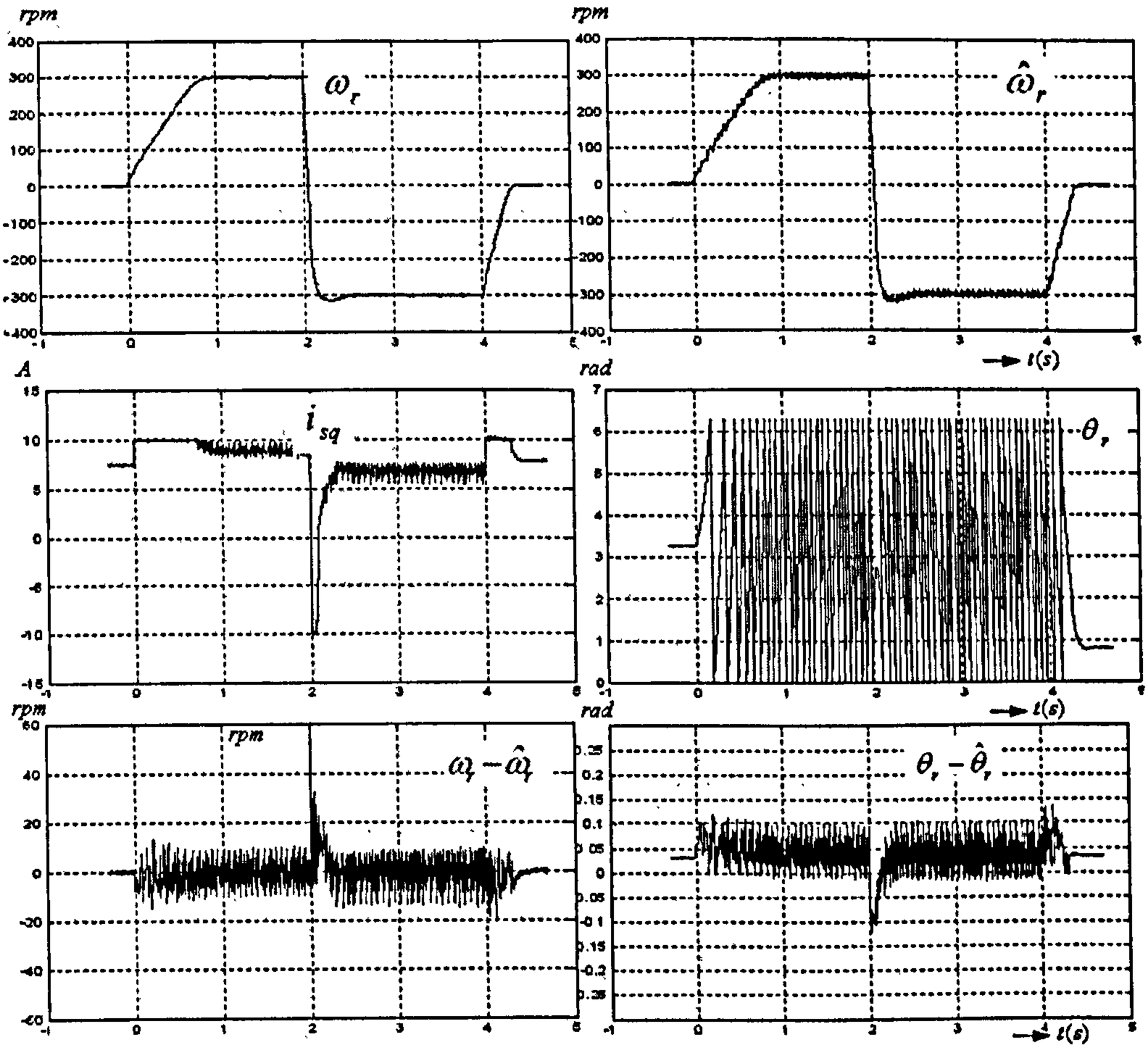

Figure 7.10: Sensorless control results for speed reversal from 300rpm to -300rpm with full load

As expected, the estimated speed signal is more noisy than the encoder measured speed signal. But the sensorless control results are still very good. The estimation speed error and position error are very small. The cogging effect can still be seen from the torque current waveform.

7.4.2 High Speed Control

The position estimation scheme using only fundamental PWM sequence is also applicable to the high speed operation. At high speed the vector extension happens much less than that at low speed. Using the sampling of di/dt during null vectors, the in-

fluence from the back EMF and resistance voltage drop can be almost cancelled, and they will not influence the position estimation results. The experimental results of the sensorless control when the motor is accelerating up to 1000rpm, and then decelerating in steps, are shown in Fig 7.11. The measured position signal, the estimated position signal, and the speed and position error signals are exhibited.

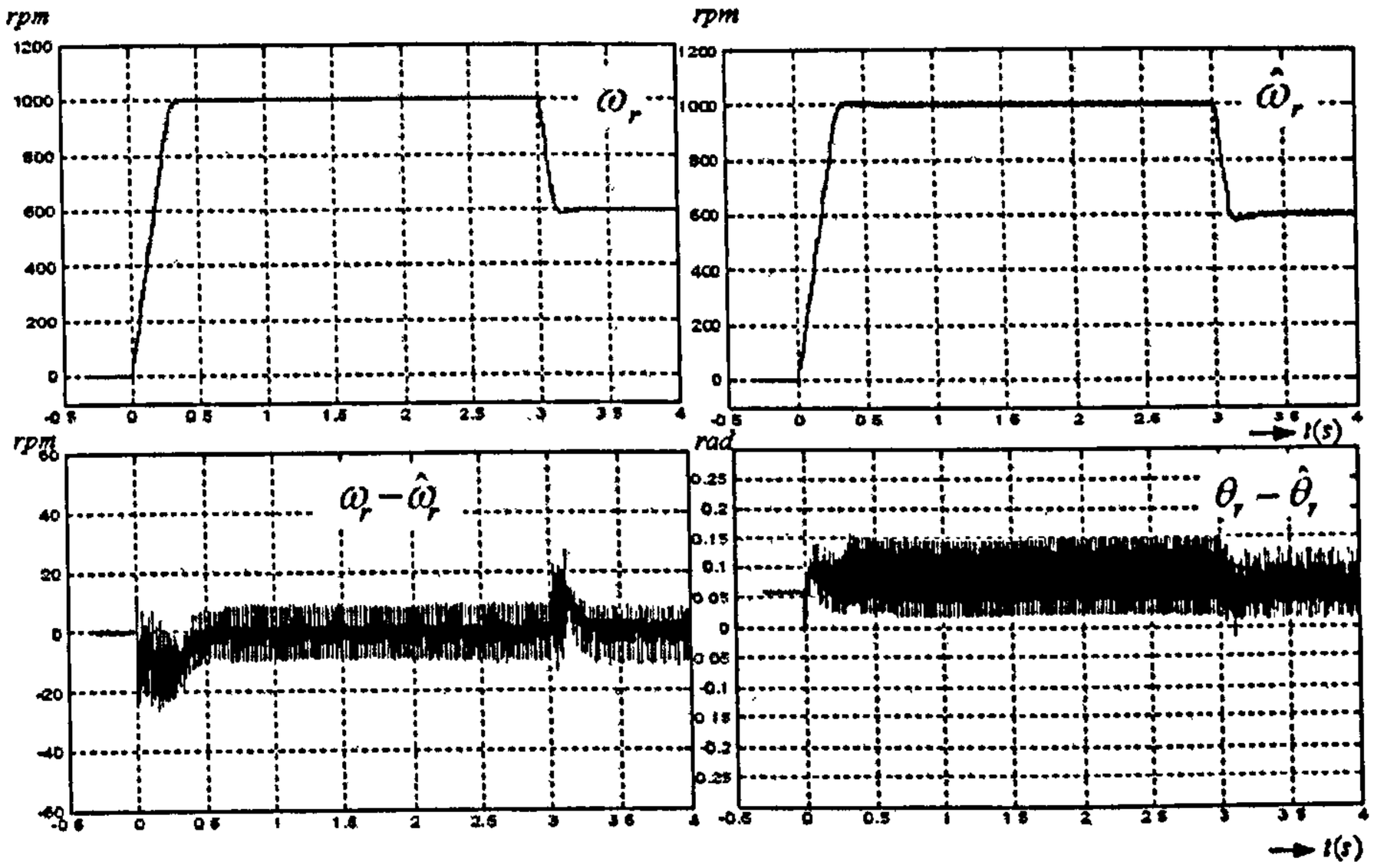

Figure 7.11: Sensorless speed control at high speed

7.4.3 Load Disturbance during Sensorless Speed Control

The characteristics of the sensorless speed control under the load impact are investigated. Sudden changes of the load torque occur, when the machine is running at a constant speed under sensorless control. The step change of loading condition is realized by suddenly starting and stopping the load drive system.

At Low Speed

The machine responses to full load impact at low speed are shown in Fig 7.12. The whole process is that the machine is started up to 10rpm from $t = 0sec$, then 100%

nominal load torque is applied at $t = 1.6sec$, the load is removed until $t = 5.6sec$, and finally the motor is stopped at the $8th$ second. The encoder measured rotor speed ω_r, the estimated rotor speed $\hat{\omega}_r$, the torque current i_{sq} and the measured rotor position θ_r are all shown in Fig 7.12. The loading status in the whole precess is reflected by the waveform of i_{sq}. It can be seen that, the estimation error is acceptable during both the steady state and the dynamic period.

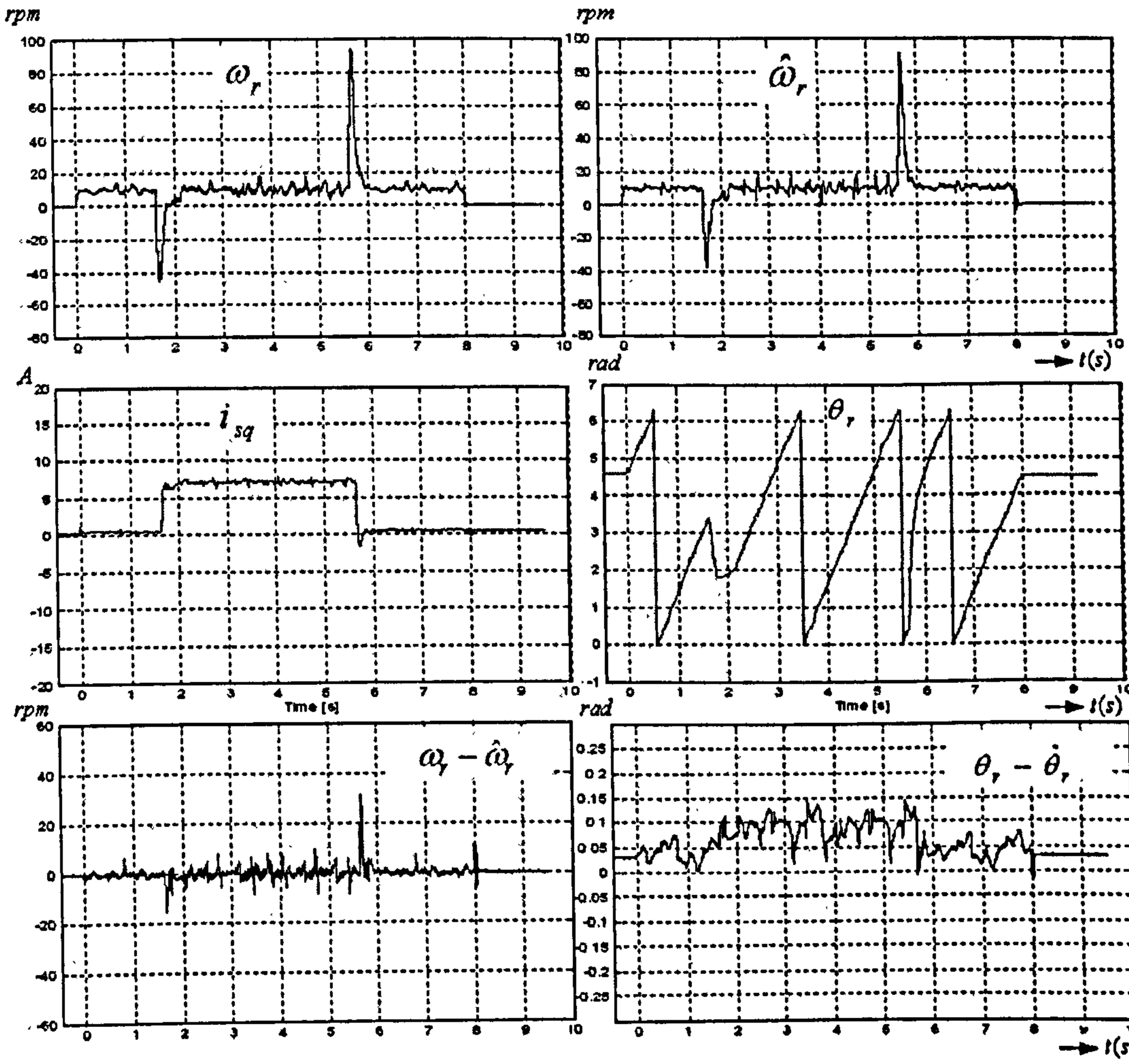

Figure 7.12: Full load impact on the sensorless speed control at 10rpm

At Higher Speed

The same load impact test is carried out on the sensorless speed control system when the machine is running at 300rpm. The machine responses are shown in Fig 7.13. The load bearing ability and the dynamic performance of this sensorless control system are excellent.

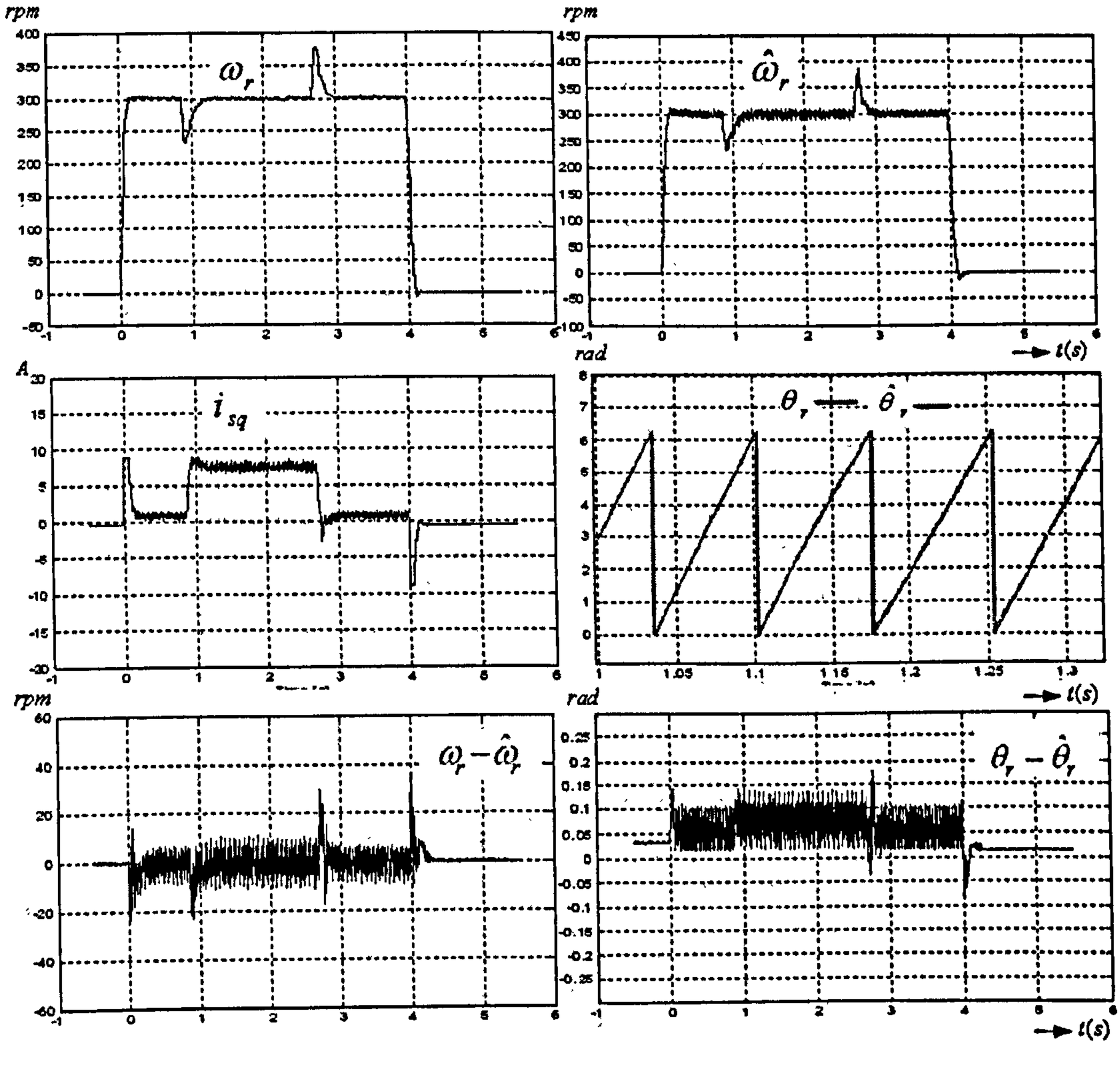

Figure 7.13: Full load impact on the sensorless speed control at 300rpm

7.5 Experimental Results for Sensorless Position Control

In this section, experimental results for the sensorless position control system are presented. Different tests are designed to exhibit its stability and dynamic performance.

7.5.1 Position Reversal Control

The position command is given as an absolute position angle value. In this test, the machine is firstly driven from its initial position to a specific angle position with the S-curve profile detailed in 7.3.3. After a while it is driven in the opposite direction to the new angle position . Then the machine is driven back to its original position.

With No Load

The experimental results, when the machine is driven 6 rotations from the standstill, and then 12 rotations in the opposite direction, and then back to its initial position, are exhibited in Fig 7.14. The position command is always provided as an S-curve profile and the feed-forward control is utilized. In the upper plot, the measured absolute rotor position angle follows very well with the command signal. No external load is applied during this process.

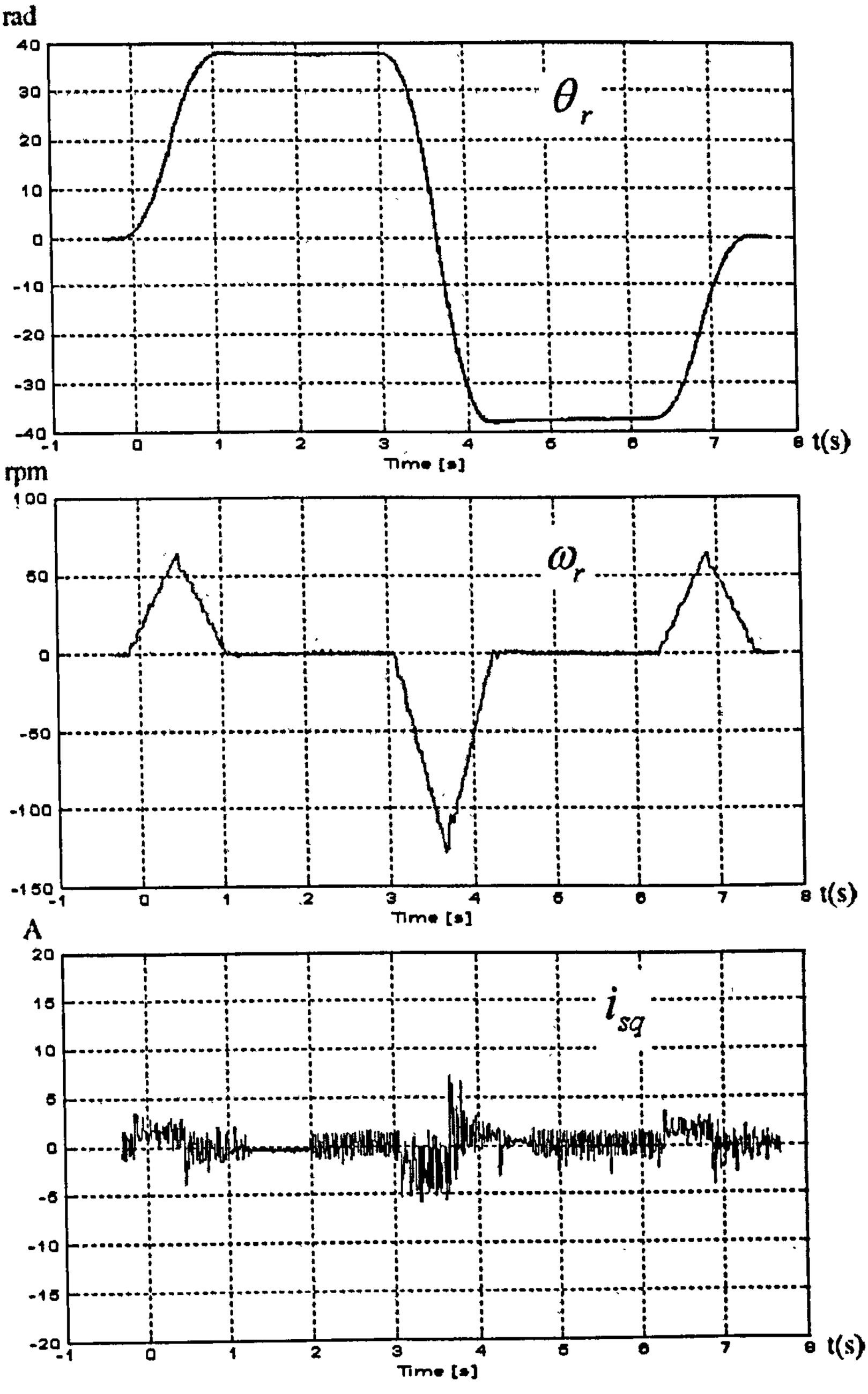

Figure 7.14: Experimental results of the position reversal without load

With Full Load

The same experimental procedure is repeated, but full load is applied during the whole process. The machine responses are shown in Fig 7.15.

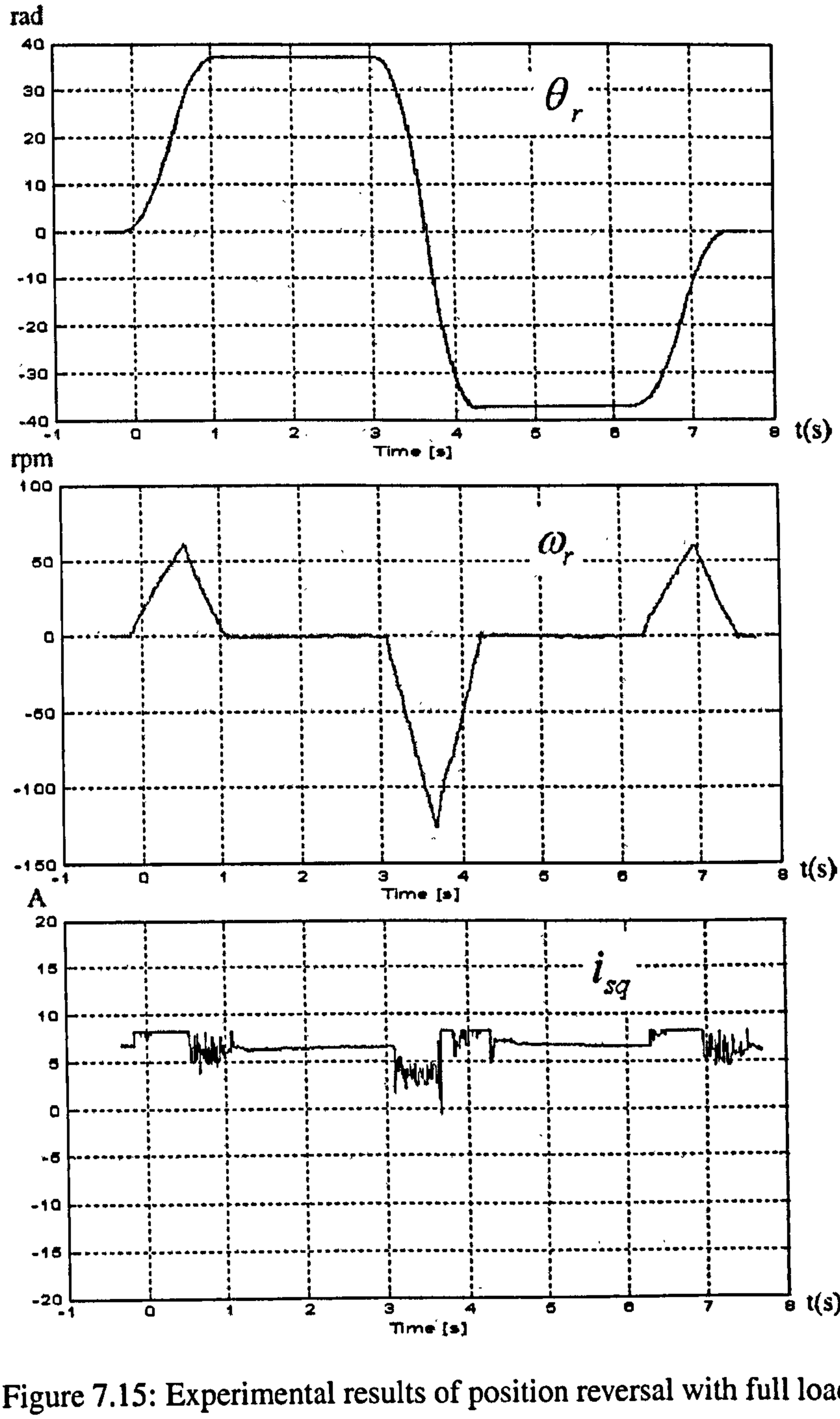

Figure 7.15: Experimental results of position reversal with full load

It can been seen that the sensorless position control is accurate and shows good dynamic performance under different load conditions.

7.5.2 Position Hold under Full Load Impact

In this experiment, the PM machine is firstly driven to a new position with 6 rotations. Full load is then added. After a while the load is removed when the rotor is still hold at that angle position. Finally the machine is driven back to its original position. The measured absolute position angle is presented in the upper plot of Fig 7.16. Small responses to the full load disturbance appear on the position waveform, which is displayed in the lowest plot. The torque current and speed responses are also presented. The sensorless position control system shows excellent robustness in this test.

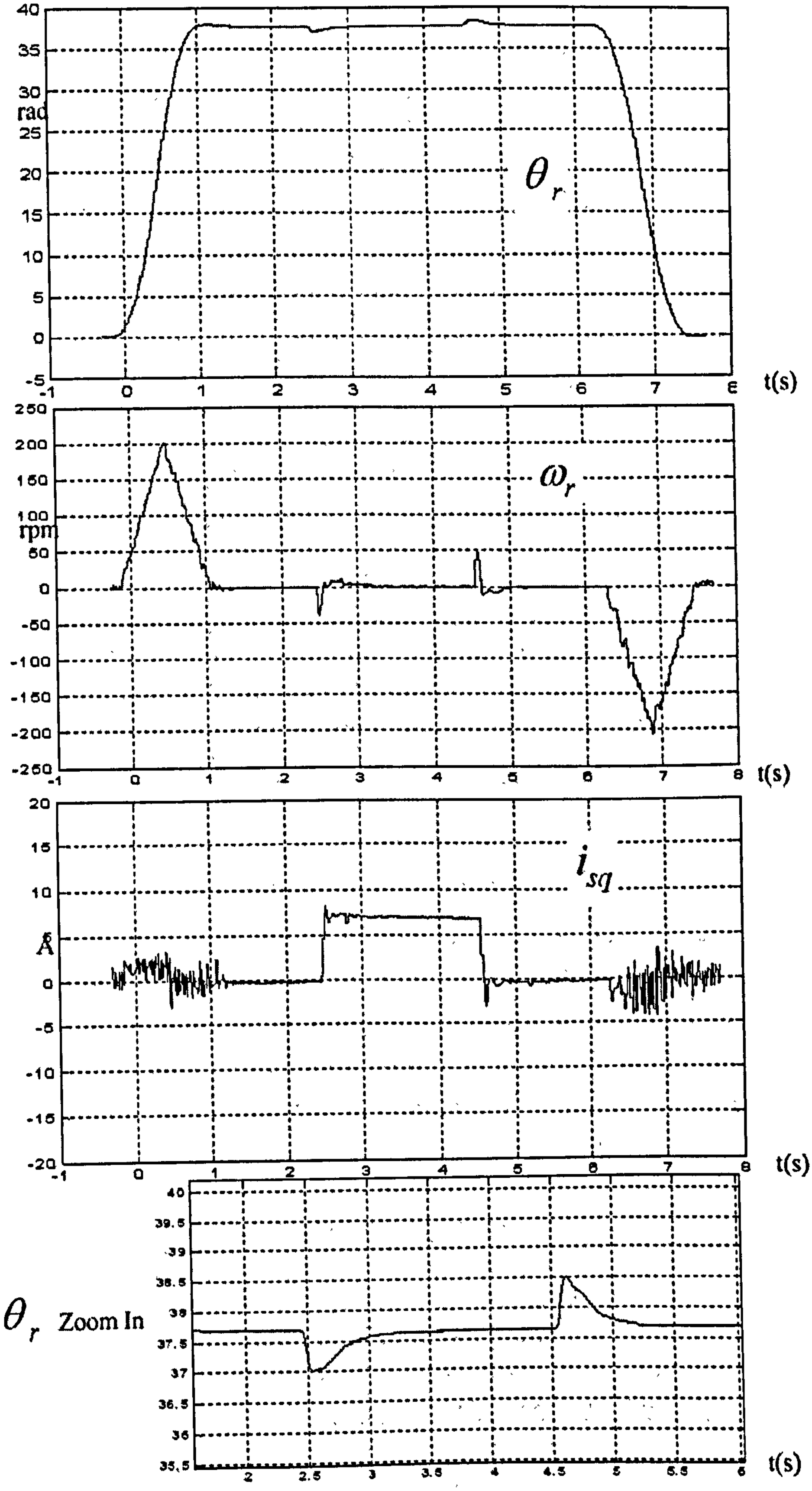

Figure 7.16: Position hold with full load disturbance

7.6 Conclusion

The whole sensorless control system based on the fundamental PWM excitation is described in this chapter. The position estimation system, including both the hardware installation and the control scheme implementation, are further explained. The current derivative signals are measured and utilized to estimate the position vector. The ADI and the mechanical observer are designed to improve the estimated position and speed signals. The design process of the current loop, the speed loop and the position loop are elaborated. S-curve command profile and feed-forward control schemes are introduced and utilized on the closed-loop position control.

The full sensorless control system has demonstrated excellent performance by the experimental results under different test conditions. The results of both the sensorless speed control and the sensorless position control have been exhibited. Satisfactory controllability and dynamic performance are shown in different tests, which include the speed reversing in different speed ranges, speed or position holding under load impact disturbance and the precise speed or position control.

Chapter 8

Conclusions and Discussions

The aim of this work has been to demonstrate the feasibility of sensorless speed control, especially at low and zero speed for a surface mounted permanent magnet machine by means of saturation saliency tracking based on fundamental PWM excitation. The conclusions and discussions are given below.

8.1 Conclusions

This thesis focuses on the use of PWM vector excitation to excite the inherent saliency of the AC machine and determine the rotor position. The INFORM method, as the basis for this kind of approach, uses pairs of opposite test vectors to provide transient excitations. The resulting transient stator currents are measured to estimate position. The INFORM method and its dependent methods are effective for position estimation, but they are limited to zero and low speed. This is because the additional test vector pairs are inserted in the null vector of the PWM sequence, which becomes shorter when the speed increases. The added test vectors incur extra stator current ripple which increase losses, add torque ripple and raise the acoustic noise level. The new method for PM motor control introduced in this thesis is based on the fundamental

PWM sequence and takes advantage of the transient excitations from the original active vectors in the fundamental PWM sequence. The current derivatives during the null vectors are also measured and used for eliminating the resistance voltage drop and back EMF influence on the position estimation. This method is applicable even in the high speed range. However, some of the active vectors may not be wide enough, and may need extending to a minimum width, because the high frequency switching oscillations in the stator current waveforms due to parasitic circuits need a period to die down. The small vector width normally happens in the low speed range or when the voltage reference vector is crossing the sector boundaries. The solution used in this thesis is to extend the narrow vectors to meet the required minimum vector width t_{dmin}. The extension effect on the output voltage should be compensated. One way is to shift the other switching edge of the extended phase and thus keep the turn-ON time for each phase the same. This method has been explained and verified in 3.2.3. This kind of extension and compensation scheme needs no additional vectors and also keeps the voltage time area in each PWM cycle unchanged. Current transients excited by the two active vectors and null vectors in the fundamental PWM sequence, can be measured to obtain the position signals. However, the disadvantage of this method is that a large current deviation appears in the current waveform, which is because the extension happens in the first half PWM period but the compensation is at the end of the second half PWM period. In order to reduce this current distortion, one new improvement is proposed in this research to compensate the extension effect in advance by using the opposite vector with the extended width. The detail is also explained in 3.2.3. Using this scheme the current deviation is significantly suppressed. Although one vector is added, it does not introduce additional current distortion, because it is only used for cancelling the current deviation. Its width is adaptive to the fundamental PWM sequence and only happens when the vector extension is made.

For the position estimation methods discussed in Chapter 3, their induced current distortions are studied. The voltage and current ripple vectors are introduced in 3.3 to

discuss these distortions. When different position estimation schemes are applied to the PM synchronous motor, the stator current waveforms are measured and compared in the same experimental test and with the same vector duration t_{dmin} for position estimation. The THD analysis shows that the scheme using only fundamental PWM sequence with the proposed compensation method exhibits the smallest current distortion. At higher speed, the PWM vector extensions can be avoided most of the time, because the active vectors normally have sufficient widths. Extension and compensation will only happen when the voltage reference vector is crossing the sector boundaries. Current distortion associated with the method based on fundamental PWM sequence will be much reduced in the higher speed range.

The requirement of the minimum vector width for di/dt sampling t_{dmin}, is the main reason for the induced additional current distortion in the position estimation schemes. With a reduction in the minimum vector duration t_{dmin}, the current distortion caused by the position estimation schemes can be reduced, which is demonstrated in 4.2.2. The required minimum vector duration t_{dmin} is due to the high frequency oscillations during the switching instants and the di/dt sampling has to be done after these oscillations die down. In this research, in order to suppress the noise and thus to reduce the minimum vector duration t_{dmin}, these high frequency switching oscillations in this AC drive system are studied. Both the common mode and the differential mode oscillations are identified. The main part of the common mode noise appears at $2 \sim 3kHz$ in this research and it can be eliminated by software compensation. A novel attempt is made to reduce the differential mode noise with the frequency about several MHz, by slowing down the IGBT turn ON/OFF speed. Increasing the gate resistance shows some influence on lessening the oscillation amplitude and duration. Its effect of reducing the high frequency oscillations has been described in 4.2.2. During the PWM cycles when the vector transient excitations are required for the position estimation, the gate resistances are increased; during the normal PWM cycles, they are kept at the nominal value. Increasing the snubber capacitance is another way to reduce the high

frequency switching oscillations. Experimental results show that the snubber circuit works well for eliminating the high voltage spikes and ensuring the device safety, but does not improve the current switching oscillations very much in this application.

An AC drive inverter has been designed and built in this project. Its power circuit is integrated using a PCB. With optimized layout and design, the contact electromagnetic noise is limited. IGBT gate drive circuits in this system are particularly designed for reducing the high frequency oscillations during the di/dt sampling. Different gate resistance values are used according to the programmed command. The circuit implementing this changeable gate resistance has been described in 5.3, which is realized by a bidirectional switch of dual-MOSFET circuit. Besides the current and voltage sensors required by the vector control, di/dt sensors and signal processing circuits are included. The Rogowski coil and the air-core mutual inductor are two types of di/dt sensors utilized by the sensorless control systems in literature. In this research three handmade air-core mutual inductors with the improved design are used, which has been explained in 4.3.1. It is found that the di/dt sensor output signals are hard to use directly, because they are dominated by high frequency noise. Thus circuits are added to filter off the noise and to amplify the di/dt signals for A/D conversion.

The experimental results verify that the saturation saliency in a surface mounted PMSM can be exploited for sensorless control. Nevertheless, harmonic disturbances arising from other existing saliencies deteriorate the estimated position signals. Harmonics at DC, f_e and $4f_e$ are the main disturbing components in this research. By analyzing these harmonics as the function of torque current i_{sq}, their origins are identified in Chapter 6. These harmonics mainly arise from the motor characteristics and the harmonic orders will not change with the speed or load. The ADI proposed in 6.1.4 is an effective method to eliminate the harmonics at specific frequencies. It uses a stack of synchronous filters to extract each target harmonic component, and then the total disturbing harmonic is removed from the estimated position signals. In the low speed

range, the synchronous filters cannot extract the harmonic correctly, because these harmonics are located very close to the desired saturation saliency signal. To overcome this problem, the ADI includes a small table with the pre-calibrated harmonic information, which provide the DC values of each harmonic component in each synchronous rotating reference frame. By using this table, these harmonics can be constructed in the low speed range, and then be eliminated from the estimated position signals. This table only needs a small memory space, and can be populated and updated at higher speeds under different load conditions.

The saturation saliency presents the air-gap flux position, instead of the rotor position. The difference between the rotor angle and the derived flux angle is proportional to the load current i_{sq}. This is verified by the experimental plots, which are then employed for online phase compensation to obtain the rotor position. The position estimation method based on the fundamental PWM sequence with an improved compensation scheme for current distortion, is used for the sensorless control in this research. In the feedback channel the mechanical observer is tuned to suppress noise in the estimated position and speed signals. The control loop and the feedback are designed separately, but a compromise is made between the system dynamic characteristics and the noise suppression level.

Experimental results of both the sensorless speed and the sensorless position control are exhibited in Chapter 7. Excellent performance, both in accuracy and in dynamics, is demonstrated under different experimental conditions. The operation at low speed, as shown when the stator fundamental frequency is $f_e = 0.5Hz$, is excellent. This sensorless control system also shows satisfactory capability to reject load disturbances, in either speed control or position control.

The final conclusion is therefore, that the aims and objectives stated in Chapter 1 have been met. A sensorless control scheme has been presented for a SMPM motor, which exploits the normal PWM sequence with minimal modification, introduces only small

additional current distortion - lower than signal injection or test pulse type techniques - and operates over a wide speed range.

8.2 Further Work

Although this project has successfully devised a sensorless PM motor drive, there are various aspects of of the scheme which would benefit from future research. Some discussions and ideas related with this system are given below.

1. Further study of the basic scheme to eliminate the impact of short vectors, allowing non-modified PWM to be used without any additional current distortion. To avoid any PWM modification, reference [59] proposes a hysteresis control and reference [60] exploits the inherent excitations in the fundamental PWM from the frequency domain. But both methods need more investigations and verifications.

2. Analysis of the effects of inverter non-linearities on the position estimation scheme and the incorporation of deadtime compensation. As explained in Chapter 2, for the methods based on high frequency signal injection, the tracked saliency position signal can be distorted by the inverter non-linearities. For the transient vector excitation methods the inverter non-linear characteristics will not introduce much disturbance on the position estimation. However, the deadtime of the IGBT switching should be considered when setting the instants of the di/dt sampling. Deadtime compensation schemes are preferred although not strictly necessary, and these can be realized by advancing the switching edges depending on the current direction[118, 119].

3. Development of di/dt sensors without further signal processing requirements. Both the Rogowski coil and the air-cored mutual inductor can be used as a di/dt sensor in the sensorless control system. Both of them have inherent good linearity over a wide spectrum, which makes them suitable for transient current measurement. However, the noise in the measured current is also much amplified due to their high frequency

response. The output signals can be overwhelmed with noise and cannot be used directly. In this research they are further filtered and amplified. The overall bandwidth of the sensor, the lowpass filter, and the amplifier needs to be optimized. In addition the labourious tuning work, the filtering and amplifying circuits add components and cost.

4. Development of integrated current sensor and di/dt sensor. Both the current sensors and the di/dt sensors are used in this research, which is not economical. Combining these two kinds of measurements should be possible. One possibility is to use mathematical differentiation of the measured current signals to calculate the di/dt value. The other possible way is to obtain the current measurements from the di/dt sensors with an integrator. This is the principle of the commercial current sensors using a Rogowski coil. The main limitation comes from the saturation and DC drift of the integrator, and the requirement of a measurement of a DC current at standstill.

5. Improvement of the performance of the ADI. The commissioning process of the ADI is carried out when the motor runs above the threshold frequency, which can be either in sensored mode or in sensorless mode. One limitation found with the sensorless commissioning occurs during the startup period, when a higher torque current is required to accelerate the machine to above the threshold frequency. If the harmonic disturbance effect is significant, sensorless startup without disturbance compensation may be difficult. For the commissioning in sensorless mode, the lookup table is updated gradually until all the data reaching their true values, which may need a relatively long period.

6. Further explanation of the disturbing harmonics in the estimated position signals. As analyzed in Chapter 6, the identified disturbing harmonics mainly reflect other saliency characteristics of the SMPM machine under transient excitations of the PWM vectors. However, a better understanding of their origins and effects could be obtained by further theoretical study, coupled with a study employing detailed magnetic ma-

chine models. Also, with different machine types, the harmonic saliencies may vary, and then another ADI commissioning may be necessary.

8.3 Publications

The present work has resulted in three conference paper, which are included in Appendix C.

Bibliography

[1] J.F.Gieras and M.Wing. *Permanent Magnet Motor Technology Design and Applications*. Marcel Dekker Inc, second edition, 2002.

[2] Blaschke Felix. Method For Controlling Asynchronous Machines, 1974.

[3] B.K.Bose. *Power Electronics and Variable Frequency Drives Technology and Applications*. Piscataway, NJ. USA, 1997.

[4] G.R.Slemon. Electrical Machines for Variable Frequency Drives. In *Proceedings of the IEEE*, volume 82, pages 1123–1139, 1994.

[5] Robert Joetten and Gerhard Maeder. Control Methods for Good Dynamic Performance Induction Motor Drives Based on Current and Voltage as Measured Quantities. *IEEE Transactions on Industry Applications*, IA-19:3, 1983.

[6] Colin Schauder. Adaptive Speed Identification for Vector Control of Induction Motors without Rotational Transducers. *IEEE Transactions on Industry Applications*, 28:5, Sept/Oct 1992.

[7] Fangzheng Peng, T. Fukao. Robust Speed Identification for Speed Sensorless Vector Control of Induction Motors. *IEEE Transactions on Industrial Applications*, 30:1234–1240, Sept/Oct 1994.

[8] George C. Verghese, Seth R. Sanders. Observers for Flux Estimation in Induction Machines. *IEEE Transactions on Industry Electronics*, 35(1):85–94, Feb 1988.

[9] H.Kubota, K.Matsuse and T.Nakano. DSP Based Speed Adaptive Flux Observer of Induction Motor. *IEEE Transactions on Industry Applications*, 29(2):344–348, March/April 1993.

[10] M.W.Degner, R.D.Lorenz. Using Multiple Saliencies for the Estimation of Flux, Position and Velocity in AC Machines. *IEEE Transaction of Industry Applications*, 34:1097–1104, Sept/Oct 1998.

[11] P.L.Jansen, R.D.Lorenz. Transducerless Position and Velocity Estimation in Induction and Salient AC Machines. *IEEE Transactions on Industrial Applications*, 31:240–247, 1995.

[12] F.Blaschke, J.Vander Burgt, A.Vandenput. Sensorless Direct Field Orientation at Zero Flux Frequency. In *IEEE Industrial Applications Conference, Thirty-first IAS Annual Meeting*, volume 1, pages 189–196, San Diego, CA, USA, Oct 1996.

[13] M.Schroedl. Sensorless Control of AC Machines at Low Speed and Standstill Based on the "INFORM" Method. In *Industry Application Conference, Thirty-first IAS Annual Meeting*, volume 4, pages 270–277, San Diego, CA, Oct 1996.

[14] Q.Gao, G.M.Asher, M.Sumner, Makys.P. Sensorless Operation of Induction Machines Including Zero Frequency using Only Fundamental PWM Excitation. In *IEEE Industrial Thirty-second Electronics Annual Conference*, pages 793–798, Nov 2006.

[15] Qiang Gao. *Sensorless Control of Induction Machines at Zero and Low Frequencies*. PhD thesis, School of Electrical and Electronic Engineering, University of Nottingham, 2005.

[16] R.E.Kalman. New Results in Linear Filtering and Prediction Theory. *Transactions of ASME, Journal of Basic Engineering*, 83:95–108, 1961.

[17] R.E.Kalman. A New Approach to Linear Filtering and Prediction Problems. *Transactions of ASME Journal of Basic Engineering*, 82:35–45, 1960.

[18] J.Holtz. Sensorless Control of Induction Machines with or without Signal Injection. *IEEE Transactions on Industrial Electronics*, 53(1):7–30, Feb 2006.

[19] D.W.Novotny, T.A.Lipo. *Vector Control and Dynamics of AC Drives*. Oxford UK, 1996.

[20] P.L.Jansen, R.D Lorenz. Accuracy Limitations of Velocity and Flux Estimation in Direct Field Oriented Induction Machines. In *Fifth European Conference on Power Electronics and Applications*, pages 312–318, Sept 1993.

[21] H.Kubota, I.Sato, Y.Tamura, K.Matsuse, H.Ohta and Y.Hori. Regeneration Mode Low speed Operation of Sensorless Induction Motor drive with Adaptive Observer. *IEEE Transactions on Industry Applications*, 38(4):1081–1086, July 2002.

[22] F.Hoffmann, S.Koch. Steady State Analysis of Speed Sensorless Control of Induction Machines. In *24th Annual Conference of the IEEE, Industrial Electronics Society*, volume 3, pages 1626–1631, Archen, Germany, Sept 1998.

[23] J.Maes and J.A.Melkebek. Speed Sensorless Direct Torque Control of Induction Motors Using Adaptive Flux Observer. *IEEE Transactions on Industrial Applications*, 36:778–785, May/Jun 2000.

[24] M.Hinkkanen. Analysis and Design of Full-order Flux Observers for Sensorless Induction Motors. *IEEE Transactions on Industrial Electronics*, 51:1033–1040, Oct 2004.

[25] F.Hillenbrand. A Method for Determining the Speed and Rotor Flux of the Asynchronous Machine by Measuring the Terminal Quantities Only. In *Control in Power Electronics and Electrical Drives IFAC*, Lausanne, Switzerland, 1983.

[26] G.Henneberger,B.J.Brunsbach, Th.Klepsch. Field Oriented Control of Synchronous And Asynchronous Drives without Mechanical Sensors using a Kalman Filter. In *EPE91*, pages 664–671, Florence, Italy, 1991.

[27] Y.R.Kim, S.K.Sul and M.H.Park. Speed Sensorless Vector Control of Induction Motor Using Extended Kalman Filter. *IEEE Transactions on Industry Applications*, 30(5):1225–1233, 1994.

[28] L.Harnefors. A Comparison between Directly Parametrised Observers and Extended Kalman Filters for Sensorless Induction Motor Drives. In *Seventh International Conference on Power Electronics and Variable Speed Drive*, volume 21-23, pages 275–280, London, UK, 1998.

[29] L.Hanefors. Design and Analysis of General Rotor-Flux-Oriented Vector Control Systems. *IEEE Transaction on Industrial Electronics*, 48(2):383–390, April 2001.

[30] D.Todd, Y.Lee.Kwang. An Approach to Sensorless Operation of the Permanent Magnet Synchronous Motor Using Diagonally Recurrent Neural Network. *IEEE Transactions on Energy Conversion*, 18(1):100–106, March 2003.

[31] C.Lascu, I.Boldea, F.Blaabjerg. Very Low Speed Sensorless Variable Structure Control of Induction Machine Drives without Signal Injection. In *IEEE Interna-*

tional Electric Machines and Drives Conference, pages 1395–1401, Madison, WI, Jun 2003.

[32] J.Ci.Lopez, L.Romeral, A.Arias, E.Aldabas. Novel Fuzzy Adaptive Sensorless Induction Motor Drive. *IEEE Transactions on Industrial Electronics*, 53(4):1170–1178, Aug 2006.

[33] C.Ilas; A.Bettini; L.Ferraris; G.Griva and F.Profumo. Comparison of Different Schemes Without Shaft Sensor for Field Oriented Control Drives. In *Proceedings of IEEE Industrial Electronics Society*, pages 1579–1588, Bologna, Italy, 1994.

[34] K.Ohyama, G.M.Asher, M.Sumner. Comparative Analysis of Experimental Performance and Stability of Sensorless Induction Motor Drives. *IEEE Transactions on Industrial Electronics*, 53(1):178–186, 2006.

[35] C.Lascu; I.Boldea and F.Blaabjerg. Comparative Study of Adaptive and Inherently Sensorless Observer for Variable-Speed Induction Motor Drives. *IEEE Transactions on Industrial Electronics*, 53(1):57–65, 2006.

[36] C.DeWit.Canudas, A.Youssef, J.P.Barbot, P.Martin, F.Malrait. Observability Conditions of Induction Motors at Low Frequencies. In *IEEE Thirty-ninth Conference on Decission and Control*, volume 3, pages 2044–2049, Sydney,NSW, Dec 2000.

[37] J.Hu and B.Wu. New Integration Algorithms for Estimating Motor Flux Over a Wide Speed Range. *IEEE Transactions on Power Electronics*, 13:969–977, 1998.

[38] J.Holtz, J.Quan. Sensorless Vector Control of Induction Motors at Very Low Speed Using a Nonlinear Inverter Model and Parameter Identification. *IEEE Transactions on Industry Applications*, 38(4):1087–1095, 2002.

[39] Jacek F. Gieras and Mitchell Wing. *Permanent Magnet Motor Technology: Design and Applications*. Electrical and Computer Engineering. Marcel Dekker Inc, New York Basel, 2 edition, 2002.

[40] J.-I.Ha, M.Ohto, J.-H.Jang, S.-K.Sul. Design and Selection of AC Machines for Saliency-Based Sensorless Control. In *Industrial Applications Conference of IEEE, Thirty-Seventh IAS Annual Meeting*, volume 2, pages 1155–1162, 2000.

[41] J.Holtz and H.Pan. Elimination of Saturation Effects in Sensorless Position Controlled Induction Motors. *IEEE Transaction of Industry Applications*, 40:623–631, March/April 2000.

[42] T.M.Wolbank, R.Woehrnschimmel, J.L.Machl. Zero Speed Sensorless Control Signals of Induction Motors with Closed Rotor Slots. In *IEEE Power Electronics Specialists Conference 33rd Annual*, volume 2, pages 997–1002, 2002.

[43] J.Holtz. Sensorless Position Control of Induction Motors - An Emerging Technology. *IEEE Transactions on Industrial Electronics*, 45(6):840–852, 1998.

[44] J.Cilia, G.M.Asher, K.J.Bradley, M.Sumner. Sensorless Position Detection for Vector-controlled Induction Motor Drives Using an Asymmetric Outer-section Cage. *IEEE Transactions on Industrial Applications*, 33:1162–1169, 1997.

[45] L.Wang, R.D.Lorenz. Rotor Position Estimation for Permanent Magnet Synchronous Motor Using Saliency Tracking Self sensing Method. In *IEEE Thirty-fifth Industry Applications Society Annual Meeting*, 2000.

[46] M.W.Degner, R.D.Lorenz. Position Estimation in Induction Machines Utilizing Rotor Bar Slot Harmonics and Carrier Frequency Signal Injection. In *Power Conversion Conference*, pages 69–72, Nagaoka, Japan, 1997.

[47] M.Corley and R.D.Lorenz. Rotor Position and Velocity Estimation for a Salient-Pole Permanent Magnet Synchronous Machines at Standstill and High Speeds. *IEEE Transactions on Industry Applications*, 34:784–789, 1998.

[48] M.Linke, R.Kennel, J.Holtz. Sensorless Speed and Position Control of Synchronous Machines using Alternating Carrier Injection. In *IEEE International Electric Machines and Drives Conference IEMDC03*, volume 2, pages 1211–1217, 2003.

[49] T. Aihara, A.Toba, T.Yanase, A.Mashimo,K.Endo. Sensorless Torque Control of Salient-pole Synchronous Motor at Zero-speed Operation. *IEEE Transactions on Power Electronics*, 14:202–208, 1999.

[50] J-L.Ha, S-K.Sul. Sensorless Field Orientation Control of an Induction Machine by High Frequency Signal Injection. In *Industrial Applications Conference of IEEE, Thrity-second IAS Annual Meeting*, volume 1, pages 426–432, 1997.

[51] J.Holtz. Acquisition of Position Error and Magnet Polarity for Sensorless Control of PM Synchronous Machines. *IEEE Transactions on Industrial Applications*, 44:1172–1180, July/August 2008.

[52] J.Holtz and H.Pan. Acquisition of Rotor Anisotropy Signals in Sensorless Position Control Systems. *IEEE Transaction of Industry Applications*, 40:1379–1387, Sept/Oct 2004.

[53] C.Carusna, G.M.Asher, J.C.Clare. Sensorless Flux Position Estimation at Low and Zero Frequency by Measuring Zero Sequence Current in Delta Connected Cage Induction Machines. *IEEE Transaction of Industry Applications*, 41:609–617, Mar/April 2005.

[54] E.Robeischl and M.Schroedl. Direct Axis Current Utilization for Intelligent Sensorless Permanent Magnet Synchronous Drives. In *industrial Applications Conference 36th IAS Annual Meeting*, volume 1, pages 475–481. IEEE, 2001.

[55] E.Robeischl and M. Schroedl. Optimized INFORM Measurement Sequence for Sensorless PM Synchronous Motor Drives with Respect to Minimum Current Distortion. *IEEE Transaction of Industry Applications*, 40:591–598, Mar/April 2004.

[56] T.M.Wolbank, H.Giuliani, R.Woehrnschimmel, J.L.Machl. Sensorless Control of Induction Machines by Combining Fundamental Wave Models with Transient Excitation Technique. In *IEEE International Conference on Electric Machines and Drives*, pages 1379–1384, May 2005.

[57] T.M.Wolbank, J.Machl. A Modified PWM Scheme in Order to Obtain Spatial Information of AC Machines without Mechanical Sensor. In *Seventeenth Annual IEEE Applied Power Electronics Conference and Exposition*, 2002.

[58] J.Holtz and J.Juliet. Sensorless Acquisition of the Rotor Position Angle of Induction Motors with Arbitrary Stator Windings. *IEEE Transaction of Industry Applications*, 41:1675–1682, Nov/Dec 2005.

[59] M.A.Vogelsberger, M.Riepler, S.Grubic, T.G.Habetler, T.M.Wolbank. Integration of Transient and Fundamental Wave Excitation for Zero Speed Sensorless Control of AC Machines. In *Proceedings of the International Conference on Electrical Machines*, 2008.

[60] R.Raute, C.Caruana, C.S.Staines, J.Cilia, M.Sumner, G.Asher. Sensorless Control of Induction Machines by Using PWM Harmonics for Rotor Bar Slotting Detection. In *IEEE Industry Applications Society Annual Meeting*, pages 1–8, Edmonton, Alta, Oct 2008.

[61] N.Teske, G.M.Asher, K.J.Bradley, M.Sumner. Analysis and Suppression of Inverter Clamping Saliency in Sensorless Position Controlled Induction Machine Drives. In *IEEE Thirty-sixth Industry Applications Society Annual Meeting*, Chicago, 2001.

[62] C.Silva, G.M.Asher, M.Sumner. Influence of Deadtime Compensation on Rotor Position Estimation in Surface Mounted PM Machines using HF Voltage Injection. In *Power Conversion Conference*, volume 3, pages 1279–1284, April 2002.

[63] J.M.Guerrero, M.Leetmaa, F.Briz, A.Zamarron, R.D.Lorenz. Inverter Nonlinearity Effects in High-frequency Signal Injection Based Sensorless Control Methods. *IEEE Transactions on Industry Applications*, 41:618–626, March-April 2005.

[64] A.Arias, G.Asher, M.Sumner, P.Wheeler, L.Empringham, C.Silva. High Frequency Voltage Injection for the Sensorless Control of Permanent Magnet Synchronous Motors Using Matrix Converters. In *IEEE Industrial Electronics Society Thirtith Annual Meeting*, volume 1, pages 969–974, 2004.

[65] T.M.Wolbank, J.L.Machl. Influence of Inverter nonlinearity and Measurement Setup on Zero Speed Sensorless Control of AC Machines Based on Voltage Pulse Injection. In *IEEE Thirty-First Industrial Electronics Society Annual Conference*, pages 1568–1573, Nov 2005.

[66] T.M.Wolbank, B.Haidvoql. Influence of Different Inverter Control and Test Pulse Generation Schemes on Sensorless Control of AC Machines. In *Eighth International Conference on Power Electronics and Variable Speed Drive*, number 475, pages 280–285, London,UK, 2000.

[67] T.M.Wolbank, B.Hadivogl, R.Woehrnschimmel. Modulation of the Transient Reactances of Inverter Fed Indution Motors by Rotor Fixed Saliencies. In *IEEE*

International Symposium on Industrial Electronics, volume 1, pages 207–212, Cholula, Puebla, Dec 2000.

[68] N.Teske, G.M.Asher, M.Sumner, K.J.Bradley. Suppression of Staturation Saliency Effects for the Sensorless Position Control of Induction Motor Drives under Loaded Conditions. *IEEE Transactions on Industrial Electronics*, 47:1142–1150, Oct 2000.

[69] Q.Gao, G.Asher, M.Sumner. Sensorless Position and Speed Control of Induction Motors using High Frequency Injection and without off-line Precommissioning. In *IEEE 31st Annual Conference of Industrial Electronics Society*, 2005.

[70] R.Kusch, D.Naunin, R.D.Lorenz. Encoderless Position Estimation of a Squirrel Cage Synchronous Reluctance Machine. In *IEEE Twenty-ninth Annual Conference of Industrial Electronics Society*, volume 2, pages 1038–1043, Nov 2003.

[71] Y.S.Jeong; R.D.Lorenz; T.M.Jahns and S.K.Sul. Intial rotor position estimation of an interior permanent magnet synchronous machine using carrier-frequency injection methods. *IEEE Transaction of Industrial Application*, 41(1):1218–1223, Jan/Feb 2005.

[72] T.Noguchi; K.Yamada; S.Kondo and I.Takahashi. Initial Rotor Position Estimation Method of sensorless PM synchronous motor with no sensitivity to armature resistance. *IEEE Transactions on Industrial Electronics*, 45:118–125, Feb 1998.

[73] N.Ishiduka; K.Yoshizaki; A.Komatsuzaki and I.Miki. Estimation of Initial Rotor Position for Slotless PM Motor. In *Internaltional symposium on Power electronics Electrical Drives Automation and Motion*, pages 1229–1232, Ischia, June 2008.

[74] H.W.Broeck, H.C.Skudelny, G.V.Stanke. Analysis and Realization of a Pulsewidth Modulator based on Voltage. *IEEE Transaction of Industry Applications*, 24:142–150, Jan-Feb 1988.

[75] P.G.Handley, J.T.Boys. Space Vector Modulation: an Engineering Review. In *4th International Conference on Power Electronics and Variable Speed Drives*, pages 87–91, London, UK, Jul 1991.

[76] J.M.Erdman, R.J.Kerkman, D.W.Schlegel, G.L.Skibinski. Effect of PWM Inverters on AC Motor Bearing Currents and Shaft Voltages. *IEEE Transactions on Industry Applications*, 32:250–259, March 1996.

[77] G.Narayanan, Di Zhao, K.K.Harish, A.Rajapandian, V.T.Ranganathan. Space Vector Based Hybrid PWM Techniques for Reduced Current Ripple. *IEEE Transactions on Industrial Electronics*, 55(4):1614–1627, 2008.

[78] Li Ran, S.Gokani, J.Clare, K.J.Bradley, C.Christopoulos. Conducted Electromagnetic Emissions in Induction Motor Drive Systems Part I: Time Domain Analysis and Identification of Dominant Modes. *IEEE Transaction on Power Electronics*, 13(4):757–767, July 1998.

[79] E.Zhong, T.A.Lipo. Improvements in EMC Performance of Inverter-Fed Motor Drives. *IEEE Transactions on Industry Applications*, 31:1247–1256, 1995.

[80] A.von Jouanne,P.N.Enjeti. Design Considerations for an Inverter Output Filter to Mitigate the Effects of Long Motor Leads in ASD Applications. *IEEE Transactions on Industry Applications*, 33:1138–1145, Sept-Oct 1997.

[81] G.Busatto, C.Abbate, F.Iannuzzo, L.Fratelli, B.Cascone, G.Giannini. EMI Characterisation of High Power IGBT Modules for Traction. In *IEEE Thirty-Six Power Electronics Specialists Conference*, pages 2180–2186, June 2005.

[82] A.Kempski. EMI Noise Splitting into Common and Differential Modes in PWM Inverter Drive System. *IEEE Compatibility in Power Electronics*, 1:200–203, 2005.

[83] M.C.Caponet, F.Profumo, R.W.DeDoncker, A.Tenconi. Low Stray Inductance Bus Bar Design and Construction for Good EMC Performance in Power Electronic Circuits. *IEEE Transactions on Power Electronics*, 17:225–231, 2002.

[84] P.T.Finlayson. Output Filters for PWM Drives with Induction Motors. *IEEE Industry Applications Magazine*, 4:46–52, Jan-Feb 1998.

[85] D.A.Rendusara, P.N.Enjeti. An Improved Inverter Output Filter Configuration Reduces Common and Differential Modes dvdt at the Motor Terminals in PWM Drive Systems. *IEEE Transactions on Power Electronics*, 13:1135–1143, 1998.

[86] A.von Jouanne, D.A.Rendusara, P.N.Enjeti, J.W.Gray. Filter Techniques to Minimize the Effect of Long Motor Leads on PWM Inverter Fed AC Motor Drive Systems. *IEEE Transactions on Industry Applications*, 32:919–926, July-Aug 1996.

[87] Yuqing Tang. High Power Inverter EMI Characterization and Improvement Using Auxiliary Resonant Snubber Inverter. Master's thesis, Virginia Polytechnic Institute and State University, 1998.

[88] J.M.Miller. Dependence of the Input Impedance of a Three-electrode Vacuum Tube upon the Load in the Plate Circuit. *Scientific Papers of the Bureau of Standards*, 15:367–385, 1920.

[89] SEMIKRON. *SEMITRANS IGBT Modules Datasheet SKM 50 GB 123D.*

[90] Y.Zhang, S.Sobhani, R.Chokhawala. Snubber Considerations for IGBT Applications. *International Rectifier Designer Manual*, 3:135–145, 1995.

[91] W.McMurray. Selection of Snubbers and Clamps to Optimize the Design of Transistor Switching Converters. *IEEE Transactions on Industry Applications*, 1A16:513–523, June 1980.

[92] Andrew Nicholas; Edward Crellier . Rogowski coil, 2000.

[93] M.Rezaee, H.Heydari. Mutual Inductances Comparison in Rogowski Coil with Circular and Rectangular Cross Sections and Its Improvement. In *IEEE third Conference on Industrial Electronics and Applications*, pages 1507–1511, Singapore, 2008.

[94] D.A.Ward. Measurement of Current Using Rogowski Coils. In *IEE Colloquium on Instrumentation in the Electrical Supply Indusry*, pages 1–3, London, 1993.

[95] W.F.Ray, C.R.Hewson. High Performance Rogowski Current Transducers. In *IEEE Industry Applications Conference*, volume 5, pages 3083–3090, Rome, Oct 2000.

[96] D.Law. *Semiconductors and Semimetals, Vol22, Lightwave Communication Technology Part D*. Academic Pr, 1985.

[97] Analog Devices. *AD711 Precision Low Cost High Speed BiFET Op Amp*. USA.

[98] A.M.R.Amaral, A.J.M.Cardoso. An Experimental Technique for Estimating the Aluminum Electrolytic Capacitor Equivalent Circuit at High Frequencies. In *IEEE International Conference on Industrial Technology ICIT*, pages 86–91, 2005.

[99] G.Terzulli, B.W.Peace. Film Technology to Replace Electrolytic Technology. www.avx.com.

[100] M.Bramoulle. Electrolytic or Film Capacitor? . In *IEEE Industry Application Conference Thirty-third IAS Annual Meeting*, volume 2, pages 1138–1141, St. Louis, MO, Oct 1998.

[101] Generic Standard on Printed Board Design.

[102] J.Adam. New Correlations between Electrical Current and Temperature Rise in PCB Traces. In *IEEE twentieth Annual Semiconductor Thermal Measurement and Management Synposium*, pages 292–299, Mar 2004.

[103] Fuji Electric Device Technology Co., Ltd, Japan. *Fuji IGBT Modules Application Manual*, Feb 2004.

[104] LEM Components, www.lem.com. *Current Transducer LAP 50P Datasheet.*

[105] LEM Components, www.lem.com. *Voltage Transducer LV 25P Datasheet.*

[106] Hewlett Packard. *Quadrature Decoder/Counter Interface ICs Datasheet.*

[107] R.Heinz. Intelligent Interfaces between Power and Control. *Siemens Components Magazine*, 1(3):8–11, 1996.

[108] Agilent Technologies Inc. *Agilent 0.6 Amp Output Current IGBT Gate Drive Optocoupler Datasheet, HCPL-3150 HCPL-315J*, April 2005.

[109] C&D Technologies(NCL) Ltd, Arizona USA. *NMH Series Isolated 2W Dual Output DC/DC Converters Datasheet.*

[110] John M. Miller. Dependence of the Input Impedance of a Three-electrode Vacuum Tube upon the Load in the Plate Circuit. *Scientific Papers of the Bureau of Standards*, 15(351):367–385, 1920.

[111] Spectrum Digital Inc. *TMS320C6713 DSK Technical Reference*, May 2003.

[112] N.Teske, G.M.Asher, M.Sumner, K.J.Bradley. Encoderless Position Estimation for Symmetric Cage Induction Machines Under Loaded Conditions. *IEEE Transactions on Industry Applications*, 37(6):1739–1800, 2001.

[113] T.M.Wolbank, J.L.Machi, Th.Jager. Combination of Signal Injection and Neural Networks for Sensorless Control of Inverter fed Induction Machines. In *IEEE 35th Annual Power Electronics Speciallists Conference*, volume 3, pages 2300–2305, June 2004.

[114] P.Garcia, F.Briz, D.Raca, R.D.Lorenz. Saliency Tracking Based Sensorless Control of AC Machines Using Structured Neural Networks. *IEEE Transactions on Industry Applications*, 43:77–86, Jan-Feb 2007.

[115] T.M.Wolbank, K.Metwally. Tracking Inherent Saliencies of Standard Induction Machines for Zero Speed Sensorless Control Using Different Signal Processing Methods. In *IEEE Power Electronics Specialists Conference*, pages 4249–4255, June 2008.

[116] C.Brezinski. *Computational Aspects of Linear Control: Numerical Methods and Algorithms*. Springer, 2002.

[117] Richard C. Dorf, Robert H.Bishop. *Modern Control Systems*. Prentic Hall, 2008.

[118] A.Munoz and T.A.Lipo. Online Deadtime Compensation Technique for Open Loop PWM VSI Drives. *IEEE Transactions on Power Electronics*, 14:683–689, 1999.

[119] J.W.Choi and S.K.Sul. Inverter Output Voltage Synthesis Using Novel Dead Time Compensation. *IEEE Transactions on Power Electronics*, 11:221–227, 1996.

Appendix A

Control Platform

This appendix describes the control platform of the overall AC drive system. It consists of three PCB boards: a TMSC6713 DSK board, an FPGA board and an HPI daughtercard. It is shown in FigA.1.

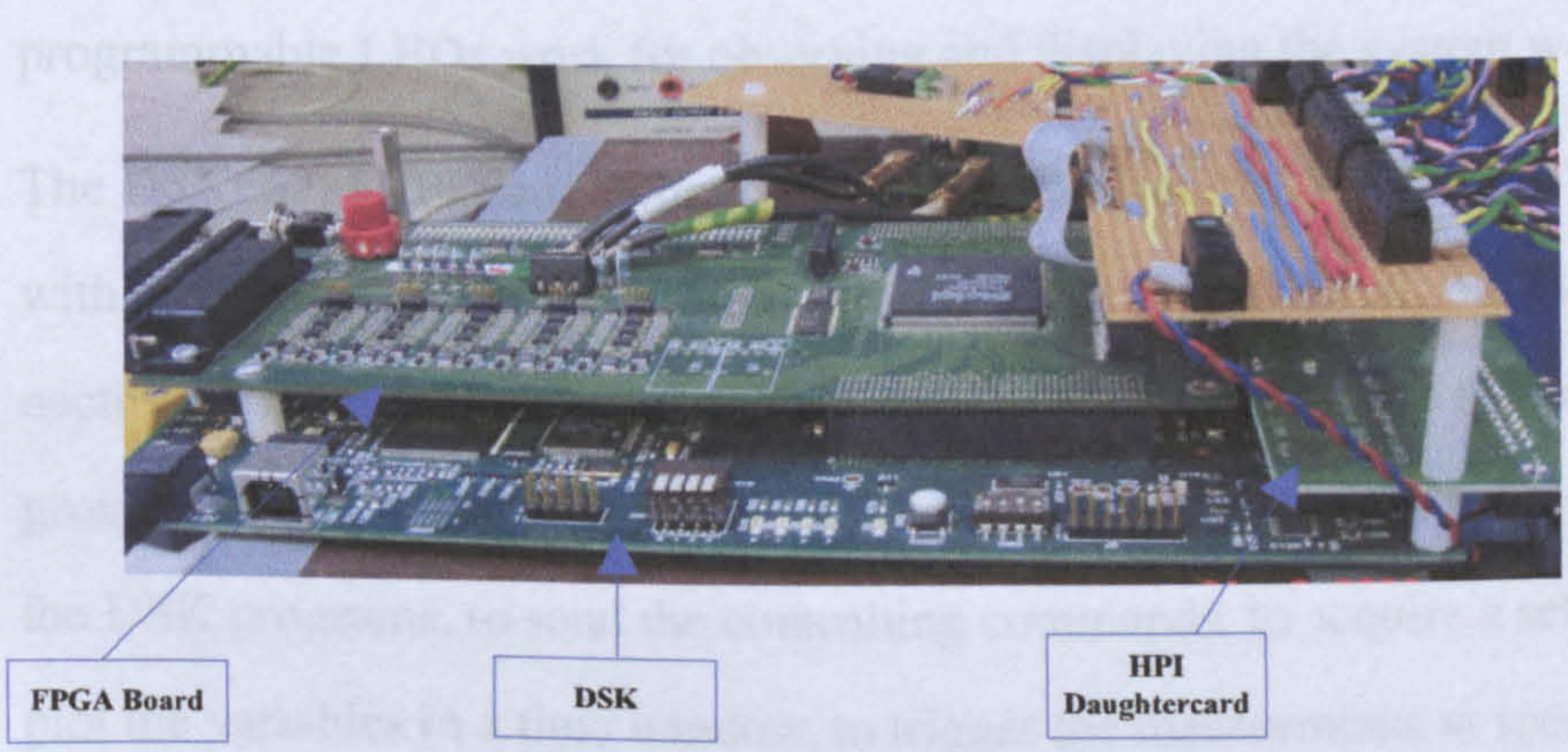

Figure A.1: Control Platform

The TMSC6713 DSK board is a low-cost standalone platform to develop applications for TI TMSC6713DSP. The DSK operates from a signal +5V external power suuply. The DSK is designed to work with TI's Code Composor Studio (CCS) development environment. Code Composer can communicate with the DSK through an embeded JTAG emulator with a USB host interface.The DSK provides three 80 pin expansion

connectors: the memory connector, the peripheral connector, and the HPI connector. These expansion connectors are used for plug-in daughtercards, which allows users to extend the DSK applications and provide specific interface.

The FPGA board is connected with the DSK board through both the memory connector and the peripheral connector. The heart of the FPGA board is an Actel ProASIC A500K050 FPGA. A crystal oscillator on the FPGA board provides the stable clock frequency of 10MHz for the whole control system. Besides the FPGA, a variety of functional circuits are designed on this borad. There are ten 12-bit A/D channels for data measurement. Each channel has a potentiometer and a comparator for setting the trip level. Each measurement channel is calibrated separately. Three groups of digital input/output ports are available, which makes it possible to send the FPGA internal programming signals out or recieve input signals. Users can indicate them as inputs or outputs independantly. Four D/A channels are also designed on this board. Fourty programmable LEDs work for observing and displaying the system working status.

The DSK66713HPI daughtercard is used to interface the TMS320C6713 DSK board with a personal computer through three possible ways: serial, parallel or USB connection. The graphical user interface software is developed by the author's research group based on the C6713DSK Matlab Interface Software. It enables the user to reset the DSK programs, to send the controlling commands, to acquire a set of variables, to plot the variables in a time window, to trigger the measurments at specific event, etc.

Appendix B

Circuit Schematics

Details regarding to the design considerations of the AC drive system have been discussed in Chapter 5. In this Appendix, the main schematic circuit diagrams are presented.

The main power circuit shown in FigB.1 is built on a big 2-layer PCB. The $+DC$ and $-DC$ link currents go through the upper and lower layers of this PCB respectively. The rectifier, DC-link capacitors, IGBT inverter, current and voltage measurement, protection circuits are all integrated by this PCB. The gate drive circuit shown in FigB.2 is designed to provide the drive signals for IGBT modules. The filter and amplifier circuit shown in FigB.3 is used to process the di/dt signals obtained by the di/dt sensors.

B.1 Power Circuit

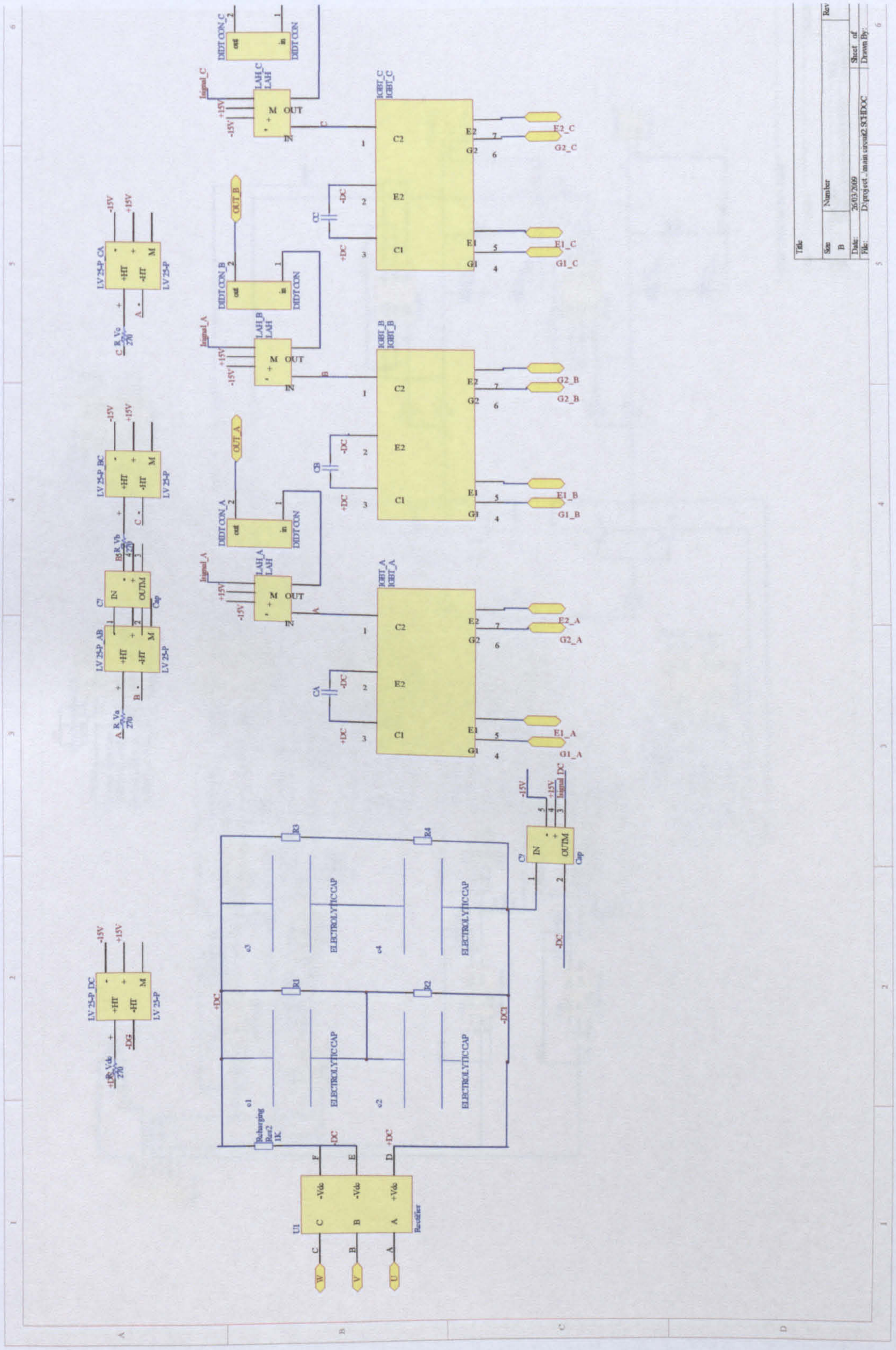

Figure B.1: Main power circuit

B.2 Gate Drive Circuit

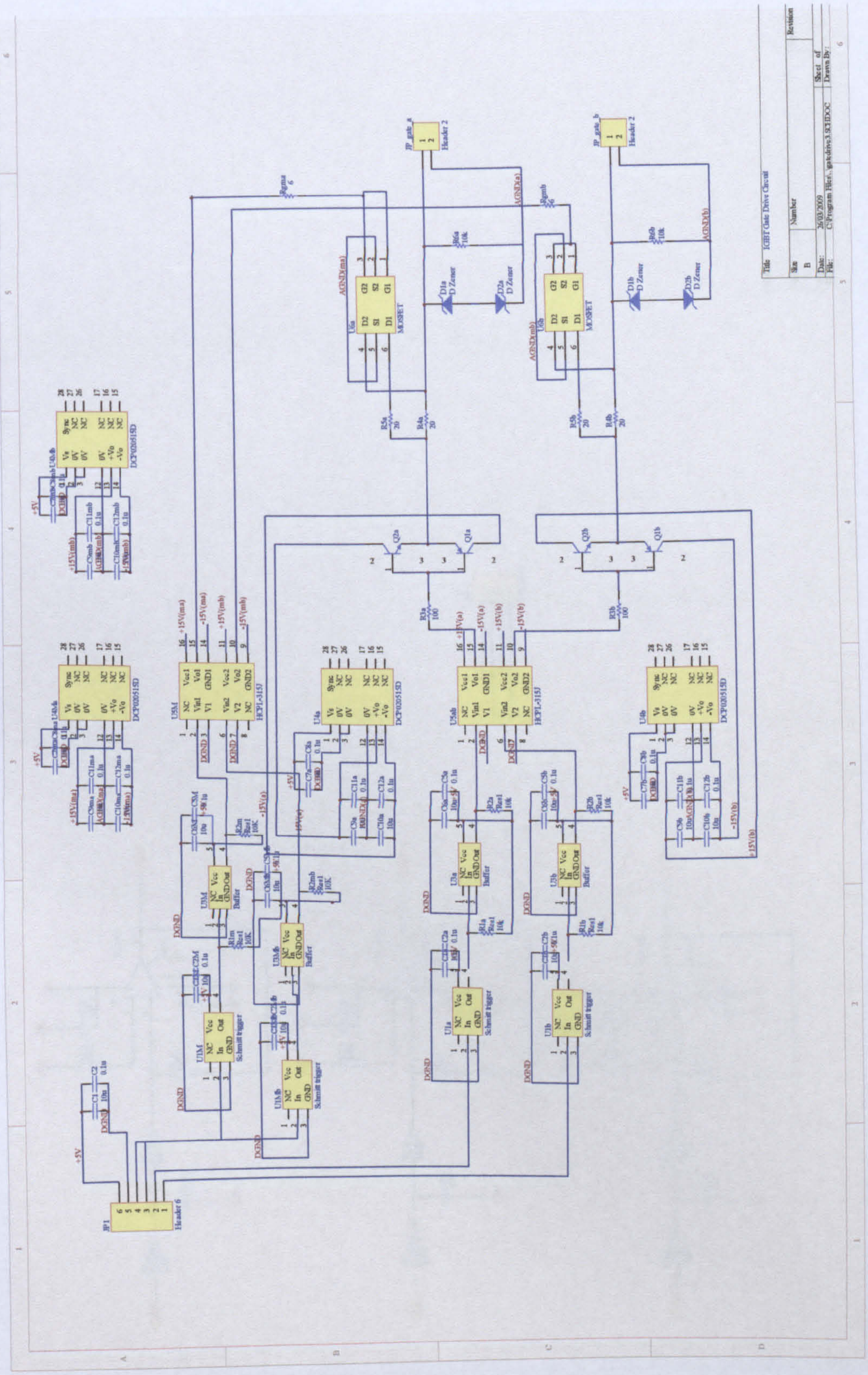

Figure B.2: Gate drive circuit for one phase

B.3 Filter and Amplifier Circuit of di/dt Signals

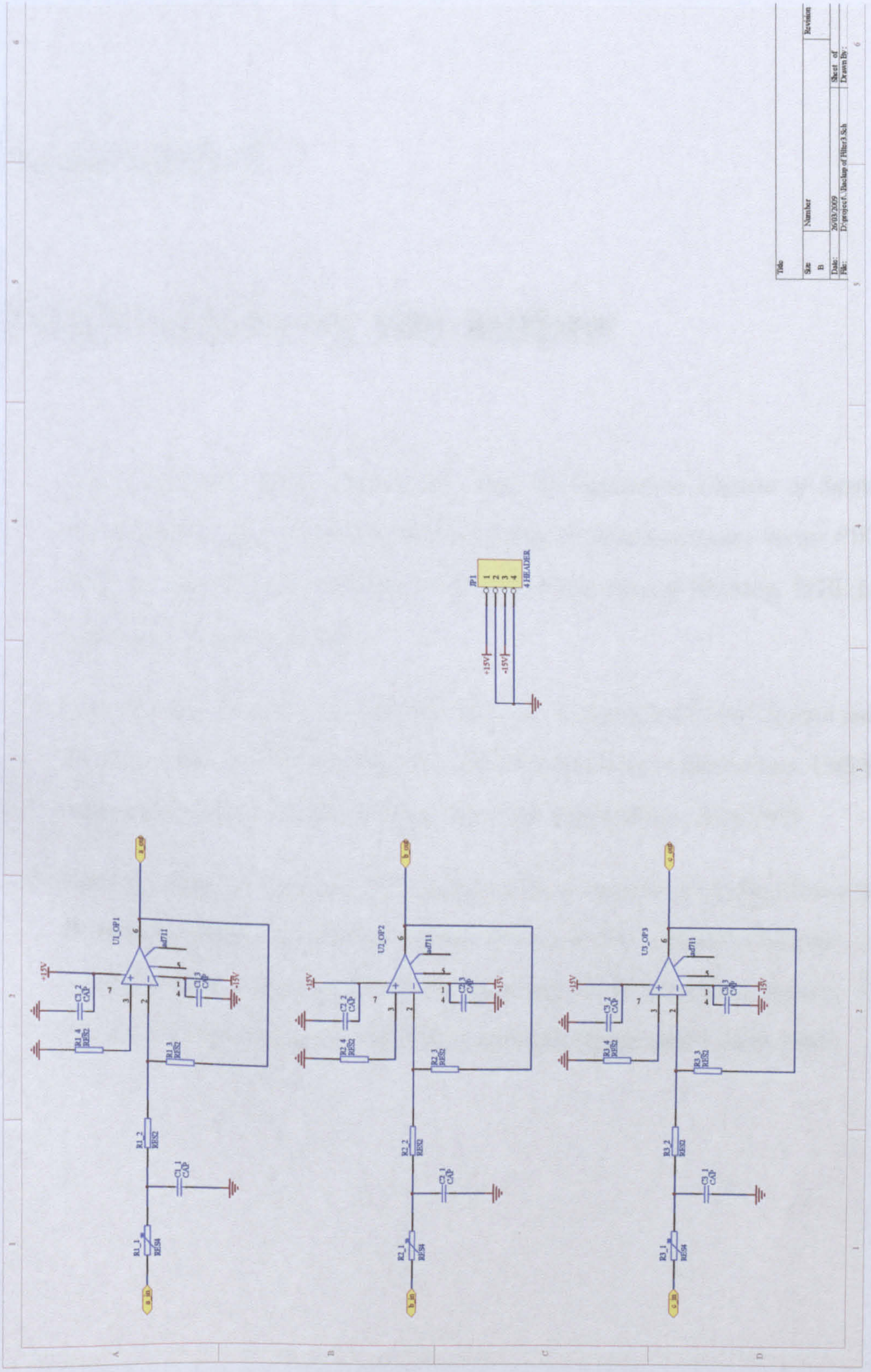

Figure B.3: Filter and amplifier circuit for the three phase di/dt signals

Appendix C

Publications by the author

1. Hua, Y.; Asher, G.M.; Sumner, M.; Gao, Q. *Sensorless Control of Surface Mounted Permanent Magnetic Machine Using the Standard Space Vector PWM.* Industry Application Conference, 2007. 42nd IAS Annual Meeting. IEEE IAS Sept. 2007, Page(s):661-667.

2. Hua, Y.; Asher, G.M.; Sumner, M.; Gao, Q. *Sensorless Control System using the Space Vector PWM Excitations with Reduced Current Distortions*, 13th European Conference on Power Electronics and Applications, Sept 2009

3. Gao, Q.; Hua, Y.; Sumner, M.; Asher, G.M. *Comparison of Two Sensorless Permanent Magnet Synchronous Motor Drives Fed by a Matrix Converter and a Voltage Source Inverter Using Fundamental PWM Excitation Signals*, 13th European Conference on Power Electronics and Applications, Sept 2009